UNIVERSITY OF TRENTO - Italy
Department of Civil, Environmental
and Mechanical Engineering

Doctoral School in Civil, Environmental and Mechanical Engineering
Curriculum 3. Modelling and Simulation - XXXI cycle 2016/2018

Doctoral Thesis - April 2019

Valentina Piccolo

Experimental and Novel Analytic Results for Couplings in Ordered Submicroscopic Systems: from Optomechanics to Thermomechanics

Supervisors
Prof. Luca Deseri, University of Trento, Italy
Prof. Daniele Zonta, University of Trento, Italy

Tutor
Dr. Andrea Chiappini, CNR-IFN, Trento, Italy

This is dedicated to everyone who looks different,
feels different, and thinks differently.
I am you.
Stay different.
Make a difference.

“The first principle is that you must not fool yourself — and you are the easiest person to fool.”

R. Feynman

Acknowledgements

This thesis would not have been possible without the inspiration and support of a number of wonderful individuals — my thanks and appreciation to all of them for being part of this journey and making this thesis possible.

I should first of all like to extend my warmest thanks to my Family who always supported my decisions, together with my "new family members" Jacopo, Angelo and Monica, to all of them goes my deepest gratitude for the continuous and precious support, funny moments and love.
I owe my deepest gratitude to my advisors Professor Luca Deseri and Daniele Zonta. I express my warmest gratitude to my associate advisor Maurizio Ferrari and especially to my tutor Andrea Chiappini, his guidance into the world of colloidal photonic crystals and his good advice has been essential for the realization of my PhD.
There were also moments that led to misunderstandings and some quarrelling, something that happens, but all in all it has been a pleasant journey.
I have been fortunate to come across many funny & good friends, without whom life would be bleak. Special thanks go Francesca for her ever-present support (since 2011) and for making me laugh as often and as loudly as she has, and to Beatrice & Veronica my "DisagioFamily".
My colleagues (and ex colleagues) who have then become my friends David Novel, Carlo Cappello, Patrick Covi and Manuel Scala, Emiliano Debiasi, Denise Bolognani, Rocco Di Filippo, Riccardo Giacomelli, Riccardo Cavuoto, Marco Rossi, Gianluca Rizzi, Alessandro Cazzolli, Roberto Guarino, Mirko Tommasini, Pietro Pollaci, Luca Argani, I give thanks for the drinks, lunches/dinners and talks we have enjoy together.
I also wish to thank my other colleagues for the enjoyable chats and support.
Talking about colleagues, I really want to thank Fiorella Pantano, with whom I had the pleasure of sharing the "Statica" course and had a really good time preparing the exams; and for all the good advice and exchanges.
I want to thank the CNR-IFN-Trento crew for their support and opportunities presented.
I deeply thank the people I met in Pittsburgh, from the reaserch side: Carmel Majidi, Sachin Velankar, Luca Pocivavsek and Kaushik Dayal whom also gave me the opportunity to continue my research projects; and Lisa, Martino and Giulia for their kindness.

I want also to thank my Professors Giorgio Cacciaguerra, Paola Gatti, Paolo Tosi, Dino Zardi, Alessandra Quendolo, Oreste S. Bursi, Nicola Tondini for their kindness, genuine interest and support. Nonetheless I want to express my gratitude to Professors Leoni, Piazza, Di Maggio, Gelisio, Piccolroaz for their interesting hints provided during my examinations for the admission to the following academic year.

Abstract

Theoretical modelling of challenging multiscale problems arising in complex (and sometimes bioinspired) solids are presented. Such activities are supported by analytical, numerical and experimental studies. For instance, this is the case for studying the response of hierarchical and nano-composites, nanostructured solid/semi-fluid membranes, polymeric nanocomposites, to electromagnetic, mechanical, thermal, and sometimes biological, electrical, and chemical agents. Such actions are notoriously important for sensors, polymeric films, artificial muscles, cell membranes, metamaterials, hierarchical composite interfaces and other novel class of materials.

The main purpose of this project is to make significant advancements in the study of such composites, with a focus on the electromagnetic and mechanical performances of the mentioned structures, with particular regards to novel concept devices for sensing. These latter ones have been studied with different configuration, from 3D colloidal to 2D quasi-hemispherical micro voids elastomeric grating as strain sensors.

Exhibited time-rate dependent behavior and structural phenomena induced by the nano/micro-structure and their adaptation to the applied actions, have been explored.

Such, and similar, ordered submicroscopic systems undergoing thermal and mechanical stimuli often exhibit an anomalous response. Indeed, they neither follow Fourier's law for heat transport nor their mechanical time-dependent behavior exhibiting classical hereditariness. Such features are known both for natural and artificial materials, such as bone, lipid membranes, metallic and polymeric "spongy" composites (like foams) and many others. Strong efforts have been made in the last years to scale-up the thermal, mechanical and micro-fluidic properties of such solids, to the extent of understanding their effective bulk and interface features. The analysis of the physical grounds highlighted above has led to findings that allow the describing of those materials' effective characteristics through their fractional-order response. Fractional-order frameworks have also been employed in analyzing heat transfer to the extent of generalizing the classical Fourier and Cattaneo transport equations and also for studying consolidation phenomenon.

Overall, the research outcomes have fulfilled all the research objectives of this thesis thanks to the strong interconnection between several disciplines, ranging from mechanics to physics, from structural health monitoring to chemistry, both from an analytical and numerical point of view to the experimental one.

Publications

As a result of the work conducted by the author during her years of doctorate, the following publications have been produced:

Journal Publications

_ G. Alaimo, **V. Piccolo**, A. Cutolo, L. Deseri, M. Fraldi, "A Fractional Order Theory of Poroelasticity", Mechanics Research Communications, March 2019, Under Review.

_ A. Chiappini, C. Armellini, **V. Piccolo**, L. Zur, D. Ristic, D. J. Jovanovic, A. Vaccari, D. Zonta, G.C. Righini, M. Ferrari, "Colloidal Crystals Based Portable Chromatic Sensor for Butanol Isomers and Water Mixtures Detection". Optical Materials, Optical Materials Volume 90 (2019), Pages 152-158, doi 10.1016/j.optmat.2019.02.039.

_ V. Piccolo, A. Chiappini, C. Armellini, M. Mazzola, A. Lukowiak, A. Seddon, M. Ferrari, D. Zonta, "Quasi-Hemispherical Voids Micropatterned PDMS as Strain Sensor". Optical Materials 86 (2018) pp. 408-413, ISSN: 0925-3467, doi: 10.1016/j.optmat.2018.10.038.

_ **V. Piccolo**, A. Chiappini, C. Armellini, M. Barozzi, A. Lukowiak, P.-J. A. Sazio, A. Vaccari, M. Ferrari, D. Zonta, "2D Optical Gratings Based on Hexagonal Voids on Transparent Elastomeric Substrate". Micromachines 9 (2018) pp. 1-9, doi: 10.3390/mi9070345

_ **V. Piccolo**, G. Alaimo, A. Chiappini, M. Ferrari, D. Zonta, L. Deseri, M. Zingales "Fractional-order theory of thermoelasticity II: Quasi-static anomalous behavior of bars". 2017. J. Eng. Mech., 2018, 144(2): 04017165, doi: 10.1061/(ASCE)EM.1943-7889.0001395.

_ G. Alaimo, **V. Piccolo**, A. Chiappini, M. Ferrari, D. Zonta, L. Deseri, M. Zingales "Fractional-order theory of thermoelasticity I: generalization of the Fourier equation and thermodynamical consistency". J. Eng. Mech., 2018, 144(2): 04017164, doi: 10.1061/(ASCE)EM.1943-7889.0001394.

Book Chapter

_ Chapter 3 “Glass Nanospheres and Artificial Opals” by A. Chiappini, C. Armellini, A. Carpentiero, L. Pasquardini, A. Vaccari, S. Pelli, **V. Piccolo**, A. Lukowiak, G. C. Righini, R. Ramponi, D. Zonta, and M. Ferrari; in “Glass micro- and nano-spheres: physics and applications” by G. Righini, Pan Stanford, Print ISBN: 9789814774635.

Conference Proceedings Publications

_ T.N.L. Tran, C. Meroni, D. Massella, L. Zur, A. Chiasera, A. Chiappini, Y.G. Boucher, A. Vaccari, **V. Piccolo**, S. Varas, C. Armellini, A. Carpentiero, D. Zonta, B. Boulard, D. Dorosz, B. Rossi, A. Lukowiak, R. Ramponi, G.C. Righini, M. Ferrari, "Light management in glass photonics: structures and applications". Proceedings REMat 2018, 5th International Conference on RARE EARTH MATERIALS, Wrocław, Poland, May 16-18.

_ **V. Piccolo**, A. Vaccari, A. Chiappini, C. Armellini, L. Deseri, M. Ferrari, D. Zonta, "Mechanochromic Response of 3D Composite Photonic Crystals by Numerical Simulation". Proc. of European Workshop on Structural Health Monitoring (EWSHM) 2018. (peer rev.)

_ **V. Piccolo**, A. Chiappini, A. Vaccari, A. Calà Lesina, M. Ferrari, L. Deseri, D. Zonta "Validating 3D Photonic Crystals for Structural Health Monitoring". Proceedings of Structural Health Monitoring 2017 (IWSHM 2017). (peer rev.)

_ **V. Piccolo**, A. Chiappini, A. Vaccari, A. Calà Lesina, M. Ferrari, L. Deseri, D. Zonta, "Finite Difference Analysis and Experimental Validation of 3D Photonic Crystals for Structural Health Monitoring". SPIE Smart Structures 2017, Portland, Oregon (USA). Proc. of SPIE Vol. 10168 101681E-1, doi: 10.1117/12.2263975. (peer rev.)

_ **V. Piccolo**, A. Piotrowska, A. Chiappini, A. Vaccari, M. Ferrari, L. Deseri, D. Zonta, "Numerical Characterization of Mechanochromic Photonic Crystals for Structural Health Monitoring". Proceedings from the 8th European Workshop on Structural Health Monitoring (EWSHM2016), Vol.21 No.08 (Aug2016) ISSN 1435-4934. (peer rev.)

_ **V. Piccolo**, A. Piotrowska, A. Chiappini, A. Vaccari, M. Ferrari, L. Deseri, D. Zonta "Photonic crystal slab strain sensors: A viable tool for

structural health monitoring". Proceedings ICTON 2016, 18th International Conference on Transparent Optical Networks, Trento, Italy, July 10-14, pp. 1-4, doi: 10.1109/ICTON.2016.7550655. (peer rev.)

_ A. Piotrowska, **V. Piccolo**, A. Chiappini, M. Ferrari, M. Pozzi, L. Deseri, D. Zonta "Mechanochromic Photonic Crystals for Structural Health Monitoring". Proceedings 10th International Workshop on Structural Health Monitoring (IWSHM 2015), doi: 10.12783/SHM2015/386. (Before the beginning of the PhD) (peer rev.)

_ A. Chiappini, S. Nodehi, C. Armellini, **V. Piccolo**, D. Zonta, S. M. Pietralunga, M. Ferrari "Engineering optical and spectroscopic properties of colloidal crystals". Atti a conferenza FOTONICA 2018.

_ A. Chiappini, A. Armellini, A. Vaccari, **V. Piccolo**, A. Piotrowska, D. Zonta, M. Ferrari "Assessment of the chromatic behavior of colloidal sensors". Atti a conferenza, FOTONICA 2017

_ L- Pocivavsek, **V. Piccolo**, K. Y. Lee, S. Velankar, M. Fraldi, M. Zingales, L. Deseri "Buckling of lipid monolayers on viscous layers mimicking lung surfactants". AIMETA 2017.

Papers to be Submitted to an International Journal

_ **V. Piccolo**, A. Chiappini, C. Armellini, A. Vaccari, L. Deseri, M. Ferrari and D. Zonta, "Stimuli-Responsive Colloidal Crystal for Structural Health Monitoring: Fabrication and Numerical Modelling".

Papers in preparation

_ **V. Piccolo**, J. Wissman, L. Deseri and C. Majidi, "Scaling Laws for Dielectric Elastomers Actuators".

_ A. R. Carotenuto, A. Cutolo, M. Fraldi, L. Lunghi, **V. Piccolo**, M. Babaei, K. Dayal, M. Zingales, M. Inamdar, and L. Deseri, "Membrane mechanobiology predicts cell response triggered by G-PCRs and why they localize on lipid rafts".

_ **V. Piccolo**, L. Pocivavsek, G. Mensitieri, M. Zingales, and L. Deseri, "Soft-to-Hard Device Scaling of Wrinkling of Solid Films Embedded in Deep Viscous Fluids".

Contents

1. Introduction

From atoms and molecules to crystals and bulk components, optical materials are naturally structured at different scales [1]. Thanks to tremendous progresses in nanotechnologies, these optical materials can also be artificially structured to the same different scales [2].
The interaction of materials with optical waves and photons is strongly dependent on the structure, which can then be used to control light field distribution and light propagation. This allows the development of a wide range of key components for optical systems and it is now a major field of photonics. Refraction, interferences, diffraction, scattering, anisotropy, absorption, light emission, and nonlinear effects are all widely used to develop photonic components [3, 4].
The applications are numerous and generally belong to what are called information and communication technologies [5] and green photonics [6]. Such materials can find application in different strategic areas such as food security [7] and civil infrastructures [8].
From a structural point of view, depending on deposition process and the material, the natural micro/nanostructure of the structures can be more or less complex. This has different consequences on the optical properties, especially depending on the assembly, meaning when the materials are periodically structured in one- (1D), two- (2D), or three-dimensions (3D) [9]. For optical coatings, the light is reflected or transmitted through the sample. On the contrary, diffraction structures are generally used to distribute the light in a controlled way in different directions of the space. The association of diffractive and interference structures in 3D components allows for controlling the directions of the propagation and the spectral distribution of the optical waves in the space. In particular, the local field and the propagation in the structure can be adjusted with the photon lifetime. The typical dimensions of the structure are in the order of a part of the wavelength. These periodically structured materials are also named photonic crystals because light waves behave similarly to the wave function of electrons in crystals [10].
Referring to the different applications in recent years, photonic sensors have seen a massive development because of the increasing demand of sensing applications in healthcare [11], defence, security [12], aerospace [14], environment [13], food quality control [15], to name a few.
Nowadays, integrated PhC-based sensors represent one of the most popular class of photonic sensors, generally employed for physical and chemical/biochemical sensing. In this context, the principal advantages

of these intriguing photonic sensor architectures are ultra-high light confinement in very small volumes, high wavelength selectivity, ultra high sensitivity and selectivity in sensing mechanism.
Among them a specific class is based on colloidal crystals (2D and/or 3D). From a fabrication point of view in the last years several methods have been developed for their realization, for example the bottom-up approach which is based on the self-assembly processes of suitable building blocks [16].
In most cases, nanospheres of silica or polystyrene can be assembled into ordered 3D and 2D structures. In this case, the obtained sample consists of a composite dielectric with a periodically varying refractive index, that induces a forbidden frequency gap where the electromagnetic wave can not be propagated. From energetic considerations, it has been verified that nanospheres are assembled in a centered cube (fcc) packing with the <111> direction perpendicular to the film surface [17]. Furthermore, it is worth mentioning that the refractive index contrast between the sphere and its surrounding environment determines the scattering strength of the single building block and thereby determines the key parameters of the final complex dielectric. In fact, under specific conditions regarding the refractive index contrast and topology of the structure [18, 19], stop bands along every direction of propagation may share a common interval of frequencies in which electromagnetic modes will be forbidden: the so called photonic band gap. The existence of stop bands instead implies forbidden frequency channels for the propagation of light along certain directions. Considering a disordered situation, the characterizing sample parameters are the mean free path and the diffusion coefficient, while in an ordered photonic crystal case, the main parameters are the width and positions of the stopbands and/or band gap. These last features have been employed for the development of engineered photonic crystal in particular for the realization of optical sensors, by infiltrating the voids with specific responsive materials [20].
As previously recalled, the position and the width of the photonic band structure mainly depends on the lattice constants and the refractive indices of the dielectrics, in particular, considering the infiltration process, it generally produces, with respect to the bare colloidal crystal, a variation of the stop band and in particular its red shift due to an increase of the effective index, on the other hands a decrease of the full width of the band gap is present as described by Shkunov et al. [21].
In this regard, colloidal crystals may represent a class of ideal candidates for fabricating optical sensors that can be used to monitor, measure, and display environmental variations in terms of color changes (which can even be easily visualized by the naked eye). As a matter of fact, such a strategy has been employed by fishes (such as the

blue damselfish) to reconfigure their skin colors in response to environmental changes.
By embedding colloidal crystals in appropriate responsive material such as polymer hydrogels, Asher et al. have demonstrated the fabrication of temperature-, pH-, and ion-responsive optical sensors [22, 23]. The hydrogel colloidal crystals developed by Hu et al. and Lyon et al. have enabled them to tune the color of diffracted light either by varying temperature or by applying an electric field [24]. In [25, 26 27]. have been demonstrated that colloidal crystals embedded in thin films of appropriate polymer matrices could serve as mechanical sensors to provide a platform for in situ monitoring of strains caused by uniaxial stretching or compressing. In all of these demonstrations, the lattice constant and thus the color exhibited by the colloidal crystal, varied in response to the environmental change(s). In a number of related studies, change in refractive index was also demonstrated as a means to detect variations in the environment. In this contest appear evident that the choice of the infiltrating material is correlated to the kind of stimuli that one wants to determine.
Finding the perfect balance between the matrix and the spheres has been the goal of this thesis for design and fabricate a new kind of strain sensor which could be a great improvement in the field of structural health monitoring. For this latter field the key parameter is the sensitivity of the sensor to the external stimuli, in this specific case the sensitivity to strain. To this aim, several other experiments and studies have been conducted in order to magnify this paramenter. This lead to 2D semi-hemispherical voids micropatterned pdms, an optical grating that shown a higher sensitivity. The drawback is that the change in the strain field could not be seen by the naked eye as in the previous structures, but this 2D structure allow one to know the direction and entity of the strain field.
This first part of the present thesis has been developed through experiments, analytical models and numerical models to prove the results of the investigations and support the potential of these novel kind of sensors.
Ordered nanostructured materials, such as the ones presented above, have different physical behaviors depending (i) on the ways in which their nano/micro-structure is organized, and (ii) on whether or not such ordering is hierarchical. In this second case, if the number of levels in which a hierarchy can be recognized is sufficiently large, often times some key features of the effective physical behaviour of such materials can be mathematically captured by fractional models. As it is well known from the literature, this is certainly the case for fractal materials, although fractional-order models may be used to accurately

approximate the effective behaviour of materials with an ordered nano/microstructures organized in a finite number of hierarchies.
The focus of the second part of this thesis deals, in fact, with novel analytical models in the context of fractional-order calculus.
This particular field of calculus is usually referred to as the generalization of the ordinary differential calculus introducing real-order integrals and derivatives. It traces back to the basic definitions by Riemann as well as to successive memories of famous mathematicians [28], while, more recently, other scientists focused on the feasibility of integral measures involved in fractional-order operators [29, 30, 31].
After having fully consolidated into the mathematical word, their introduction into continuum field theories has received significant interests worldwide [32, 33, 34, 35, 36, 37]. Indeed, the replacement of classical operators with their real-order counterparts $\left(\frac{d}{dx} \to \frac{d^{\alpha}}{dt^{\alpha}} \text{and} \frac{d}{dt} \to \frac{d^{\beta}}{dt^{\beta}} \right)$ with $\alpha, \beta \in \Re$ (where $\Re$ is the set of real numbers) has proved to be valuable in several engineering and physical contexts predicting phenomena with great accuracy [38, 32, 39, 40].
The use of fractional-order operators has been also reported in non-local continuum field theories of mechanics [41, 42, 43, 44, 45, 46, 47], non-local heat transfer [48, 49, 50, 51] stochastic analysis [52, 53, 54, 55], diffusive transport [56, 57, 58, 59], biophysics [60], rheology and many others.
Despite their rapid success, the physics beyond the use of fractional-order derivative was still lacking. The answer to this fundamental point would be of great stimulus for worldwide researchers to re-derive the classical continuum field theories in terms of fractional-order operators.
On that subject, a strong effort has been profused during last years, including this thesis, to provide a solid physical ground in the use of fractional-order derivative in the transport equations. Cases involving polymer viscoelasticity, anomalous fluid diffusion, as well as laminar flow across fractal sets have been recently provided [61, 62, 63, 64].
Fractional-order calculus has been also used in the theory of thermo-elasticity to generalize the classical Fourier and Cattaneo transport equations [65, 66, 67, 68]. However, no physical ground in the formulation of neither anomalous heat transfer nor thermo-elasticity theory has been provided, leading to a non-physical representation of the thermoelastic phenomena reported in such studies.
In the present thesis, the author obtains a fractional-order Fourier diffusion law from a multi-scale rheological model and provide a physical exact description of the fractional-order Fourier diffusion equation that is also thermodynamically consistent. Then the coupled phenomenon, meaning the thermo-elasticity problem, has been

analysed, where a measure of the signature of the anomaly based on a measure of the energy rate is explored.
This, toghether with the fractional-order consolidation, provides a step forward to the answer of the physics beyond the use of fractional-order derivatives. In fact, the memory formalism in the flux-pressure constitutive relation, ruling the water diffusion phenomenon occurring in several classes of porous media have been studied. The resulting flux-pressure law has been applied to the classical 1D Terzaghi's consolidation problem. The memory formalism, useful to capture non-Darcy behavior, is modeled by the Caputo's fractional derivative. It has been shown that the time-evolution of both the degree of consolidation and the pressure fields is strongly influenced by the order of Caputo's fractional derivative. It has been demonstrated that in a classical Terzaghi's consolidation process of a sand sample, the classical Darcy equation may lead to inaccurate estimates of the consolidation time.
This clearly shows the importance of taking into account the submicrometric structure of the medium in which a physical phenomenon occurs.

The aim of the thesis is to develop experimental and novel analytical models for couplings in ordered submicroscopic systems, ranging from optomechanics to thermomechanics.
To this end, the structure of the thesis is the following:
the second chapter provides a comprehensive state of the art of glass nanospheres and artificial opals, with the description of the mechanisms of growth for the synthesis of monodisperse dielectric nanospheres and the condition for the realization of colloidal crystals. After this overview on fabrication processes, structural and optical properties have been discussed. And at the end, several examples of opals systems are reported and analysed, exploiting their potential applications.
The third chapter is linked with the second one because it presents a focus on one particular 3D colloidal crystal structure that has been tailored specifically for structural health monitoring application. This colloidal crystal structure has been investigated both with experiments that coupled optic and mechanics and then validated through an analytical model and then a numerical one that takes into account the nanostructures that changes with the application of an external stimuli.
The fourth and fifth chapters deals with a 2D optical grating made via colloidal route. These structures have been studied in order to make a step forward to the enhancement of the sensitivity for structural health monitoring sensors. In this frame both experiments and new analytical models for the interpretation of the results have been performed.

The sixth chapter revisits the 3D colloidal structure which have been investigated to see its response to organic solvents in order to study the swelling and diffusion process.
These kind of analysis regarding diffusive and transport problems have been carried out from a purely analytical point of view in the last three chapters, employing the fractional-order operators and taking into account the memory effect of structured systems, which has been discussed above.

References

[1] Russell J. Gehr, and Robert W. Boyd "Optical Properties of Nanostructured Optical Materials" Chem. Mater., 1996, 8 (8), pp 1807–1819.
[2] Jess Mathew "An Overview of Recent Progresses in Nanotechnology" Journal of Electrical Engineering and Science, Vol. 2016, 2(1), pp. 8-16
[3] Martín-Palma, R.J., Martínez-Duart, J.M. "Nanotechnology for Microelectronics and Photonics." 2017 Elsevier pp. 1-317.
[4] Bahaa E. A. Saleh Malvin Carl Teich "Fundamentals of Photonics" Wiley 2012
[5] Ferrari, M., Taccheo, S., "Special Section on Glass Photonics for Integrated Optics" Optical Engineering (2014) 53 pp. 071801-1/2
[6] Eisenstein, G., Bimberg Green, D. "Photonics and Electronics" Springer International Publishing, 2017
[7] Estevez, M.C., Alvarez, M., Lechuga, L.M. "Integrated optical devices for lab-on-a-chip biosensing applications" Laser Photonics Rev., (2012) 6(4) pp. 463-487.
[8] De, M., Kumar Gangopadhyay, T. and Kumar Singh, V. "Prospects of Photonic Crystal Fiber as Physical Sensor: An Overview." Sensors 2019, 19(3), pp. 464-491.
[9] Bellingeri, M., Chiasera, A., Kriegel, I., Scotognella, F. "Optical properties of periodic, quasi-periodic, and disordered one-dimensional photonic structures" Optical Materials (2017) 72, 403-421
[10] Klein, L., Aparicio, M., Jitianu, A. "Handbook of Sol-Gel Science and Technology" Springer 2018 Chapter 72 Makoto Kuwabara Photonic Crystals Fabricated by Sol-Gel Process 2128-2154.
[11] Inan, H., Poyraz, M., Inci, F., Lifson, M. A., Baday, M., Cunningham, B. T. "Photonic crystals: emerging biosensors and their promise for point-of-care applications" Chem Soc Rev. (2017) 46(2) pp. 366–388.

[12] Li, C., Zhou, X., Wang, K., Li, K., Song, Y. “Progress of electrically responsive photonic crystals” Composites Communications (2019) 12, pp. 47-53.
[13] Katyba, G. M., Zaytsev, K. I., Chernomyrdin, N.V., Shikunova, I.A., Komandin, G.A., Anzin, V.B., Lebedev, S.P., Spektor, I.E., Karasik, V.E., Yurchenko, S.O., Reshetov, I.V., Kurlov, V.N., Skorobogatiy, M. “Sapphire Photonic Crystal Waveguides for Terahertz Sensing in Aggressive Environments” Advanced Optical Materials (2018) 6(22), pp. 1800573/1-10
[14] Falconi, M.C., Palma, G., Starecki, F., Nazabal, V., Troles, J., Adam, J.L., Taccheo, S., Ferrari, M., Prudenzano F. “Novel pumping schemes of Mid-IR photonic crystal fiber lasers for aerospace applications” International Conference on Transparent Optical Networks (2016) 2016, 7550623/1-5.
[15] Malinin, A.V., Zanishevskaja, A.A., Tuchin, V.V., Skibina, Yu.S., Silokhin, I.Yu. “Photonic crystal fibers for food quality analysis Progress in Biomedical Optics and Imaging” - Proceedings of SPIE (2012) 8427, pp. 842746/1-8.
[16] Galisteo-López, J.F., Ibisate, M., Sapienza, R., Froufe, L., Blanco, A., Lopez, C. “Self-Assembled photonic structures” Adv. Mater. (2011) 23, pp.30-69.
[17] Woodcock, L.V. “Entropy Difference Between Face-Centered Cubic and Hexagonal Close Packed Crystal Structure” Nature 385 (1997) pp. 141-143.
[18] Galisteo-López, J. F., Palacios-Lidón, E., Castillo-Martínez, E. and López, C. “Optical study of the pseudogap in thickness and orientation controlled artificial opals” Phys. Rev. B (2003) 68, 115109/1-8.
[19] Maurin, I., Moufarej, E., Laliotis, A. and Bloch, D. “Optics of an opal modeled with a stratified effective index and the effect of the interface” Journal of the Optical Society of America B (2015) 32, pp. 1761-1772.
[20] Kim, S., Kurihara, S. “Photoactive Functional Soft Materials A Photoresponsive” Wiley 2018 Chapter 10 Multi-Bilayered Film for a Tunable Photonic Crystal. (2018) 341–360.
[21] Shkunov, M.N., Vardeny, Z.V., DeLong, M.C., Polson, R.C., Zakhidov, A.A., Baughman, R.H. “Tunable, Gap-State Lasing in Switchable Directions for Opal Photonic Crystals” Adv. Funct. Mat. (2002) 12, pp. 21–26.
[22] Bohn, J.J., Tikhonov A. and Asher, S.A. “Colloidal Crystal Growth Monitored by Bragg Diffraction Interference Fringes” Journal of Colloid and Interface Science, (2010) 350, pp. 381-386
[23] Cai, Z., Kwak, D.H., Punihaole, D., Hong, Z., Velankar, S., Liu, X. and Asher, S.A. “A Photonic Crystal Protein Hydrogel Sensor

for Candida albicans" Angewandte Chemie International Edition (2015) 54 pp. 13036-13040.

[24] Debord, J. D., Eustis, S., Byul Debord, S., Lofye, M.T., Lyon, L. A. "Color-Tunable Colloidal Crystals from Soft Hydrogel Nanoparticles" Adv. Mater. (2002) 14, pp. 658-662

[25] Foulger, S. H., Jiang, P., Ying, Y., Lattam, A. C., Smith Jr., D. W., Ballato, J. "Photonic Bandgap Composites" Adv. Mater. (2001) 13, pp.1898-1901.

[26] Fudouzi, H., Tsuchiyaa, K., Todoroki, S. "Smart photonic coating for civil engineering field: for a future inspection technology on concrete bridge" Proc. of SPIE (2017) 10168, pp. 1016820/1-6.

[27] Meng, Y., Tang, B., Ju, B., Wu, S., Zhang S. "Multiple Colors Output on Voile through 3D Colloidal Crystals with Robust Mechanical Properties" ACS Appl. Mater. Interfaces, 2017 9, pp. 3024–3029.

[28] Samko, S., Kilbas, A., and Marichev, O. (1989). "Fractional integrals and derivatives", Gordon Breach, Amsterdam, Netherlands.

[29] Bongiorno, D. (2009). "On the problem of regularity in the Sobolev space $W^{1;n}_{loc.}$" Topol. Appl., 156(18), 2986–2995.

[30] Bongiorno, D. (2014). "Metric differentiability of Lipschitz maps." J. Aust. Math. Soc., 96(1), 25–35.

[31] Bongiorno, D., and Corrao, G. (2015). "On the fundamental theorem of calculus for fractal sets." Fractals, 23(2), 1550008.

[32] Metzler, R. (2000). "Generalized Chapman-Kolmogorov equation: An unified approach to the description of anomalous transport in external fluids." Phys. Rev. E, 62(5), 6233–6245.

[33] Hilfer, R., and Anton, L. (1995). "Fractional master equations and fractal time random walks." Phys. Rev. E, 51(2), R848.

[34] Podlubny, I. (1998). Fractional differential equations, Accademic Press, New York.

[35] Zaslavsky, G. (2002). "Chaos, fractional kinetics, and anomalous transport." Phys. Rev., 371(6), 461–580.

[36] Tarasov, V. E., and Zaslavsky, G. M. (2008). "Conservation laws and Hamiltonian's equations for systems with long-range interaction and memory." Commun. Nonlinear Sci. Numer. Simil., 13(9), 1860–1878.

[37] Schiessel, H., Metzler, R., Blumen, A., and Nonnenmacher, T. (1995). "Generalized viscoelastic models: Their fractional equations with solutions." J. Phys. A, 28(23), 6567–6584.

[38] Meerschaert, M. M., and Tadjeran, C. (2006). "Finite difference approximations for two-sided space-fractional partial differential equations." Appl. Numer. Math., 56(1), 80–90.

[39] Mainardi, F. (1996a). “Fractional relaxation-oscillation and fractional diffusion-wave phenomena.” Chaos Solitons Fractals, 7(9), 1461–1477.
[40] Caputo, M. (1999). “Diffusion of fluids in porous media with memory.” Geothermics, 28(1), 113–130.
[41] Lazopoulos, K. (2006). “Non-local continuum mechanics and fractional calculus.” Mech. Res. Commun., 33(6), 753–757.
[42] Di Paola, M., and Zingales, M. (2008). “Long-range cohesive interactions of non-local continuum faced by fractional calculus.” Int. J. Solids Struct., 45(21), 5642–5659.
[43] Di Paola, M., and Zingales, M. (2011). “Fractional differential calculus for 3d mechanically-based non-local elasticity.” Int. J. Multiscale Comput. Eng., 9(5), 579–597.
[44] Cottone, G., Di Paola, M., and Santoro, R. (2010). “A novel exact representation of stationary colored Gaussian processes (fractional differential approach).” J. Phys. A, 43(8), 085002.
[45] Cottone, G., Di Paola, M., and Zingales, M. (2009). “Elastic waves propagation in 1d fractional non-local continuum.” Physica E, 42(2), 95–103.
[46] Tarasov, V. E., and Aifantis, E. C. (2014). “Toward fractional gradient elasticity.” J. Mech. Behav. Mater., 23(1–2), 41–46.
[47] Challamel, N., Zorica, D., Atanackovi´c, T. M., and Spasi´c, D. T. (2013). “On the fractional generalization of Eringen’s nonlocal elasticity for wave propagation.” Comptes Rendus Mécanique, 341(3), 298–303.
[48] Povstenko, Y. Z. (2009). “Theory of thermoelasticity based on space-time fractional heat conduction equation.” Phys. Scr., 2009(T136), 014017.
[49] Mongioví, M., and Zingales, M. (2013). “A non-local model of thermal energy transport: The fractional temperature equation.” Int. J. Heat Mass Transfer, 67, 593–601.
[50] Zingales, M. (2014). “A fractional-order non-local thermal energy transport in rigid conductors.” Commun. Nonlinear Sci. Numer. Simul., 19(11), 3938–3953.
[51] Zingales, M., and Failla, G. (2015). “The finite element method for fractional non-local thermal energy transfer in non-homogeneous rigid conductors.” Commun. Nonlinear. Sci. Numer. Simul., 29(1), 116–127.
[52] Di Paola, M., Failla, G., and Pirrotta, A. (2012). “Stationary and nonstationary stochastic response of linear fractional viscoelastic systems.” Probab. Eng. Mech., 28, 85–90.
[53] Di Lorenzo, S., Di Paola, M., Pinnola, F. P., and Pirrotta, A. (2014). “Stochastic response of fractionally damped beams.” Probab. Eng. Mech., 35, 37–43.

[54] Alotta, G., Failla, G., and Pinnola, F. P. (2017). “Stochastic analysis of a non-local fractional viscoelastic bar forced by Gaussian white noise.” ASCE-ASME J. Risk Uncertainty Eng. Syst. Part B, 3(3), 030904.
[55] Di Matteo, A., Kougioumtzoglou, I. A., Pirrotta, A., Spanos, P. D., and Di Paola, M. (2014). “Stochastic response determination of nonlinear oscillators with fractional derivatives elements via the wiener path integral.” Probab. Eng. Mech., 38, 127–135.
[56] Sayed, A. E. (1996). “Fractional-order diffusion wave equation.” Int. J. Theory Phys., 35(2), 311–322.
[57] Hanyga, A. (2002). “Multidimensional solutions of time-fractional diffusion wave equations.” Proc., Royal Society of London A: Mathematical, Physical and Engineering Sciences, Vol. 458, Royal Society, London, 933–957.
[58] Metzler, R., and Klafter, J. (2000). “The random walk’s guide to anomalous diffusion: A fractional dynamics approach.” Phys. Rep., 339(1), 1–77.
[59] Mainardi, F., Luchko, Y., and Pagnini, G. (2001). “The fundamental solution of the space-time fractional diffusion equation.” Frac. Calc. Appl. Anal., 4(2), 153–192.
[60] Craiem, D., and Armentano, R. (2013). “A fractional derivative model to describe arterial viscoelasticity.” Biorheology, 44(4), 251–263.
[61] Di Paola, M., and Zingales, M. (2012). “Exact mechanical models of fractional hereditary materials.” J. Rheol., 56(5), 983–1004.
[62] Di Paola, M., Pinnola, F. P., and Zingales, M. (2013). “Fractional differential equations and related exact mechanical models.” Comput. Math. Appl., 66(5), 608–620.
[63] Deseri, L., and Zingales, M. (2015). “A mechanical picture of fractionalorder Darcy equation.” Commun. Nonlinear Sci. Numer. Simul., 20(3), 940–949.
[64] Alaimo, G., and Zingales, M. (2015). “Laminar flow through fractal porous materials: The fractional-order transport equation.” Commun. Nonlinear Sci. Numer. Simul., 22(1–3), 889–902.
[65] Fourier, J. B. (1882). Theorie Analitiqué de le Chaleur, Dover Publications, Paris.
[66] Cattaneo, C. (1948). “Sulla conduzione del calore.” Atti del Seminario di Mat. Fis. Universitá di Modena, Modena, Italy (in Italian).
[67] Metzler, R., and Nonnematcher, T. F. (1998). “Fractional diffusion, waiting time distribution and Cattaneo-type equation.” Phys. Rev. E, 57(6), 6409–6414.

[68] Compte, A., and Metzler, R. (1997). “The generalized Cattaneo equation for the description of anomalous transport process.” J. Phys. A, 30(21), 7277–7289.

2. Glass Nanospheres and Artificial Opals

By A. Chiappini, C. Armellini, A. Carpentiero, L. Pasquardini, A. Vaccari, S. Pelli, V. Piccolo, A. Lukowiak, G. C. Righini, R. Ramponi, D. Zonta, and M. Ferrari

Abstract

The potential of glass materials in the field of photonics can be enhanced by providing them with a submicrometer structure. This can strongly affect the light–matter interaction, e.g., adding to the material a structural color or a tailored porosity at the micro- and/or nanoscale. Colloids and opals have fascinating properties, both as model systems to probe fundamental phenomena in condensed matter physics and as templates for patterned materials useful for different applications, ranging from optics to energy storage. In the present chapter we provide a comprehensive account on the state of art of glass nanospheres and artificial opals by describing the mechanisms of growth for the synthesis of monodisperse dielectric nanospheres and the conditions for the realization of colloidal crystals. Structural and optical properties of these structures are also discussed. Finally, different examples of opal systems are reported and analyzed, putting in evidence their possible applications.

2.1 Introduction

Colloids are usually referred to as small particles with at least one characteristic dimension in the range of a few nanometers to micrometers, dispersed in a different phase [1]. Since the pioneering work by Graham [2] and Ostwald [3], begun more than 140 years ago, colloids have become a subject of extensive research in the context of chemistry, biology, materials science, condensed matter physics, and applied optics [4]. Fundamental studies on colloidal particles require the production of monodisperse beads that are uniform in size, shape, composition, and surface properties. Thanks to many years of continuous efforts, a variety of colloids can now be synthesized as monodisperse particles where size, shape, and charges chemically fixed on their surface are identical within 1–2% [5]. Over the past several decades, complementary chemical routes have been developed to synthesize colloidal particles, with controlled features (shape, size, substructure, and surface functional groups) from various materials, including polymers and inorganic materials.

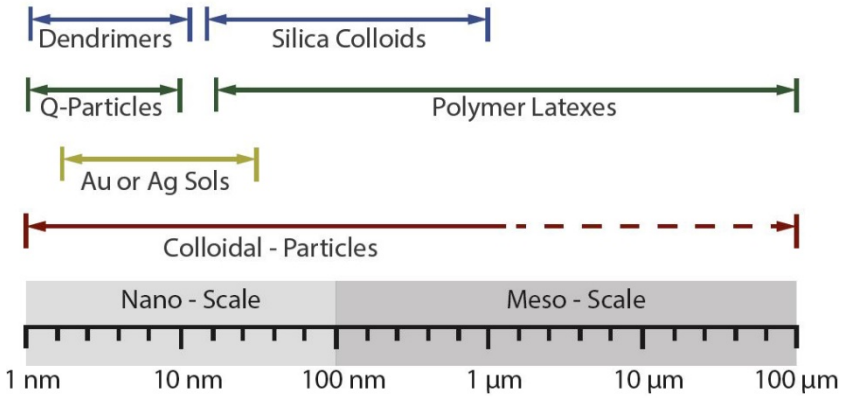

Figure 2.1 *A list of some representative colloidal systems, together with their typical ranges of dimensions. In this chart the upper limit of the critical dimension for colloids has been extended from 1 μm to 100 μm.*

Among them, glass micro- and nanospheres are important in the fields of both basic and applied physics since they can be widely employed in a large area covering information communication technologies, health and biology, structural engineering, and environment monitoring. In particular, glass spheres, arranged in close-packed structures, lead to the formation of optical passive devices such as switches, mirrors, filters, and superprisms [6–9]. On the other hand, silica spheres of tailored size and shape, activated with defined concentration of rare earth (RE) ions, like Er3+ or Eu3+, have significant potential for use in optical devices such as active photonic bandgap materials [10, 11], luminescent markers [12–14], nanosensors, and microlasers [15, 16]. Moreover, spherical colloids represent a class of ideal building blocks that could be assembled into long-range-ordered lattices, such as opals, also called colloidal crystals. The ability to crystallize spherical colloids into spatially periodic structures allows us the observation of interesting and often useful functionalities not only from the constituent material of the colloidal particles, but also from the long-range order exhibited by these periodic lattices. The beautiful, iridescent, and attractive colors of opals, already described in Chapter 2 of this book, are caused by the three-dimensionally periodic lattices of colloids that are colorless by themselves. In this context, recent studies on the optical properties of these materials have now evolved into a new and active field of research that is usually referred to as photonic crystals or photonic bandgap (PBG) structures. The unique features associated with this class of materials can be exploited as a directly observable model system to study various fundamental phenomena such as crystallization, phase transition, and light–matter interaction. At the same time, they have a technological importance because they might lead to the fabrication of

more efficient light sources, waveguiding structures, and diffractive elements to fabricate sensors, filters, and switches. For a more detailed description of PBG's properties and their numerical simulation, the interested reader is referred to Chapter 2.
The present chapter focuses on both glass-based nano-objects and opals, as well as on their potential applications being explored nowadays. Firstly, we describe dielectric nanoparticles of tailored shape and dimensions which are being used as components of artificial opals, as well as the processing techniques currently employed to achieve complex nanostructures which allow us to tailor light–matter interaction. After introducing the mechanisms of growth for the synthesis of monodisperse dielectric nanospheres, we focus attention on the conditions for the realization of colloidal crystals and describe the main structural and optical features, putting in evidence the characterization approaches for their determination. Finally, we discuss novel applications of opals related to the modification of the spontaneous emission, and to the implementation of physical, chemical, and biological sensors.

2.2 Synthesis of Dielectric Nanospheres

Numerous chemical methods can be used for the preparation of dielectric nanoparticles (NPs). The aim of this section is to describe the mechanism of growth and to report the conditions necessary for the realization of monodisperse particles of different materials such as (i) polystyrene, (ii) silica, (iii) silica activated with rare earth ions, and (iv) gold-silica core–shell particles. Let us now briefly discuss each of the four cases.

2.2.1 Polystyrene Nanospheres

Polystyrene (PS) or latex spheres can be easily synthesized by means of the emulsion polymerization process, which is based on the dispersion of a monomer in water [17–19]. There, the formation of long polymeric chains occurs, because of the reaction with the initiator. In order to improve the dispersion of monomer in water, a surfactant is added to the emulsion. The presence of the surfactant in aqueous dispersion results in the formation of micelles, which act as reservoirs for monomers. Thus, the reaction between the monomers dissolved inwater and the free radicals fromthe initiator generates nucleo-oligomers in the form of tiny particles. The nucleus grows into large chains until all monomers encapsulated into the micelles have been eliminated. It appears evident that by modifying the quantity of surfactant in the emulsion it is possible to control the dimensions of the

particles and to obtain building blocks with a size distribution that goes from 100 nm to 1 μm [1, 5]. Furthermore, the surface charge of latex spheres depends on the nature of the initiator used in the synthesis.
Experimentally, the synthesis of polystyrene NPs with an average dimension of about 235 nm can be obtained using a polymerization process based on formation and growth of polymeric nuclei dispersed in an emulsion constituted by water, styrene, potassium persulfate (KPS), and sodium docecyl sulfate (SDS). The polymerization is carried out in an all-glass reactor of 500 ml equipped with a stirrer, a reflux condenser, and a heating jacket to control the temperature. Twomain parameters have to be controlled during the synthesis: temperature and impeller speed. In our case, temperature was set at 80 ± 2°C by means of a heating jacket connected to a PID controller. The mechanical stirrer has a speed equal to 300 rpm, with a variation estimated to be 1 rpm. The standard procedure consists in premixing 190 g of water and 20 ml of styrene monomer in the reactor at the temperature of 80°C for 2 min. The polymerization starts when 0.70 g of KPS and 0.092 g of SDS are dissolved in 10 ml of water and added to the reactor; after 4 hours the polymerization is completed. After cooling down, the colloidal solution is purified by repeated centrifugation/redispersion cycles followed by dilution to the final volume fraction. Figure 2.2 shows an image of the experimental setup used for the synthesis of polystyrene NPs, together with a TEM (transmission electronic microscope) image of the nanoparticles obtained using the protocol above described.

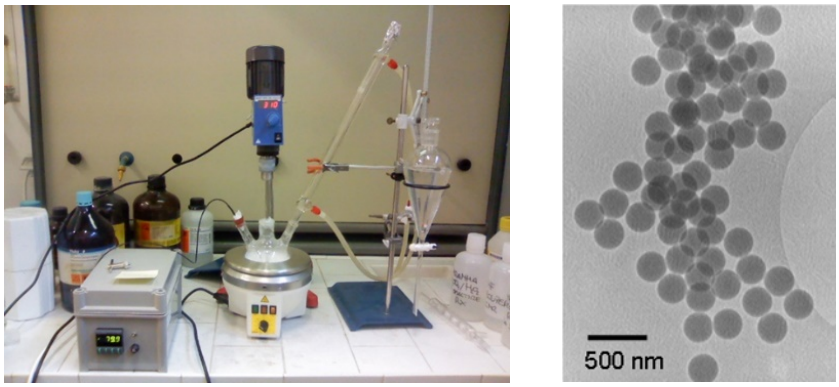

Figure 2.2 *Left: Photograph of the experimental setup for the synthesis of polystyrene (PS) nanoparticles. Right: TEM image of the PS NPs with a diameter of about 235 nm [19].*

2.2.2 Silica Nanospheres

The best-known method to synthesize monodisperse SiO2 spheres was originally developed by Stöber et al. [20] and relies on the hydrolysis (1) of a silicon alkoxide and successive condensation (2) of alcohol and water to form siloxane groups:

(1) $Si(OC_2H_5)_4 + 4H_2O \rightarrow Si(OH)_4 + 4C_2H_5OH$
(2) $Si(OH)_4 \rightarrow SiO_2 + 2H_2O$

In fact, under appropriate conditions of temperature, pH, and reactants concentrations, this synthesis process yields spheres with diameters ranging from 100 to 600 nm with a few percent standard deviation in diameter [21, 22]. For larger sizes, a strategy based on seeded growth technique has been developed [22]. Modifying the quantity of catalyst (ammonia) as well as the water content in the reaction, it is possible to vary the dimensions of the SiO_2 particles keeping low the polydispersity of the NPs. Moreover, it is possible to predict the final dimension of these spheres using an experimental expression proposed by Bogush et al. [22] that specifies the connection between D (average diameter of the spheres) and the reagent concentration expressed in mol/L.
Experimentally, the synthesis of SiO_2 NPs with an average diameter of 250 nm can be obtained using the “Stöber method”, where tetraethyl orthosilicate (TEOS), ethanol, concentrated ammonia (NH_3), and distilled water are used as reagents. Generally, two mother solutions are prepared, one containing TEOS and ethanol and a second one with ammonia/water/ethanol. The two solutions are quickly combined in a reaction vessel and stirred for 24 h by using amagnetic stirrer. Typical molar concentration values used are TEOS 0.22 M, distilled water 15 M, and NH_3 1 M. It is important to underline that the condensation reaction occurs after a few minutes (typically, 5 min). This can be easily observed because, after an invisible hydrolytic reaction forming silicic acid, the condensation of the supersaturated silicic acid is indicated by an increasing of the opalescence of the mixture after the addition of TEOS. After this initial phase, the transition to a turbid white suspension occurs, as is noticeable in Fig. 2.3.
Finally, the silica suspension is centrifuged at 3000 rpm for 30 min and washed with water. The centrifuging/washing procedure is repeated several times and finally the particles are dried at 80°C overnight. A typical SEM (scanning electron microscope) image of the NPs obtained is shown in Fig. 2.3.

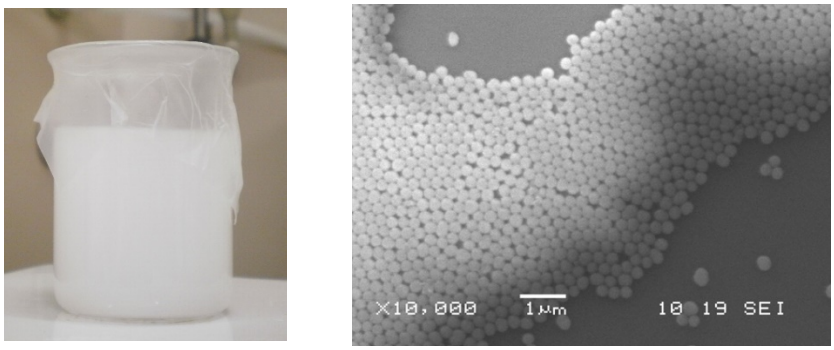

Figure 2.3 *Left: Photograph of the silica suspension after 24 h. Right: SEM image of the SiO_2 NPs with a diameter of 250 nm [23].*

2.2.3 RE-Activated Silica Core-Shell Particles

The synthesis of core–shell particlesis a successful method to fabricate novel materials with different compositions and morphologies. There is much interest in the synthesis of nanoscale particles doped with lanthanide ions; in particular, silica colloids of predictable size and shape, doped with a controllable concentration of lanthanide ions, have significant potential for their use as microlasers, luminescentmarkers and nanosensors. In this scenario, one of the main requests is the synthesis of silica monosize nanoparticles activated with RE ions. They can be formed by either an acid-catalyzed reaction [24–26] or a base-catalyzed (Stöber) reaction [20]. However, the incorporation of the RE ions in the silica matrix using a base-catalyzed reaction fails because the RE ions immediately form an insoluble RE hydroxide [25]. On the other hand, the acid-catalyzed hydrolysis of TEOS results in the formation of large particles with sizes and size distributions that are difficult to control [27]. Recently, it has been shown by Moran et al. that it is possible to incorporate lanthanide ions during the growth of silica particles with a polidispersity of about 10% by using an acid catalyzed reaction.
An alternative approach for the synthesis of monodispersed silica nanoparticles activated with RE ions is based on core–shell structures. These systems are constituted by a core of silica, synthesized by a base-catalyzed process, and a RE-doped silica shell, e.g., Er_2O_3-SiO_2, obtained using a seeded growth method and an acid catalyst. Figure 2.4 (left) shows a SEM image of silica Er^{3+}-activated core–shell structures, where the absence of clusters of particles is evident, thus indicating that the shell growth occurs on individual particles [21].

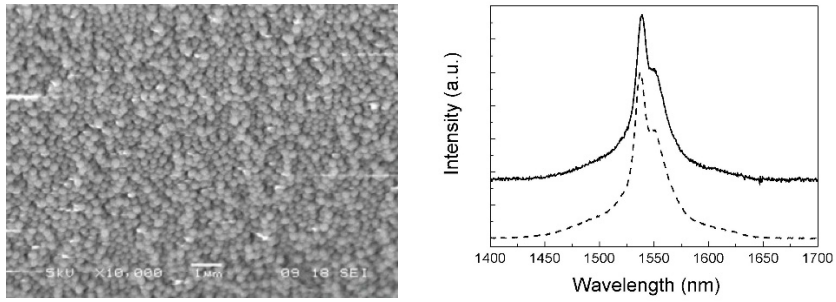

Figure 2.4 *Left: SEM image of Er3+-activated core–shell particles after seeded growth using the acid-based reaction. Right: Room temperature photoluminescence spectrum of the* $^4I_{13/2} \rightarrow {}^4I_{15/2}$ *transition of* Er^{3+} *ions for these particles, upon excitation at 514.5 nm (dashed line) and upon excitation at 980 nm (straight line) [21].*

Photoluminescence measurements, reported in Fig. 2.4 (right), confirm the incorporation of Er^{3+} ions in the silica shell; in fact, the shape of the $^4I_{13/2} \rightarrow {}^4I_{15/2}$ emission band is typical of Er^{3+}-activated silica glasses with a main emission peak at 1533 nm.

2.2.4 Gold-Silica Nanospheres

The core–shell configuration is also a suitable tool to obtain hybrid nanoparticles with low polydispersity. Nowadays, in particular, researchers are interested in synthesizing nanoparticles constituted by a metallic core with a dielectric shell. Among the different structures, gold-silica core–shell particles have attracted a wide interest not only as probes but also as building blocks for the creation of hybrid nano-objects. Experimentally, the realization occurs through a two-step approach: (i) the synthesis of Au nanoparticles with a typical dimension of tens of nanometers, and (ii) the growth of a silica shell with desired thickness. One of the main approaches for the realization exploits the Turkevich method, which allows producing gold particles of spherical shape and high monodispersity [28]. With this method the synthesis occurs through the reduction of chloroauric acid (HAuCl4) at 80°C, under vigorous stirring, by a reducing agent such as sodium citrate. In this way a burgundy-red solution appears in few minutes due to the formation of spherical gold nanoparticles (see Fig. 2.5). The gold nanoparticles thus prepared are then diluted in 2-propanol and used as seeds in a coating process based on the Stöber method. Aqueous ammonia is added to the alcoholic gold colloidal solution under vigorous stirring. Silica coating is started by adding tetraethylorthosilicate. The addition of TEOS and ammonia in proper molar ratio allows controlling the shell thickness [29]. A typical SEM

image of the goldsilica core–shell spherical nanoparticles is shown in Fig. 2.5.

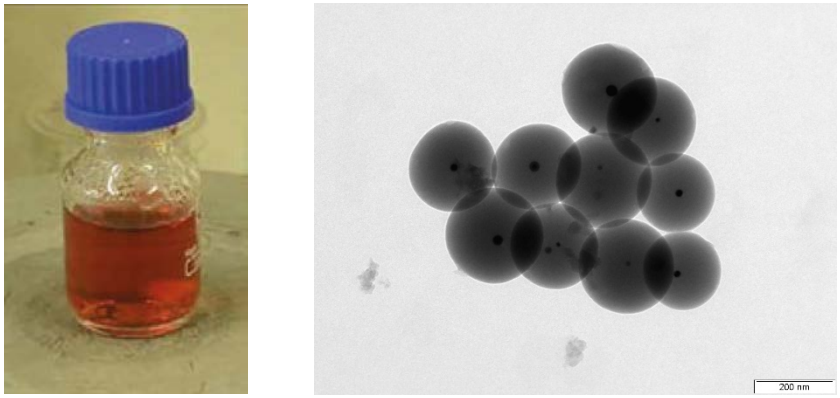

Figure 2.5 *Left: Photograph of gold spherical nanoparticles suspension with amean diameter of about 10 nm. Right: TEM image of gold-silica core–shell particles with a dimension of about 200 nm.*

2.3 Artificial Opals by Self-Assembly Approach

Artificial opals, also called colloidal crystals, are confined structures composed of assemblies of elements having identical shape and size, crystallized in an ordered structure [21, 30]. The first requirement, in order to make good self-assembled photonic structures, is the monodispersity in the size of the building blocks. In the previous section we described four complementary approaches to realize monodisperse nanoparticles of different materials (organic and inorganic). A further aspect to be considered is the technique used for the formation of colloidal crystals. In the last few years, different techniques have been developed to obtain self-assembled structures for photonic applications. The principal ones can be summarized as follows: sedimentation, Langmuir–Blodgett, motor drawing, shearinduced, spin coating, and vertical deposition [31]. Among them, the most widely used method is the vertical deposition, also known as convective deposition method. This technique is based on the evaporation of the liquid (generally ethanol or water) forcing the spheres to arrange in the meniscus formed between the vertical substrate, the suspension and the air, as sketched in Fig. 2.6. This method, as demonstrated by Jang et al. [33], provides a precise control over the thickness, with a higher crystalline quality with respect to other deposition techniques [31]. Colvin et al. [34] demonstrated that it is possible to predict the thickness of the systems as a function of the number of particle layers, *K*, from the following expression:

$$K \propto \frac{L \cdot \varphi}{0.605 \cdot D \cdot (1-\varphi)} \tag{1}$$

where L is the meniscus length, φ is the particle volume fraction in suspension, and D is the dimension of the nanoparticles. Experimentally, the growth of the polystyrene opal occurs dispersing 0.036 wt% of PS nanoparticles in 3 ml of water [35]; a hydrophilic substrate is placed vertically in a beaker containing the suspension, as shown in Fig. 2.6. The deposition occurs in an oven at the temperature of 45°C. After 1–2 days, we have the total evaporation of the solvent with the formation of the crystallized structure (colloidal crystal). A typical image of the opal is reported in the photograph in Fig. 2.6 (right), where an evident opalescence is present.

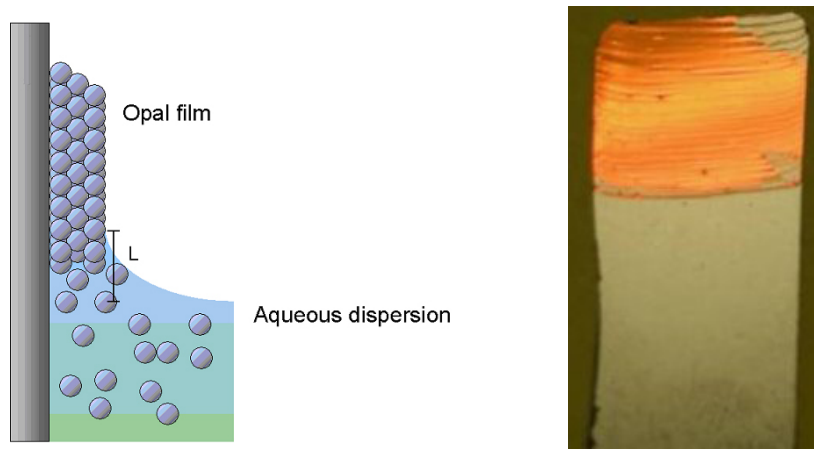

Figure 2.6 *Left: Schematic illustration of the vertical deposition technique for the growth of opals. The substrate is immersed in a beaker containing a suspension of small spheres in water. The spheres are self-assembled into a face-centered cubic lattice at the meniscus formed at the interface between water, air, and substrate. (Reproduced with modifications from the website of the Tyndall Institute [32].) Right: A photograph of an opal obtained usingpolystyrene NPs of 270 nm.*

2.4 Properties of Opals

For what concerns the structure of these artificial opals, Woodcock theoretically demonstrated that when hard spheres self-assemble in thermodynamical equilibrium, the face-centered cubic (fcc) arrangement is more stable than the hexagonal close packed (hcp) one [36]. This assumption was also confirmed by experimental studies, as exemplified by the SEM images in Fig. 2.7 [23, 37].

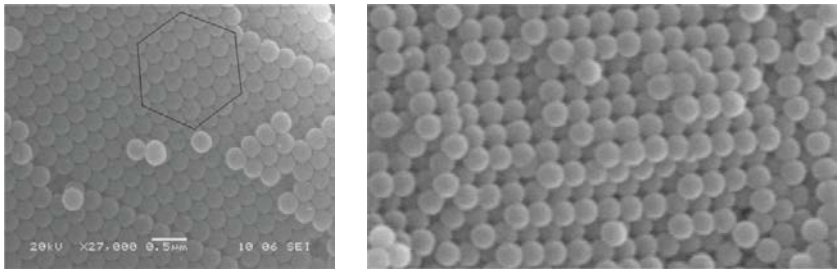

Figure 2.7 *Left: SEM image of top surface of an opal structure, where a hexagonal alignment is present, corresponding to the plane <111> of an fcc structure. Right: Quadratic alignment assigned to the plane <100> of an fcc structure can be discovered when the opal is cleaved along the axis [23].*

In fact, analyzing the SEM images in Fig. 2.7, we can clearly observe the presence of a hexagonal alignment that can be attributed to the <111> plane of the ordered structure. Instead, a quadratic alignment assigned to the plane <100> of an fcc structure becomes evident when the opal is cleaved along the axis. The periodic pattern in an fcc arrangement produces a bandgap where light cannot propagate in the structure, as is evident from the diagram of bands reported in Fig. 2.8. In this case there is the formation of a pseudo gap in the Γ-L direction that can be associated with the plane <111> of the structures.

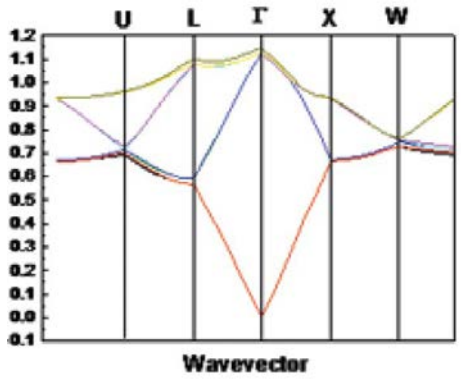

Figure 2.8 *Diagram of bands for a direct opal structure constituted by polystyrene NPs of size 236 nm, assembled in a face cubic centered system.*

From an optical point of view, the central wavelength position of the pseudo bandgap can be determined by the modified Bragg's law.

$$\lambda = 2 \cdot d_{111} \cdot (n_{eff}^2 - \sin^2 \theta)^{1/2} \qquad (2)$$

where d_{111} corresponds to the interplanar spacing of fcc <111> planes and n_{eff} is the effective refractive index in the opal structure, which can be calculated from the following equation for fcc structure

$$n_{eff}^2 = f \cdot n_{spheres}^2 + (1 - f) \cdot n_{medium}^2 \tag{3}$$

Here, $n_{spheres}$ and n_{medium} are the refractive indixes of the nanoparticles and the surrounding medium, respectively; f corresponds to the filling factor of the spheres and it is very close to the fcc ideal value of 74%. Moreover, for the fcc lattice with unit cell parameter a, the interplanar spacing d_{hkl} is given by the equation

$$d_{hkl} = \frac{a}{\sqrt{(h^2 + k^2 + l^2)}} = \frac{2}{\sqrt{(h^2 + k^2 + l^2)}} \cdot D \tag{4}$$

where the relationship between the unit cell parameter and the diameter of the nanospheres is given by

$$a = \sqrt{2} \cdot D \tag{5}$$

Therefore, d_{111} is defined as

$$d_{111} = \sqrt{2/3} \cdot D \tag{6}$$

In this way, the equation (2.2) can be rewritten as a function of the diameter of the nanoparticles:

$$\lambda = 2 \cdot D \cdot (n_{eff}^2 - \sin^2 \theta)^{1/2} \tag{7}$$

Analyzing eq. (2.7) it is evident that it is possible to tune the position of the band by various means, e.g., by (i) modifying the dimension D of the NPs or (ii) varying the incident angle (θ), but also (iii) infiltrating the voids of the opal structure with a desired material. It has been experimentally demonstrated that a blue shift of the position of the diffraction peak occurs when increasing the incident angle (θ) of the light respect to the normal to the <111> plane, as evidenced in Fig. 2.9. Moreover, as shown in the same Fig. 2.9, by fitting the position in wavelength of the bandgap as a function of the incident angle (θ) and

using equation (2.7), it is possible to estimate important values such as the size *D* of the nanoparticles and the effective refractive index of the opal. The comparison of this last value, n_{eff}, with the theoretical one determined using equation (2.3) permits to have a clear indication of the quality of the structure realized.

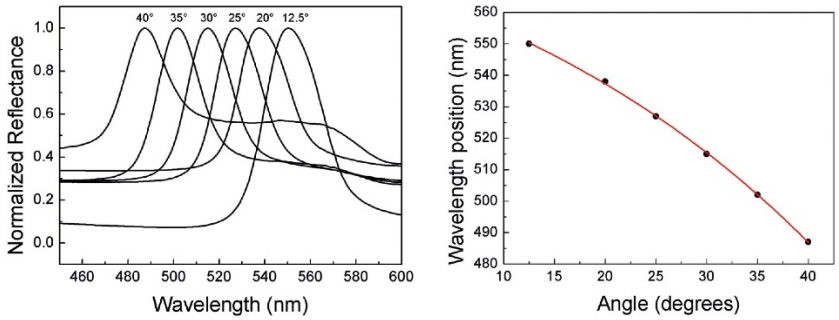

Figure 2.9 *Left: Reflectance spectra at different incidence angles taken on the opal produced by the vertical deposition method with 236 nm silica spheres [21]. Right: Plot of the angle of incidence θ to the surface normal versus the pseudo bandgap position.*

An additional approach to tune (red shift) the position of the bandgap of the opal structure concerns the infiltration of the voids of the opal with a given material. As a matter of fact, by infiltrating the voids of the colloidal crystal with a material that presents a high refractive index it is possible to enhance the value of the effective refractive index (see eq. (2.3)): this produces a red shift, as expressed by the equation (2.7), of the wavelength position of the bandgap. A typical example is reported in Fig. 2.10.

It is also important to remember that the frequency gap of the opal ν (with implied *hkl* indices) can be determined by the contrast between the refractive index of the spheres ($n_{spheres}$) and the medium (n_{medium}), as reported by Shkunov et al. [39]. Precisely, the frequency gap can be expressed as follows:

$$\frac{\nu}{\Delta\nu} = \frac{|\, n_{spheres} - n_{medium} \,|}{n_{spheres}} \tag{8}$$

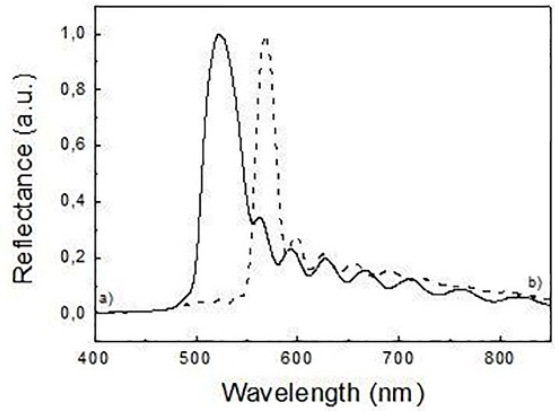

Figure 2.10 *Reflectance spectra: (a) straight curve corresponds to the bare opal with NPs of 230 nm; (b) dashed curve represents the same opal infiltrated with poly-dimethylsiloxane (PDMS) [38].*

Analyzing Fig. 2.10 we can clearly notice a red shift of the position of the bandgap after the infiltration, together with a narrowing of the frequency bandgap as predicted by the equation (2.8).
Finally, the thickness of the opal can be determined by means of reflection measurements. Let us, for example, analyze the spectrum reported in Fig. 2.11. It is possible to observe both the main peak attributed to the Bragg diffraction (λ_b) and several peaks known as Fabry–Pérot (FP) oscillations for wavelengths higher than λ_b, which are due to the interference of the light reflected by opposite surfaces of the opal films. Now, using the approach proposed by Reculusa et al. [40], considering in a first approximation the opal system as a layer of index n_{eff} and thickness t deposited on a glass substrate, and taking into account the wavelength difference of two consecutive FP maxima, the thickness (t) can be determined through the expression (2.9):

$$m \cdot \lambda_p \cdot \lambda_{p+m} = 2 \cdot n_{eff} \cdot (\lambda_{p+m} - \lambda_p) \cdot t \qquad (9)$$

From eq. (2.9) it appears to be clear that the plot of $m\lambda_p\lambda_{p+m}$ versus $2n_{eff}(\lambda_{p+m}-\lambda_p)$ is a linear regression with a slope equal to the thickness t of the sample. This approach could be seen as an alternative and nondestructive way to estimate the thickness of the opal structures.

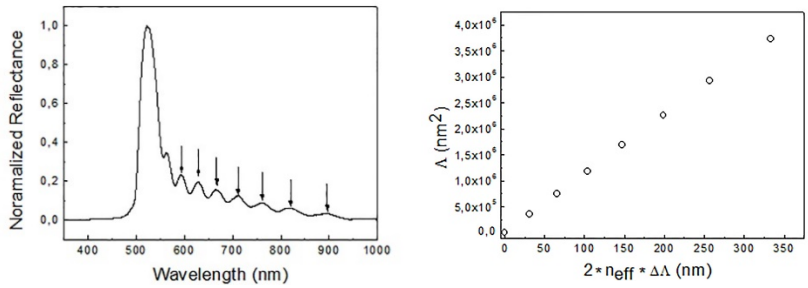

Figure 2.11 *Left: Reflectance spectrum acquired at normal incidence on the inverse silica opal, the arrows correspond to the position of the Fabry–Pérot fringes considered for the estimation of the thickness. Right: Experimental values of plotted Λ that corresponds to $m\lambda_p\lambda_{p+m}$, as a function of $2n_{eff}\Delta\Lambda$, where $\Delta\Lambda$ is $(\lambda_{p+m}-\lambda_p)$.*

2.5 Heterostructures

In the previous section we described the structural and the optical properties of opals. In particular, we saw that colloidal crystals show opalescent colors due to the Bragg reflections by the lattice planes defined by the nanoparticles. The photonic bandgap of these materials mainly depends on the size of the constituting colloidal spheres and on the dielectric constant. A complementary confined system based on opal structures is constituted by the so-called heterostructures (HT). These systems have attracted considerable attention from both the scientific and engineering points of view [34, 41, 42] due to their many attractive features, such as multi-stop band [43] and extended photonic bandgap [44, 45]. A heterostructure is based on multiple layers of opal films with different lattice constant or different dielectric constant, or both.

In this section we want to describe the fabrication of HT systems and the structural and optical properties of an heterostructure based on opal films of different materials such as silica and polystyrene (PS). The formation of the HT can, as reported in this example, be induced by depositing an opal structure of PS NPs on the SiO_2 NPs colloidal film that presents analogous dimensions [35]. Actually, using the vertical deposition technique, described in section 2.3, it is possible to grow opal films of different nature, as reported in Chiappini et al. [35]. Figure 2.12 presents, on the right, a typical SEM image relative to the cross section of an heterostructure, where it is possible to notice the growth of the two photonic layers as well as a good ordering of the structures realized. From a structural point of view, the two opal films preserve the face cubic centered configuration, as one can see in Fig. 2.12 (left).

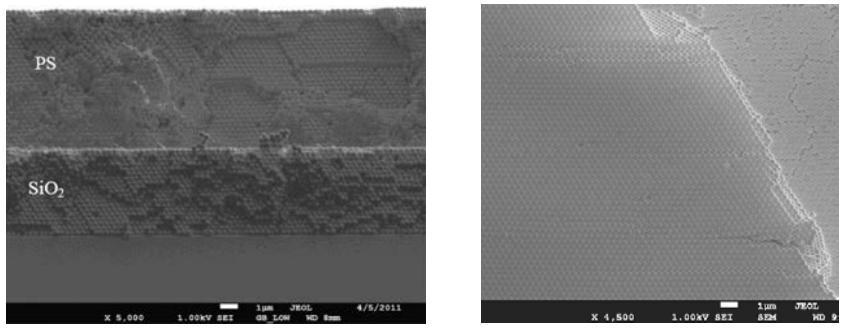

Figure 2.12 *Left: SEM image of cross section of a cleaved edge of a heterostructure constituted by silica (320 nm) and polystyrene (350 nm) spherical NPs. Right: Top view of the HT where large domains of the top layer are present [35].*

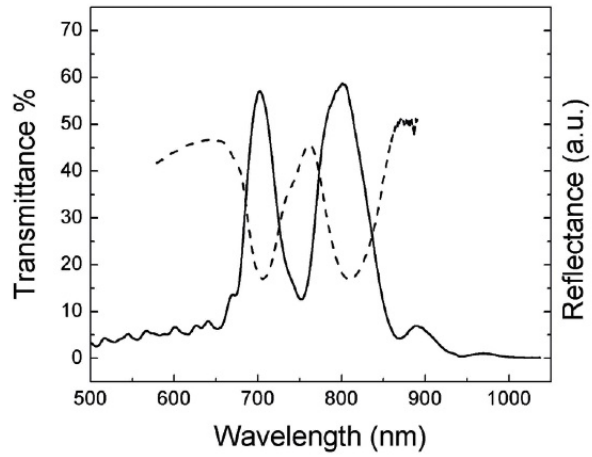

Figure 2.13 *Transmittance (dashed line) and reflectance (solid line) spectra of the heterostructure of Fig. 3.12. The peaks centered at about 800 and 700 nm are attributed to the top (PS) and bottom (SiO_2) layer, respectively [35].*

Regarding the optical properties, the Fig. 2.13, which shows the transmission and reflectance spectra measured for the the HT of Fig. 2.12 (nanospheres of silica (320 nm) and polystyrene (350 nm)), reveals the presence of a double peakwhose components are centered at about 800 and 700 nm. Comparing the position in wavelength of the stop bands of the double layer of the HT with the stop band of each single layer, we clearly notice that there is an excellent agreement, indicating that the double peak of the HT can be seen as just the superposition of the properties of each individual layer [34].
The optical quality of this heterostructure, however, is lower than that of each individual layer; this effect can be mainly attributed to the roughness at the interface between the two opal layers [42, 46]. Liu et

al. [47] have demonstrated that it is possible to enhance the optical quality of the heterostructures depositing a thin layer of TiO_2 NPs on the bottom opal film, thus reducing the roughness at the interface.

2.6 Infiltrated Opals

An additional confined system based on opal structure is constituted by a composite material based on polystyrene colloidal nanoparticles assembled and embedded in an elastomeric matrix. These types of systems can be designed in order to operate in the visible range, by choosing properly the nature and the dimensions of the nanoparticles. To date, colloidal crystals are used to realize several types of responsive photonic devices that can be employed in different fields such as color displays [48, 49], biological and chemical sensors [50–52], physical sensors [53–56], inks, and paints [57, 58]. Their main feature concerns the capability to change color under an external stimulus, due to a variation of the structural and optical properties, so that their response can be visually tracked by naked eyes. The versatility of this type of structures allows one to develop responsive materials, sensitive to physical and chemical stimuli. Looking at the literature, several papers report on the use of colloidal crystals as responsive materials: Asher and coworkers [59] have pioneered the fabrication of hydrogel-based photonic crystal sensors for temperature, pH, ionic species, creatinine, etc.; Takeoka and coworkers [49] have extensively studied gels that exhibit switchable colors over the visible region when exposed to external stimuli; Kand et al. [57] have studied solvent-swelling colloidal crystals with tunable colors that served as a photonic paper for colored writing; Gu et al. [60] have studied the stop-band shift of PCs based on the refractive index change; Stein et al. [58] have reported solvent-filling effects on the optical properties of ceramic inverse opals, which could be used in detecting organic solvents through the change in refractive index. Focusing the attention on mechanochromic systems, Fudouzi et al. [61] and Zonta et al. [62] have demonstrated their potential application to the structural health monitoring through the detection of mechanical deformations. From a physical point of view, the working scheme of this type of infiltrated opals can be explained by the following example (see Fig. 2.14).

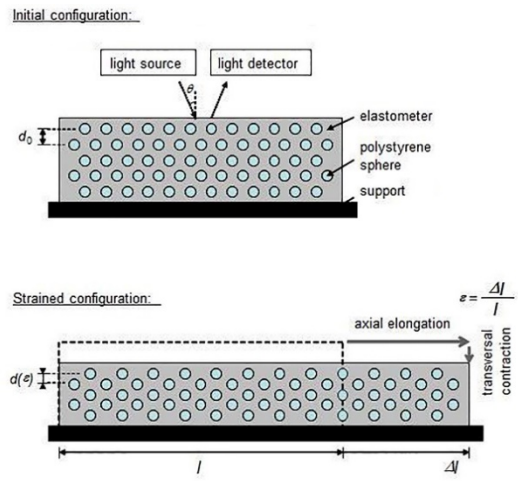

Figure 2.14 *Dependence of interplanar spacing from the applied strain. Comparison between the initial (upper figure) and strained (lower figure) configurations [62].*

When an axial strain is applied to the infiltrated opal, the interplanar spacing d is modified by the transversal contraction as a function of the applied strain value ε. As a side effect, the refractive index n_{eff} is also linearly affected by the stress variation [62]. The combination of these two effects makes the reflectance properties of the colloidal crystal, and particularly the position in wavelength of the diffraction peak, sensitive to the applied strain (ε). Once the relation is known, a measure of the color reflected by the opal system can be used to estimate the strain inherited from the structure to which it is attached. In Fig. 2.15 two typical photograph images of a mechanochromic structure before and during the application of strain are reported: the variation of the color of the structure can be easily observed by the naked eye.

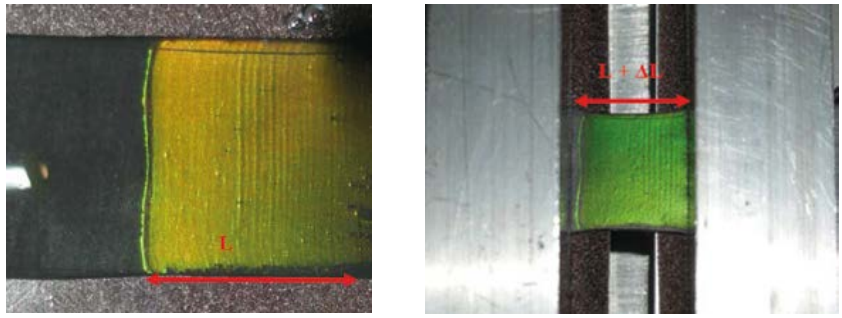

Figure 2.15 *Changes in the structural color of the colloidal crystal film deposited on a Viton substrate (1.6 × 1.6 cm^2): (a) photographic image of the initial sheet (length L); (b) photographic image of the stretched sheet (length L+Δ L) [23].*

From a quantitative point of view, reflectance measurements reported in Fig. 2.16 evidence a blue shift of the diffraction peak as a function of the applied strain. Furthermore, when plotting the wavelength position of the diffraction peak as a function of the elongation it is evident that a linear relationship exists for elongations as large as 2 mm. In this region, the lattice distance of the <111> planes, *d*, also decreases at the same rate. For higher elongation values, instead, the position of the peak does not change significantly, because the interplanar distance remains constant also for higher applied mechanical strain since the PS spheres have already been forced in contact with each other.

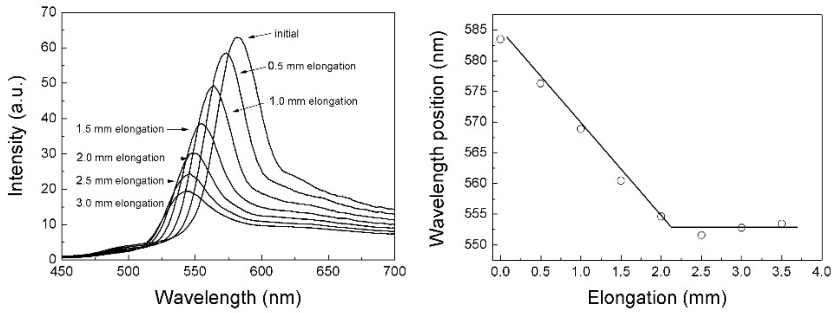

Figure 2.16 *Relationship between the peak positions and elongation of composite sheet (from initial 0 to 3 mm) owing to stretching. Left: Reflectance of the photonic crystal. Right: Diffraction peak wavelength position as a function of the elongation [63].*

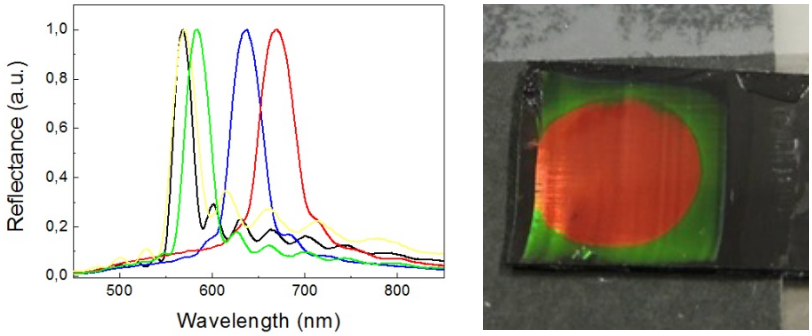

Figure 2.17 *Colorimetric sensor. Left: Black line corresponds to the reflectance of the polymeric composite system. Reflectance spectra acquired after spotting 0.5 μl (one drop) of different solvents onto the "sensor" surface, and monitoring the optical change of the diffraction peak: (yellow line) ethylene glycol, (green line) methanol, (blue line) ter-butyl alcohol and (red line) 1 cSt silicone fluid. Right: Optical photograph showing naked eyes detection (from green to red) of a drop of the silicon fluid [38].*

On the other hand, the variation of the interplanar distance and the consequent variation in color can be exploited for the development of colorimetric solvent sensor, as demonstrated by Chiappini et al. [38]. In

this case, the infiltrated opals present a different response as a function of the organic solvent dropped on the surface. This is attributed to the different capability of the solvents to swell the polymeric matrix.
Analyzing Fig. 2.17 (left) it is possible to observe a red shift of the diffraction peak respect to the initial position, as a function of the solvent applied. Higher is the capability of the solvent to swell the composite system [8], bigger is the red shift of the Bragg peak obtained, due to the variation of the interplanar distance of the colloidal crystal. This approach allows one to realize low-cost, flexible, and highly sensitive chemical sensors with the advantage to present a reversible signal change [38].

2.7 Inverse Opals

Further structures that can be obtained starting from a colloidal crystal are the so-called inverse opals. This type of systems can be used in different fields, as platforms for the realization of optical sensors [64–66], or for the development of photonic devices such as channel waveguides [67, 68] or random laser systems [69].
Experimentally, an inverse opal is realized by infiltrating the voids of the direct one with a suitable material and removing the beads that formed the original colloidal crystal. Several techniques have been used for the fabrication of these systems such as chemical vapour deposition, atomic layer deposition, sol–gel route, etc. In particular, the sol–gel technique is a low-cost approach that does not require highly expensive and sophisticated equipment for the realization of inverse opals. In this case, the formation of the inverse structures occurs by means of the following steps: (i) realization of a stable sol (a typical example is reported in Ref. [70]), (ii) infiltration of the opal structure with the sol, and (iii) removal of the beads through chemical or thermal process. From a structural point of view, the inverse opal can be seen as just a negative replica of the direct opal. Typical SEM images of inverse silica structures are reported in Fig. 2.18.
Analyzing this type of structures we can observe the presence of hollow regions of air spheres well-ordered in a hexagonal lattice corresponding to the <111> planes of an initial fcc crystalline structure [71]. As to the optical properties of these systems, the periodic variation of the refractive index produces an interval of frequencies where the light cannot propagate inside the inverse structures. This phenomenon can be described using the equation (2.7) from section 2.4, where D, in this case, corresponds to the center-to-center distance of the hollow spheres.

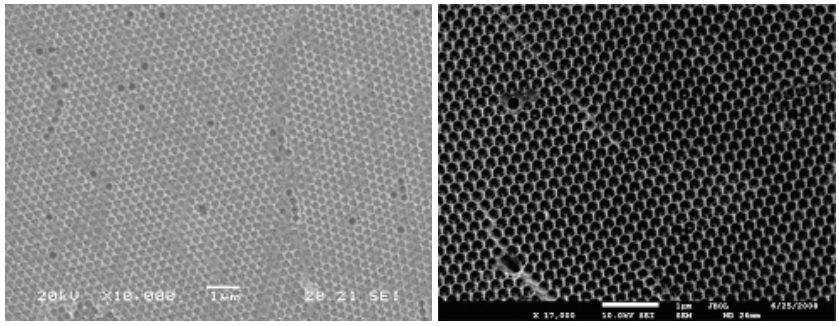

Figure 2.18 *SEM images of the top surface of inverse silica opal obtained using NPs of the dimension of 270 nm (left) and NPs of the dimension of 236 nm (right) [70].*

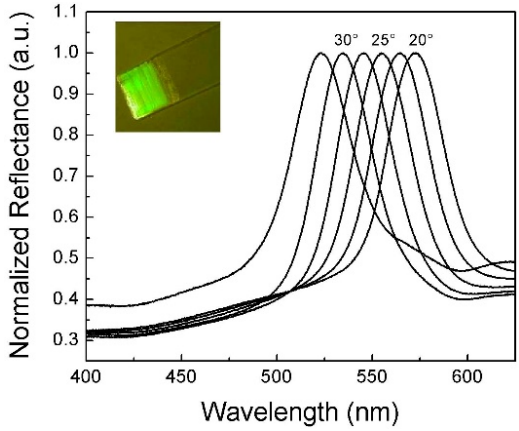

Figure 2.19 *Reflectance spectra at different incident angles (step of 2.5°) obtained from an inverse silica opal with voids dimension of about 320 nm. The inset shows a photographic image of the inverse silica opal where a green opalescence is evident.*

For the inverse structures as well it is possible to determine important parameters such as neff and the filling factor by plotting the wavelength position of the diffraction peak as a function of the value of the incidence angle. In this way it has been possible to verify that these structures present a filling factor of 23%, indicating the presence of a large surface area [70]. Moreover, colloidal crystals are structures able to modify the density of states (DOS). In the bandgap DOS is zero, while at the band edge the group velocity vg tends to zero and the DOS⇒∞. In this case, the photons propagate slowly through the photonic crystal. As discussed above, the optical characteristics of photonic crystals make them ideally suited to several light-relevant applications. Through the introduction of defects that locally disrupt the periodicity, allowed states can be created within the bandgap, thereby producing light localization close to the defect [72]. The exploitation of

this effect is ideal for trapping and/or guiding light and for the creation of specific devices suitable for optics and optoelectronics, energy storage, communications, sensors, and biological applications. Among the different applications of inverse structures that have been explored, sensors are probably the most developed and provide an excellent showcase of the advantageous properties of these structures.
Sensing can benefit from several attributes of inverse systems, including their structural colors, their highly accessible surfaces, and their nanostructured features. Here we report two possible examples of silica inverse structures: (i) structures functionalized with DNA aptamers labeled with Cy3 fluorophore for the realization of biosensors in dye-labeled fluorescence detection scheme, and (ii) structures where gold nanoparticles are immobilized on the silica network of the inverse opal for the development of metallodielectric colloidal structures (MDCS) suitable for the realization of omnidirectional absorbers [73] and chemical-biological sensors.

2.7.1 Fluorescent Aptamer Immobilization on Inverse Colloidal Crystals

The development of confined structures and of inverse colloidal crystals in particular has potential interest for the implementation of a biosensor platform in a dye-labeled fluorescence detection scheme. However, the definition of a robust, easy, stable, and costeffective procedure that allows the whole functionalization of an inverse structure is still a challenge. The use of inverse colloidal crystals, however, will permit to achieve photonics-based biosensors combining the optical and structural properties of the colloidal crystals with the selectivity due to the specific probe immobilization. Kim et al. [74] have demonstrated that exploiting the high porosity (increased surface area) it is possible to obtain a fluorescence signal 100 times stronger than from the conventional planar reference platform. Moreover, by taking advantages of the bandgap properties of the colloidal crystals it is possible to control the emission of the fluorescent aptamers, thus opening new horizons at the interface between biology and the nanosciences, showing the potential of combining biological systems with nanophotonics. This biophotonic engineering may be extended to control emission rates and complex Forster energy-transfer systems obtained by protein engineering [75]. A typical result is reported in Fig. 2.20, which makes evident the possibility to modify and tailor the emission of the fluorescent aptamers as an internal light source in a photonic crystal by varying the position of the bandgap of the inverse colloidal crystal. This effect is due to the fact that the photons whose energy lies within the PBG cannot propagate along the <111> direction.

The black line corresponds to the typical emission of the Cy3-aptamer where there is no overlap between PGB and fluorescence emission [76]. Increasing the detection angle (i.e., 20° red line and 40° green line), the bandgap starts to overlap to the spontaneous emission of the Cy3-DNA, thus inducing a variation in the shape of the emission spectra.

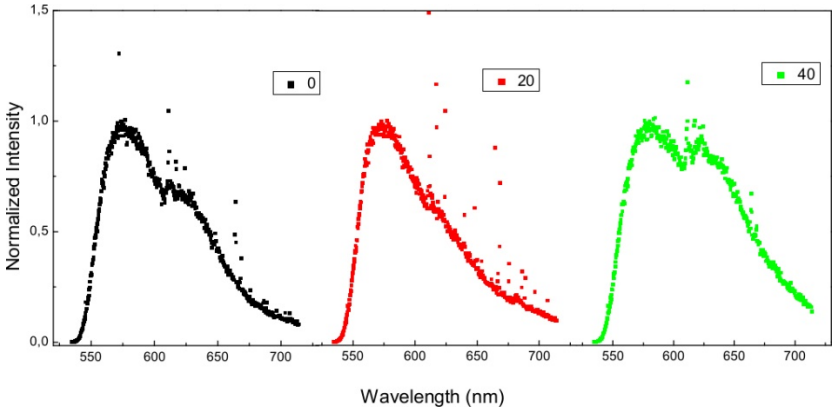

Figure 2.20 *DNA-Cy3 fluorescence of the inverse opal obtained using for excitation the Ar^+ line at 514.5 nm and collecting the emission at 0°, 20°, and 40° detection angles, respectively. At 0° there is no overlapping between DNA-Cy3 and PBG, whereas at 40°, due to its blue shift, the photonic bandgap overlaps with the emission of the DNA-Cy3 [77].*

A possible approach to quantify the effect of the bandgap of the colloidal crystal, and its efficiency, on the emission spectrum of the DNA-Cy3 concerns the determination of the intensity ratio I_{620}/I_{575} of the fluorescence emission at I_{575} and I_{620} of the spectra reported in Fig. 2.20. In this case, a variation equal to 25% has been determined that is comparable with the photonic bandgap depth of the inverse structure. In a future perspective, the possibility to functionalize silica inverse structures with specific sequences (sensitive and selective transducer), combined with the features of the colloidal crystals to tailor the emission of fluorescent molecules, paves the way to design immunosensors for the diagnosis of pathogens [78].

2.7.2 Metallo-Dielectric Colloidal Crystals

Metallo-dielectric colloidal structures (MDCS) have attracted an intense research activity [79–82] during the last decade, thanks to their combined features, namely the localized surface plasmon resonance (LSPR) of noble metallic nanoparticles and the photonic bandgap of colloidal crystals. From an application point of view, these systems can be employed as omnidirectional absorbers in a broadband range from

visible to near-IR [83], and as chemical sensors [60] or SERS (surface-enhanced Raman scattering) substrates. [84, 85] Among different techniques, the wet chemistry approach is a very interesting, cheap, and easymethod that allows one to realize different metallo-dielectric structures such as colloidal photonic crystals doped with gold [76, 86], long-range-ordered broccolilike arrays [87], and self-organized arrays of Au nanocrescents deposited over a compact monolayer of polymeric nanospheres [88]. A complementary further example concerns the realization of MDCS based on the immobilization of gold spherical nanoparticles in the network of an inverse silica opal (ISO). From an optical point of view, this type of system again combines the properties of the localized surface plasmon resonance of Au NPs with the photonic bandgap features of the colloidal crystal structures, as evidenced in the absorbance spectra reported on the right of Fig. 2.21.

In Fig. 2.21 we can notice that the MDCS structures present two characteristic peaks, one centered at about 600 nm and the second one, smaller, at 520 nm. The peak centered at about 600 nm is attributed to the stop-band of the inverse structure which has originated from the diffraction of the 3D ordered system. Moreover, we can notice that the position of the diffraction peak remains fixed at 600 nm for all the spectra reported, suggesting that the Au Nps are predominantly immobilized on the surface of the structures or infiltrated just in the first layers of the PCs. The peak centered at 520 nm, on the contrary, can be assigned to the localized surface plasmon resonance (LSPR) of the Au NPs immobilized on the silica network of the inverse structure. In fact, this peak is almost in the same position as that obtained for the synthesized gold colloidal nanoparticles in aqueous solution [23, 80, 89]. In order to prove that this type of systems can be used as SERS substrate, we performed Raman measurements using benzenethiol (BT) as a probe molecule. Figure 2.22 shows the Raman signal obtained from a MDCS (a), compared with the signal from a gold film deposited by sputtering, where the same amount of BT is absorbed (b), and the signal obtained when pouring (and letting to dry) a 5 μL drop of pure BT onto an inverse silica opal (ISO) (c) [23].

Observing Fig. 2.22, we can underline that the typical Raman bands of BT can be very easily identified only in the case of the MDCS structure (curve a). Moreover, one clearly notices that the spectrum (a) appears significantly enhanced compared to the Raman spectra obtained from gold film and ISO structures, thereby suggesting that metallo-dielectric colloidal structures can be used for the detection of biomolecules at low concentrations.

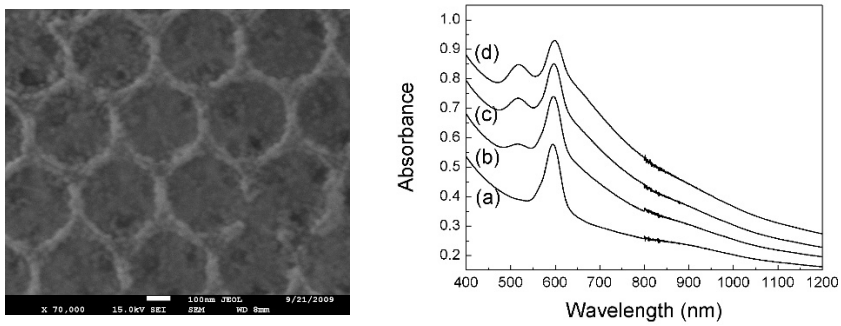

Figure 2.21 *A metallo-dielectric colloidal structure (MDCS) where Au NPs of the dimension of about 10 nm are immobilized in the network of an inverse silica opal (ISO). Left: SEM image of the MDCS. Right: Absorbance spectra of (a) an inverse silica opal and (b–d) metallo-dielectric structures obtained after immersion of ISO into the Au Nps colloidal solution for different times: 1 h, 2 h, and 4 h, respectively [89].*

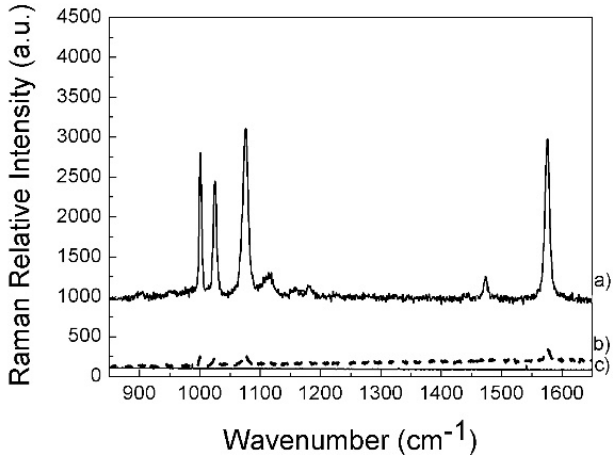

Figure 2.22 *Raman spectra of benzenethiol adsorbed (a) on the metallicdielectric colloidal structure, (b) on sputtered gold film, and (c) on an ISO covered with a 5 μL drop of pure (BT) and then dried [23].*

2.8 Conclusions

In this chapter, various colloidal systems were discussed. The first section described a variety of chemical methods to make up colloidal systems consisting of spherical particles, with diameters ranging from 20 nm to 1 μm, with different functionalities. Specifically, by controlling the chemistry of the reactions, it is possible to synthesize monodisperse nano- and microparticles, based on organic and inorganic materials, with tailored dimensions, that can be activated with rare earth ions, as well as hybrid particles in core–shell configuration. Starting

from these nanospheres, some possible approaches were described for the fabrication of 3D colloidal crystals, considering the main deposition parameters such as particles volume fraction, spheres dimensions, and deposition temperature.

The second section focused on the structural and optical properties of different confined colloidal systems such as direct opals, infiltrated opals, inverse colloidal crystals, heterostructures, and metallo-dielectric colloidal systems. Their optical features, such as photonic bandgap position, peak broadening effect, and frequency gap, were considered and analyzed by means of an analytical model, which was validated through comparison with experimental results.

The last section was devoted to the discussion of the properties and the possible applications in different fields. As an example, properly designed structural colored composite systems can be exploited as strain and chemical sensors, where detection can be obtained by naked eyes. Inverse structures functionalized with specific fluorescent aptamers can find potential interest as a biosensor platform in a dye-labeled fluorescence detection scheme, taking advantage of the bandgap properties of the colloidal crystals that allow us to control the emission of the fluorescent aptamers.

Finally, metallo-dielectric structures based on the immobilization of gold nanoparticles in the network of an inverse silica opal can be applied as SERS substrates, combining the properties of the localized surface plasmon resonance of Au NPs with the structural features of colloidal crystals.

The great design flexibility of the various ordered structures based on glass and polymeric nanospheres leaves great room for the ingenuity of researchers and engineers, thus providing high potential for novel or advanced photonic applications.

References

[1] Caruso, F. (2004). Colloids and Colloid Assemblies (Wiley-VCH Verlag, Weinheim).

[2] Graham, T. (1861). Liquid diffusion applied to analysis, Philos. Trans. R. Soc. London 151, pp. 183–224.

[3] Ostwald, W. (1971). An Introduction to Theoretical and Applied Colloid Chemistry: The World of Neglected Dimensions (John Wiley), translation from German by M. H. Fischer edition.

[4] Wilkinson, K. J. and Lead, J. R. (2006). Environmental Colloids and Particles: Behaviour, Separation and Characterisation (Wiley VCHVerlag, Weinheim).

[5] Xia, Y. N., Gates, B. and Yin, Y. D. (2000). Monodispersed colloidal spheres: old materials with new applications, Adv. Mater. 12, p. 693.
[6] Yang, S. M., Miguez, H. and Ozin, G. A. (2002). Opal circuits of lightplanarized microphotonic crystal chip, Adv. Funct. Mater. 12, p. 425.
[7] Morandi, V., Marabelli, F., Amendola, V., Meneghetti, M. and Comoretto, D. (2007). Colloidal photonic crystals doped with gold nanoparticles: spectroscopy and optical switching properties, Adv. Funct. Mater. 17, p. 2779.
[8] Lee, H. S., Kubrin, R., Zierold, R., Petrov, A. Y., Nielsch, K., Schneider, G. A. and Eich, M. (2013). Photonic properties of titania inverse opal heterostructures, Opt. Mater. Express 3, p. 1007.
[9] Fenollosa, R., Ibisate, M., Rubio, S., Lopez, C., Meseguer, F. and Sanchez-Dehesa, J. (2003). Photonic crystal microprisms obtained by carving artificial opals, J. Appl. Phys. 12, p. 671.
[10] Lukowiak, A., Chiappini, A., Chiasera, A., Ristic, D., Vasilchenko, I., Armellini, C., Carpentiero, A., Varas, S., Speranza, G., Taccheo, S., Pelli, S., Battisha, I. K., Righini, G. C., Strek, W. and Ferrari, M. (2015). Sol–gelderived photonic structures handling erbium ions luminescence, Opt. Quantum Electron. 47, p. 117.
[11] Shrivastava, V. P., Sivakumar, S. and Kumar, J. (2015). Green color purification in tb3+ ions through silica inverse opal heterostructure, Appl. Mater. Interfaces 7, p. 11890.
[12] Azevedo, C. B., Batista, T., de Faria, E. H., Rocha, L., Ciuffi, K. and Nassar, E. (2015). Nanospherical silica as luminescent markers obtained by solgel, J. Fluoresc. 25, p. 433.
[13] Azevedo, C. B., Batista, T., de Faria, E. H., Rocha, L., Ciuffi, K. and Nassar, E. (2008). Luminescent amino-functionalized or erbium-doped silica spheres for biological applications, Ann. N. Y. Acad. Sci. 1130, p. 262.
[14] Dood, M. J. A. D., Knoester, J., Tip, A. and Polman, A. (2005). Förster transfer and the local optical density of states in erbium-doped silica, Phys. Rev. B 71, p. 115102.
[15] Risti´c, D., Berneschi, S., Camerini, M., Farnesi, D., Pelli, S., Trono, C., Chiappini, A., Chiasera, A., Ferrari, M., Lukowiak, A., Dumeige, Y., Féron, P., Righini, G., Soria, S. and Conti, G. N. (2016). Photoluminescence and lasing in whispering gallery mode glass microspherical resonators, J. Lumin. 170, p. 755.
[16] Hun, X. and Zhang, Z. (2007). Preparation of a novel fluorescence nanosensor based on calcein-doped silica nanoparticles, and its

application to the determination of calcium in blood serum, Microchim. Acta 159, p. 255.
[17] Holland, B. T., Blanford, C. F., Do, T. and Stein, A. (1999). Synthesis of highly ordered, three-dimensional, macroporous structures of amorphous or crystalline inorganic oxides, phosphates, and hybrid composites, Chem. Mater. 11, p. 795.
[18] Barros Filho, D. A., Hisano, C., Bertholdo, R., Schiavetto, M. G., Santilli, C., Ribeiro, S. J. L. and Messaddeq, Y. (2005). Effects of self-assembly process of latex spheres on the final topology of macroporous silica, J. Colloid Interface Sci. 291, p. 448.
[19] Chiappini, A., Armellini, C., Chiasera, A., Ferrari, M., Fortes, L., Gonc¸alves, M. C., Guider, R., Jestin, Y., Retoux, R., Conti, G. N., Pelli, S., Almeida, R. M. and Righinii, G. (2009). An alternative method to obtain direct opal photonic crystal structures, J. Non-Cryst. Solids 355, p. 1167.
[20] Stober, W., Fink, A. and Bohn, E. (1968). Controlled growth of monodisperse silica spheres in the micron size range, J. Colloid Interface Sci. 26, p. 62.
[21] Chiappini, A., Armellini, C., Chiasera, A., Ferrari, M., Jestin, Y., Mattarelli, M., Montagna, M., Moser, E., Nunzi Conti, G., Pelli, S., Righini, G. C., Clara Goncalves, M. and Almeida, R. M. (2007). Design of photonic structures by sol-gel-derived silica nanospheres, J. Non-Cryst. Solids 353, p. 674.
[22] Bogush, G., Tracy, M. and IV, C. Z. (1988). Preparation of monodisperse silica particles: control of size andmass fraction, J. Non-Cryst. Solids 104, p. 95.
[23] Chiappini, A., Chiasera, A., Berneschi, S., Armellini, C., Carpentiero, A., Mazzola, M., Moser, E., Varas, S., Righini, G. and Ferrari, M. (2011). Sol–gel-derived photonic structures: fabrication, assessment, and application, J. Sol-Gel Sci. Technol. 60, p. 408.
[24] Righini, G. C., Armellini, C., Chiasera, A., Jestin, Y., Ferrari, M., Chiappini, A., Montagna, M., Arfuso Duverger, C., Feron, P., Berneschi, S., Brenci, M., Nunzi Conti, G., Pelli, S., Goncalves, C. and Almeida, R. M. (2007). Er3+-activated sol-gel silica derived spherical microresonators, Glass Technol.: Eur. J. Glass Sci. Technol., Part A. 48, p. 200.
[25] de Dood, M., Berkhout, B., van Kats, C. M., Polman, A. and van Blaaderen, A. (2002). Acid-based synthesis of monodisperse rare-earth-doped colloidal SiO2 spheres, Chem. Mater. 14, p. 2849.
[26] Moran, C. E., Hale, G. D. and Halas, N. J. (2001). Synthesis and characterization of lanthanide-doped silicamicrospheres, Langmuir 17, p. 8376.

[27] Karmakar, B., De, G. and Ganguli, D. (2000). Dense silica microspheres from organic and inorganic acid hydrolysis of teos, J. Non-Cryst. Solids 272, p. 119.
[28] Kimling, J., Maier, M., Okenve, B., Kotaidis, V., Ballot, H. and Plech, A. (2006). Turkevich method for gold nanoparticle synthesis revisited, J. Phys. Chem. B 110, p. 15700.
[29] Liz-Marz´an, L. M., Giersig, M. and Mulvaney, P. (1996). Synthesis of nanosized gold-silica core–shell particles, Langmuir 12, p. 4329.
[30] Garcia-Santamaria, F., Miyazaki, H. T., Urquia, A., Ibisate, M., Belmonte, M., Shinya, N.,Meseguer, F. and Lopez, C. (2002). Nanorobotic manipulation of microspheres for on-chip diamond architectures, Adv. Mater. 14, p. 1144.
[31] Galisteo-Lopez, J., Ibisate, M., Sapienza, R., Froufe, L., Blanco, A. and Lopez, C. (2011). Self-assembled photonic structures, Adv. Mater. 23, p. 30.
[32] http://project.tyndall.ie/phat/summary.html (Last accessed on 30 June 2017.)
[33] Jiang, P., Bertone, J., Hwang, K. and Colvin, V. (1999). Singlecrystal colloidal multilayers of controlled thickness, Chem. Mater. 11, p. 2132.
[34] Jiang, P., Ostojic, G., Narat, R., Mittleman, D. and Colvin, V. (2001). The fabrication and bandgap engineering of photonic multilayers, Adv. Mater. 13, p. 389.
[35] Chiappini, A., Armellini, C., Bazzanella, N., Carpentiero, A., Righini, G. C. and Ferrari, M. (2012). Hybrid colloidal crystal for photonic application, Opt. Photonics J. 2, p. 206.
[36] Woodcock, L. V. (1997). Entropy difference between the face-centred cubic and hexagonal close-packed crystal structures, Nature 385, p. 141.
[37] Miguez, H., Meseguer, F., Lopez, C., Mifsud, A., Moya, J. and Vazquez, L. (1997). Evidence of fcc crystallization of SiO2 nanospheres, Langmuir 13, p. 6009.
[38] Chiappini, A., Armellini, C., Carpentiero, A., Minati, L., Righini, G. and Ferrari, M. (2014). Solvent sensitive polymer composite structures, Opt. Mater. 36, p. 130.
[39] Shkunov, M. N., Vardeny, Z. V., DeLong, M. C., Polson, R. C., Zakhidov, A. A. and Baughman, R. H. (2002). Tunable, gap-state lasing in switchable directions for opal photonic crystals, Adv. Funct. Mater. 12, p. 21.
[40] Reculusa, S. and Ravaine, S. (2003). Synthesis of colloidal crystals of controllable thickness through the Langmuir–Blodgett technique, Chem. Mater. 15, p. 598.

[41] Khunsin, W., Romanov, S., Torres, C. S., Ye, J. and Zentel, R. (2008). Optical transmission in triple-film heteroopals, J. Appl. Phys. 104, p. 013527-1.
[42] Ding, B., Bardosova, M., Povey, I., Pemble, M. E. and Romanov, S. G. (2010). Engineered light scattering in colloidal photonic heterocrystals, Adv. Funct. Mater. 20, p. 853.
[43] Yan, Q., Teh, L., Shao, Q., Wong, C. and Chiang, Y. (2008). Layer transfer approach to opaline hetero photonic crystals, Langmuir 24, p. 1796.
[44] Hwang, D. K., Noh, H., Cao, H. and Chang, R. P. H. (2009). Photonic bandgap engineering with inverse opal multistacks of different refractive index contrasts, Appl. Phys. Lett. 95, p. 091101-1.
[45] Kubrin, R., Lee, H. S., Zierold, R., Petrov, A. Y., Janssen, R., Nielsc, K., Eich, M. and Schneider, G. A. (2012). Stacking of ceramic inverse opals with different lattice constants, J. Am. Ceram. Soc. 95, p. 2226.
[46] Khokhar, A. Z., Rahman, F. and Johnson, N. P. (2011). Photonic crystal heterostructures from self-assembled opals, Appl. Phys. A: Mater. Sci. Proc. 102, p. 281.
[47] Liu, G. Q., Wang, Z. S., Liao, Y. B., Hu, H. H. and Chen, Y. (2009). Highquality photonic crystal heterostructures fabricated by a modified selfassembly method, Appl. Opt. 48, p. 2480.
[48] Ge, J., Kwon, S. and Yin, Y. (2010). Niche applications of magnetically responsive photonic structures, J. Mater. Chem. 20, p. 5777.
[49] Takeoka, Y., Honda, M., Seki, T., Ishii, M. and Nakamura, H. (2009). Structural colored liquid membrane without angle dependence, Appl. Mater. Interfaces 1, p. 982.
[50] Fleischhaker, F., Arsenault, A. C., Peiris, F., Kitaev, V., Manners, I., Zentel, R. and Ozin, G. (2006). DNA designer defects in photonic crystals: optically monitored biochemistry, Adv. Mater. 18, p. 2387.
[51] Shen, Z., Yang, Y., Lu, F., Bao, B., You, B. and Shi, L. (2013). Self-assembly of colloidal spheres and application as solvent responding polymer film, J. Colloid Interface Sci. 389, p. 77.
[52] Pan, Z., Ma, J., Yan, J., Zhou, M. and Gao, J. (2012). Response of inverseopal hydrogels to alcohols, J. Mater. Chem. 22, p. 2018.
[53] Ying, Y. and Foulger, S. H. (2009). Color characteristics of mechanochromic photonic bandgap composites, Sens. Actuators B 137, p. 574.
[54] Minati, L., Chiappini, A., Armellini, C., Carpentiero, A., Maniglio, D., Vaccari, A., Zur, L., Lukowiak, A., Ferrari, M. and Speranza,

G. (2017). Gold nanoparticles 1D array as mechanochromic strain sensor, Mater. Chem. Phys. 192, p. 94.
[55] Chan, E. P., Walish, J. J., Urbas, A. M. and Thomas, E. L. (2013). Mechanochromic photonic gels, Adv. Mater. 25, p. 3934.
[56] Fudouzi, H. and Sawada, T. (2006). Photonic rubber sheets with tunable color by elastic deformation, Langmuir 22, p. 1365.
[57] Kang, P., Ogunbo, S. O. and Erickson, D. (2011). High resolution reversible color images on photonic crystal substrates, Langmuir 27, p. 9676.
[58] Aguirre, C. I., Reguera, E. and Stein, A. (2010). Tunable colors in opals and inverse opal photonic crystals, Adv. Funct. Mater. 20, p. 2565.
[59] Xu, X., Goponenko, A. and Asher, S. (2008). Polymerized polyhema photonic crystals: ph and ethanol sensor materials, J. Am. Chem. Soc. 130, p. 3113.
[60] Gu, Z. Z., Horie, R., Kubo, S., Yamada, Y., Fujishima, A. and Sato, O. (2002). Fabrication of a metal-coated three dimensionally ordered macroporous film and its application as a refractive indexsensor, Angew. Chem. Int. Ed. 41, p. 1153.
[61] Fudouzi, H., Sawada, T., Tanaka, Y., Ario, I., Hyakutake, T. and Nishizaki, I. (2012). Smart photonic coating as a new visualization technique of strain deformation of metal plates, Proc. SPIE 12, p. 425.
[62] Zonta, D., Chiappini, A., Chiasera, A., Ferrari, M., Pozzi, M., Battisti, L. and Benedetti, M. (2009). Photonic crystals for monitoring fatigue phenomena in steel structures, Proc. SPIE 7292, p. 729215-1.
[63] Chiappini, A., Alombert-Goget, G., Armellini, C., Berneschi, S., Boulard, B., Brenci, M., Cacciari, I., Duverger-Arfuso, C., Guddala, S., Ferrari, M., Moser, E., Rao, D. N. and Righini, G. C. (2010). Opal-type photonic crystals: fabrication and application, Adv. Sci. Technol. 71, pp. 50–57.
[64] Gu, Z., Horie, R., Kubo, S., Yamada, Y., Fujishima, A. and Sato, O. (2002). Fabrication of a metal-coated three-dimensionally ordered macroporous film and its application as a refractive index sensor, Angew. Chem. Int. Ed. 41, p. 1154.
[65] Tan, Y., Qian, W., Ding, S. and Wang, Y. (2006). Gold-nanoparticleinfiltrated polystyrene inverse opals: a three-dimensional platform for generating combined optical properties, Chem. Mater. 18, p. 3385.
[66] Abdelsalam, M. E., Bartlett, P. N., Baumberg, J. J., Cintra, S., Kelf, T. A. and Russell, A. E. (2005). Electrochemical sers at a structured gold surface, Electrochem. Commun. 7, p. 740.

[67] Lousse, V. and Fan, S. (2006). Waveguides in inverted opal photonic crystals, Opt. Express 14(2), pp. 866–878.
[68] Safriani, L., Cai, B., Komatsu, K., Sugihara, O. and Kaino, T. (2008). Fabrication of inverse opal tio2 waveguide structure, Jpn. J. Appl. Phys. 47(2S), p. 1208.
[69] Scharrer, M., Yamilov, A.,Wu, X., Cao, H. and Chang, R. P. H. (2006). Ultraviolet lasing in high-order bands of three-dimensional zno photonic crystals, Appl. Phys. Lett. 88, p. 201103-1.
[70] Chiappini, A., Armellini, C., Chiasera, A., Jestin, Y., Ferrari, M., Moser, E., Nunzi Conti, G., Pelli, S., Retoux, R. and Righini, G. C. (2009). Er3+- activated sol-gel silica confined structures for photonic applications, Opt. Mater. 31, p. 1275.
[71] Teh, L., Yeo, K. and Wong, C. (2006). Isotropic photonic pseudogap in electrodeposited zno inverse opal, Appl. Phys. Lett. 89, p. 051105.
[72] Nikolaev, I. S., Vos, W. L. and Koenderink, A. F. (2009). Accurate calculation of the local density of optical states in inverse-opal photonic crystals, J. Opt. Soc. Am. B 26(5), pp. 987–997.
[73] Teperik, T. V., de Abajo, F. J. G., Borisov, A. G., Abdelsalam, M., Bartlett, P. N., Sugawara, Y. and Baumberg, J. J. (2008). Omnidirectional absorption in nanostructured metal surfaces, Nat. Photonics 2, p. 299.
[74] Kim, H. J., Kim, S., Jeon, H., Ma, J., Choi, S. H., Lee, S., Ko, C. and Park, W. (2007). Fluorescence amplification using colloidal photonic crystal platform in sensing dye-labeled deoxyribonucleic acids, Sens. Actuators B 124, p. 147.
[75] Blum, C., Mosk, A. P., Nikolaeva, I. S., Subramaniam, V. and Vos, W. L. (2008). Color control of natural fluorescent proteins by photonic crystals, Small 4, p. 492.
[76] Chiappini, A., Armellini, C., Carpentiero, A., Pasquardini, L., Lunelli, L., Vaccari, A., Pelli, S., Lukowiak, A., Pederzolli, C., Righini, G. C., Ramponi, R. and Ferrari, M. (2017). Glass-derived photonic crystal structures, Adv. Sci. Technol. 98, p. 11.
[77] Chiappini, A., Armellini, C., Carpentiero, A., Pasquardini, L., Lunelli, L., Vaccari, A., Pelli, S., Lukowiak, A., Pederzolli, C., Righini, G., Ramponi, R. and Ferrari, M. (2017). Glass-derived photonic crystal structures, Adv. Sci. Technol. 98, p. 11.
[78] Choi, Y., Choi, E. and Park, J. (2012). Highly sensitive protein detection using quenching effects from aptamer-functionalized photonic crystals, IEEE 25th International Conference on Micro Electro Mechanical Systems (MEMS) 9, p. 839.
[79] Lu, L., Randjelovic, I., Capek, R., Gaponik, N., Yang, J., Zhang, H. and Eychmuller, A. (2005). Controlled fabrication of gold-

coated 3D ordered colloidal crystal films and their application in surface-enhanced raman spectroscopy, Chem. Mater. 17, p. 5731.

[80] Guddala, S., Kamanoor, S., Chiappini, A., Ferrari, M. and Desai, N. (2012). Experimental investigation of photonic band gap influence on enhancement of raman-scattering in metal-dielectric colloidal crystals, J. Appl. Phys. 112, p. 084303.

[81] Gaponenko, S. V., Gaiduk, A. A., Kulakovich, O. S., Maskevich, S. A., Strekal, N. D., Prokhorov, O. A. and Shelekhina, V. M. (2001). Raman scattering enhancement using crystallographic surface of a colloidal crystal, JETP Lett. 74, p. 309.

[82] Kubo, S., Gu, Z.-Z., Tryk, D. A., Ohko, Y., Sato, O. and Fujishima, A. (2002). Metal-coated colloidal crystal film as surface-enhanced raman scattering substrate, Langmuir 18, p. 5043.

[83] Chou, J. B., Yeng, Y. X., Lee, Y. E., Lenert, A., Rinnerbauer, V., Celanovic, I., Soljacic, M., Fang, N. X., Wang, E. N. and Kim, S.-G. (2014). Enabling ideal selective solar absorption with 2D metallic dielectric photonic crystals, Adv. Mater. 26, p. 8041.

[84] Baumberg, J., Kelf, T., Sugawara, Y., Cintra, S., Abdelsalam, M., Bartlett, P. and Russell, A. (2005). Angle-resolved surface-enhanced raman scattering on metallic nanostructured plasmonic crystals, Nano Lett. 5, p. 2262.

[85] Li, Y., Sun, J., Wang, L., Zhan, P., Cao, Z. and Wang, Z. (2008). Surface plasmon sensor with gold film deposited on a twodimensional colloidal crystal, Appl. Phys. A 92, p. 291.

[86] Morandi, V., Marabelli, F., Amendola, V., Meneghetti, M. and Comeretto, D. (2007). Colloidal photonic crystals doped with gold nanoparticles: spectroscopy and optical switching properties, Adv. Funct. Mater. 27, p. 2779.

[87] Chen, J., Qin, G., Shen, W., Li, Y. and Das, B. (2015). Fabrication of longrange ordered, broccoli-like sers arrays and application in detecting endocrine disrupting chemicals, J. Mater. Chem. C 3, p. 1309.

[88] Giordano, M. C., Foti, A., Messina, E., Gucciardi, P. G., Comoretto, D. and de Mongeot, F. B. (2016). Sers amplification from self-organized arrays of plasmonic nanocrescents, Appl. Mater. Interfaces 8, p. 6629.

[89] Chiappini, A., Guddala, S., Armellini, C., Berneschi, S., Cacciari, I., Duverger-Arfuso, C., Ferrari, M. and Righini, G. C. (2010). Fabrication and characterization of colloidal crystals infiltrated with metallic nanoparticles, Proc. SPIE 7725, p. 77250W-1.

3. Stimuli-Responsive Colloidal Crystal for Structural Health Monitoring: Fabrication and Numerical Modelling

By V. Piccolo, A. Chiappini, C. Armellini, A. Vaccari, L. Deseri, M. Ferrari and D. Zonta

Abstract

In this reaserch the concept and development of a strain sensing system for a future structural application based on the properties of stimuli-responsive opals is presented. One type of colloidal crystals can be seen as a periodic arrangement of regularly shaped materials with different dielectric constants. Their optical properties are tailored by the periodicity in the refractive index, changing this one means that the wavelength of reflectance will change. This effect makes the opal structures a convenient tool for sensing, especially if the effect can be made specific for the stimulus. Once the colloidal crystal is designed to work in the visible range, a distortion in the periodicity of such structure results in a change in its apparent color. Such effect makes them amenable to visual readout by untrained operators. This latter aspect could be a huge improvement for permanent monitoring of structural elements, as any critical changes in the strain field can be immediately and easily detected by visual inspection. Here we provide the basic information concerning the physical principle and expected performance of stimuli-responsive colloidal crystals and the fabrication of these structures, then a finite difference time domain analysis has been performed and compared to the experimental results. Finally, we discuss the results in terms of possible applications to structural health monitoring of civil structures.

3.1 Introduction

One of the most common malfunction causes in civil, industrial and transportation structures is fatigue damage, involving initiation of cracks in critical sites and their propagation until eventual catastrophic failure. Often these structures are exposed to complicated (sometimes stochastic) operational and environmental conditions that, in combination with complex geometrical features, make the prediction of their life cycle very difficult. The uncertainty about the structural integrity of in-service structures forces designers to damage-tolerant-design approaches relying on periodic inspections to ensure that the

structure is free of critical defects able to jeopardize the functionality/safety before the next scheduled inspection. Since size, location and propagation behaviour of potential critical defects may not be known exactly, the number of inspections is often overestimated, thus incrementing maintenance costs and idle times. The uncertainty about the actual state of a structure can be considerably reduced by structural health monitoring (SHM), which has been defined by Housner et al. [12] as "the continuous or regular measurement and analysis of key structural and environmental parameters under operating conditions, for the purpose of warning of abnormal states or accidents at an early stage". Therefore, many SHM strategies are devoted to timely detect fatigue cracks for continuous real-time damage estimation and condition-based maintenance. In the past, several non-destructive damage detection (NDD) techniques has been envisaged and applied for SHM purposes. They are based on a wide variety of physical characteristics, such as damping [20], natural frequencies [7], modal shapes [17], mechanical guided (Lamb) waves scattering [14], [15], nonlinear acoustic-ultrasonic methods [5], electric potential drop [22]. Although these methods have certain advantages, their applicability is impaired by some drawbacks, among them sensitivity to boundary and/or environmental conditions (e.g. temperature, varying operative load conditions), utilization of invasive sensors/actuators and in many cases inability to estimate size and location of the defect.

One promising NDD technique is based on strain field measurements aimed at revealing anomalous perturbations exerted by cracks [16]. In this case, the strategies to identify, locate and quantify a crack depend on the type of strain sensors employed in the SHM technique. Strain sensors, like electrical resistance-based or optical fibre Bragg grating (FBG) strain gauges [19], have relatively short gauge lengths resulting in engineering information collected at a single point. Consequently, a network of sensors placed at certain critical points of the structure is required to accomplish a global evaluation of a large structure [11]. These 'point monitoring' methods are feasible only if the hot spots of the structure, where the point sensors will be installed, have been identified accurately. Moreover, as cracks generally produce a very localized perturbation of the strain field, a large number of point strain sensors is required to detect cracks whose size is still compatible with the integrity/functionality of the structure [3]. To overcome this drawback, long-gauge optical strain sensors have been developed [8]. In this case, local effects caused by the crack on the strain field are lost, while changes in global dynamic response of the structure are detected by integrating the response along the length of the structure. As in the approaches based on the change in natural frequency and modal shapes, the crack is detected indirectly from the global response of the structure

and therefore the method suffers from similar environmental limitations.

If a large structure with many possible crack nucleation sites needs to be monitored, a distributed crack monitoring method becomes necessary [23]. Line-distributed strain sensors are generally based on the modulation of light intensity in optical fibres. More specifically, in the optical time domain reflectometry (OTDR) Rayleigh and Fresnel scatterings are used for sensing structural perturbations, while Brillouin scattering detects the Doppler shift in light frequency which is related to the strain measurement [10]. These techniques have been successfully applied in SHM of aircraft and civil structures [10], [27]: the onset of a crack is detected as a peak or discontinuity in the strain field monitored along the fibre. The appealing feature of these methods would be even greater if the entire stress field of the structure could be monitored by employing a 2D-distributed strain sensor. Therefore, the possibility of applying on the structure surface polymeric films as strain sensors is arousing increasing interest. For instance, some new concepts exploit piezoelectric or capacitor smart layers [26], [9], [18] as well as thin-film full-bridge strain sensors [25] for determining not only crack length and location but also fracture mechanics parameters [1]. On the other hand, the required data acquisition system and the signal-processing algorithm make this approach cumbersome and still not ready for practical applications.

In the present paper we propose to use for SHM purpose stimuli-responsive colloidal crystals (CCs) as a 2D distributed sensors based on a low cost technology. They could serve as an easy tool for the in situ monitoring of mechanical deformations by stretching or compressing. Specifically, CCs change their reflectance properties depending on the applied strain field, so that a deformation of the film results in a change in its apparent colour (once they have been design to work in the visible range). In principle, this feature makes the sensor suitable for the permanent monitoring of structural elements, as any particular changes in the strain field could be immediately and easily seen by visual inspection without complicated systems for data acquisition and signal processing. Despite the state of the art on similar devices is still at the initial level [6], and the application are limited to laboratory tests (only few in situ application on small structural parts), this technology is very promising for the fatigue damage detection, as it allows the identification of the strain field in critical zones, e.g. around cracks. In a future scenario, this kind of sensor could be directly integrated in the structural elements' production or used as a coating spread into the surface. Many practical issues, such as the in situ maintenance and duration, are still to be overcome, but the present research is a first step in that direction.

This paper is organized as follows: Section 2 presents the approximate analytical optomechanical solution; Section 3 presents the briefly the fabrication protocol and the results of the experimental characterization; Section 4 illustrates the Finite Difference Time Domain (FDTD) model that has been written to both validate the experimental results and to elaborate a new design tool for this kind of nanomaterials with the comparison between its output and the experiments, then some concluding remarks are provided in the last section.

3.2 Colloidal Photonic Crystals: Approximate Optomechanical Approach and Expected Performance

The idea of using CC as a sensor for SHM is based on the observation that a distortion in the crystal structure produces a change in the reflected bandwidth. Fiber Bragg Gratings (FBGs) are a well-known example of photonic structure commonly used as sensors in civil and mechanical applications [8], although they normally operate in the infrared field. Whenever a photonic crystal is designed to work in the visible range of the spectrum, a variation in the crystal lattice results in a change in its apparent colour. Fuduozi [6] has suggested these crystals can also be utilized for obtaining optical strain sensors, suitable for monitoring and displaying structural and environmental variations in terms of colour variations, which can be visualized by appropriate optical instruments or even by the naked eye. This feature makes CCs suitable for monitoring in continuus structural elements, as any changes in the strain field can be immediately and easily detected by visual inspection.
Consider the 3D CC deposited on a substrate, having colloidal spheres in an elastomeric matrix of refractive indices n_1 and n_2, respectively, and filling factor f, illuminated by white light, as depicted in Figure 1. The crystal will reflect the light around a specific bang-gap wavelength λ. As a first approximation this could be expressed by the modified form of Bragg's law:

$$\lambda = 2 \cdot d_{111} \cdot \sqrt{\left(n_{eff}\right)^2 - (\sin\theta)^2} \qquad (3.1)$$

where d_{111} is the inter-planar distance, neff is the effective refractive index and θ is the angle of the incident light measured with respect to the crystal surface. For the effective refractive index, a mixture theory-like approximation is adopted, namely:

$$n_{eff}{}^2 = f \cdot n_1^2 + (1 - f) \cdot n_2^2 \tag{3.2}$$

where f is the composite filling factor, in this case the rate between sphere volume and matrix volume. Assuming an incidente angle equal to zero, equation (3.1) reduces to the classical form of Bragg's law:

$$\lambda = 2 \cdot n_{eff} \cdot d \tag{3.3}$$

Assuming the refractive index invariant with strain, the reflected wavelegnth is directly proportional to the interplanar spacing d_{111}. Thus, a relatively small change in the interplanar spacing d_{111} will result in a change in the reflected wavelength according to:

$$\Delta\lambda = 2 \cdot n_{eff} \cdot \Delta d \tag{3.4}$$

With a first order approximation, the change in the d can be evaluated as $\Delta d = d_0 \cdot \varepsilon_3$ where ε_3 is the crystal small strain in the orthogonal direction to its plan and d_0 is the interplanar spacing in unstrained conditions. Thus, in general, the following expression holds:

$$\Delta\lambda = 2 \cdot n_{eff} \cdot d_0 \cdot \varepsilon_3 \tag{3.5}$$

From the deformation of the substrate one can predict the change in band-gap wavelength. Although the magnitude of the strain reached in this device is the order of 15%, hence we are in the regime of finite deformations, the isotropic Kirchhoff-Saint Venant consitutive relation is assumed in this paper. This has the advantage that looks exactly like the Hook's law for linear isotropic elastic solids. Henceforth, the strain tensor of the crystal ε is related to its stress tensor σ through classical linear and isotropic elasticity as follows:

$$\varepsilon = E\,\sigma\,; \begin{bmatrix}\varepsilon_1\\ \varepsilon_2\\ \varepsilon_3\end{bmatrix} = \frac{1}{E}\begin{bmatrix}1 & -\nu & -\nu\\ -\nu & 1 & -\nu\\ -\nu & -\nu & 1\end{bmatrix}\begin{bmatrix}\sigma_1\\ \sigma_2\\ \sigma_3\end{bmatrix} \tag{3.6}$$

where E and ν are the equivalent Young modulus and Poisson's ratio of the crystal, and the subscripts 1-2-3 indicate the principal directions. For the envisaged application, the CC is typically in a state of plain

stress, meaning $\sigma_3 = 0$. In this case, the direct relationship between strain and in-plain stress simplifies to:

$$\begin{bmatrix}\varepsilon_1\\ \varepsilon_2\end{bmatrix} = \frac{1}{E}\begin{bmatrix}1 & -\nu\\ -\nu & 1\end{bmatrix}\begin{bmatrix}\sigma_1\\ \sigma_2\end{bmatrix}; \begin{bmatrix}\sigma_1\\ \sigma_2\end{bmatrix} = \frac{E}{1-\nu^2}\begin{bmatrix}1 & \nu\\ \nu & 1\end{bmatrix}\begin{bmatrix}\varepsilon_1\\ \varepsilon_2\end{bmatrix} \qquad (3.7^{a,b})$$

and from equation 6 one can simply obtain:

$$\varepsilon_3 = -\frac{\nu}{E}\cdot(\sigma_1 + \sigma_2) \qquad (3.8)$$

Replacing in equation 8 the strain as in equation 3.7b, one can obtain the following fundamental raltionship between the vertical strain ε_3 and in-plain strain tensor:

$$\varepsilon_3 = -\frac{\nu}{1-\nu}\cdot(\varepsilon_1 + \varepsilon_2) \qquad (3.9)$$

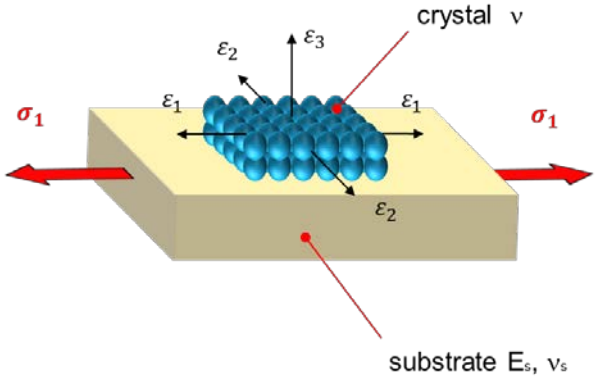

Figure 3.1: *Three dimensional CC on the substrate with applied stress (σ_1) and the related strain distribution ($\varepsilon_1, \varepsilon_2, \varepsilon_3$); Es, vs, are Young modulus and Poisson's ratio of the substrate, ν is the Poisson's ratio of the CC.*

Because the CC adhers to the substrate, equation 3.9 can be seen as the raltionship between the vertical strain of the CC and the in-plane strain of the substrate surface.
If a stress σ_1 is applied to the support, its in-plane strain results:

$$\begin{cases}\varepsilon_1 = \dfrac{\sigma_1}{\mathrm{Es}}\\ \varepsilon_2 = \dfrac{-\nu\mathrm{s}\cdot\sigma_1}{\mathrm{Es}}\end{cases} \qquad (3.10)$$

where E_s, ν_s are the Young modulus and Poisson's ratio of the substrate. With the assumption of isotropy of the material the strain in the same plane of the substrate, ε_2, can be evaluated with the following formula:

$$\varepsilon_2 = -\nu_s \cdot \varepsilon_1 \tag{3.11}$$

and replacing (3.11) in (3.9), we obtain:

$$\varepsilon_3 = -\nu \cdot \frac{1-\nu_s}{1-\nu} \cdot \varepsilon_1 \approx -\nu \cdot \varepsilon_1 \tag{3.12}$$

where the approximation is valid as long as the two Poisson's rations are close enough. Equation 12 states that when the substrate is stretched under a uniaxial stress in one in-plane direction, it and the crystal itself contracts approximately ν times the elongation along the stress direction. Combining (3.12) with (3.5) lead to the determination of the change in reflected wavelength $\Delta\lambda$ as follows:

$$\Delta\lambda = -2 \cdot n_{eff} \cdot \nu \cdot \frac{1-\nu_s}{1-\nu} \cdot \varepsilon_1 \approx -2 \cdot n_{eff} \cdot \nu \cdot d_0 \cdot \varepsilon_1 \tag{3.13}$$

In the most general case both the refractive index n_{eff} and Poisson's ratio ν could change with strain. Henceforth, the relationship between the bandgap wavelength and the transverse strain becomes nonlinear. In this case the sensitivity of $\Delta\lambda$ with the change in longitudinal strain takes approximately the following form:

$$\frac{\Delta\lambda}{\mathrm{d}\varepsilon_1} \approx -2 \cdot d_0 \cdot \left\{\frac{\mathrm{d}n_{eff}}{\mathrm{d}\varepsilon_1} \cdot \nu \cdot \varepsilon_1 + n_{eff} \cdot \frac{\mathrm{d}\varepsilon_3}{\mathrm{d}\varepsilon_1}\right\} \tag{3.14}$$

Making the assumption of a linearly elastic behavior of the material and the effective refraction index n_{eff} constant with strain, Equation (3.14) reduces to the following expression:

$$\frac{\Delta\lambda}{\mathrm{d}\varepsilon_1} = -2 \cdot n_{eff} \cdot \nu \cdot \frac{1-\nu_s}{1-\nu} \approx -2 \cdot n_{eff} \cdot \nu \cdot d_0 \tag{3.15}$$

which basically shows in first approximation that the crystal sensitivity to strain is proportional to its refractive index, lattice spacing and Poisson's ratio.

3.3 Fabrication Protocol of Colloidal Photonic Crystals and Testing

3.3.1 Fabrication Protocol

In the last decade, several methods have been developed to create CCs, such as: vertical deposition, electrostatic repulsion, capillary forces induced convective self-assembly [40] and electric field induced assembly. Depending on the technique, the production time ranges from days to weeks. The authors of this paper already performed a simple and effective method to obtain monosize polystyrene spheres and consequently, to realize colloidal photonic crystal structures from these spheres, based on spin coating technique. Despite of the array of advanced techniques available, the CCs developed as strain sensors for the application presented in this paper have been produced by using the most classical technique, meaning vertical deposition. This is the simplest and cheapest technique at the state of the art, while its drawback is essentially the high time-consuming and the size of the final crystal.

The sample that has been made was constituted by polystyrene spheres (PSs) embedded into a poly-dimethylsiloxane (PDMS) elastomer. The applied technique is basically made by three main steps: the first step is the fabrication of the PSs; second step consists into the deposition of the PSs in a lattice structure, finally the infiltration with the elastomer.

The fabrication of the spheres is characterized by the mixture of styrene, water, a surfactant (SDS), and a polymerization initiator (K2S2O8), in temperature and stirring speed control (see figure 3.2a) . As a result of the selected parameters, the PSs have been produced with a diameter of about 230nm. This value was chosen to obtain a suitable color of the CC, although the size can be modified by applying a different fabrication protocol.

Then, in the second phase, a highly mono-disperse PSs suspension is deposited on a highly deformable rubber substrate (Viton) with size 50x15x1mm. This substrate was vertically placed in a beaker containing the aqueous suspension and put in an oven at constant temperature of 50°C. A couple of days were necessary to deposit the CC on the support. In this time, the crystallization is initially driven by strong attractive capillary forces acting between particles at the drying front when the liquid film reaches a thickness of the particle diameter (see figure 2b). This effect drives particles to aggregate in layers and creates a porous structure with high specific surface area. The large surface area facilitates solvent evaporation. The thickness of the PC is in the order of 10μm.

The third step was the infiltration with PDMS (Sylgard 184, Dow Corning) (see figure 2c). The elastomer is made of two separate components: base and curing agent. The base and curing agent were mixed in a 3:1 ratio. After infiltration the PDMS was cured for 4h at 65°C and then the excess elastomer was peeled-off from the crystal. Several infiltration cycles were necessary to completely fill the voids among the PS spheres, before any re-infiltration step the sample was swollen in a silicone fluid (Dow Corning 1cSt). The obtained composite film was a 3D lattice of PS spheres embedded in a PDMS matrix. The elastomer has the fundamental function to allow a flexible CC structure which can be handled. Furthermore, this process affects the range of deformability of the CC.

a)

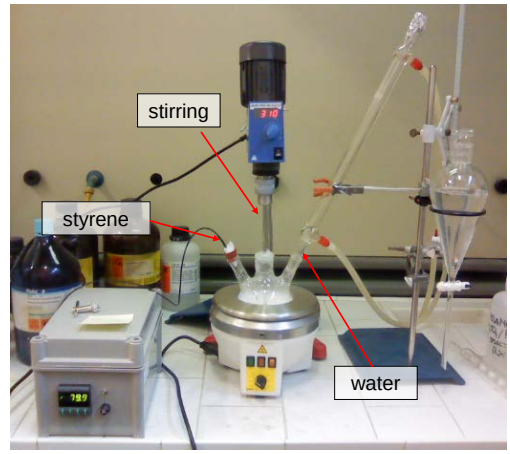

b)

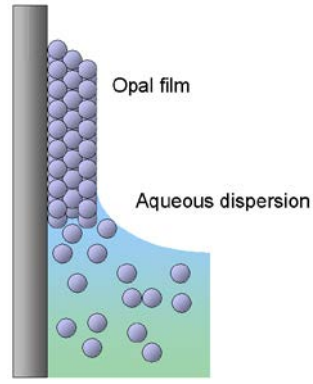

c) 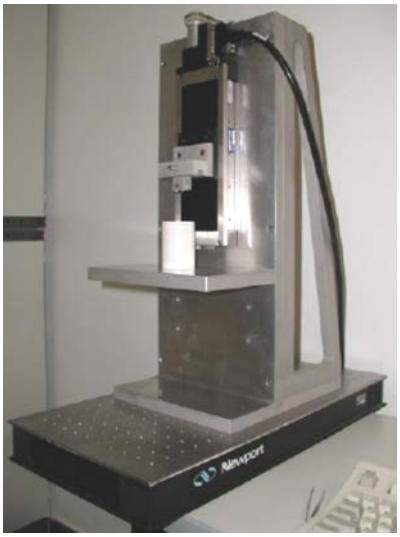

Figure 3.2: *Production of the Photonic crystals: fabrication of the Polystyrene Spheres (a), vertical deposition (b), and infiltration (c) (Hatton2010).*

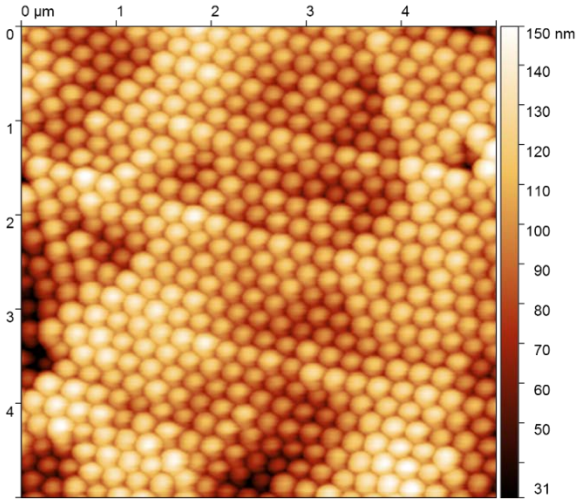

Figure 3.3: *shows an AFM (Atomic Force Microscope) image of the of the final CC sample.*

3.3.2 Testing

A sample of CC, produced with the fabrication protocol presented in the previous section, has been tested in the laboratory for identifying the relationship between the applied strain and the wavelength of the

reflected peak. The CC is a 10x10mm patch and, as described before, it has been deposited onto a 50x15x1mm rubber support.

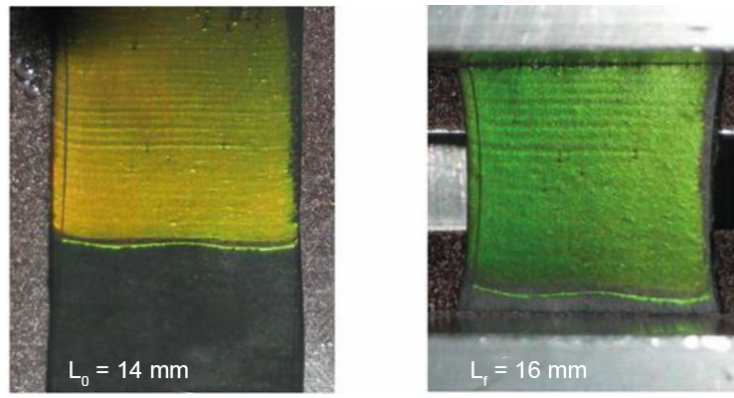

Figure 3.4: *On the left the sample in the reference configuration, characterized by a length of 14mm, which exhibit an orange color, on the right the sample with a final length of 16 mm, exhibiting a green opalescence.*

As shown in Figure 3.4 the sample appears orange in the reference configuration (not stressed) and it turns green as a tensile strain is applied.
During the test, the strip has been fixed to two micrometric linear stages, so that the center of the sample is kept almost fixed, while symmetrically elongating the ends. Thus the applied field is basically a mono-axial strain, and the test is carried by elongating the support. Figure 3.5 shows the experimental set-up.

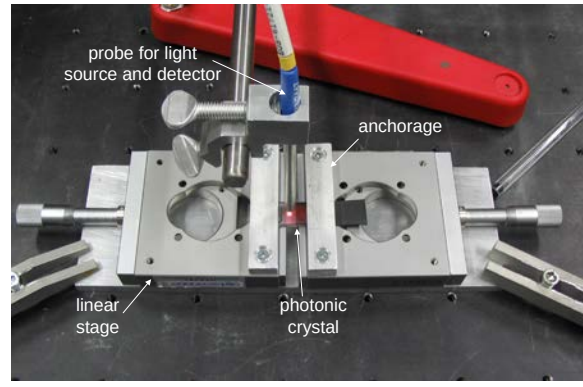

Figure 3.5: *Set-up for the laboratory test on the CC sample.*

The diffraction characteristic of the CC has been recorded by using a spectrometer.This is composed by a light source, a light receiver and a spectrometer analyzer. Both source and receiver are connected with a

probe that permits to easily inspect the sample surface. During the test the probe was kept perpendicular to the strip. The outcome of this instrument is the full spectrum of the received light in the visible range (350-750nm), with a wavelength resolution in the order of 0.1nm. The area of the CC inspected by the device is about 4 mm^2: hence it is a local measure. The sample underwent a deformation cycle, from an original length of 14.0 mm up to 16.0mm, corresponding to a maximum elongation of 2 mm and a strain 14.3%, and then down to the reference configuration. The outcomes are reported below in Figure 3.6.

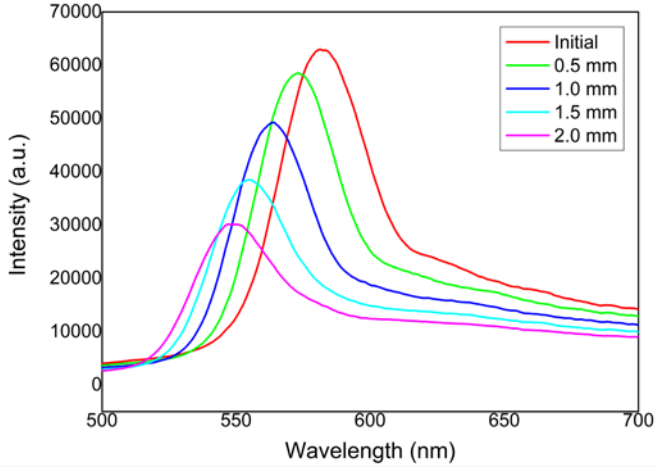

Figure 3.6: *Reflectance spectra of the CC sample recorded during the elongation test.*

The attenuation at each step of elongation (depending from the strain) is a well known phenomenon [6]. Each spectrum presents a clear bell-shape, with a width of about 30 nm and a wavelength shift of the peak around 9 nm at aech recorded step. Figure 7 reports the relationship between the peak wavelength and the applied strain, recorded during the load cycle. The wavelength decreases as the strain increases as expected from the formulas described in the previous section. The performance of the device in terms of sensitivity is around 3.5 με /pm.
There are several possible explanations of the sample behaviour in terms of its reflection spectra whenever such device undergoes imposed deformations.
The decrease in the reflection intensity is proportional to the ratio between the difference of the refractive index of the materials (which is assumed to be constant in the model) and the effective refractive index as shown in the following formula [28].

$$I \propto \Delta n / neff \tag{3.16}$$

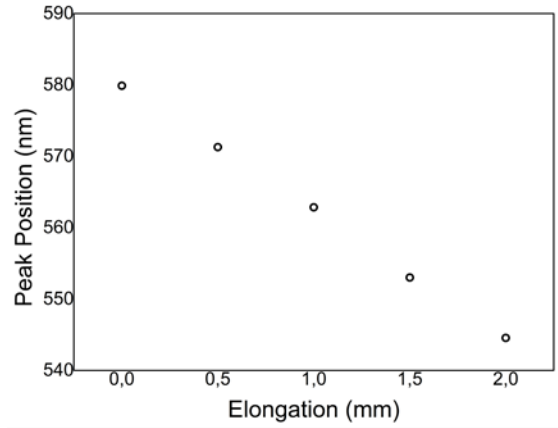

Figure 3.7: *Experimental relationship between the peak positions and the applied elongation.*

This demonstrates that the effective refractive index is changing due to the change in the volume fraction of the system, as it was highlighted above. Such a volume fraction for the FCC lattice can be evaluated as follows [29]:

$$f = 2\pi/3 \;\; d^3/a^3 \tag{3.17}$$

where d is the diameter of the spheres and a is the lattice parameter ($a=d_{111}\sqrt{3}$).
The asymmetry in the shape of the reflection spectra in the experiments is due to the cracks that are present into the sample[30] and to the interrogation system, for example the influence of the lamp that has an own particular spectrum as shown in figure 3.8.
If the effect of the particular shape of the spectrum of the lamp could be purged, the effects of defects is unavoidable while measuring, since the illuminated area is much larger (the unit are millimeters squared) than the domain without them (of the order of micrometers). Those cracks, which arises during the drying process of the PhC films, are not entirely avoidable and some other groups are working on this fabrication problem [31, 32, 33].

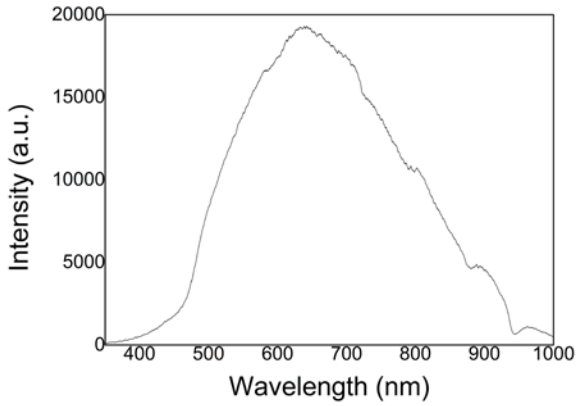

Figure 3.8: *Spectrum of the lamp that has been used to perform the optic measurements.*

The shape of the experimental spectra changes also with the applied strain showing a broadening of it. This behaviour is probably due to the coexistence of two phenomena that happen during the deformation of the sample: the opening of the cracks described above and an inhomogeneous differential displacement of the different planes of the crystal, nonetheless the measurements itself that is not restricted into a very small area. This differential displacement of planes could lead to an analogy with the reflectance spectra of a heterostructure [34, 35, 36], where there is the convolution of the contributions that every different inner structure gives.

3.4 Numerical Simulation with Finite Difference Time Domain Code and Comparison with the Experimental Results

In this section a computational approach is presented. It has been used not only for validating the experimental results showed before, but also for better understanding the behavior of this highly complex physical system, and pave the way to the design of innovative and versatile photonic sensors. The experimental optical behavior has been compared with the corresponding solution for the electromagnetic field obtained from the governing Maxwell's equations. Due to their analytical complexity, they can be solved only approximately, by means of a numerical approach. Using the Finite-Difference Time-Domain (FDTD) method, we directly implemented the two Maxwell's curl equations in an in-house developed C/C++ code. The remaining two divergence free scalar equations (there are no free electric charge inside the structure) are automatically obeyed for all the subsequent instants of time *t*, if the initial electromagnetic field distribution satisfies them

at *t=0*. In fact, we use a causal approach, in which an electromagnetic plane wave linearly polarized pulse of finite duration impinges on the structure, starting from a zero-field situation. The particular geometry of the structure (reported in figure 3.9) is included on the FDTD spatial grid by modifying, at the electric field sampling points, the coefficients of the relevant finite-difference equations with the values of the electric permittivity of the PDMS slab (relative permittivity $\varepsilon_r=n^2$ with n the refractive index of the PDMS medium: $n=1.40$) or the polystyrene spheres ($n=1.55$). Outside these materials, the electric permittivity equals that of vacuum, $\varepsilon_0=8.854\times10^{-12}$ Farad/meter, a value practically coinciding with that of air. No magnetic effects are considered at all, meaning that the magnetic permeability is everywhere the vacuum permeability, $\mu_0=4\pi\times10^{-7}$ Henry/meter.
Thirteen consecutive planes of spheres are considered, from a face-centered cubic (fcc) three-dimensional arrangement, taken along the Λ path direction of the Brillouin zone.

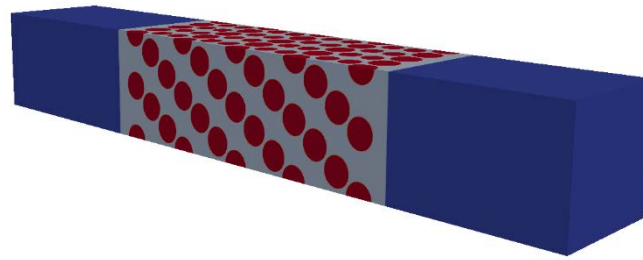

Figure 3.9: *Image of the ripartition of the FDTD volume between vacuum (depicted in blu), PDMS (grey), and PS (red). The longest side is arranged in the direction of propagation of the electromagnetic wave.*

Space steps of the FDTD Yee unit cell nearly equal along the three coordinate directions were used, of about 4 nm each, for a total of 200×1200×200 Yee cells. The time step for the evolution of the explicit FDTD algorithm was chosen to obey the Courant-Friedrichs-Lewy stability condition [39], guaranteeing numerical stability. Given that our spatial scheme was of second order accuracy, we assume a relative error accuracy in the final calculated values of the electric field components of 1%, as reported in literature. In fact, we used space steps very small compared to the wavelengths contained in the main part of the exciting pulse. This was a compact pulse of the “smoothed raised cosine” type. It has to be recognized, however, that eventually the final result can further be affected by the “staircasing” in the geometrical structures approximate representation.
When the impinging initial electromagnetic pulse interacts with the dielectric structure, a secondary field is produced, which overlaps to the initial one, mixing with it and giving rise to a total electromagnetic field

inside the computational volume. After a sufficiently long time interval, such total field falls off to zero, because the initial forcing field has finite duration and no other sources are present.
By in-line Fourier transforming the response of the system, obtained via a buffering of the field values calculated at each FDTD time step multiplied by the correct exponential time phase factor, it is possible to calculate the frequency response at any given frequency (or vacuum wavelength) of analysis [38].
In order to work properly the FDTD algorithm requires special boundary conditions at the outer surface of the FDTD spatial grid. Such boundary conditions are needed to emulate an infinite extension even if only a limited RAM is allowable, thus avoiding any spurious back reflection from the outer surface into the computational domain. Such a feature is implemented through perfectly matched layers (PML) able to absorb outgoing waves without any reflection and attenuate them to zero inside the layer thickness. In this specific case, the so called CPLM (convolutionary PLM) implementation [37] has been used. CPML boundary conditions were used only along the direction corresponding to the initial beam propagation direction. On the other surfaces Periodic Boundary Conditions have been applied in order to emulate infinite transverse dimensions. Particular attention has been paid to assume the correct periodicity of the transverse edges of the structure, to avoid the introduction of artificial structural defects in the numerical calculations. The incident plane wave pulse has been injected on a surface in front of the structure, allowing the reflected field to pass freely through such a surface without any constrains. We calculated the reflected power flux by integrating numerically the real part of the Poynting vector for the Fourier transformed reflected field on a transverse surface made of 200×200 Yee cells. It was normalized with the corresponding flux contained in the incident pulse at the same frequency (wave wavelength), thus getting the reflectance spectra in the range 350÷750 nm.

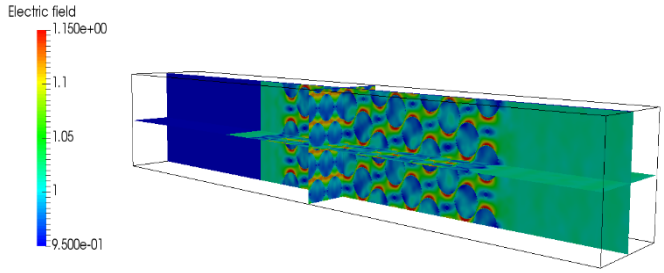

Figure 3.10: *Internal sections of the FDTD computational volume, which report the electromagnetic field maps normalized with respect to the injected wave. The blu part is where there is only the reflected field and where the reflectance of the structure is calculated.*

From a mechanical point of view, the phenomenon is modeled as a progressive change of the relative distance of the PS spheres inside the PDMS matrix that represents, approximately, the manifestation of the deformation of the device during the experiments. At each value the response of the sample in terms of reflectance spectra is acquired and then compared with the experimental one, as reported in Figure 3.11.

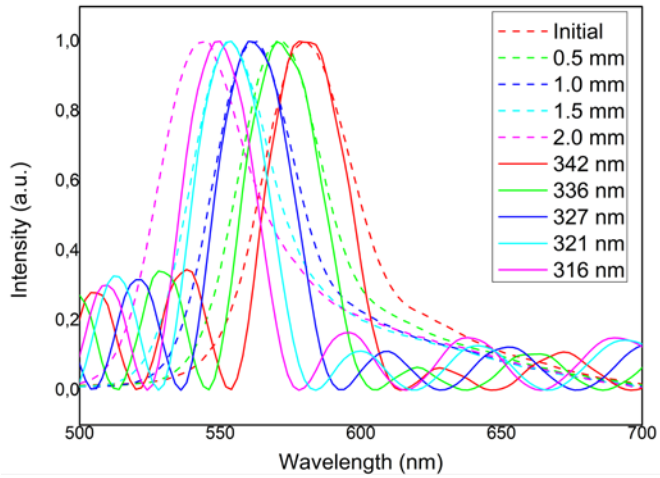

Figure 3.11: *Comparison between the experimental reflectance spectra (continuous line) and the numerical ones (dashed line).*

At each programmed step in which we have vary the lattice constant of the CC, that means varying the distance between the centre of the spheres, a change in the reflectance specta is observed, as shown in Figure 3.11. A change in the lattice constant means a change in the geometry of the nanostructured device, which directly impact on the filling factor that in turn, as shown in Equation (2), implies a change in the effective refractive index. This latter parameter plays a key role in the process of understanding the behaviour of this kind of structures and it is the cause of several features on both the experimental and numerical spectra.

Comparing the normalized spectra, where the influence of the lamp in the experiment has been purged, reported in Figure 3.11, one can see an optimum agreement between the behaviour of the simulated structure and the real one.

Analyzing the trend, reported in Figure 3.12, one can notice good agreement between the experimental data and those obtained by the FDTD model. From the practical point of view the key aspect for SHM is the sensitivity of sensor. As we highlighted in section 3.2, the

sensitivity of the sample was around 3.5 με /pm and it results in good agreement with the numerical one, which is around 3.8 με /pm. One can state with confidence that the numerical model approximates at the best the experiment.

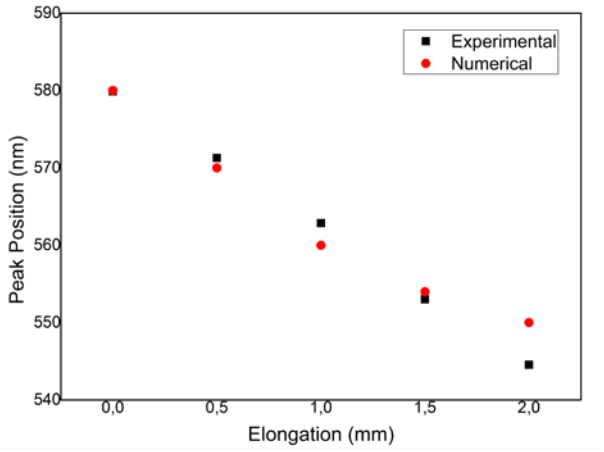

Figure 3.12. *Peaks' position of the experimental results (black dots) and the numerical ones (red dots).*

3.5 Conclusions

In this contribution the possibility of using mechanocromic colloidal photonic crystals as strain sensors has been discussed. The fabrication protocol and the materials involve have been discussed, then we demonstrated that the photonic properties of the sample change with an applied deformation to the substrate according to theoretical prediction. This property is what makes colloidal crystals attractive for strain sensing. For this kind of specimens produced so far, the strain resolution is in the order of 350 me, insufficient for structural applications if compared to the Fiber Bragg Grating sensors, whose resolution is in the order of few me. The crystal sensitivity to strain depends directly on its interplanar spacing and Poisson's ratio and it's limited to the material employed. Despite the low strain resolution of these systems, they are a promising new generation of sensors to be employed as a sort of skin for structural elements.

References

[1] D. Bäcker, A Ricoeur and M. Kuna. Sensor concept based on piezoelectric PVDF films for the structural health monitoring of fatigue crack growth, Structural Durability and Health Monitoring 7 (2011) 1-22.

[2] M. Benedetti, V. Fontanari, D. Zonta (2011). Structural health monitoring of wind towers: remote damage detection using strain sensors. Smart Mater. Struct. 20 (2011) 055009.

[3] M. Benedetti, V. Fontanari, L. Battisti (2013). Structural health monitoring of wind towers: residual fatigue life estimation. Smart Mater. Struct. 22 (2013) 045017.

[4] M. Benedetti, V. Fontanari and C. Santus. Crack growth resistance of MAG butt-welded joints of S355JR construction steel, Eng. Fract. Mech. 108 (2013) 305-315.

[5] C. Biemans, W.J. Staszewski, C. Boller, G.R. Tomlinson, Crack detection in metallic structures using broadband excitation of acousto-ultrasonics, Journal of Intelligent Material Systems and Structures 12 (8) (2001) 589–597.

[6] H. Fudouzi, T. Sawada, Y. Tanaka, I. Ario, T. Hyakutake and I. Nishizaki. Smart photonic coating as a new visualization technique of strain deformation of metal plates, Proceedings of SPIE - The International Society for Optical Engineering, Vol. 8345 (2012) 83451S.

[7] V. Giurgiutiu, A. Cuc, Embedded non-destructive evaluation for structural health monitoring, damage detection, and failure prevention, The Shock and Vibration Digest 37 (2) (2005) 83–105, (2005 Sage Publications).

[8] B. Glisic, D. Hubbell, D. Sigurdardottir and Y. Yao. Damage detection and characterization using long-gauge and distributed fiber optic sensors, Opt. Eng. 52 (2013) 087101

[9] H. Gu, Y. Zhao and M.L. Wang. A wireless smart PVDF sensor for structural health monitoring, Structural Control and Health Monitoring 12 (2005) 329–343.

[10] A. Guemes, A. Fernandez, B. Soller, Optical fiber distributed sensing—physical principles and applications, Struct. Health Monit. 9 (3) (2010) 233–245.

[11] G. Heo, M.L. Wang and D. Satpathi. Optimal transducer placement for health monitoring of long span bridge. Soil Dyn. Earthq. Eng. 16 (1997) 495–502

[12] G.W. Housner, L.A. Bergman, T.K. Caughey, A.G. Chassiakos, R.O. Claus, S.F. Masri, et al., Structural control: past, present, and future, J. Eng. Mech. 123 (9) (1997) 897–971.

[13] IEC61400–1 Ed.3 CD. 2. Revision 2005 Wind Turbines. Part 1: Design Requirements (Geneva: International Electrotechnical Commission).
[14] J.B. Ihn, F.K. Chang. Detection and monitoring of hidden fatigue crack growth using a built-in piezoelectric sensor/actuator network: I. Diagnostics. Smart Mater. Struct. 13 (2004) 609–620.
[15] J.B. Ihn, F.K. Chang. Detection and monitoring of hidden fatigue crack growth using a built-in piezoelectric sensor/actuator network: II. Validation using riveted joints and repair patches. Smart Mater. Struct. 13 (2004) 621–630.
[16] Ch.E. Katsikeros and G.N. Labeas. Development and validation of a strain-based Structural Health Monitoring system, Mechanical Systems and Signal Processing 23 (2009) 372-383.
[17] J.T. Kim, Y.S. Ryu, H.M. Cho and N. Stubbs. Damage identification in beam-type structures: frequency-based method vs mode-shape-base method. Eng. Struct. 25 (2003) 57-67.
[18] S. Laflamme, H.S. Saleem, B.K. Vasan, R.L. Geiger, D. Chen, M.R. Kessler and K. Rajan. Soft Elastomeric Capacitor Network for Strain Sensing Over Large Surfaces, IEEE Transactions on Mechatronics 18 (2013) 1647-1654.
[19] M. Majumder, T.K. Gangopadhyay, A.K. Chakraborty, K. Dasgupta and D.K. Bhattacharya. Fibre Bragg gratings in structural health monitoring—present status and applications, Sensors Actuators A 147 (2008) 150–64.
[20] T. Mickens, M. Schulz, M. Sundaresan, A. Ghoshal, Structural health monitoring of an aircraft joint, Mechanical Systems and Signal Processing 17 (2) (2003) 285-303.
[21] D. Ryu and K. J. Loh. Multi-modal sensing using photoactive thin films, Smart Mater. Struct. 23 (2014) 085011.
[22] M. Saka, M. Nakayama, T. Kaneko and H. Abe. Measurement of stress-intensity factor by means of A-C potential drop technique. Exp. Mech. 31 (1991) 209-212.
[23] C. Sbarufatti, A. Manes and M. Giglio. Application of sensor technologies for local and distributed structural health monitoring. Structural Control and Health Monitoring 21 (2014) 1057-1083.
[24] F. Trivellato, L. Battisti and G. Miori. The ideal power curve of small wind turbines from field data, J. Wind Eng. Ind. Aerodyn. 107–108 (2012) 263–273.
[25] S.T. Tung, Y. Yao and B. Glisic. Sensing sheet: the sensitivity of thin-film full-bridge strain sensors for crack detection and characterization. Meas. Sci. Technol. 25 (2014) 075602.
[26] A.F. Vaz and R. Bravo. Smart piezoelectric film sensors for structural control. IEEE Transactions on Instrumentation and Measurement 53 (2004) 472 - 484

[27] S. Villalba and J.R. Casas. Application of optical fiber distributed sensing to health monitoring of concrete structures, Mechanical Systems and Signal Processing 39 (2013) 441–451.
[28] T. Ding, S. K. Smoukov, and J. J. Baumberg, Stamping colloidal photonic crystals: a facile way towards complex pixel colour patterns for sensing and displays, Nanoscale, DOI: 10.1039/c4nr05934d, 2014.
[29] R. D. Pradhan, I. I. Tarhan, and G. H. Watson, Impurity modes in the optical stop bands of doped colloidal crystals, Phys. Rev. B, Vol 54, No 19, 1996.
[30] Y. A. Vlasov, V. N. Astratov, A. V. Baryshev, A. A. Kaplyanskii, O. Z. Karimov, and M. F. Limonov, Manifestation of intrinsic defects in optical properties of self-organized opal photonic crystals, Phys. Rev. E, vol 61, no 5, 2000.
[31] B. Hatton, L. Mishchenko, S. Davis, K. H. Sandhage and J. Aizenberg, Proc. Natl. Acad. Sci. U. S. A., 107, 2010.
[32] J. Zhou, J. Wang, Y. Huang, G. Liu, L. Wang, S. Chen, X. Li, D. Wang, Y. Song and L. Jiang, NPG Asia Mater., 4, 2012.
[33] Y. Huang, J. Zhou, B. Su, L. Shi, J. Wang, S. Chen, L. Wang, J. Zi, Y. Song and L. Jiang, J. Am. Chem. Soc., 134, 2012.
[34] H. S. Lee, R. Kubrin, R. Zierold, A. Y. Petrov, K. Nielsch, G. A. Schneider, and M. Eich, Photonic properties of titania inverse opal heterostructures, Optical Material Express, Vol 3, No 8, 2013.
[35] A. Chiappini, C. Armellini, N. Bazzanella, G. C. Righini, M. Ferrari, Opal-based photonic crystals heterostructures, Optics and Photonic Journal 2, 206-210, 2012.
[36] D. K. Hwang, H. Noh, H. Cao, and R. P. H. Chang, Photonic bandgap engineering with inverse opal multi-stacks of different refractive index contrast, Appl. Phys. Lett., 95, 2009.
[37] J. A. Roden and S. D. Gedney, “Convolution PML (CPML): An efficient FDTD implementation of the CFS-PML for arbitrary media," Microwave and Optical Technology Letters 27(5), 334-339 (2000).
[38] R. Pontalti, L. Cristoforetti, and L. Cescatti, \The frequency dependent FD-TD method for multi-frequency results in microwave hyperthermia treatment simulation," Phys. Med. Biol., vol. 38, 1283-1298 (1993).
[39] R. Courant, K. O. Friedrichs, and H. Lewy, “On the partial difference equations of mathematical physics," IBM Jour. of Res. and Dev. 11, 215-234 (1967). English translation of the original 1928 paper.
[40] Chiappini, A., Armellini, C., Chiasera, A., Ferrari, M., Jestin, Y., Mattarelli, M., Montagna, M., Moser, E., Nunzi Conti, G., Pelli, S., Righini, G.C., Gonçalves, M.C., Almeida, R.M. 2007. “Design

of photonic structures by sol–gel-derived silica nanospheres", J. of Non-Cryst. Solids, 353: 674-678.

4. 2D Optical Gratings Based on Hexagonal Voids on Transparent Elastomeric Substrate

By V. Piccolo, A. Chiappini, C. Armellini, M. Barozzi, A. Lukowiak, Pier-John A. Sazio, A. Vaccari, M. Ferrari and D. Zonta

Abstract

A chromatic vectorial strain sensor constituted by hexagonal voids on transparent elastomeric substrate has been successfully fabricated via soft colloidal lithography. Initially a highly ordered 1.6 microns polystyrene spheres monolayer colloidal crystal has been realized by wedge-shaped cell method and used as a suitable mold to replicate the periodic structure on a polydimethylsiloxane sheet. The replicated 2D array is characterized by high periodicity and regularity over a large area, as evidenced by morphological and optical properties obtained by means of SEM, absorption and reflectance spectroscopy. In particular, the optical features of the nanostructured elastomer have been investigated in respect to uniaxial deformation up to 10% of its initial length, demonstrating a linear, tunable and reversible response, with a sensitivity of 4.5 ± 0.1 nm/%. Finally, it has been demonstrated that the specific geometrical configuration allows determining simultaneously the vectorial strain-stress information in the x and y directions.

4.1 Introduction

Among the different fabrication techniques that allow obtaining micro/nanostructured surfaces, colloidal lithography is attracting big interest due to low cost, time efficiency, simplicity, and the possibility to pattern over a large surface area [1].
This bottom-up approach exploits the self-assembly of hard dielectric micro and nano spheres such as silica or polystyrene (PS) in order to fabricate two dimensional arrays. In recent literature, 2D colloidal crystals have been realized by self-assembly under electrophoresis deposition [2], Langmuir–Blodgett deposition [3], spin coating [4] and capillary forces [5]. Considering this last approach, Sun et al. [6] have demonstrated that the use of wedge-shaped cell allows obtaining large domains 2D colloidal crystals, with centimeter size, taking advantage on the capillary forces and drying front formed in the cell.
In this contest it is worth mentioning that 2D colloidal crystals are interesting and promising systems for micro and nanopatterning due to their periodicity and specific size [7]. In micro and nano patterning

field, colloidal crystals can be employed as lithographic masks or as molds for the production of micro and nanostructures for light trapping applications [8] or for the realization of SERS (Surface Enhanced Raman Spectroscopy) substrates [9]. Furthermore, they can act as masters by means of soft lithography in order to produce hexagonally arrayed structures.

These types of systems can be employed for the realization of responsive materials able to measure physical quantities such as magnetic fields [10], and temperature [11], or detect different chemicals, [12–14] including important analytes such as glucose [15], creatinine [16] and nerve gas agents [17].

Focusing the attention on mechanical parameters (i.e., strain), periodic polymeric photonic materials demonstrated sensitivity to deformation, in particular different configurations have been employed such as opal-type photonic crystals infiltrated with elastomeric materials [18,19]; 1D grating based on buckled thin film with periodic sinusoidal patterns on a transparent elastomeric substrate [20]; 1D array of gold nanoparticles on flexible substrate [21] and double sided 1D orthogonal polydimethylsiloxane (PDMS) gratings [22].

In particular, the realization of surface stress-based sensors has become fundamental in several fields in order to detect acoustic waves and forces on different structures such as spacecrafts, submarines, buildings or bridges.

Recently Guo et al. [22] have demonstrated that a double sided 1D orthogonal polydimethylsiloxane grating can be used as a vector mechanical sensor, able to detect mechanical parameters and giving information about their direction and strength.

In this work we have developed a strain/stress vector sensor based on hexagonal voids on a transparent elastomeric substrate: due to the specific geometric configuration, the application of a horizontal strain induces an opposite movement of the diffraction spots created by a white light impinging on the structure. The relative displacement of these spots can be investigated to estimate the vectorial strain/stress information and to characterize the applied strain in both the x and y directions.

This structure paves the way for the development of low cost vector strain sensor systems.

4.2 Materials and Methods

4.2.1 Materials

The PS latex beads were delivered by Thermo Scientific (Waltham, MA, USA), the PDMS Sylgard 184 by Dow Corning (Midland, MI,

USA) and all the chemicals (Absolute ethanol, Clorothrimethylsilane and Dimethylformamide), used as received, by Aldrich (St. Louis, MO, USA).

4.2.2 PS Colloidal Particles and Substrate Preparation

Monodisperse latex particles 1.6 microns in diameter and size distribution of 0.021 μm, 1.3% CV were purchased from Thermo Scientific and used as received at standard concentration of 1 wt% suspension in water. The v-SiO2 substrates were cleaned firstly by brushing with neutral glassware detergent and then by ethanol. Finally, they were treated in an ozone cleaner for 30 min.

4.2.3 Assembly of the PS 2D Template

The PS spheres monolayer was used as a template for the fabrication of the PDMS grating and was deposited on v-SiO_2 by means of the wedge-shaped cell method. This growth method allows the deposition of large domains two-dimensional colloidal crystals that self-organize by controlling the drying front of evaporation when the constituting particles are confined within two slides holding at an angle of about 2. After the infiltration of 125 μl of PS suspension, the cell was maintained at room temperature (RT) and relative humidity (RH) of 40% for 1 day. Due to the evaporation of the solvent in the suspension, the latex beads crystallized in an ordered hexagonal structure.

4.2.4 Functionalization and Infiltration of the PS 2D Template

The 2D PDMS grating was obtained by infiltrating the template with the elastomer. Before the infiltration, to facilitate the following peeling off from the glassy substrate, the PS monolayer was functionalized by silanization with clorotrimethylsilane in a Petri dish for 90 min. As a second step a mixture of a 10:1 base:curing Sylgard 184 elastomer was poured on the functionalized template and thermally cured for 4 h at 65°C. Finally, the PDMS with embedded PS spheres was gently removed from the glass substrate by peeling off the elastomer.

4.2.5 PS Particles Chemical Etching

The last step of the fabrication protocol was the etching of the PS particles in the elastomeric matrix that was performed by immersion of the PDMS slab in dimethylformamide for 90 min. Dimethylformamide is a solvent for PS and a non-solvent for PDMS, hence it provides a

selective etching of the latex beads allowing the formation of an inverse replica of the template based on hexagonal voids in elastomeric matrix. After the etching process the sample was rinsed in water and blown with nitrogen.

4.2.6 Sample Characterization

Morphological investigation of the samples has been carried out by means of scanning electron microscopy (SEM) measurements using a SEM JEOL JSM 7401-F FEG (Akishima, Tokyo, Japan). Transmittance measurements have been performed using a double beam VIS-NIR spectrophotometer Varian Cary 5000 (Palo Alto, CA, USA) in the range between 1000 and 2500 nm. The spectra of the samples were obtained illuminating the whole sample with a white light (halogen lamp) and collecting the diffracted light using a fiber-optic UV-Vis spectrometer Ocean Optics USB 4000 (Edinburgh, UK) as shown in Figure 4.1. Measurement of wavelength shift has been performed analyzing the displacement of two different diffraction spots, under the application of a horizontal strain. For both spots, this effect has been investigated by means of the wavelength shift of the 1st order of the transmittance diffraction, keeping the detection angle fixed at a specific value in order to have an initial spectrum centered in the visible region.

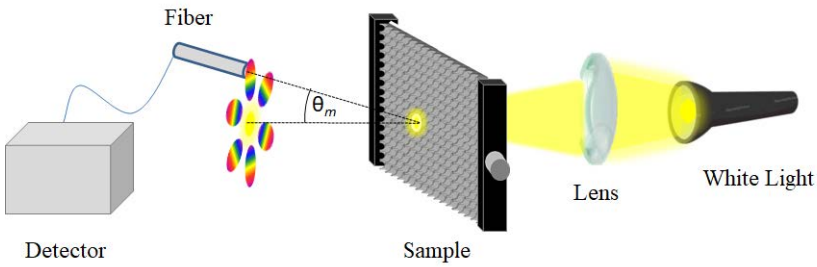

Figure 4.1 *Sketch of the experimental set-up for the 2D diffraction grating measurements.*

4.3 Results and Discussion

The first step, as shown in Figure 4.2a, concerned the realization of two-dimensional assembly of PS colloidal particles later used as a mold; Figure 4.3a reports a typical optical image of an ordered 2D colloidal crystal obtained by wedge-shaped cell method, where we can notice the presence of large areas of ordered domains (about 100 × 70 μm with few punctual defects). In Figure 4.3b, three transmission dips at λ =

1954 nm, 1598 nm, 1480 nm can be distinguished at normal incidence ($\theta = 0°$) and are the result of the excitation of the photonic eigenmodes of the periodic dielectric structure due to its coupling with the incident light as proposed by Sun et al. [6], which, confirm the high optical quality. Furthermore, we can notice a decrease in the transmittance values attributed to an increase in the scattered radiation for lower wavelength affecting the collection of the zero order transmitted signal.

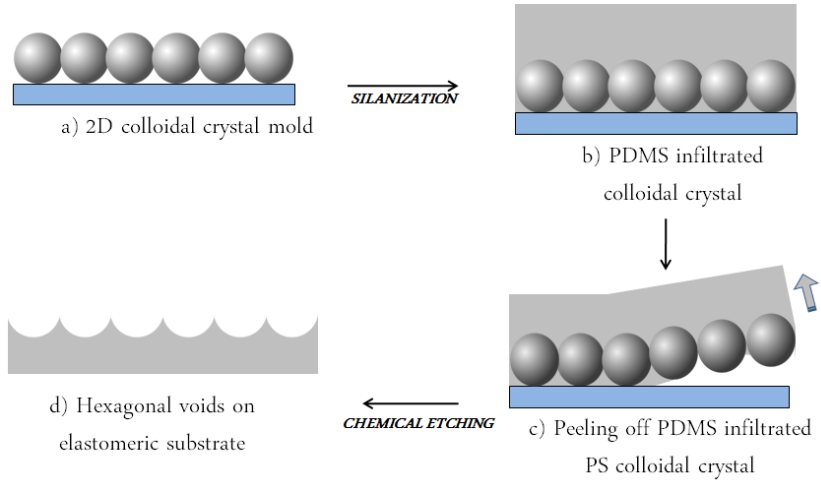

Figure 4.2 *Schematic illustration of the experimental approach employed for the realization of 2D PDMS replica patterns (a) formation of 2D colloidal crystal by means of wedge-shaped cell (b) functionalization and infiltration of PDMS by capillary force; (c) peeling off PDMS infiltrated PS colloidal crystal; (d) chemical etching of the PS spheres.*

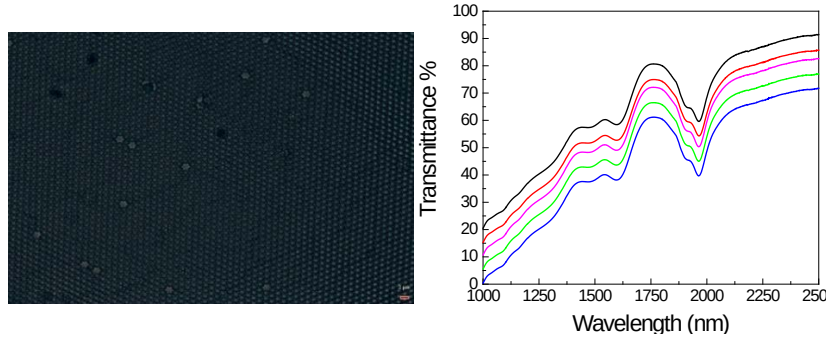

Figure 4.3 *(a) Optical microscopy image of a typical area of the 2D colloidal crystals self-assembled using a wedge-shaped cell (scale bar of 2 μm). (b) Transmittance spectrum obtained on a 2D colloidal crystal deposited on a v-SiO2 substrate. The individual spectra are offset vertically by 5% for clarity (the black spectrum is the original one).*

Following the procedure described in Figure 4.2, a hexagonal voids regular structure (sketched in Figure 4.4a), has been fabricated via soft colloidal lithography. Figure 4.4b,c shows SEM-images of the resulting patterned polymeric structure where the reciprocal morphology of the PS mold has been successfully obtained. From a morphological point of view, the hexagonal voids structure presents a periodicity of about 1600 nm with a depth of the voids of about 460 nm.

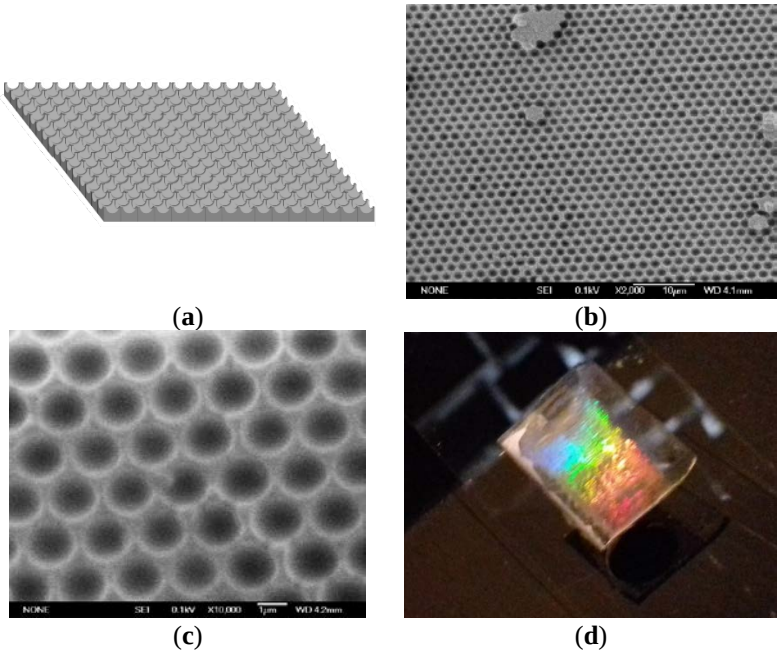

Figure 4.4 *(a) Sketch of the concave structure obtained via soft lithography (not in scale) (b) SEM surface image of PDMS inverted colloidal crystal. (c) detail of the ordered hexagonal array. (d) Photograph of hexagonal voids on transparent elastomeric substrate.*

Furthermore, as shown in Figure 4.4d, the hexagonal voids structure, that can be seen as a 2D grating, presents an iridescent color that is attributed to the high order over a large area. In this case the morphology of the periodic hexagonal pattern satisfies the diffraction features that can be expressed through the simple law of diffraction (equation 4.1).

$$n \cdot \sin(\theta_m) - n_i \cdot \sin(\theta_i) = \frac{m \cdot \lambda}{d} \qquad (4.1)$$

where θ_i is the incident angle while θ_m corresponds to the m^{th} diffraction order angle; n_i and n are the refractive indices of the incident medium

and of the medium where the diffracted orders propagate respectively; λ represents the wavelength of the incident light; and d is the period of the grating.
From an optical point of view illuminating the grating by white light, and collecting the diffraction projected on a screen, we can clearly notice the presence of a chromatic hexagonal pattern (see Figure 4.5) due to the arrangement of the semispherical voids.
In order to verify the optical response of the system to mechanical deformation, the structure has been mounted on a linear stage and a deformation in the horizontal direction was applied.
As evidenced in Figure 4.5b, the application of a horizontal strain produces a change in the diffraction pattern. In this case it is worth mentioning that the movement of the first-order diffraction spot (see points 1 and 6 as labeled in the inset) is attributed to the variation of the grating period as a function of the strain, as predicted by the multi-slit Fraunhofer diffraction theory.

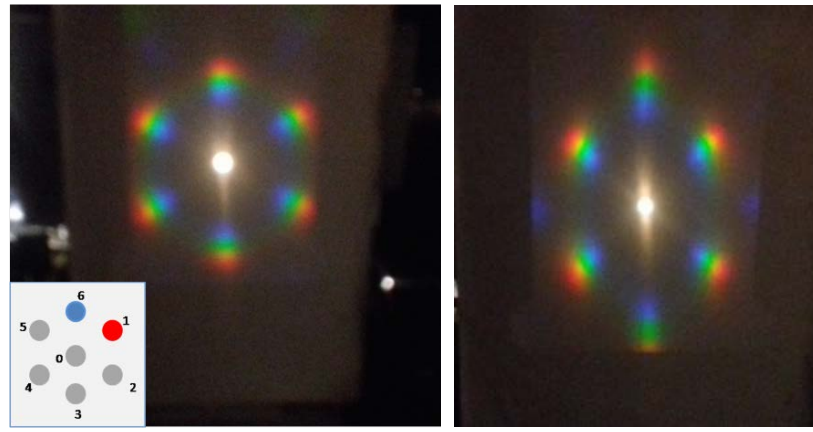

(**a**) (**b**)

Figure 3.5 *Strain induced diffraction spot movements: (a) Optical diffraction pattern without strain; inset: labelling of the investigated spots (1 and 6); (b) optical diffraction with a strain (ε) ε = 10% along the horizontal direction.*

In particular comparing Figure 4.5a,b, focusing the attention on spot number 1, we can observe its movement towards the center (0), while if we consider spot number 6 we can notice that it moved away from the zero order. This effect can be attributed to an increase in the diffraction pitch in the parallel direction of the strain, and a consequent decrease (contraction) in the opposite side.
These features have been investigated by means of reflectance measurements detecting the wavelength shift of the 1st order of the transmittance diffraction, maintaining fixed the detector and applying a different strain to the grating.

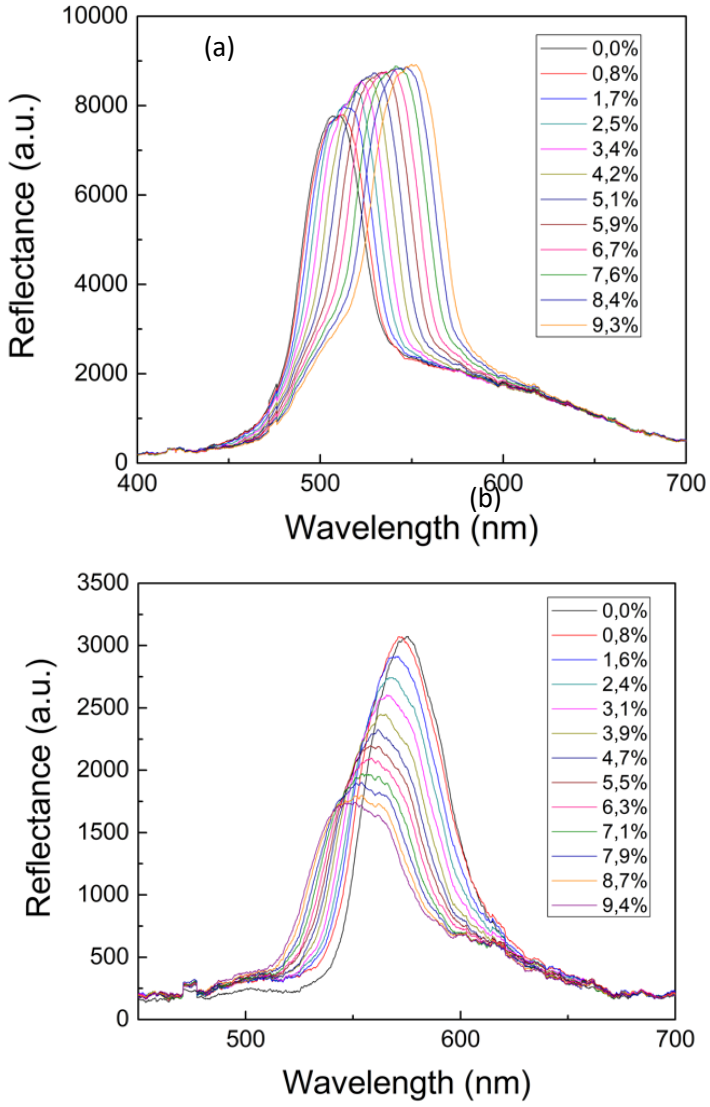

Figure 4.6 *Reflectance spectra collected considering: (a) spot 1 as a function of the applied strain; (b) spot 6 as a function of the applied strain.*

Analyzing Figure 4.6a, related to spot number 1, we can notice that the first order of the diffraction peak presents a noticeable red-shift when increasing the applied strain. The diffraction peak wavelength passes from 510 to 553 nm for a uniaxial deformation of the structure up to 10% of its initial length. On the other hand, for spot 6 we have observed a decrease in wavelength of the diffraction peak from 575 to 551 nm. The images shown in Figure 4.5 and the difference in the peak

wavelength shifts indicate that the strain induces an elliptical modification of the voids. Evidently, Figure 4.5 is suggestive of the fact that the grating's sensitivity is much higher against longitudinal geometrical changes then transversal ones. Indeed, the former are due to the imposed strain while the latter are due to Poisson's effect. Clearly, the initially circular semi-voids become elongated ellipses in the direction of the applied strain.

Moreover, we can see an increase of the intensity of the transmitted diffracted light at longer wavelength. To explain this effect, we have devised a simple model of its optical response. According to this model, the grating optical behavior is assimilable to two 2D arrays of secondary sources, both having the periodicity of the hexagonal semi-voids structure. The two arrays however, are half shifted in the grating plane, because one of them corresponds to rays emerging from the semi-void tops and the other corresponds to rays emerging from the semi-void bottoms. The two kinds of rays have an inherent optical path length difference due to the difference in the top and bottom substrate height. After calculations, the resulting intensity pattern for the downstream interference formula is thus depending from the primary beam wavelength, and in such a way that at an increase of its value necessarily implies an increase in the revealed intensity of a given secondary maximum [23].

Now in order to determine the sensitivity of the 2D grating as strain sensor we have analyzed the variation in wavelength of the diffraction peak as a function of the applied strain. In Figure 4.7 we report the variation of the peak positions of the diffracted light (a) for spot 1 and (b) spot 6 in respect to the % applied strain. First of all, we can notice a linear behavior, moreover we can determine a sensitivity equal to 4.5 ± 0.1 nm/% and 2.5 ± 0.1 nm/% for spot 6 and 1 respectively. These results, if compared with those reported in the literature for mechanochromic systems, permit to include the developed structure among the most sensitive as strain sensors [21].

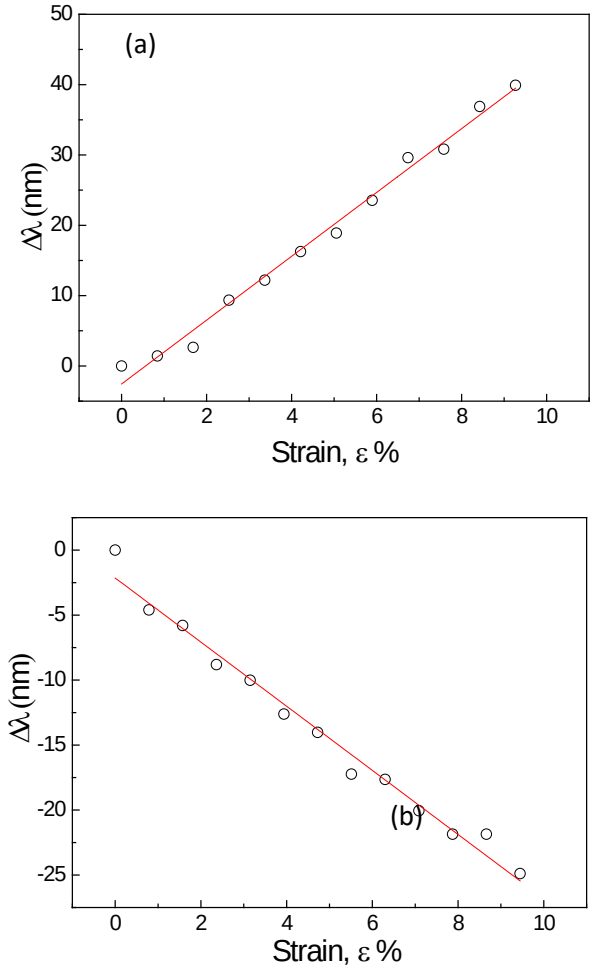

Figure 4.7 *Experimental relationship between the peak position of the diffracted light (a) for spot 1 and (b) spot 6 in respect of the strain as a result of the elongation tests, (error bars are hidden by the circle points).*

4.4 Conclusions

A chromatic strain sensor based on hexagonal voids on a transparent PDMS elastomeric substrate has been realized via soft colloidal lithography. The fabricated 2D grating can be employed for the development of a low cost and innovative sensor able to determine simultaneously the vectorial strain - stress information in the x and y directions.
Moreover, we have demonstrated that the sensor exhibits a tunable and reversible response under the application of a mechanical strain.

Optical reflection measurements have evidenced a linear behavior under the application of a horizontal strain up to 10% of its original length. The sensitivity of 4.5 ± 0.1 nm/%, when compared with mechanochromic photonic systems already present in literature, permits to classify the structure developed among the most sensitive strain sensors, paving the way for its applications in several fields such as smart sensing, mechanical sensing, and strain imaging.

References

[1] Weiler, M.; Pacholski, C. Soft colloidal lithography. *RSC Adv.* **2017**, *7*, 10688–10691, doi:10.1039/C7RA00338B.

[2] Liao, C.-H.; Hung, P.-S.; Cheng, Y.; Wu, P.-W. Combination of microspheres and sol-gel electrophoresis for the formation of large-area ordered macroporous SiO_2. *Electrochem. Comm.* **2017**, *85*, 6–10, doi:10.1016/j.elecom.2017.10.009.

[3] Askar, K.; Phillips, B.M.; Fang, Y.; Choi, B.; Gozubenli, N.; Jiang, P.; Jiang, B. Self-assembled self-cleaning broadband anti-reflection coatings. *Colloids Surf., A* **2013**, *439*, 84–100, doi:10.1016/j.colsurfa.2013.03.004.

[4] Luo, C.-L.; Yang, R.-X.; Yan, W.-G.; Zhao, J.; Yang, G.-W.; Jia, G.-Z. Rapid fabrication of large area binary polystyrene colloidal crystals. *Superlattices Microstruct.* **2016**, *95*, 33–37, doi:10.1016/j.spmi.2016.04.015.

[5] Ye, X.; Qi, L. Two-dimensionally patterned nanostructures based on monolayer colloidal crystals: Controllable fabrication, assembly, and applications. *Nano Today* **2011**, *6*, 608–631, doi:10.1016/j.nantod.2011.10.002.

[6] Sun, J.; Tang, C.J.; Zhan, P.; Han, Z.L.; Cao, Z.S.; Wang, Z.L.; Fabrication of Centimeter-Sized Single-Domain Two-Dimensional Colloidal Crystals in a Wedge-Shaped Cell under Capillary Forces. *Langmuir* **2010**, *26*, 7859–7864, doi:10.1021/la9047165.

[7] Fournier, A.C.; Cumming, H.; McGrath, K.M. Assembly of two- and three-dimensionally patterned silicate materials using responsive soft templates. *Dalton Trans.* **2010,** *39*, 6524–6531, doi:10.1039/c0dt00067a.

[8] Kohoutek, T.; Parchine, M.; Bardosova, M.; Fudouzi, H.; Pemble, M. Large-area flexible colloidal photonic crystal film stickers for light trapping applications. *Opt. Mater. Express* **2018**, *8*, 960–967, doi:10.1364/OME.8.000960.

[9] Guddala, S.; Kamanoor, S.A.; Chiappini, A.; Ferrari, M.; Desai, N.R. Experimental investigation of photonic band gap influence

on enhancement of Raman-scattering in metal-dielectric colloidal crystals. *J. .Appl. Phys.* **2012**, *112*, 084303–1–7, doi:10.1063/1.4758315.

[10] Wang, W.; Fan, X.; Li, F.; Qiu, J.; Umair, M.M.; Ren, W.; Ju, B.; Zhang, S.; Tang, B. Magnetochromic Photonic Hydrogel for an Alternating Magnetic Field-Responsive Color Display. *Adv. Opt. Mater.* **2018**, *6*, 1701093–1–9. doi:10.1002/adom.201701093

[11] Yu, B.; Song, Q.; Cong, H.; Xu, X.; Han, D.; Geng, Z.; Zhang, X.; Usman, M. A smart thermo- and pH-responsive microfiltration membrane based on three-dimensional inverse colloidal crystals. *Sci. Rep.* **2017**, *7*, 12112–1–10, doi:10.1038/s41598-017-12426-z.

[12] Cai, Z.; Kwak, D.H.; Punihaole, D.; Hong, Z.; Velankar, S.S.; Liu, X.; Asher, S.A. A Photonic Crystal Protein Hydrogel Sensor for Candida albicans. *Angew. Chem. Int. Ed.* **2015**, *54*, 13036–13040, doi:10.1002/anie.201506205.

[13] Zhang, J.-T.; Cai, Z.; Kwak, D.H.; Liu, X.; Asher, S.A. Two-dimensional photonic crystal sensors for visual detection of lectin concanavalin A. *Anal. Chem.* **2014**, *86*, 9036–9041, doi:10.1021/ac5015854.

[14] Zhang, J.-T.; Chao, X.; Liu, X.; Asher, S.A. Two-dimensional array Debye ring diffraction protein recognition sensing. *Chem. Comm.* **2013**, *49*, 6337–6339, doi:10.1039/c3cc43396j.

[15] Chen, C.; Dong, Z.-Q.; Shen, J.-H.; Chen, H.-W.; Zhu, Y.-H.; Zhu, Z.-G. 2D Photonic Crystal Hydrogel Sensor for Tear Glucose Monitoring. *ACS Omega* **2018**, *3*, 3211–3217, doi:10.1021/acsomega.7b02046.

[16] Xu, D.; Zhu, W.; Jiang, Y.; Li, X.; Li, W.; Cui, J.; Yin, J.; Li, G. Rational design of molecularly imprinted photonic films assisted by chemometrics. *J. Mater. Chem.* **2012**, *22*, 16572–16581, doi:10.1039/c2jm32833j.

[17] Souder, B.; Prashant, P.; Seo, S.S. Hafnium polystyrene composite particles for the detection of organophosphate compound. *Soft Mater.* **2013**, *11*, 40–44, doi:10.1080/1539445X.2011.570633.

[18] Fudouzi, H.; Tsuchiya, K.; Todoroki, S.-I.; Hyakutake, T.; Nitta, H.; Nishizaki, I.; Tanaka, Y.; Ohya, T. Smart photonic coating for civil engineering field: For a future inspection technology on concrete bridge. *Proc. SPIE* **2017**, *10168*, 1016820–1–7, doi:10.1117/12.2259822.

[19] Piccolo, V.; Chiappini, A.; Vaccari,A.; Calà Lesina, A.; Ferrari, M.; Deseri, L.; Perry, M.; Zonta, D. Finite difference analysis and experimental validation of 3D photonic crystals for structural health monitoring. *Proc. SPIE* **2017**, *10168*, 101681E–1–9, doi:10.1117/12.2263975.

[20] Yu, C.; O'Brien, K.; Zhang, Y.H.; Yu, H.; Jiang, H. Tunable optical gratings based on buckled nanoscale thin films on transparent elastomeric substrates. *Appl. Phys. Lett.* **2010**, *96*, 041111–1–3, doi:10.1063/1.3298744.
[21] Minati, L.; Chiappini, A.; Armellini, C.; Carpentiero, A.; Maniglio, D.; Vaccari, A.; Zur, L.; Lukowiak, A.; Ferrari, M.; Speranza, G. Gold nanoparticles 1D array as mechanochromic strain sensor. *Mater. Chem. Phys.* **2017**,*192*, 94–99, doi:10.1016/j.matchemphys.2017.01.073.
[22] Guo, H.; Tang, J.; Qian, K.; Tsoukalas, D.; Zhao, M.; Yang, J.; Zhang, B.; Chou, X.; Liu, J.; Xue, C.; Zhang, W. Vectorial strain gauge method using single flexible orthogonal polydimethylsiloxane gratings. *Sci. Rep.* **2016**, *6*, 23606–1–9, doi:10.1038/srep23606.
[23] Born, M.; Wolf, E. *Principles of Optics*, 4th ed.; Pergamon Press: Oxford, United Kingdom, 1970; pp. 401–414, ISBN: 0072561912.

5. Quasi-Hemispherical Voids Micropatterned PDMS as Strain Sensor

By V. Piccolo, A. Chiappini, C. Armellini, M. Mazzola, A. Lukowiak, A. Seddon, M. Ferrari, D. Zonta

Abstract

Polydimethylsiloxane elastomers are largely employed in soft lithographic replication for the realization of microstructures that find application in microfluidic and micro-engineering. In the last years micro and nano patterned ordered structures have gained remarkable attention for their employment in the development of biomedical devices, smart displays, chemical and physical sensors. Here a 2D quasi-hemispherical micro voids elastomeric grating has been successfully realized and it has been demonstrated that this structure can be considered a simple, low cost reversible strain sensor. Specifically, the sensor permits simultaneous determination of the strain-stress information analyzing the voids' spacing based on Debye diffraction distance. A model from Continuum Mechanics has been employed in order to assess its optical response, meaning to predict the mechanical deformation of the patterned surface of the sample and to corroborate the accuracy of the optical measurements. The results demonstrate that the 2D quasi-hemispherical micro voids sensing system can be considered as a complementary approach respect to the traditional strain sensors.

5.1 Introduction

Polydimethylsiloxane (PDMS) has been broadly used as a material for the realization of lab-on-a-chip [1] and for the depositions of thin films [2, 3] or the fabrication of membranes [4]. Nowadays PDMS is the most common polymer utilized for the manufacturing of microfluidic devices [1]. The chemical and physical features of PDMS and its practical application have been reported in detail [5]. In the specific its success is due to low cost, fast and easy fabrication and optical transparency ranging from 240 to 900 nm with a transparency over 90% [6]. Moreover, it presents low shrinkage rates and the capability to replicate micro-scale features making it suitable for soft lithography processes.
PDMS can be patterned in different forms by means of molds realized by optical lithography or via soft lithography [7].

Moreover, its peculiar elastic properties have driven the research on its mechanical features [8]. In fact, several studies on mechanical properties of PDMS concerned different applications such as material elasticity for the realization of accelerometers [9], the deposition of thin film for sensors [10], and biomedical devices [11]. Focusing the attention on strain sensors, PDMS is one of the main materials employed for the realization of low cost and stretchable conductive [12] or chromatic strain sensor [13]. For the last category, different mechanisms and geometries can be used to obtain mechanochromic sensors. Typical examples concern the use of gold nanoparticles embedded in a PDMS matrix or immobilizing them on its surface as demonstrated by Duarte [14], where the sensing mechanism is based on the variation of the plasmonic response [14]. A complementary approach exploits elastomeric materials doped with specific chromophores [15], for instance Cellini et al. correlated the fluorescent signals to the mechanical strain applied [16].
Finally, mechanochromic sensors have been realized exploiting the optical properties of photonic crystals, that give rise to diffraction phenomena. Considering 1-dimensional (1D) structures, several examples have been reported in the literature, where specific 1D systems based on submicron wrinkling shape grating [17] and on aligned gold nanoparticle 1D arrays [18] are used as strain sensors. Here, the modification of the sample periodicity, caused by the elastic deformation, produces a variation in the optical diffraction response. Few examples report on 3D structures, among them the pioneering work of Fudouzi et al. [19] demonstrates the application of a polymeric opal embedded in a PDMS matrix. In this case the working principle is based on a linear shift of the Bragg diffraction peak of the photonic crystal as a function of mechanical strain in elastic deformation. Although the above systems allow the easy determination of strain, nowadays the research is focused on the development of optical sensors able to detect both amplitude and direction of mechanical deformation. In this contest a new approach is based on the realization of a double-sided PDMS 1D-diffraction gratings structure [20], where the analysis of the displacement of the diffraction spots allows obtaining the stress/strain information in x and y directions.
In this paper we propose the design and the fabrication of an alternative structure constituted by quasi-hemispherical micro-voids arranged in hexagonal configuration for the determination of the applied strain field.
The advantages of the 2D structure which has been developed are the fast and simple fabrication method and the easy interrogation system based on Debye diffraction distances that permits to reconstruct the strain field.

To validate the applied interrogation method and its suitability to the detection of strain, a model from Continuum Mechanics has been employed that predicts the mechanical behavior of the 2D PDMS nanostructured grating.

5.2 Experimental

2D nanostructured grating based on quasi-hemispherical micro-voids arranged in hexagonal configuration has been obtained by means of soft lithography as described in Ref. [21]. Briefly a multi steps process, based on the following three steps, has been developed: (a) realization of a 2D hexagonal ordered polystyrene (PS) monolayer, to be used as a mold; (b) its infiltration with polydimethylsiloxane and (c) chemical etching of PS microparticles allowing the formation of quasi-hemispherical micro-voids on elastomeric matrix (see Figure 5.3).
The morphological properties have been investigated using a Scanning Electron Microscopy (SEM) JEOL JSM 7401-F FEG (Akishima, Tokyo, Japan); while the optical response of the grating at the initial stage and under the application of the uniaxial strain has been characterized analyzing the modification of the diffraction pattern projected on a screen and acquired by a Charged-Coupled Device (CCD) camera using as excitation source 632.8 nm He-Ne laser, as sketched in Figure 5.1.

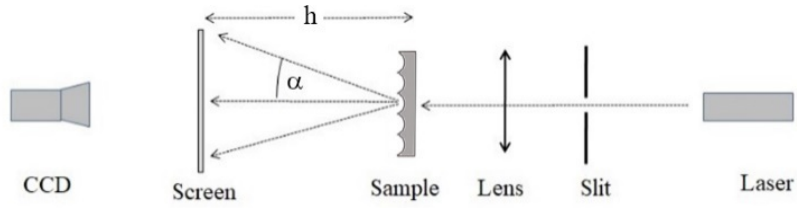

Figure 5.1 *Scheme of the experimental setup for diffraction measurements on stretchable PDMS grating.*

It is worth mentioning that at normal incidence the diffracted light on the screen, orthogonal to the laser, allows determination of the spacing of the 2D voids through the analysis of the hexagonal diffraction pattern.
In fact, it is well known that the neighboring voids' spacing, d, can be calculated through the modified diffraction equation (see equations (5.1-5.3)) measuring the so called Debye distance D [22] and the distance h of the screen from the 2D quasi-hemispherical micro-voids nanostructured sample. The application of the strain, as evidenced in Figure 2b, produces a modification in the diffraction pattern that

imposes to replace the Debye distance D with the length of the major (D') and minor axis (d') of the ellipse in order to take into account the elongation and the contraction in the two directions, respectively.
Finally, the analysis of the acquired images in term of intensity of the spots and their displacement has been obtained by means of MATLAB software in order to reduce the error from the measurement setup. In the specific the software allows determination of the shift of the six spots with respect to the zero order and measurements of the values D, D' and d'. Furthermore, analyzing the pixel intensity, related to each laser spot, with respect to the total image intensity, it is possible to determine the intensity variation as a function of the applied strain.

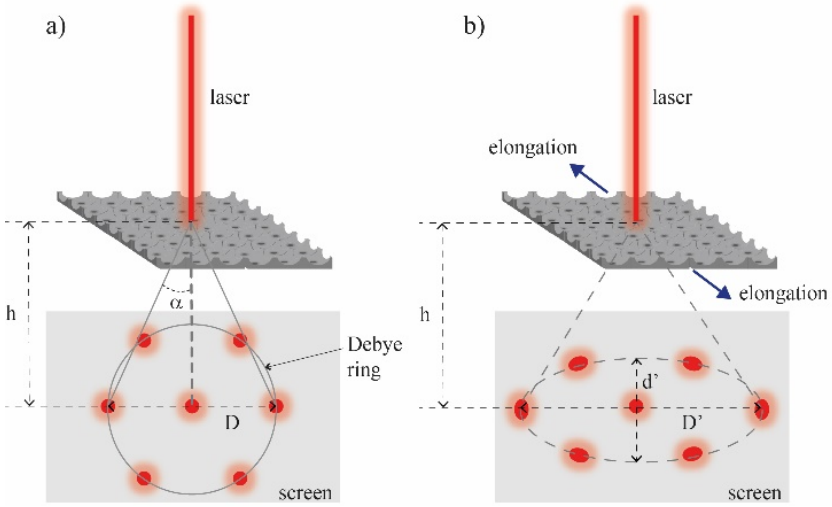

Figure 5.2 *(a) Schematic illustration of the projected hexagonal diffraction pattern at the initial stage and (b) under application of an applied strain.*

5.3 Results and Discussion

Figure 5.3 shows the typical SEM image of the 2D quasi-hemispherical micro-voids' grating where a hexagonal order is evident, moreover it has been verified that the grating presents a period of ~ 1.6 μm with a depth of the voids of about 460 nm over a whole sample thickness of around 1 mm.
Now, it is possible to correlate the variation of the micro-voids' spacing with the application of the applied strain through the analysis and the measurement of the Debye diffraction distances.

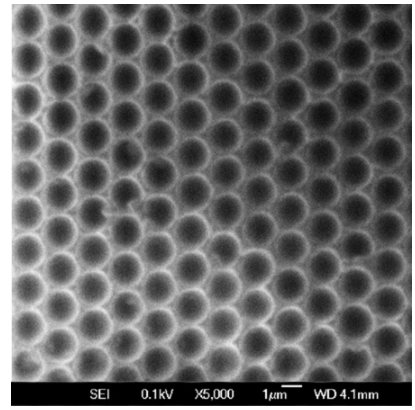

Figure 5.3 *Typical SEM image of the 2D quasi-hemispherical micro-voids' grating where a hexagonal order is present.*

First of all, it is worth mentioning that at normal incidence, the forward diffracted light, from 2D array monolayer, forms a hexagonal diffraction pattern on the screen. The first Debye diffraction of the 2D array can be expressed by the following equations:

$$\sin\alpha = \frac{2\lambda_{laser}}{\sqrt{3}d} \tag{5.1}$$

where α is the forward diffraction angle of the Debye diffraction distance, λ_{laser} is the incident wavelength, and d is the adjacent voids' spacing.
Furthermore, from a geometrical point of view, as shown in Figure 5.2a:

$$\alpha = \tan^{-1}\left(\frac{D}{2h}\right) \tag{5.2}$$

where h is the distance between 2D array and the screen, D is the Debye diffraction distance.
Now, combining equation (5.1) and (5.2), the micro-voids' spacing of 2D grating can be easily determined, by measuring the Debye distance D, D' and d', through equation (5.3) substituting each time these last three values to the parameter M.

$$d = \frac{4\lambda_{laser}\sqrt{(M/2)^2 + h^2}}{\sqrt{3}M} \tag{5.3}$$

From an experimental point of view, the application of an uniaxial strain produces a distortion (an elliptical modification) in the diffraction pattern. As evidenced in Figure 5.4b, it is observed, that the first-order spots oriented in the Γ-M direction moves towards the center (0^{th} order spot), while for the Γ-K direction the first-order spots move away from the zero order spot.
This effect is associated to an increase in the diffraction period in the direction parallel to the strain, and is due to a contraction in the vertical direction.

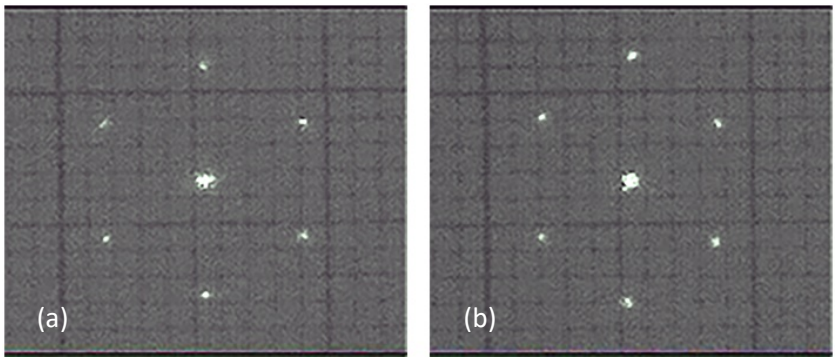

Figure 5.4 *(a) Diffraction patter at zero applied strain; (b) optical diffraction with a strain (ε) ε ~ 9% along the horizontal direction (perpendicular to the laser).*

In order to determine the optical response and the sensitivity of the 2D grating to the applied strain, the sample has been mounted on a linear stage applying an elongation in the Γ-M direction along the PDMS grating (see Figure 5.6).
Now analyzing the images, in particular the spots' displacement by means of MATLAB program and considering the equation (5.3), it is possible to determine the voids' spacing as a function of the ε%, as reported in Figure 5.5.
From Figure 5.5 it is evident that the application of the strain produced an almost linear variation, for both the directions, with a sensitivity of 14.0 nm/ε% for Γ-M (red) and 5.7 nm/ ε % for Γ-K (black) respectively. Moreover, it is possible to observe a higher voids' spacing in Γ-M longitudinal direction with respect to the Γ-K direction. This behavior is associated to the fact that the strain is applied in the longitudinal direction, while the Γ-K direction is affected by Poisson's effect.
This particular change in the diffraction patterns, means the variation in the voids' spacing is correlated to the modification of the patterned surface from hemispherical to elliptical voids.

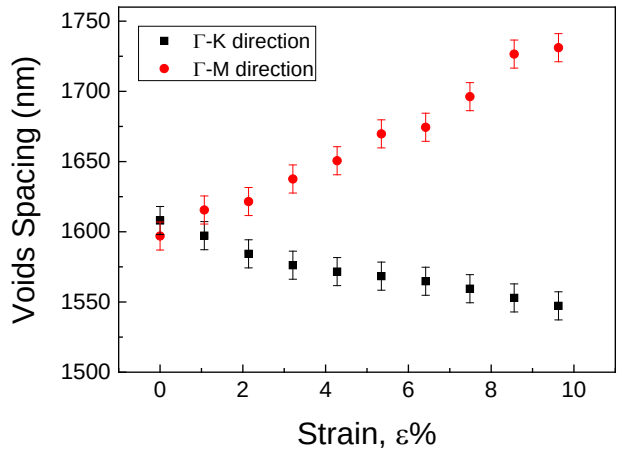

Figure 5.5 *Strain, ε% applied dependence of 2D array voids spacing in the two directions Γ-M (black) and Γ-K (red) respectively.*

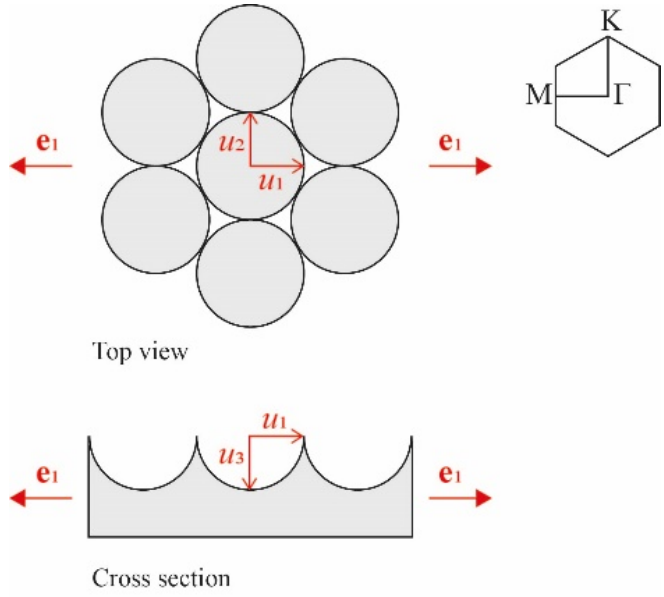

Figure 5.6 *Schematic representation of the top view and cross section of the sample with the direction of the extension e1 and the associated component of the displacements.*

In order to understand better and demonstrate this geometrical change in the patterned surface, a model from Continuum Mechanics has been employed. Thanks to this model one can locally map the principal directions of deformation of the whole structure. From the mechanical stand point, the investigated sample is a bulky parallelepiped; one of

the two larger surfaces presents texturing. The dimensions in x, y and z directions are infinitesimal when compared to the whole sample. A uniaxial tensile test for the nominal strains of interest, for example about 10%, practically incompressible behavior and homogenous deformation across each is expected. The fact that the size of each indentation is 10^{-6} times smaller than the thickness of the body suggests that only a very small boundary layer across the indentations is characterized by a non-homogeneous perturbation of the strain imposed through the uniaxial test.
For the reasons highlighted above, a homogeneous isochoric extension in the direction e_1 (see Figure 5.6) is assumed for the sample. In such a case, the associated components of the displacements (as shown in Figure 5.6) are the following affine functions:

$$\begin{cases} u_1(x_1) = (\mu - 1)x_1 + C_1 & \text{(5.4a)} \\ u_2(x_2) = \left(\frac{1}{\sqrt{\mu}} - 1\right)x_2 + C_2 & \text{(5.4b)} \\ u_3(x_3) = \left(\frac{1}{\sqrt{\mu}} - 1\right)x_3 + C_3 & \text{(5.4c)} \end{cases}$$

where x_1, x_2 and x_3 are the coordinates of the material points of the body in the assumed undeformed reference configuration and μ is the assumed constant stretch. The gradient of such a displacement is obviously constant and it can be represented as follows:

$$\nabla u = F - I = \begin{bmatrix} \mu - 1 & 0 & 0 \\ 0 & \frac{1}{\sqrt{\mu}} - 1 & 0 \\ 0 & 0 & \frac{1}{\sqrt{\mu}} - 1 \end{bmatrix} \quad \text{(5.5)}$$

where:

$$F = \mu \cdot e_1 \otimes e_1 + \mu^{-1/2} \cdot (e_2 \otimes e_2 + e_3 \otimes e_3) \quad \text{(5.6)}$$

is the corresponding constant deformation gradient. The symbol ⊗ denotes the standard dyadic product between vectors. It is worth recalling that isochoric deformations are such that det F =1, which is the case for assumed kinematics. As it is well known, the engineering strain tensor, E, takes the following form [23]:

$$E = \frac{F^T F - I}{2} = \begin{bmatrix} \frac{\mu^2 - 1}{2} & 0 & 0 \\ 0 & \frac{1}{2}\left(\frac{1}{\mu} - 1\right) & 0 \\ 0 & 0 & \frac{1}{2}\left(\frac{1}{\mu} - 1\right) \end{bmatrix} \tag{5.7}$$

It is worth mentioning that such a strain coincides with the regular one, namely the symmetric part of the gradient of the displacement whenever the applied nominal strain is very small, i.e. of the order of 10^{-1} %. Such a simple form of the strain tensor allows one to estimate the deformations in the three principal directions of the quasi-hemispherical micro-voids. The imposed nominal strain, here henceforward consistently denoted by E_{11}, actually determines the value of the associated stretch μ through the first component of the engineering tensor through the relation:

$$\mu = (1 + 2E_{11})^{1/2} \tag{5.8}$$

Substituting μ in (5.4) one can find the deformation in all three directions, meaning the deformations of the hemispherical voids, that in turn are the change in their spacing, and the variation of the voids' depth, depending on the applied strain.

As mentioned above, the deformation of the voids in the Γ-K direction is affected by Poisson's effect, which, in turn, is a function of the strain. In fact, as expected, one can experimentally confirm that under imposed finite strain, even though the considered deformation is isochoric, the Poisson's ratio *ν* does vary with such a strain and, hence, it is the case that the following relations hold for an isotropic material:

$$\nu = -\frac{E_{22}}{E_{11}} = -\frac{E_{33}}{E_{11}} \neq \frac{1}{2} \tag{5.9}$$

In particular, the explicit form of the second term in such a relation is as follows:

$$\nu = -\frac{E_{22}}{E_{11}} = \frac{\frac{1}{\mu} - 1}{\mu^2 - 1} = \frac{1}{\mu(\mu+1)} = \tilde{\nu}(\mu) \tag{5.10}$$

Here, the function $\tilde{\nu}(\mu)$ emphasizes the fact that the Poisson's ratio has to vary with the stretch and, hence, with the imposed longitudinal strain E_{11}. Of course, in the case of infinitesimal strain, namely $\mu=1$, $\nu=1/2$ as expected for a linear elastic incompressible material. Otherwise, for the imposed values of the nominal uniaxial strain, the Poisson's ratio actually does decrease and influences the deformation of the voids.
If instead of considering the nonlinear geometry (set of equations 5.4), one would have accounted for a linear response of the material, ν would obviously be constant as sad above. Henceforth, this would have led to miss the key-geometric effect captured by equation 5.10, according to which ν decreases by increasing the strain, thereby reveling values up to 15% lower than the one predicted by assuming linear elasticity for the revealed level of longitudinal strain. In other words, the transverse contraction exhibited by the sample is actually amplified by the nonlinearity and the experimental results do show a good quantitative agreement with this effect as shown below.
Following this approach, the values determined from the analytical model, u_1 and u_2, are compared with those obtained by the optical measurements (see Figure 5.5) as shown in Figure 5.7.
Analyzing the trend, reported in Figure 5.7, one can notice good agreement between the experimental data and those obtained by the analytical model. Through the analysis of the diffraction patterns one can say with a very good approximation how the micropattering is changing, showing also the fidelity of the optical investigation approach. Moreover, we can claim that the use of the model from Continuum Mechanics allows design of first approximation responsive sensors that is characterized by a superficial texturing with respect to the total dimension of the system.

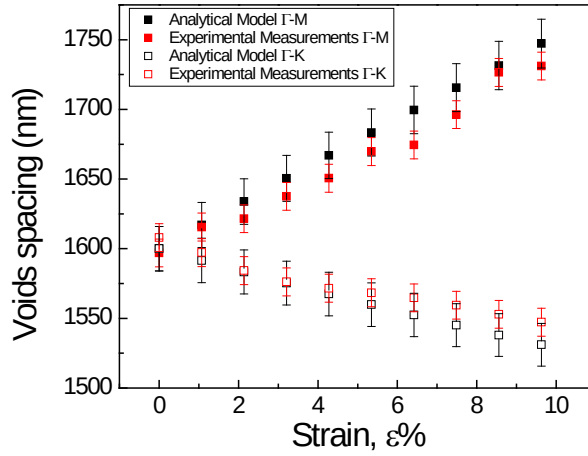

Figure 5.7 *Comparison between the voids' spacing determined by means of the analytical model (black) and optical measurements (red) in Γ-M (full) and Γ-K (empty), respectively.*

To investigate the effect of the modification of the voids' depth on the optical response of the 2D grating, a comparison between the calculated values obtained using equation 4c and the analysis of the intensity of the diffraction images has been carried out. In Figure 5.8(a) and 5.8(b) are reported the pixel contour intensity of the diffraction patterns of the initial state and under the application of a longitudinal strain of about 9 ε%, respectively. From Figure 5.8, in both case, it is possible to notice that, initial state and elongated one, the intensity distribution of the first order diffraction is equivalent for the six spots with an incertitude of ± 1%. This is in agreement with the values obtained through the mechanical model previously described and reported in Figure 5.8(c), where a variation of 2 nm/ε% has been determined, indicating that for values up to 9 □ % of applied strain the decrease in the voids' depth is negligible and therefore the detected intensity is almost constant.
Finally, to fully characterize the quasi-hemispherical micro-voids hexagonal arrays in term of the reversibility, and the reproducibility of the response as a strain sensor, the diffraction pattern variation has been investigated during cyclic elongation and release under the application of 14 ε%.

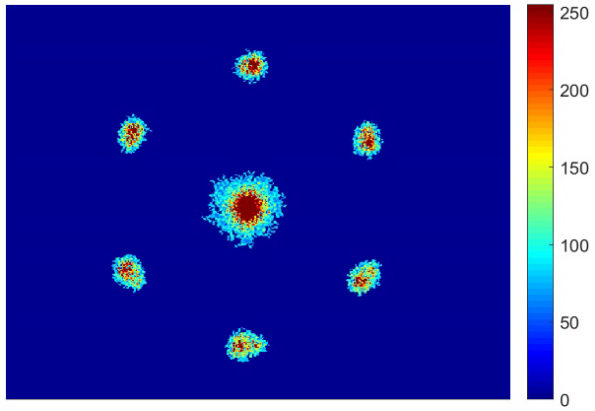

(a)

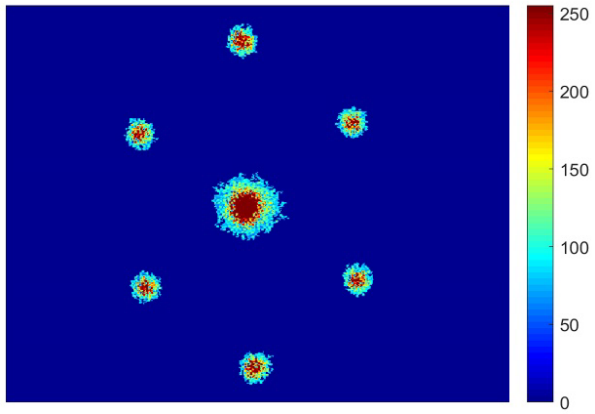

(b)

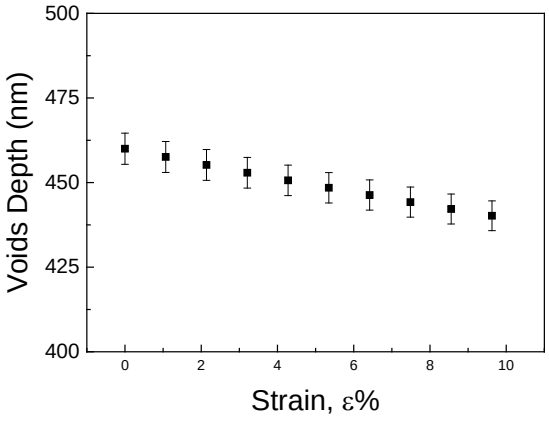

(c)

Figure 5.8 *(a) Pixel intensity as contour plot spectra for the initial stage and (b) after application of ~ 9 ε%. (c) voids' depth as a function of the applied ε % strain.*

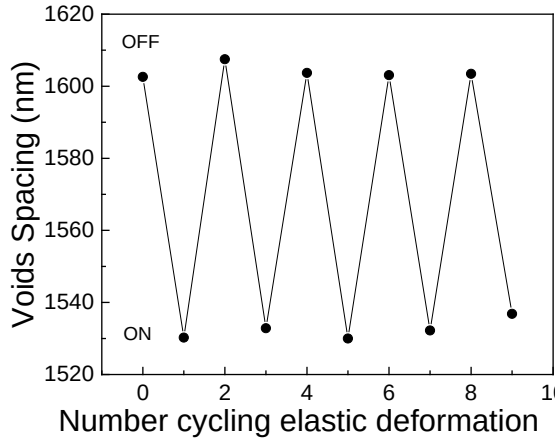

Figure 5.9 *Tuning voids' spacing position by repeating the elongation and the release steps under the application of 14 ε %.*

Figure 5.9 shows the variation of the voids' spacing at the initial, elongated, and recovered states, considering several deformation cycles for the Γ-M direction. Equivalent results in terms of reversibility and repeatability have been obtained for the Γ-K direction (data not reported).
Under mechanical strain, considering the Γ-M direction, the voids' spacing decreases as expected, whereas when the stress is released it returns almost to the initial value, indicating that the tuning voids' spacing position is reversible and reproducible. Moreover, Figure 5.9 indicates that the microstructured 2D grating possesses a good mechanical stability and flexibility under cyclic deformation.

5.4 Conclusions

A 2D quasi-hemispherical voids micropatterned elastomer has been successfully realized. It has been demonstrated that this structure can be considered a simple, low cost and reversible strain sensor. In the specific, it has been verified that the developed structure and the method employed for the interrogation of the system permit simultaneous determination of stress-strain information in the x and y directions. In addition, the application of a model from Continuum Mechanics has allowed the behavior to be predicted of the patterned surface of the PDMS sample and to corroborate the accuracy of the optical interrogation and analysis.
Finally, the realized system and the interrogation approach can be seen as a useful tool for the development of a safe device also suitable for

untrained end-users that can be employed in different fields such as the aerospace industry and structural health monitoring.

References

[1] M.P. Wolf, G.B. Salieb-Beugelaar, P. Hunziker, PDMS with designer functionalities—Properties, modifications strategies, and applications, Prog. Polym. Sci. 83 (2018) 97-134. 10.1016/j.progpolymsci.2018.06.001

[2] Kim, S., Hwang, H.J., Cho, H., Choi, D., Hwang, W. Repeatable replication method with liquid infiltration to fabricate robust, flexible, and transparent, anti-reflective superhydrophobic polymer films on a large scale, Chem. Eng. J. 350 (2018) 225-232. https://doi.org/10.1016/j.cej.2018.05.184.

[3] S. Dogru, B. Aksoy, H. Bayraktar, B.E. Alaca, Poisson's ratio of PDMS thin films, Polym. Test. 69 (2018) 375-384. https://doi.org/10.1016/j.polymertesting.2018.05.044.

[4] S. Torino, L. Conte, M. Iodice, G. Coppola, R.D. Prien, PDMS membranes as sensing element in optical sensors for gas detection in water, Sensing and Bio-Sensing Research 16 (2017) 74-78. https://doi.org/10.1016/j.sbsr.2017.11.008.

[5] D. Zhu, S. Handschuh-Wang, X. Zhou, Recent progress in fabrication and application of polydimethylsiloxane sponges, J. Mater. Chem. A 5 (2017) 16467-16497. 10.1039/C7TA04577H.

[6] D.K. Cai, A. Neyer, R. Kuckuk, H.M. Heise, Optical absorption in transparent PDMS materials applied for multimode waveguides fabrication, Opt. Mater. 30 (2008) 1157–1161. https://doi.org/10.1016/j.optmat.2007.05.041

[7] X. Chen, L. Zhang, Review in manufacturing methods of nanochannels of bio-nanofluidic chips, Sens. Actuators, B 254 (2018) 648-659. 10.1016/j.snb.2017.07.139.

[8] Johnston, I.D., McCluskey, D. K., Tan, C.K.L., Tracey, M.C., 2014. Mechanical characterization of bulk Sylgard 184 for microfluidics and microengineering. Journal of Micromechanics and Microengineering. 24, 035017. https://doi.org/10.1088/0960-1317/24/3/035017.

[9] K.L. Phan, A. Mauritz, F.G.A. Homburg, A novel elastomer-based magnetoresistive accelerometer, Sens. Actuators, A 145-146 (2008) 109-115. 10.1016/j.sna.2007.10.055.

[10] C. Song, X. Ding, L. Que, High-resolution, flexible, and transparent nanopore thin film sensor enabled by cascaded Fabry–Perot effect, Opt. Lett. 43 (2018) 3057-3060. 10.1364/OL.43.003057.

[11] D. Wang, D. Ba, Z. Hao, Y. Li, F. Sun, K. Liu, G. Du, Q. Mei, A novel approach for PDMS thin films production towards application as substrate for flexible biosensors, Mater. Lett. 221 (2018) 228-231. 10.1016/j.matlet.2018.03.114.

[12] Y.S. Chong, K.H. Yeoh, P.L. Leow, P.S. Chee, Piezoresistive strain sensor array using polydimethylsiloxane-based conducting nanocomposites for electronic skin application, Sensor Review 38 (2018) 494-500. https://doi.org/10.1108/SR-11-2017-0238.

[13] R. Zhang, Q. Wang, X. Zheng, Flexible mechanochromic photonic crystals: Routes to visual sensors and their mechanical properties, J. Mater. Chem. C 6 (2018) 3182-3199. 10.1039/C8TC00202A.

[14] M.A. Correa-Duarte, V. Salgueiriño-Maceira, A. Rinaldi, K. Sieradzki, M. Giersig, L.M. Liz-Marzán, Optical strain detectors based on gold/elastomer nanoparticulated films, Gold Bulletin 40 (2008) 6-14. https://doi.org/10.1007/BF03215287

[15] J.-C.G. Bünzli, K.-L. Wong, Lanthanide mechanoluminescence, Journal of Rare Earths 36 (2018) 1-41. https://doi.org/10.1016/j.jre.2017.09.005.

[16] F. Cellini, L. Zhou, S. Khapli, S.D. Peterson, M. Porfiri, Large deformations and fluorescence response of mechanochromic polyurethane sensors,Mech. Mater. 93 (2016) 145-162. https://doi.org/10.1016/j.mechmat.2015.10.013.

[17] Yu, C., O'Brien, K., Zhang, Y.H., Yu, H., Jiang, H., 2010. Tunable optical gratings based on buckled nanoscale thin films on transparent elastomeric substrates. Applied Physics Letters. 96, 041111. https://doi.org/10.1063/1.3298744.

[18] L. Minati, A. Chiappini, C. Armellini, A. Carpentiero, D. Maniglio, A. Vaccari, L. Zur, A. Lukowiak, M. Ferrari, G. Speranza, Gold nanoparticles 1D array as mechanochromic strain sensor. Mater. Chem. Phys. 192 (2017) 94–99. https://doi.org/10.1016/j.matchemphys.2017.01.073.

[19] H. Fudouzi, T. Sawada, Photonic Rubber Sheets with Tunable Color by Elastic Deformation, Langmuir 22 (2006) 1365-1368. 10.1021/la0521037.

[20] Guo, H., Tang, J., Qian, K., Tsoukalas, D., Zhao, M., Yang, J., Zhang, B., Chou, X., Liu, J., Xue, C., Zhang, W., 2016. Vectorial strain gauge method using single flexible orthogonal polydimethylsiloxane gratings. Sci. Rep. 6, 23606. https://doi.org/10.1038/srep23606.

[21] Piccolo, V., Chiappini, A., Armellini, C., Barozzi, M., Lukowiak, A., Sazio, P.J.A., Vaccari, A., Ferrari, M., Zonta, D., 2018. 2D Optical Gratings Based on Hexagonal Voids on Transparent Elastomeric Substrate Micromachines. 9, 345. doi:10.3390/mi9070345.

[22] F. Xue, Z. Meng, F. Qi, M. Xue, F. Wang, W. Chen, Z. Yan, Two-dimensional inverse opal hydrogel for pH sensing, Analyst 139 (2014) 6192-6196. 10.1039/C4AN00939H.
[23] D. Bigoni, Nonlinear Solid Machanics: bifurcation theory and material instability, first ed., Cambridge University Press, 2012.

6. Colloidal Crystals Based Portable Chromatic Sensor for Butanol Isomers and Water Mixtures Detection

By A. Chiappini, C. Armellini, V. Piccolo, L. Zur, D. Ristic, D. J. Jovanovic, A. Vaccari, D. Zonta, G.C. Righini, M. Ferrari

Abstract

In this work, we report on a structurally-colored composite colloidal crystal able to change its color in presence of different polar solvents such as butanol and to distinguish its isomers. Herein, polydimethylsiloxane (PDMS) infiltrated polystyrene opals are fabricated by means of a two steps approach and their final structure exhibits a green opalescence, the diffraction peak wavelength position changes as a function of the analytes spotted on the surface. In fact, the realized composites present a colorimetric variation in their response, since a remarkable red-shift of the diffraction peak is observed. An analytical model has been proposed and validated in order to assess the optical chromatic response, according to which the changing of the filling factor is the main element that produces the variation in the optical response. The selectivity, sensitivity and the reusability of the sensor have been investigated by monitoring the static reflectance spectra considering a mixture of 2-Methylpropan-2-ol (TerB) and water.
Dynamic reflection spectra have been employed as an appropriate technique for the recognition of butanol isomers such as TerB, Butan-1-ol (NB) and Butan-2-ol (2B). The results demonstrate that the prepared photonic crystal sensing material and the interrogation approach used are a suitable tool for the development of low cost, portable sensors for homologues and isomers.

6.1 Introduction

After the publication of the pioneering papers of Yablonovich [1] and John [2] in 1987, several attempts have been carried out to fabricate Photonic Crystal (PC) structures with photonic band gaps (PBGs) [3, 4]. The great attention attracted in recent years by PCs is due to their potential applications in many fields, such as anti-counterfeiting [5], displays [6], photonic paper [7], and chemical and biological sensors [8, 9, 10]. Nowadays, focusing the attention on these application areas, PC sensors have been employed to detect different chemicals and

parameters such as organic solvents [11, 12, 13], gases and volatile organic compounds [14]; temperature [15], humidity [16; 17] and pH [18]. Generally, PC sensors are constructed using responsive photonic crystals (RPCs) that change their photonic structures and reflectance under external stimuli. Because of the tunable crystal structure and the behavior of its optical signal under external stimuli or in different environment, the RPCs are intrinsically suitable for portable and visually detectable sensors. Actually, many papers are present in literature concerning the use of complementary methods for the determination of volatile alcohols, such as quartz crystal microbalance based on polymers [19], electrical resistance response exploiting the features of metal oxides [20], and colorimetric PCs approach [8, 12, 21]. Some of them need specific apparatus or high temperature, while chromatic sensing, which working principle is based on the change of optical response, has attracted considerable attention because of its simplicity, safe operation and the possibility to detect by the naked eye. The importance of the determination of the water volume fraction in different chemicals is crucial from a commercial point of view in particular in the case of high purity gases for semiconductor industry [22]. In the field of renewable energy, alcohol biofuels produced from biological sources, have attracted intense research and commercial interest because they may offer significant benefits in terms of reduced emissions, improved price stability, and more distributed production facilities [23]. The use of bioderived fuel such as ethanol is increasing worldwide but, due to higher energy content and better blending compatibility with gasoline, butanol is under consideration to replace ethanol as an alternative fuel to gasoline and diesel [24]. Moreover, the employment of alcohols and alcohol/water mixtures in the field of pharmaceutical processes represents a solution in case of hydrophobic and insoluble active principles that can not be freeze dried adequately with water-based formulations [25]. 2-Methylpropan-2-ol (TerB) and its water mixtures has been progressively used in many pharmaceutical processes, the control of the composition of the mixture is one of the main freezing parameters that heavily affects the final results in terms of solubility, sublimation rates and times, costs and product stability [26]. In this contest the development of economic-fast-portable methods to determine water in alcohols and distinguish between different isomers, is greatly needed. In this paper we report an easy and practical method for the fabrication of composite colloidal crystals based on polystyrene (PS) nanoparticles (NPs) embedded in elastomeric matrix such as PDMS which is optically responsive to solvents considering in the specific butanol isomers and alcohol/water mixtures. Starting from the experimental data, an analytical model has been proposed and validated in order to assess the chromatic response

of the colloidal crystal, making the assumption of an isotropic displacement of the spheres assembled in its periodic lattice fcc. Finally, we have demonstrated that such developed structures are a suitable tool for the determination of water content in homologues, in particular butanol and to distinguish different isomers.

6.2 Experimental

6.2.1 Chemicals

Styrene monomer, sodium dodecyl sulfate (SDS), potassium persulfate (KPS), sodium hydroxide (NaOH), 2-Methylpropan-2-ol (TerB), Butan-1-ol (NB), Butan-2-ol (2B), methanol (MetOH) were purchased from Aldrich. Sylgard 184 (PDMS) was purchased from Dow Corning. Polyethylene terephthalate (PET) sheet was purchased from Polymer House and used as polymeric substrate.

6.2.2 Synthesis of Monodisperse Polystyrene Particles

Polystyrene spheres have been synthesized following a single-stage polymerization process [27]. The reaction was performed using a 500 ml glass bowl equipped with a stirrer, a reflux condenser and a heating jacket. Most of the chemicals were used as received; but, in order to remove the polymerization inhibitor, the styrene monomer was washed with NaOH and water. For the typical procedure 245 ml of water, 0.081 g of SDS, dissolved in 13.6 ml of water, and 27.2 ml of styrene monomer, were premixed at 80°C for 2 min in the reactor with a stirrer speed of 300 rpm. 0.952 g of KPS dissolved in 13.6 ml of water were injected to start the polymerization. The polymerization was completed after 4 h and the colloidal solution was purified by repeated centrifugation/redispersion cycles.

6.2.3 Preparation of the colloidal crystal template and infiltration with PDMS

The polymeric composite based on PS spheres embedded in the PDMS matrix was obtained as reported in Fig. 6.1:

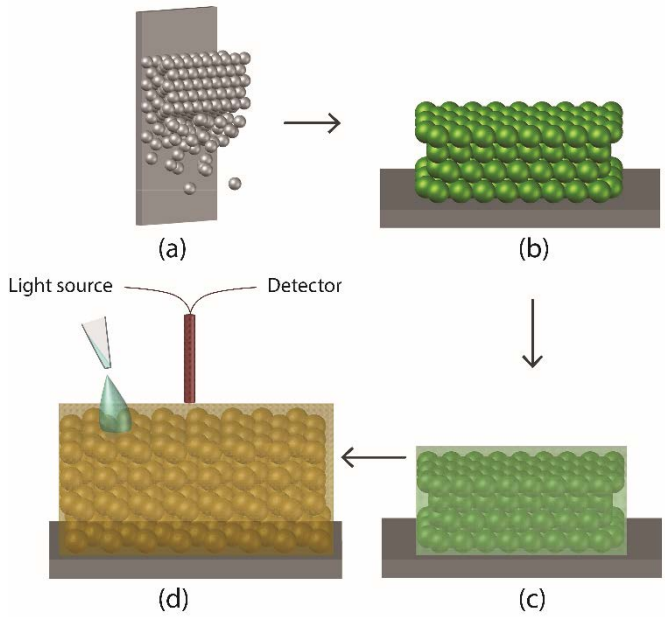

Figure 6.1 *Schematic of the fabrication and detection process. (a) assembly of the colloidal structure by vertical deposition (VD) (b) sketch of the ordered system (c) infiltration with responsive material (PDMS) (d) detection of the analytes by absorption and swelling of the composite structure.*

The composite structure is assembled into 3D ordered PCs on a PET sheet using the vertical deposition (VD) technique as shown in Figure 1a. First the substrate was hydrophilized using an ozone cleaner for 30 min. Then, the clean PET sheet was placed in a cylindrical vessel. The PS suspension was added to the vessel and then evaporated in a homemade proportional-integral-derivative (PID) oven at set temperature of 45°C for 48h to form a film (Figure 1b). The infiltration of the 3D structure is obtained by pouring a PDMS solution into the voids of the colloidal crystal. The elastomer was supplied as a kit with two separate components: base and curing agent; we mixed base and curing agent in a 10:1 ratio. After infiltration the structure was cured for 4 h at 65 °C and then the excess elastomer was peeled-off from the crystal as reported in ref [28].

6.2.4 Characterization

The morphology and the size of the obtained colloidal crystals and the particles were investigated using scanning electron microscopy (SEM-FEG Jeol JSM-7001F). The optical features of the colloidal crystals were characterized using an UV-VIS reflection fiber optic spectrometer

(Ocean Optics USB 200) equipped with a halogen lamp. The incident white light was aligned perpendicular to the <111> planes of the colloidal crystal, UV-VIS spectra were collected by a probe placed orthogonally to the surface. Dynamic spectra were continuously recorded by Ocean Optics USB 200 spectrometer coupled to a six-around one reflection probe (6 illumination fibers around 1 read fiber) with incident and reflection angles fixed at 0° (Figure 1d). The reflection spectra were collected every 2 sec by the spectrometer after spotting 5 µl of solvent on the surface of the colloidal crystal. In 12 min about 360 spectra were imported to the matrix table of software "Origin", which was further used to plot the contour map with time (t) on x-axis, reflection wavelength (λ) on y-axis and reflection intensity (R) in color.

6.3 Results and Discussion

6.3.1 Choice of the Materials and Sensor Design

We have shown previously that 3D PCs can be prepared very efficiently via controlled assembly of periodic dielectric monodisperse PS spheres [27] and that it is possible to tailor their optical response infiltrating specific responsive materials [28]. It is worth mentioning that PDMS is one of the most widely used silicon-based elastomers, since is a viscoelastic, biocompatible, chemically and mechanically robust material with low glass transition temperature and high transmittance. Moreover, it is resistant to most aqueous solutions and alcoholic solvents, even if some homologues are able to swell it [29]. Exploiting these properties, here we present the fabrication of a 3D colloidal crystal film infiltrated with PDMS elastomer to form a composite chromatic and portable system able to detect alcohol/water mixtures and butanol isomers. In Fig. 6.2 is reported a typical SEM image of the top surface of the opal infiltrated with PDMS, where we can observe a long order periodicity and a hexagonal arrangement attributable to the <111> plane of the fcc structure. The inset (Fig. 6.2) shows a photograph of the infiltrated opal, where a clear green opalescence is evident.

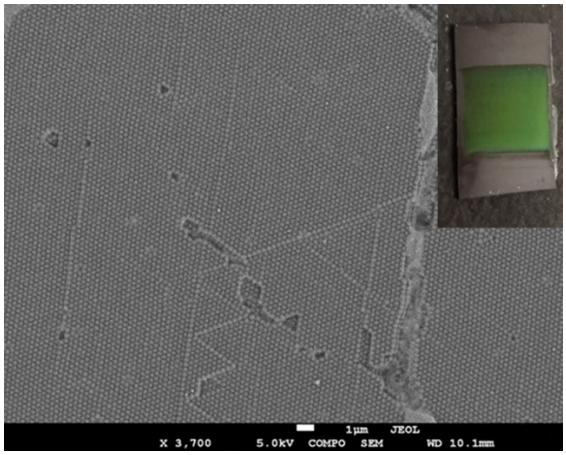

Figure 6.2 *SEM image of the infiltrated opal; in the inset: a photograph of the composite opal where a green opalescence can be seen by naked eyes.*

The assessment of the chromatic behavior of the infiltrated opal and its variation in the optical response under external stimuli is the "key" point in order to properly design this type of sensors and render them selective. Generally, the opalescence and, therefore, the reflectance wavelength for normal incidence, is based on the Bragg's law reported in equation (6.1)

$$\lambda = 2 \cdot d_{111} \cdot n_{eff} \tag{6.1}$$

where λ is the wavelength of reflected light, $d_{111}=0.816 \cdot D$ is the interplanar spacing in the <111> direction, D represents the diameter of PS nanoparticles and n_{eff} is the effective refractive index of the sample. The effective refractive index of a two-phase structure can be expressed by

$$n_{eff}^2 = n_{spheres}^2 \cdot f_i + n_{medium}^2 \cdot (1 - f_i) \tag{6.2}$$

Where, in the initial state, $f_i = 0.74$ is the filling factor of the porous structure for an ideal fcc package, $n_{spheres}=1.55$ and $n_{medium}=1.40$ represent the refractive index, at 631.8 nm, of PS and PDMS materials respectively.
The application of an external stimulus produces a specific change in lattice constant value a_i ($ai=(d_{111})_i \cdot \sqrt{3}$) and therefore in the filling factor f_i, as expressed by the equation (6.3).

$$f_i = \frac{2\pi}{3} \cdot \frac{D^3}{a_i^3} \tag{6.3}$$

where D is the diameter of the nanoparticles.
The stimulus is responsible of a modification in the volume fraction of the PS NPs in the crystal as sketched in Fig. 6.3, and therefore results in a new value of f_i that induces a red shift in the optical response as expressed by equation (6.1).
Now, in the simplest case it's possible to assume an isotropic displacement of the spheres assembled in the periodic lattice fcc (Fig. 6.3), that causes a variation in the value of effective refractive index n_{eff} as well as on the d_{111}.
The swelling is a kinetic process coupling mass transport and mechanical deformation, which depends on the interaction between the polymer network and the solvent and is generally determined via changes in linear dimensions or volume.
The swelling coefficient S can be defined by equation (6.4)

$$S = \frac{(d_{111})_S}{(d_{111})_0} \tag{6.4}$$

where $(d_{111})_{s,0}$ is the interplanar spacing in presence of the analyte (swelled state) and for initial configuration (initial state), respectively.
It's worth recalling that a crosslinked polymer network can absorb a large amount of solvent without dissolving, considering this, in order to validate the analytical model previously described, homologues such as MetOH and TerB have been taken into account. Figure 6.4 shows the reflectance spectra acquired after spotting respectively 5 μl of MetOH and TerB onto the ''sensor'' surface and monitoring the optical change of the diffraction peak.
Analyzing Fig. 6.4 we can observe a red shift in the wavelength position of the diffraction peak as a function of the different types of solvents used. We can clearly see that higher is the swelling coefficient of PDMS with the solvent (equation (6.4)), bigger is the red shift of the diffraction peak. From the wavelength position of the diffraction peak as a function of the applied solvents (Figure 4) and taking into account the equations 6.1, 6.2, 6.3 and 6.4 we have determined the swelling values S.

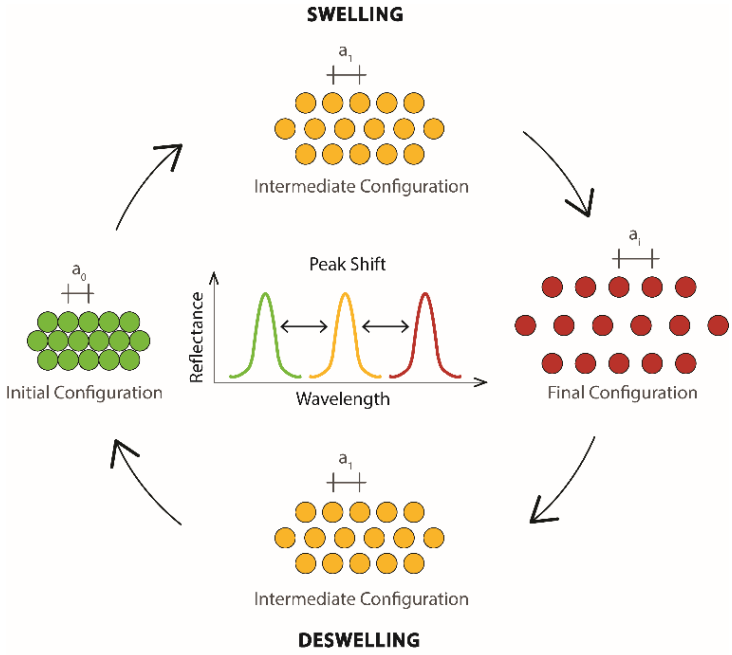

Figure 6.3 *Sketch of the isotropic displacement of the spheres assembled in the periodic lattice fcc of the colloidal crystal after solvent application. Clock wise: initial state (green colour), intermediate state (orange colour), and final state (red colour) with their respective reflectance peak shift. The process is completely reversible.*

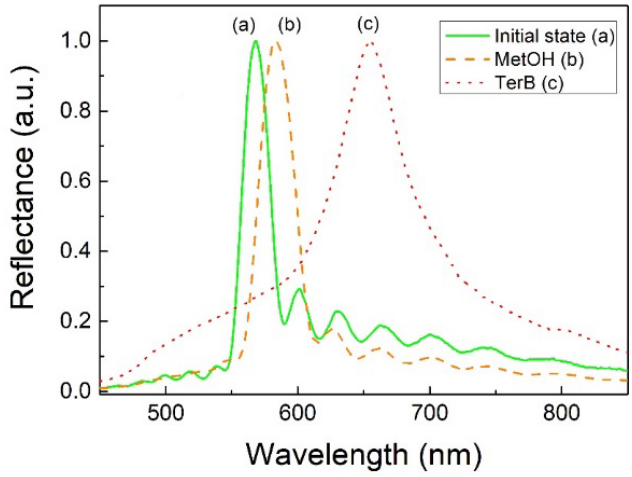

Figure 6.4 *Reflectance spectra of the composite colloidal crystal before (green solid line) and after spotting 5 μl of different solvents onto the ''sensor'' surface: (orange dash line) MetOH, (red dot line) TerB.*

The calculated values compared with the tabulated ones, have evidenced an optimum agreement as shown in Table 6.1.

Analyte	S Tabulated [29]	S Calculated
MetOH	1.02	1.03
TerB	1.21	1.19

Table 6.1 *Swelling coefficient S of the solvent used to validate the model, an error of 5% is attributed to the measured values.*

Hence, the analytical model discussed, can be seen as a suitable approach in order to describe the working principle of the colloidal structure and it allows a proper design of the chromatic sensor.

6.3.2 Tert-butyl Alcohol Concentration Detection

As described in the previous section, a change in the filling factor f causes a variation in the photonic band gap features which can be observed as a shift in the wavelength of the light reflected from the crystal (color change). Taking advantage of this, we have used the composite colloidal crystal for the analysis of butanol-water mixture concentration. It is worth noting that the determination of water concentration in organic solvents, in particular ethanol and butanol, is of great interest for industry e.g. in pharmaceutical and chemical ones for the efficiency of drugs and usefulness of chemical products as pointed out in the introduction. Using the same approach applied for the model validation, 5 µl of different concentrations of TerB and water mixtures have been spotted on the surface of the composite colloidal crystal. Alcohol concentration was expressed in % Vol, mixtures were prepared by measuring the respective volumes with micropipettes.
Fig. 6.5 shows the variation of peak position ($\Delta\lambda$), respect to the initial state, as a function of different mixtures of TerB and H_2O, that allows to investigate the sensitivity of the composite colloidal crystal structure as chemical responsive material.
At a first glance we can notice that the $\Delta\lambda$ is not proportional to the alcohol volume fraction. Since the PDMS elastomer hardly swells in pure water, the peak shift is negligible due to the hydrophobic condition, however we can clearly distinguish two main regions, the first one goes from 10% to 80% of TerB, in which only a moderate shift in term of wavelength (17 nm) is observable, while in the second one, that goes from 90% to 99%, there is a much steeper slope with a variation of 23 nm.

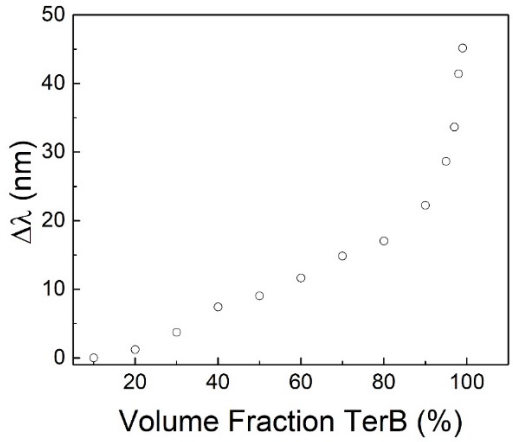

Figure 6.5 *Relationship between the variation of peak position (Δλ), with respect to the initial state, and the TerB concentration (v/v₀). The error bars are ± 1nm.*

This trend can be explained due to the fact that the value of the solubility parameter for a mixture of solvents is not volume-wise proportional to the solubility parameters of the components [30]. In fact, anomalies of the physicochemical properties of mixtures, such as solubility, depend on microhetereogeneity caused by separation at molecular level. In alcohol-water mixtures, when the water concentration is very low, the molecules of alcohols can be considered in the same environment as those in the pure liquid alcohols, while the H_2O molecules are well dispersed in the organic phase [31].
Considering the solution behavior of the PDMS-solvent system, it is well known that to have the solubility of two materials, since the molecules of the solute have to permit the insertion of the solvent, the cohesive energy densities have to be similar. In case of cross-linked polymers, that do not dissolve, solubility is expressed by the degree of swelling. As already reported by Lee et al. [29] and Rumens et al. [32] the relationship between solubility and swelling is not linear and is distinctive for each polymer-solvent system.
In conclusion, we have demonstrated that the photonic crystal sensing material developed is a suitable tool that allows the detection of water in TerB by using a simple and portable spectroscopic system.

6.3.3 Isomers Detection

Traditional photonic sensing based on the change of balanced reflection of photonic structures can hardly distinguish chemical species with similar refractive indices, in this case composite colloidal crystals are able to discriminate also isomers. In order to differentiate among

isomers, dynamic measurements, compared to static reflectance spectra, can efficiently distinguish them even if they present similar physico-chemical features, exploiting their capability to diffuse in and swell PDMS.

The approach based on dynamic reflectance spectra has been applied for the recognition of different species such as demonstrated by Lova et al. [10] and Ge's group [12], to detect volatile organic compounds (VOC) and homologues respectively.

The advantage of dynamic measurements is that they allow following different processes happening when the solvent is applied on the surface of the composite. As a function of time the solvent diffuses into the structure and evaporates into the atmosphere, leading to continuous variation of the observed pattern.

Fig. 6 a, b, c show the reflectance-time diagram obtained from three butanol isomers (TerB, NB, and 2B). On these figures, the horizontal axis represents time, the vertical one represents wavelength and the colours give the normalized measured intensity. Pattern changes, which are a result of swelling induced deformations, can be readily and easily visualized in this way, allowing the discrimination of the butanol isomers.

Analyzing Fig. 6.6 a', b', c', where some significative spectra extracted from the maps have been reported, we can observe that the time needed to reach the maximum red shift and intensity of the reflectance diffraction peak is different and typical of each isomer, moreover we can observe that the intensity follows the phenomenological formula [7]:

$$I \propto \frac{\Delta n}{n_{eff}} \tag{6.5}$$

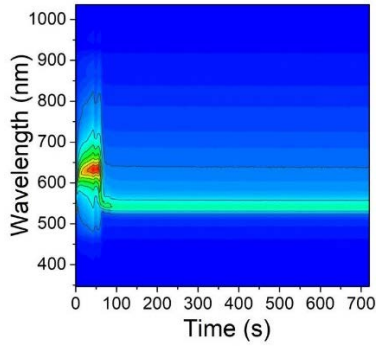

(a)

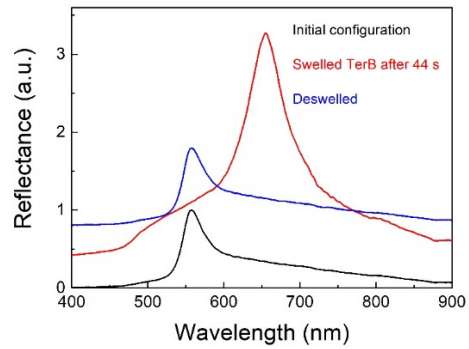

(a')

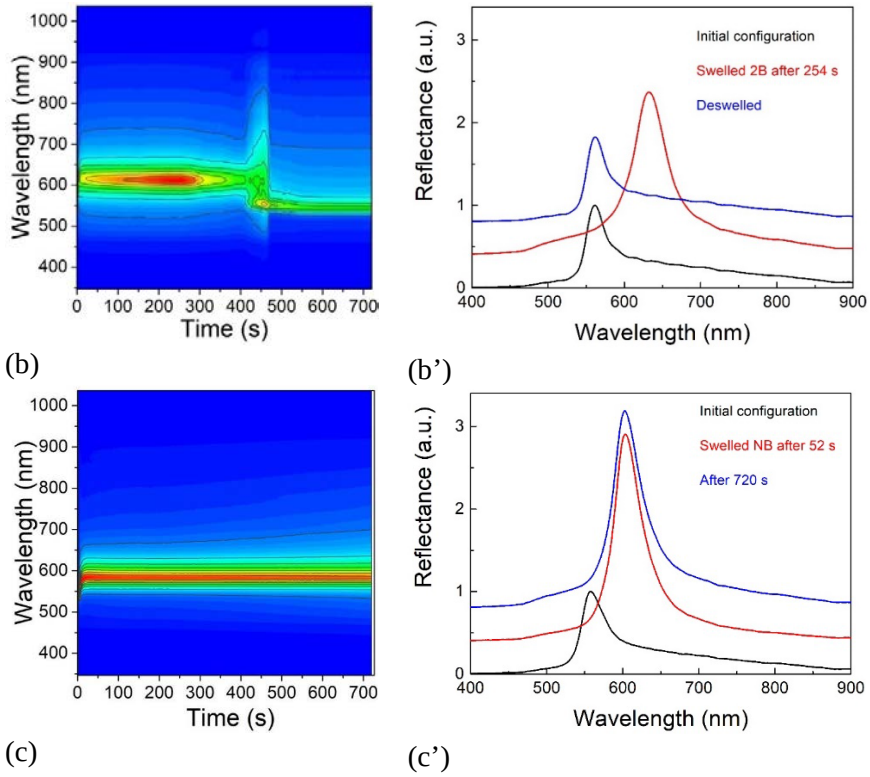

Figure 6.6 *Dynamic Reflectance contour-plots spectra of: (a) 2-Methylpropan-2-ol (TerB), (b) Butan-2-ol (2B) and (c) Butan-1-ol (NB) and time resolved optical response (a'), (b'),(c') highlighting differences typical of each isomer and the reversibility of the process.*

where Δn is the difference of refractive index between spheres and the infiltrating medium, and n_{eff} is the effective refractive index after swelling of the structure; this can be associated to the fact that, as predicted in the model described in section 6.3.1, the swelling induces a decrease in the neff value.

Moreover, we can notice that the change induced to the composite structure is totally reversible after the complete evaporation into the atmosphere of the solvent (Fig 6.6 a', b'); in the case of NB, due to the low vapor pressure of the solvent, after 720 s the reflectance peak was not yet returned to the initial position, however for a time of 30 min we have observed a complete reversibility of the process. Furthermore, the measurements were repeated several times, and the material was found to display highly reproducible changes in the optical spectra upon cycling.

Finally, it is worth highlighting that the analytes can diffuse into the PDMS matrix, swell it and evaporate with different kinetics, depending

on their chemical properties (polarity, viscosity, chemical affinity, vapor pressure), and this produces a sort of finger print that allows a quite fast recognition even if they present similar features.

6.4 Conclusions

In this paper we have reported an easy and reliable method for the fabrication of composite colloidal crystals based on PS nanoparticles embedded in an elastomeric matrix such as PDMS. These systems can be employed as low cost and reversible chromatic sensors for the investigation of mixtures and to distinguish among different kind of isomers. Moreover, we have highlighted the working principle of this class of sensors, assessing the crucial role that the filling factor f plays in the position of the diffraction peak. It has been demonstrated that the developed structures are a suitable tool for the determination of small water ($\geq$ 1 vol%) content in butanol indicating that this structure can be seen as a portable spectroscopic system. Dynamic measurements have permitted to selectively distinguish the isomers exploiting their intrinsic features. Finally, the presented approach suggests that is possible to realize a colorimetric responsive sensor, which potentially does not require any signal transduction and it could be a safe device suitable for untrained end-users.

References

[1] E. Yablonovitch, Inhibited spontaneous emission in solid-state physics and electronics, Phys. Rev. Lett. 58 (20) (1987) 2059-2062.
[2] S. John, Strong localization of photons in certain disordered dielectric superlattices, Phys. Rev. Lett. 58 (23) (1987) 2486-2489.
[3] C. Lopez, Materials aspects of photonic crystals, Adv. Mater. 15 (20) (2003) 1679-1704.
[4] A. Chiappini, C. Armellini, A. Chiasera, M. Ferrari, Y. Jestin, M. Mattarelli, M. Montagna, E. Moser, G. Nunzi Conti, S. Pelli, G.C. Righini, M. Clara Gonçalves, R.M. Almeida, Design of photonic structures by sol–gel-derived silica nanospheres, J. Non-Cryst Solids 353 (5-7) (2007) 674-678.
[5] J.Y. Shieh, J.Y. Kuo, H. Weng, H.H. Yu, Preparation and evaluation of the bioinspired PS/PDMS photochromic films by the self-assembly dip-drawing method, Langmuir 29 (2) (2013) 667-672.
[6] T. Ding, S.K. Smoukov, J.J. Baumberg, Stamping colloidal photonic crystals: a facile way towards complex pixel colour

patterns for sensing and displays, Nanoscale 7 (5) (2015) 1857-1863.
[7] A.C. Arsenault, D.P. Puzzo, I. Manners, G.A. Ozin, Photonic-crystal full-colour displays, Nat. Photonics 1 (8) (2007) 468-472.
[8] J. Liu, Y. Zhang, R. Zhou, L. Gao, Volatile alcohol-responsive visual sensors based on P(HEMA-co-MA)-infiltrated SiO2 inverse opal photonic crystals, J. Mater. Chem. C 5 (24) (2017) 6071-6078.
[9] F. Xiao, G. Li, Y. Wu, Q. Chen, Z. Wu, R. Yu, Label-Free Photonic Crystal-Based β-Lactamase Biosensor for β-Lactam Antibiotic and β-Lactamase Inhibitor, Anal. Chem. 88 (18) (2016) 9207-9212.
[10] P. Lova, C. Bastianini, P. Giusto, M. Patrini, P. Rizzo, G. Guerra, M. Iodice, C. Soci, D. Comoretto, Label-free vapor selectivity in poly(p-Phenylene Oxide) photonic crystal sensors, ACS Appl. Mater Inter 8 (46) (2016) 31941-31950.
[11] W.K. Kuo, H.P. Weng, J.J. Hsu, H.H. Yu, Photonic crystal-based sensors for detecting alcohol concentration, Appl. Sci. 6 (3) (2016) 67-1-67-13.
[12] Y. Zhang, Q. Fu, J. Ge, Photonic sensing of organic solvents through geometric study of dynamic reflection spectrum, Nature Comm. 6 (2015) 7510-1-7510-7.
[13] C. Xiong, J. Zhao, L. Wang, H. Geng, H. Xu, Y. Li, Trace detection of homologues and isomers based on hollow mesoporous silica sphere photonic crystals, Mater. Horiz. 4 (5) (2017) 862-868.
[14] Y. Zhang, J. Qiu, R. Hu, P. Li, L. Gao, L. Heng, B. Z. Tang, L. Jiang, A visual and organic vapor sensitive photonic crystal sensor consisting of polymer-infiltrated SiO2 inverse opal, Phys. Chem. Chem. Phys. 17 (15) (2015) 9651-9658.
[15] M. Chen, Y.P. Zhang, S.Y. Jia, L. Zhou, Y. Guan, Y.J. Zhang, Photonic crystals with a reversibly inducible and erasable defect state using external stimuli, Angew. Chem. Int. Ed. 54 (31) (2015) 9257-9261.
[16] B. Yu, H. Cong, Z. Yang, S. Yang, Y. Wang, F. Zhai, Y.Wang, Preparation of humidity-sensitive Poly(Ethylene Glycol) inverse opal micropatterns using colloidal lithography, Materials 10 (9) (2017) 1035-1-1035-11.
[17] E. Colusso, G. Perotto, Y. Wang, M. Sturaro, F. Omenetto, A. Martucci, Bioinspired stimuli-responsive multilayer film made of silk–titanate nanocomposites, J. Mater. Chem. C 5 (16) (2017) 3924-3931.
[18] J.T. Zhang, L.L. Wang, J. Luo, A. Tikhonov, N. Kornienko, S.A. Asher, 2-D array photonic crystal sensing motif, J. Am. Chem. Soc. 133 (24) (2011) 9152-9155.

[19] X. Fan, B. Du, Selective detection of trace 1-butanol by QCM sensor coated with copolymer P(HEMA-co-MA), Sens. Actuators B 160 (1) (2011) 724-729.
[20] D. Han, P. Song, S. Zhang, H. Zhang, Q. Xu, Q. Wang, Enhanced methanol gas-sensing performance of Ce-doped In2O3 porous nanospheres prepared by hydrothermal method, Sens. Actuators B 216 (2015) 488-496.
[21] Y.L. Ko, H.P. Tsai, K.Y. Lin, Y.C. Chen, H. Yang, Reusable macroporous photonic crystal-based ethanol vapor detectors by doctor blade coating, J. Colloid Interf Sci. 487 (2017) 360-369.
[22] S.I. Ohira, K. Goto, K. Toda, P.K. Dasgupta, A capacitance sensor for water: trace moisture measurement in gases and organic solvents, Anal. Chem. 84 (20) (2012) 8891-8897.
[23] X. Hui, K.E. Niemeyer, K.B. Brady, C.J. Sung, Reduced Chemistry for Butanol Isomers at Engine-Relevant Conditions, Energy Fuels 31 (1) (2017) 867-881.
[24] M. Lapuerta, J.J. Hernández, D. Fernández-Rodríguez, A. Cova-Bonillo, Autoignition of blends of n-butanol and ethanol with diesel or biodiesel fuels in a constant-volume combustion chamber, Energy 118 (2017) 613-621.
[25] R. Daoussi, S. Vessot, J. Andrieu, O. Monnier, Sublimation kinetics and sublimation end-point times during freeze-drying of pharmaceutical active principle with organic co-solvent formulations, Chem. Eng. Res. Des. 87 (7) (2009) 899-907.
[26] S. Vessot, J. Andrieu, A Review on freeze drying of drugs with tert-Butanol (TBA) + Water systems: characteristics, advantages, drawbacks, Drying Technol. 30 (4) (2012) 377-385.
[27] A. Chiappini, C. Armellini, A. Chiasera, M. Ferrari, L. Fortes, M.C. Gonçalves, R. Guider, Y. Jestin, R. Retoux, G. Nunzi Conti, S. Pelli, R.M. Almeida, G.C. Righini, An alternative method to obtain direct opal photonic crystal structures, J. Non-Cryst Solids 355 (18-21) (2009) 1167-1170.
[28] A. Chiappini, C. Armellini, A. Carpentiero, L. Minati, G.C. Righini, M. Ferrari, Solvent sensitive polymer composite structure, Opt. Mater. 36 (1) (2014) 130-134.
[29] A. Chiappini, A. Chiasera, S. Berneschi, C. Armellini, A. Carpentiero, M. Mazzola, E. Moser, S. Varas, G.C. Righini, M. Ferrari, Sol–gel-derived photonic structures: fabrication, assessment, and application, J. Sol Gel Sci. Technol 60 (3) (2011) 408-425.
[30] J.N. Lee, C. Park, G. M. Whitesides, Solvent Compatibility of Poly(dimethylsiloxane)-Based Microfluidic Devices, Anal. Chem. 75 (23) (2003) 6544-6554.

[31] A. Barton, Solubility parameters, Chem. Rev. 75 (6) (1975) 731-753.
[32] P. Tomza, M.A. Czarnecki, Microheterogeneity in binary mixtures of propyl alcohols with water: NIR spectroscopic, two-dimensional correlation and multivariate curve resolution study, J. Molec. Liquids 209 (2015) 115-120.
[33] C.V. Rumens, M.A. Ziai, K.E. Belsey, J.C. Batchelor, S.J. Holder, Swelling of PDMS networks in solvent vapours; applications for passive RFID wireless sensors, J. Mater. Chem. C 3 (39) (2015) 10091-10098.

7. Fractional-Order Theory of Thermoelasticicty. I: Generalization of the Fourier Equation

By G. Alaimo, V. Piccolo, A. Chiappini, M. Ferrari, D. Zonta, L. Deseri and M. Zingales

Abstract

The paper deals with the generalization of the Fourier-type relations in the context of fractional-order calculus. The instantaneous temperature-flux equation of the Fourier-type diffusion is generalized introducing a self-similar, fractal type mass clustering at the micro-scale. In this setting the resulting conduction equation at the macro-scale yields a Caputos' fractional derivative with order $\beta \in [0,1]$ of temperature gradient that generalizes the Fourier conduction equation. The order of the fractional-derivative has been related to the fractal assembly of the micro-structure and some preliminary observations about the thermodynamical restrictions of the coefficients and the state functions related to fractional-order Fourier equation has been introduced. The distribution and the temperature raising in simple rigid conductors have been also reported to investigate the influence of the derivation order in the temperature field.

7.1 Introduction

Fractional-order calculus is usually referred as the generalization of the well-known ordinary differential calculus introducing real-order integrals and derivatives. It traces back to the basic definitions by Riemann as well as to successive memories of famous mathematicians, among the others (see e.g. [41]), while, more recently, other scientists focused on the feasibility of integral measures involved in fractional-order operators [4, 5, 6]

After definitions and feasibility of fractional-order operators, their introduction into continuum field theories has received significant interests worldwide [33, 26, 39, 46, 45, 43]. Indeed the replacement of classical operators with their real-order counterparts $\left(\frac{d}{dx} \to \frac{d^{\alpha}}{dt^{\alpha}} \text{and} \frac{d}{dt} \to \frac{d^{\beta}}{dt^{\beta}} \right)$ with $\alpha, \beta \in \Re$ has proved to be valuable in several engineering and physical contexts predicting phenomena with great accuracy [32, 33, 28, 7]. The use of fractional-order operators has been also reported in non-local continuum field theories of mechanics [27, 20, 21, 11, 12, 44, 9], non-local heat transfer [40, 36, 47, 49]

stochastic analysis [18, 16, 3, 17], diffusive transport [42, 25, 34, 31], biophysics [13], rheology and many others.
Despite the wider and wider use of fractional-order operators an important question has not been answered: "What is the physics beyond the use of fractional-order derivatives?" The answer to this fundamental issue would be of great stimulus for worldwide researchers to re-derive the classical continuum field theories in terms of fractional-order operators.
On that subject, a strong effort has been profused during last years to provide a solid physical ground in the use of fractional-order derivative in the transport equations. Cases involving polymer viscoelasticity, anomalous fluid diffusion, as well as laminar flow across fractal sets have been recently provided [22, 19, 15, 2].
Fractional-order calculus has been also used in the theory of thermo-elasticity to generalize the classical Fourier and Cattaneo transport equations [23, 8, 35, 10]. However, no physical ground in the formulation of neither anomalous heat transfer nor thermo-elasticity theory has been provided, leading to a non-physical representation of the thermoelastic phenomena reported in such studies.
In the present work, the authors obtain a fractional-order Fourier diffusion law from a multi-scale rheological model. This is done by means of the introduction of an inhomogeneous conductor leading to an anomalous time evolution as t^{β} with $0 \le \beta \le 1$ [48]. Such consideration is used in the paper to provide a physical exact description of the fractional-order Fourier diffusion equation that is also thermodynamically consistent. Numerical experiments have been reported to show the evolution of the temperature field in different domains with different boundary conditions. Anomalous thermo-elasticity is analyzed in Part II of this paper [38], where a measure of the signature of the anomaly based on a measure of the energy rate is explored.

7.2 The Thermodynamical Model of Power-Law Temperature Evolution

In this section the authors show that anomalous rising of temperature in the form of power-law t^{β} is obtained using arguments presented extensively in [38].
It is assumed a distribution of $n+1$ masses $m_j = A_j \Delta z$ with $j = 1, 2, ..., n+1$, where A_j represents the cross-sectional area of the j^{th} mass and $\Delta z = l/(n+1)$ its length, being $l = (n+1)\Delta z$ the overall length of the conductor Fig. (7.1a). The masses, located at abscissas

$z_j = j\Delta z$ and separated by adiabatic walls from the external environment, are connected each other by a perfect conductor, so that thermal energy exchange may occur only along the z direction. The thermodynamic state variables describing the system are assumed as the macroscopic temperatures $T_j(t)$ of the masses m_j for $j = 1,2,...,n+1$.

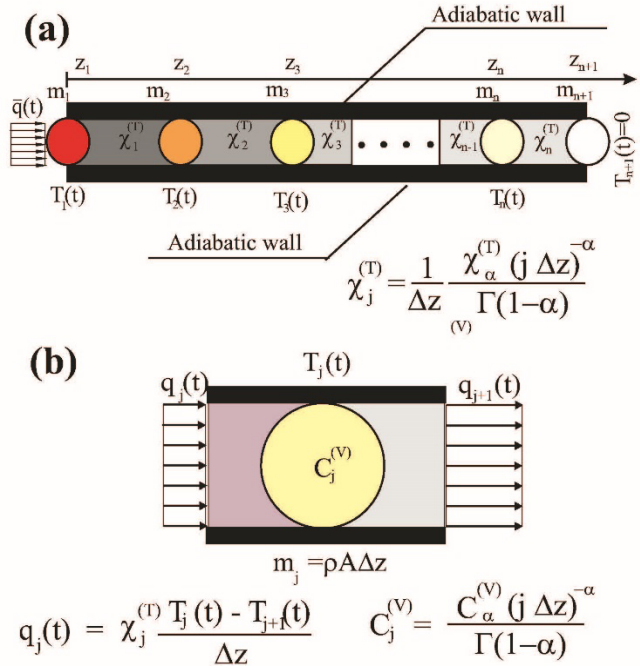

Figure 7.1 *Thermodynamical model of anomalous temperature rising: (a) the concentrated mass system; (b) thermal energy balance of the j^{th} mass.*

The energy balance of the j^{th} mass m_j involves the rate of the internal energy U_j and the energy flux along the conductors m_j, namely, $q_j(t)$ and $q_{j-1}(t)$ that can be written as:

$$\frac{dU_j(t)}{dt} = m_j\frac{du_j(t)}{dt} = m_j C_j^{(V)}\frac{dT_j(t)}{dt} = A_{j-1}q_{j-1}(t) - A_j q_j(t) \qquad (7.1)$$

where with $C_j^{(V)} = \left(\frac{\partial u_j}{\partial T}\right)_{T_0}$ is denoted the specific thermal capacity at constant volume that is assumed to be uniform for the considered

temperature interval; $u_j(t)$ is the internal energy function density of the mass m_j.

Given the assumption that only diffusive phonon-phonon interaction yields thermal energy transport, the thermal energy flux $q_j(t)$ of the mass located at abscissa z_j may be expressed as:

$$q_j(t) = -\chi_j^{(T)} \frac{T_{j+1}(t) - T_j(t)}{z_{j+1} - z_j} = -\chi_j^{(T)} \frac{T_{j+1}(t) - T_j(t)}{\Delta z} \tag{7.2}$$

where with $\chi_j^{(T)}$ the thermal conductivity of the j^{th} conductor is denoted. Substitution of (7.2) in (7.1) yields the thermal energy balance as an ordinary differential equation system in the temperatures $T_j(t)$.

$$\rho \Delta z C_j^{(V)} \dot{T}_j(t) = \frac{1}{\Delta z}\left[\chi_{j+1}^{(T)} T_{j+1}(t) - \left(\chi_j^{(V)} + \chi_{j+1}^{(V)}\right) T_j(t) + \chi_{j-1}^{(T)} T_{j-1}(t)\right] \tag{7.2}$$

where it is assumed that $A = A_j$ for $j = 1, 2, ..., n+1$ and that the masses $m_j = \rho A \Delta z$ (see fig. (7.1)) where ρ is the mass density. The energy balance equations reported in eq. (7.3) involve masses m_j with $j = 2, 3, ..., n$ as the temperature of the m_{n+1} mass of the system has been set to the value $T_{n+1} = 0$ without loss of generality. Energy balance of mass m_1 of the thermodynamical system in fig. (7.1) involves an external thermal energy flux, denoted in the following formula as $\bar{q}(t)$, yielding:

$$C_1^{(V)} \Delta z \rho \dot{T}_1(t) + \chi_1^{(T)} \frac{T_2(t) - T_1(t)}{\Delta z} = \bar{q}(t) \tag{7.4}$$

The anomalous time-scaling of the temperature field is achieved assuming that the spatial distribution of the thermal conductivity $\chi_j^{(V)}$ and the specific thermal capacity $C_j^{(V)}$ varies along the masses m_j with the relations:

$$C_j^{(V)} = \frac{C_\alpha^{(V)} (j \Delta z)^{-\alpha}}{\Gamma(1-\alpha)} \tag{7.5a}$$

$$\chi_j^{(T)} = \frac{\chi_\alpha^{(T)} (j\Delta z)^{-\alpha} \Gamma\left(\frac{1+\alpha}{2}\right)}{\Gamma(1-\alpha)} \tag{7.5b}$$

where $\Gamma(\bullet)$ is the Euler-Gamma function and the real exponent α belongs to the interval $-1 \le \alpha < 1$ for diffusion-type phenomena. It must be remarked that the assumption of a power law variation of the thermal properties of the non-homogeneous rigid conductor is the fundamental hypothesis from which comes out the fractional constitutive relation between the heat flux and the temperature gradient. Indeed, for the case $\alpha = 0$, an homogeneous conductor and, consequently, the classical Fourier transport equation is obtained.
Coefficients $C_\alpha^{(V)}$ and $\chi_\alpha^{(T)}$ are the thermal capacity and the thermal conductivity, respectively, with anomalous physical dimensions in the International System of Units (SI) as:

$$\left[C_\alpha^{(V)}\right] = m^{2+\alpha} K^{-1} s^{-2} \quad ; \quad \left[\chi_\alpha^{(T)}\right] = kg\, m^{1+\alpha} K^{-1} s^{-3} \tag{7.6}$$

In order to show that the discrete mass system yields a power-law time rising of the temperature field it is supposed that, at the same time, $n \to \infty$, $\Delta z \to 0$ and $l \to \infty$. In this framework the functions $T_j(t)$ and $q_j(t)$ represents local values of the fields $T_j(t) \to T(z_j, t)$ and $q_j(t) \to q(z_j, t)$.
Under these circumstances the balance equation reported in (7.1) becomes:

$$\rho C^{(V)}(z) \frac{\partial T(z,t)}{\partial t} = -\frac{\partial q(z,t)}{\partial z} \tag{7.7}$$

Eq. (7.8) describes the balance at location z between the rate of the thermal energy $\dot{U} = \rho \frac{\partial u}{\partial t}$ and the difference of the outgoing thermal energy $q(z+dz,t)$ and the incoming one $q(z,t)$ in unit time. Introducing the following Fourier transport equation, obtained for $\Delta z \to 0$

$$q(z,t) = -\chi^{(T)}(z) \frac{\partial T(z,t)}{\partial z} \tag{7.8}$$

in eq.(7.8), the heat equation is obtained as:

$$\rho C^{(V)}(z)\frac{\partial T(z,t)}{\partial t} = \frac{\partial}{\partial z}\left[\chi^{(T)}(z)\frac{\partial T(z,t)}{\partial z}\right] \qquad (6.9)$$

In eq.(7.10) the thermodynamical properties of the distributed mass system are described through the continuous counterparts of eqs. (7.1 a,b), i.e. $C_j^{(V)} \to C^{(V)}(z_j)$ and $\chi_j^{(T)} \to \chi^{(T)}(z_j)$ that read:

$$C^{(V)}(z) = \frac{C_\alpha^{(V)} z^{-\alpha}}{\Gamma(1-\alpha)} \quad ; \quad \chi^{(T)}(z) = \frac{\chi_\alpha^{(T)} z^{-\alpha}\Gamma\left(\frac{1+\alpha}{2}\right)}{\Gamma(1-\alpha)} \qquad (7.10)$$

Accordingly, the boundary conditions associated to the heat equation (7.10) are obtained as the continuous conditions on the first mass m_1 and the last mass m_{n+1} of the discrete system (see fig. (7.1) under consideration as:

$$\overline{q}(t) = \lim_{z\to 0} -\chi^{(T)}(z)\frac{\partial T(z,t)}{\partial z} \quad ; \quad \lim_{z\to\infty} T(z,t) = 0 \qquad (7.11)$$

The temperature field $T(z,t)$ may be obtained introducing the Laplace transform of (7.10), yielding to an ordinary differential equation in Laplace domain as:

$$\frac{d}{dz}\left[\chi^{(T)}(z)\frac{d\hat{T}(z,s)}{dz}\right] = s\rho C^{(V)}(z)\hat{T}(z,s) \qquad (7.12)$$

where $\hat{T}(z,s)$ represents the Laplace transform of the temperature field $T(z,t)$. Relation (7.13) can be cast, after some straightforward manipulation, as:

$$\frac{d^2\hat{T}(s,z)}{dz^2} + \frac{\left[\chi^{(T)}(z)\right]'}{\chi^{(T)}(z)}\frac{d\hat{T}(s,z)}{dz} - \frac{C^{(V)}(z)}{\chi^{(T)}(z)}s\rho\hat{T}(s,z) = 0 \qquad (7.13)$$

Substituting for the thermal conductivity coefficient $\chi^{(T)}(z)$ and the specific heat $C^{(V)}(z)$ with the corresponding power-laws reported in eqs. (7.11), the differential equation ruling the temperature field becomes:

$$\frac{d^2\hat{T}(z,s)}{dz^2} - \frac{\alpha}{z}\frac{d\hat{T}(z,s)}{dz} - \tau s\hat{T}(z,s) = 0 \tag{7.14}$$

where:

$$\tau = \rho\frac{C_\alpha^{(V)}}{\chi_\alpha^{(T)}}\frac{1}{\Gamma\left(\frac{1+\alpha}{2}\right)} \tag{7.15}$$

is constant with respect to space z and time t and its value changes with α as shown in (7.16). However, physical dimensions of τ are $[\tau] = sm^{-2}$, consequently they do not depend on the exponent α. A canonical Bessel equation of second kind may be obtained from eq. (7.16) introducing the auxiliary function $\overline{T}(z,s)$ by means of the mapping $\hat{T}(z,s) = z^\alpha\overline{T}(z,s)$ yielding:

$$z^2\frac{d^2\overline{T}(z,s)}{dz^2} + \alpha z\frac{d\overline{T}(z,s)}{dz} - \left(z^2\tau s + \alpha\right)\overline{T}(z,s) = 0 \tag{7.16}$$

Solution of eq.(7.17) involves modified Bessel functions denoted $Y_\beta\left(z\sqrt{\tau s}\right)$ and $K_\beta\left(z\sqrt{\tau s}\right)$, respectively (see [48] for details) as: where β is related to the scaling exponent α as:

$$\beta = \frac{1+\alpha}{2} \tag{7.17}$$

Boundary conditions in Laplace domain yield the integration constants, namely, B_1 and B_2 as:

$$B_1 = 0 \quad ; \quad B_2 = \frac{2^\beta\Gamma(2-2\beta)\sin(\pi\beta)\left(s\tau\right)^{-\frac{\beta}{2}}}{\pi\chi_\alpha^{(T)}}\hat{\overline{q}}(s) \tag{7.18}$$

with $\left[B_2\right] = Ksm^{-\beta}$, so that the temperature field of the distributed mass systems reads:

$$\hat{T}\left(z,s\right) = \frac{2^{\beta}\Gamma(2-2\beta)\sin(\pi\beta)\left(s\tau\right)^{-\frac{\beta}{2}}}{\pi\chi_{\alpha}^{(T)}}\hat{\overline{q}}(s)z^{\beta}K_{\beta}\left(z\sqrt{\tau s}\right) \tag{7.19}$$

Power-law time rising of the temperature field is obtained evaluating the temperature at $z = 0$ as:

$$\hat{T}_0\left(s\right) = \lim_{z\to 0}\hat{T}\left(z,s\right) = \frac{1}{R_{\beta}}s^{-\beta}\hat{\overline{q}}(s) \tag{7.20}$$

where the anomalous thermal diffusivity coefficient, R_{β} reads:

$$R_{\beta} = \frac{2^{1-2\beta}\pi\chi_{\alpha}^{(T)}\csc(\pi\beta)\tau^{\beta}}{\Gamma(2-2\beta)\Gamma(\beta)} \tag{7.21}$$

and $\left[R_{\beta}\right] = kgK^{-1}s^{\beta-3}$. Special cases of eq. (7.22) can be obtained looking at some representative values of β ans α as follows:

$$\lim_{\substack{\beta\to 0\\ \alpha\to -1}} R_{\beta} = \frac{2\chi_{-1}^{(T)}}{\pi} \tag{7.22a}$$

$$\lim_{\substack{\beta\to \frac{1}{2}\\ \alpha\to 0}} R_{\beta} = \sqrt[4]{\pi}\sqrt{\rho\chi_0^{(T)}C_0^{(V)}} \tag{7.22b}$$

$$\lim_{\substack{\beta\to 1\\ \alpha\to 1}} R_{\beta} = \rho C_1^{(V)} \tag{7.22c}$$

Under the assumption of stationary thermal energy flux $\overline{q}(t) = \overline{q}_0 U(t)$, the time-varying temperature function $T_0(t)$ is obtained applying the inverse Laplace transform to eq. (7.21), yielding:

$$T_0(t) = \frac{\overline{q}_0}{R_{\beta}\Gamma(1+\beta)}t^{\beta} \propto t^{\beta} \tag{7.23}$$

that is the power-law temperature time scaling observed in fig. (7.1) for the discretized mass system considered in the analysis with $\beta \in [0,1]$ (see e.g.[48] for details).

7.3 The Fractional-order generalization of Fourier heat transport equation

In this section the authors introduce a fractional-order generalization of the Fourier transport equation according to the physical model of the power-law described in previous section. To this aim, the basic framework of fractional-order calculus is first provided followed by the physical model used to generalize the Fourier equation and its compatibility with the second law of thermodynamics.

7.3.1 Preliminary Remarks on Fractional-Order Calculus

Fractional calculus may be considered the extension of the ordinary differential calculus to non-integer powers of derivation orders (e.g. see [37], [42]). In this section the authors address some basic notions about this mathematical tool.
The Euler-Gamma function $\Gamma(z)$ may be considered as the generalization of the factorial function because, when z assumes integer values, it follows that $\Gamma(z+1) = z!$. The Euler-Gamma is defined as the result of the integral as follows:

$$\Gamma(z) = \int_0^{\infty} e^{-x} x^{z-1} dx. \tag{7.24}$$

The Riemann-Liouville fractional integrals and derivatives with $0 < \beta < 1$ of functions defined on the entire real axis have the following forms:

$$\left(\mathrm{I}_{+}^{\beta} f\right)(t) = \frac{1}{\Gamma(\beta)} \int_{-\infty}^{t} \frac{f(\tau)}{(t-\tau)^{1-\beta}} d\tau \tag{7.25a}$$

$$\left(\mathrm{D}_{+}^{\beta} f\right)(t) = \frac{1}{\Gamma(1-\beta)} \frac{d}{dt} \int_{-\infty}^{t} \frac{f(\tau)}{(t-\tau)^{\beta}} d\tau. \tag{7.25b}$$

The Riemann-Liouville fractional integrals and derivatives with $0 < \beta < 1$ of functions defined over intervals of the real axis, namely $f(t)$ such that $t \in [a,b] \subset \mathbb{R}$, have the following forms:

$$\left(\mathrm{I}_a^{\beta} f\right)(t) = \frac{1}{\Gamma(\beta)} \int_a^t \frac{f(\tau)}{(t-\tau)^{1-\beta}} d\tau \tag{7.26}$$

$$\left(\mathrm{D}_a^{\beta} f\right)(t) = \frac{f(a)}{\Gamma(1-\beta)(t-a)^{\beta}} + \frac{1}{\Gamma(1-\beta)} \int_a^t \frac{f'(\tau)}{(t-\tau)^{\beta}} d\tau \tag{7.27}$$

Beside Riemann-Liouville fractional operators defined above, another class of fractional derivative that is often used in the context of fractional calculus is represented by Caputo fractional derivatives defined as:

$$\left({}_C\mathrm{D}_{a^+}^{\beta} f\right)(t) := \mathrm{I}_{a^+}^{m-\beta} \left(\mathrm{D}_{a^+}^{m} f\right)(t) \quad m-1 < \beta < m \tag{7.28}$$

and whenever $0 < \beta < 1$ it reads as follows:

$$\left({}_C\mathrm{D}_{a^+}^{\beta} f\right)(t) = \frac{1}{\Gamma(1-\beta)} \int_a^t \frac{f'(\tau)}{(t-\tau)^{\beta}} d\tau \tag{7.29}$$

A closer analysis of eq. (7.28) and eq. (7.29) shows that Caputo fractional derivative coincides with the integral part of the Riemann-Liouville fractional derivative in bounded domain. Moreover, the definition in eq. (7.28) implies that the function $f(t)$ has to be absolutely integrable of order m (e.g. in eq. (7.29) the order is $m = 1$). Whenever $f(a) = 0$ Caputo and Riemann-Liouville fractional derivatives coalesce.

Similar considerations hold true also for Caputo and Riemann-Liouville fractional derivatives defined on the entire real axis. Caputo fractional derivative may be considered as the interpolation among the well-known integer-order derivatives, operating over functions $f(\circ)$ that belong to the class of Lebesgue integrable functions ($f(\circ) \in L^1$); consequently it is very useful in the mathematical description of complex system evolution. It is worth noting that the Laplace and Fourier integral transforms are defined as follows:

$$\mathcal{L}[f(t)] = \int_0^{\infty} f(t) \mathrm{e}^{-st} dt \tag{7.30a}$$

$$\mathcal{F}[f(t)] = \int_{-\infty}^{+\infty} f(t) \mathrm{e}^{i\omega t} dt \tag{7.30b}$$

It is worth introducing integral transforms for fractional operators and, similarly to classical calculus, the Laplace integral transform $\mathcal{L}(\circ)$ is defined in the following forms:

$$\mathcal{L}\left[\left(\mathrm{D}_0^{\beta} f\right)(t)\right] = s^{\beta}\mathcal{L}[f(t)] - \left[\left(\mathrm{D}_0^{\beta-1} f\right)(t)\right]_{t=0} \quad \text{if } 0 < \beta \le 1 \tag{7.31a}$$

$$\mathcal{L}\left[\left({}_C\mathrm{D}_0^{\beta} f\right)(t)\right] = s^{\beta}\mathcal{L}[f(t)] - s^{\beta-1} f(0) \quad \text{if} \quad 0 < \beta \le 1 \tag{7.31b}$$

$$\mathcal{L}\left[\left(\mathrm{I}_{0^+}^{\beta} f\right)(t)\right] = s^{-\beta}\mathcal{L}[f(t)] \tag{7.31c}$$

In the same way, the Fourier integral transform $\mathcal{F}(\circ)$ assumes the following forms:

$$\mathcal{F}\left[\left(\mathrm{D}_{+}^{\beta} f\right)(t)\right] = (-i\omega)^{\beta}\mathcal{F}[f(t)] = (-i\omega)^{\beta}\,\hat{f}(\omega) \tag{7.32a}$$

$$\mathcal{F}\left[\left(\mathrm{I}_{+}^{\beta} f\right)(t)\right] = (-i\omega)^{-\beta}\mathcal{F}[f(t)] = (-i\omega)^{-\beta}\,\hat{f}(\omega) \tag{7.32b}$$

7.3.2 The Fractional-Order Generalization of the Fourier Equation

Power-law rising of temperature field described in previous sections corresponds, in the context of a linear-order heat transport to a fractional-order relation among thermal flux and temperature. Indeed, assuming that the thermal energy flux across the $x = 0$ cross-section is a time-dependent function, inverse Laplace transform of (7.21) yields:

$$T_0(t) = \frac{1}{R_{\beta}}\frac{1}{\Gamma(\beta)}\int_0^t (t-\tau)^{\beta-1}\overline{q}(\tau)d\tau = \frac{1}{R_{\beta}}\left(\mathrm{I}_{0^+}^{\beta}\overline{q}\right)(t) \tag{7.33}$$

that is a Riemann-Liouville fractional-order integral of order $\beta \in [0,1]$ as in (7.26).
The inverse relation of eq.(7.33) could be obtained introducing the $\beta-$ order fractional derivative of both sides of (7.33) yielding:

$$\overline{q}(t) = R_{\beta}\left(\mathrm{D}_{0^+}^{\beta} T_0\right)(t) \tag{7.34}$$

that is a fractional-order description of the temperature-flux in terms of Caputos' fractional-order derivatives analogous to fractional-order generalization of the Darcy equation ([15]).
A close observation of eq. (7.34) reveals that it does not correspond to the fractional-order generalization of the Fourier heat transport equation in terms of fractional derivatives, because no spatial gradient of the temperature field is involved, in spite of what occurs in Fourier equation rewritten with fractional calculus formalism, as:

$$\overline{q}(t) = -K_0 \left[\left(\mathrm{D}^0_{0^+} \frac{\partial T}{\partial x} \right)(t) \right] \tag{7.35}$$

where $\left(\mathrm{D}^0_{0^+} f(t) \right)(t) = \frac{d^0 f(t)}{dt^0} = f(t)$ is the 0^{th}-order derivative of the function $f(t)$ with respect to t. Fractional-order generalization of the Fourier equation will involve the presence of the real-order derivative $D^0 \to D^\beta$ with $0 \le \beta < 1$ that is not present in eq. (7.34).
In order to provide a generalization of eq. (7.34) in terms of fractional-order derivative of order β, the authors introduce a self-similar conductor micro-structure (see, for example, [14]).
In this framework, an 1D conductor with macroscopic thermal conductivity χ_T, mass density ρ and specific heat $C^{(V)}$ is considered. The conductor is referred to an one-dimensional abscissa x and it occupies the interval $[0, l]$ of the real line (see fig. (7.2a) for further details) where A is the cross-sectional area of the conductor. A spatial discretization of the conductor with interval $\Delta x = x_{j+1} - x_j$ is considered along with a spatial thermal energy flux along the positive direction of the x-axis (fig. 7.2b).
For an homogeneous conductor, the thermal energy across the cross-section at abscissa x_j, namely $q_j(t)$, depends only on the thermal conductivity χ_T and on the temperature gradient $\frac{\partial T}{\partial x}$ as in classical Fourier equation:

$$q_j(t) = -\chi \lim_{\Delta x \to 0} \frac{\Delta T}{\Delta x} = -\chi \lim_{\Delta x \to 0} \frac{T_{j+1} - T_j}{\Delta x} \tag{7.36}$$

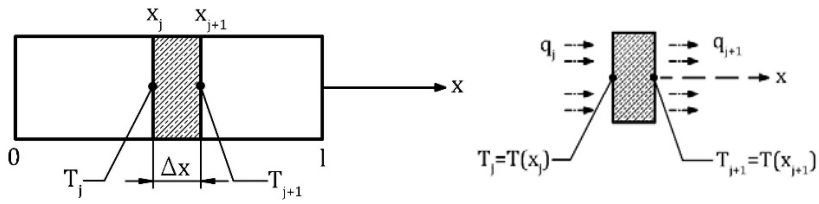

Figure 7.2 *(a) Macroscopic thermal conductor; (b) thermal energy flux.*

According to eq. (7.36), the study of thermal energy flux across the cross-section at abscissa x_j can be conducted, without any loss of generality, assuming that $T_j(t) = -\Delta T$ and $T_{j+1}(t) = 0$. The latter assumption is equivalent to the choice of the zero-temperature condition, coincident with the temperature of the cross-section $T_{j+1}(t)$ as in Fig. 7.3(a).

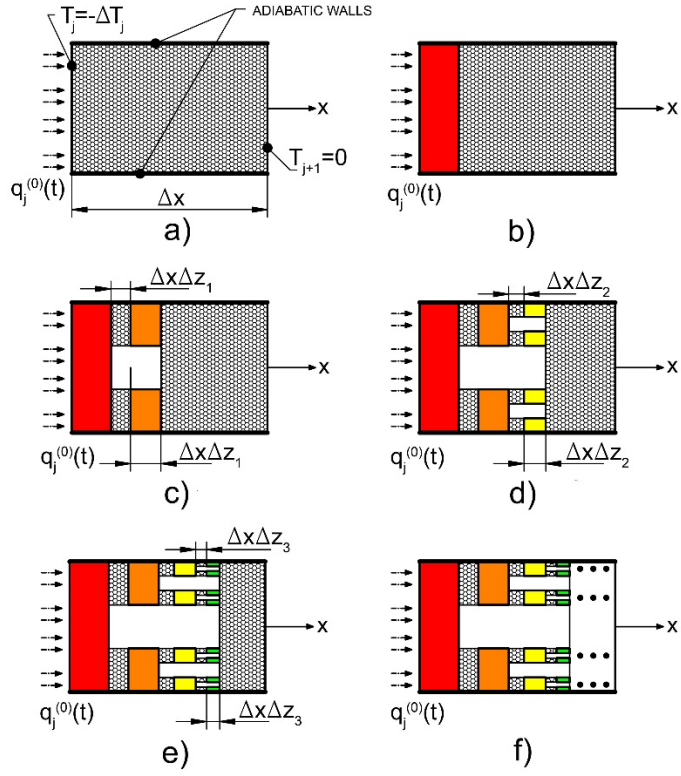

Figure 7.3 *Scheme of the self similar mass distribution: (a) definition of thermodynamical quantities; (b) $z_0=1$; (c) $z_1=3$; (d) $z_2=3^2$; (e) $z_3=3^3$; (f) $z_k=3^k$.*

In the following the authors assume that the mass density within the element of length Δx is not uniformly distributed at any resolution scale. Given such assumption and introducing a scale factor z, a self-similar cluster of mass-distribution is observed as in Fig. 7.3(b-e). The longitudinal cross-sections of the conductor along the x-axis is shown in Fig. 7.3(a) assuming a Sierpinski-like mass clustering with the observation scale z_k for illustrative' sake. In passing, the authors observe that the proposed self-similar micro-structure organization is very different from the fractal mass curdling. Indeed, in the considered self-similar clustering, all the masses observed at resolution scales $z_0, z_1, \ldots, z_{k-1}$ are present examining the mass condensation at resolution z_k.

Thermal energy exchange across the mass micro-structure is assumed in the form of phononic-phononic diffusion, ruled by the Fourier relation, in a material with uniform thermal conductivity χ_0. Under these circumstances, masses m_k and distances l_k at resolution scale z_k read:

$$m_k = \rho A_k l_k = \rho a^k \left(\frac{b_0}{z_k} \right)^2 \Delta z_k \Delta x \tag{7.37}$$

where $\Delta z_k = z_{k-1} - z_k$, b_0 is the edge of the conductor cross-section assumed squared at resolution $z_0 = 1$ and a^k is the number of self-similar elements at resolution z_k; for the proposed fractal scheme $a = 2$. The equivalent measure condition is achieved incrementing the resolution factor of a quantity z_k and introducing an anomalous dimension-dependent density ρ_d in eq. (7.37) yielding:

$$\overline{m}_k = \rho_d a^k b_0^d z_k^{1-d} \Delta z_k \Delta x = \rho_d a^k b_0^d z_k^{-\alpha} \Delta z_k \Delta x \tag{7.38}$$

where $d = \dfrac{\log 2}{2 \log 3}$ for the considered mass assembly at the microscale and it represents the Housdorff dimension of the geometric self-similar set describing mass curdling. Thermal energy balance of mass $\overline{m}_k$

involves a dynamic equilibrium among the rate of internal energy and the net thermal flux across the generic mass $\overline{m}_k / a^k$ yielding:

$$\frac{\overline{m}_k}{a^k}\dot{u}_j^{(k)} = \rho_d b_0^d z_k^{-\alpha}\Delta z_k \Delta x C^{(V)}\dot{\theta}_j^{(k)}(t) = -q_j^{(k-1)}(t)A_{k-1} + q_j^{(k)}(t)A_k =$$
$$= -\frac{\chi_T A_{k-1}^{(c)}}{\Delta z_{k-1}\Delta x}\left(\theta_j^{(k)}(t) - \theta_j^{(k-1)}(t)\right) + \frac{\chi_T A_k^{(c)}}{\Delta z_k \Delta x}\left(\theta_j^{(k-1)}(t) - \theta_j^{(k)}(t)\right) \tag{7.39}$$

where the relative temperature $\theta_j^{(k)}(t)$ of the mass $\overline{m}_k$ at the k^{th} resolution scale (corresponding to the volume element located at the macroscopic abscissa x_j) is introduced; moreover, $A_k^{(c)} = A_k / a^k$ is the cross-sectional area of the conductor at the resolution z_k. Bearing in mind that $A_k^{(c)} = b_0^d z_k^{-\alpha}$, eq. (7.39) can be rewritten as:

$$z_k^{-\alpha}\dot{\theta}_j^{(k)}(t) =$$
$$= \frac{\chi_T}{\rho_d C^{(V)}(\Delta x)^2}\left[\frac{z_k^{-\alpha}\theta_j^{(k+1)}(t)}{\Delta z_k} - \left(\frac{z_k^{-\alpha}}{\Delta z_k} + \frac{z_{k-1}^{-\alpha}}{\Delta z_{k-1}}\right)\theta_j^{(k)}(t) + \frac{z_{k-1}^{-\alpha}\theta_j^{(k-1)}}{\Delta z_{k-1}}(t)\right] \tag{7.40}$$

With some straightforward manipulations and letting $\Delta z_k \to 0$, so that a continuous resolution scale is achieved, eq. (7.40) becomes:

$$z_k^{-\alpha}\dot{\theta}_j^{(k)}(z,t) = \frac{1}{\tau_d(\Delta x)^2}\frac{\partial}{\partial z}\left(z^{-\alpha}\frac{\partial\theta(z,t)}{\partial z}\right) \tag{7.41}$$

Eq. (7.41) is formally analogous to eq. (7.13) for inhomogeneous conductor presented in previous section but, it is formulated for the micro-structure observed at abscissa x_j. The boundary conditions associated with the temperature equation (7.41) read:

$$q_j(t) = q_j(t) = \frac{1}{\Delta x}\lim_{z\to 0}\frac{\partial\theta_j(z,t)}{\partial z} \tag{7.42a}$$

$$\lim_{z\to\infty}\theta_j(z,t) = \theta_{j-1}(z,t) = 0 \tag{7.42b}$$

Solution of eq. (7.41), accounting for boundary the conditions (7.42a) and (7.42b) can be obtained relying on similar arguments as in previous sections, yielding:

$$\hat{\theta}_j\left(z,s\right)=\frac{2^{\beta}\Gamma(2-2\beta)\sin(\pi\beta)\left(s\tau\right)^{-\frac{\beta}{2}}}{\pi\chi_T}\hat{q}_j(s)z^{\beta}K_{\beta}\left(z\sqrt{\tau_d s}\right) \tag{7.43}$$

where $\beta=(\alpha+1)/2=(2-d)/2$.

Letting $z\to 0$, the temperature $\hat{\theta}_j\left(z,s\right)$ tends to $\hat{\theta}_j\left(s\right)=\hat{\theta}_j\left(x_j,s\right)=-\Delta\hat{T}\left(x_j,s\right)$ yielding:

$$-\Delta\hat{T}\left(x_j,s\right)=\lim_{z\to 0}\hat{\theta}_j\left(z,s\right)=\frac{1}{R_{\beta}}s^{-\beta}\Delta x\hat{q}_j(s) \tag{7.44}$$

where:

$$R_{\beta}=\frac{2^{1-2\beta}\pi\chi_T\csc(\pi\beta)\tau_d^{\beta}}{\Gamma(2-2\beta)\Gamma(\beta)} \tag{7.45}$$

Recasting relation (7.44) the fractional-order generalization of the Fourier equation is obtained as:

$$q\left(x,t\right)=-\lim_{\Delta z\to 0}R_{\beta}s^{\beta}\frac{\Delta\hat{T}}{\Delta x}=-R_{\beta}\left(\mathrm{D}_{0^+}^{\beta}\frac{\partial T}{\partial x}\left(x,t\right)\right)\left(t\right) \tag{7.46}$$

that has the formal structure of eq. (7.35) but also involves derivative of order $\beta=(2-d)/2$ that depends on the fractal-like clustering of mass micro-structure. When $d=2$, $\beta=0$ and the classical Fourier equation is obtained.

Summing up in this section the authors observe that an approach based on a self-similar clustering of micro-scale masses in a macroscopically homogeneous conductor yields, at the macro-scale, to a fractional-order generalization of the Fourier equation in terms of Caputo fractional derivatives. The order of the derivative is related to the topological features of the microscopic set of mass clustering as $\beta=\frac{2-d}{2}$.

The analysis has been obtained for an 1D case and it may be generalized, straightforwardly to more complete case, repeating the

analysis for an isotropic conductor in a three dimensional domain V of the Euclidean space R referred to a three dimensional coordinate system (O, x_1, x_2, x_3). In this case identical micro-structure is observed along any direction and, therefore, the fractional-order Fourier equation may be generalized in term of the spatial gradient of the temperature field, namely, $\nabla[\bullet] = \frac{\partial}{\partial x_k}[\bullet] i_k$ (i_k the unit vector of the coordinate system) as:

$$q(x,t) = -R_\beta I \cdot \left(\mathrm{D}^{\beta}_{0^+} \nabla T\right)(x,t) = -R_\beta \cdot \left(\mathrm{D}^{\beta}_{0^+} \nabla T\right)(x,t) \qquad (7.47)$$

where $IR_\beta = R_\beta$ is the isotropic second-order tensor of the anomalous conductivities.

7.3.3 Thermodynamical Consistency of the Fractional-Order Fourier Conduction

Thermodynamical assessment of eq.(7.46) must be formulated in terms of the irreversible entropy production rate $\dot{s}_u(x,t)$ for unit volume, must be satisfied for any thermodynamical process at the macro-scale $T(x,t)$. In this section the authors report some basic considerations that correspond to the thermodynamical consistency of the model with a bottom-up approach from the self-similar micro-scale considered. In this circumstances the Gibbs inequality yields $\dot{s}_u(x,t) \geq 0$ that must be fulfilled for any $t \geq 0$ and at any location of the conductor $x_j \in V$ and for any micro-scale location z_j.

To this aim, the second principle of thermodynamics, written for the observation scale z, reads:

$$\rho(z_j)\dot{s}(z_j,t) \geq -\frac{1}{\theta(z_j,t)} \frac{\partial q(z_j,t)}{\partial z_j} \qquad (7.48)$$

where $\dot{s}$ represents the entropy rate. Introducing the irreversible specific entropy rate $\dot{s}_u(z_j,t)$, relation (7.48) is rewritten as:

$$\rho\left(z_j\right)\dot{s}(z_j,t)+\frac{1}{\theta\left(z_j,t\right)}\frac{\partial q\left(z_j,t\right)}{\partial z_j}=\rho\left(z_j\right)\dot{s}_u(z_j,t)\geq 0 \qquad (7.49)$$

The entropy rate $\dot{s}\left(z_j,t\right)$ could be cast in terms of the balance among the incoming and outcoming entropy flux, namely $J\left(z_j,t\right)$, as:

$$\dot{s}(z_j,t)=-\frac{1}{\rho\left(z_j\right)}\frac{\partial J\left(z_j,t\right)}{\partial z_j}+\dot{s}_u(z_j,t) \qquad (7.50)$$

Introducing eq. (7.50) into eq. (7.49), the relevant inequality among the balance of the entropy flux and the the balance of the heat flux, at location z, is obtained in the form:

$$\frac{\partial J\left(z_j,t\right)}{\partial z_j}\geq\frac{1}{\theta\left(z_j\right)}\frac{\partial q\left(z_j,t\right)}{\partial z_j} \qquad (7.51)$$

In the context of classical irreversible thermodynamics it is assumed that the entropy flux is a function of a state variable $u(z_j,t)$ that corresponds to the specific internal energy of the conductor at location z as:

$$J\left(z_j,t\right)=\varphi\left(u\right)q\left(z_j,t\right) \qquad (7.52)$$

that, after substitution in eq.(7.51) (omitting arguments) it leads to:

$$\left[\varphi\left(u\right)-\frac{1}{\theta}\right]\frac{\partial q}{\partial z_j}+\frac{\partial\varphi}{\partial z_j}q\left(z_j,t\right)\geq 0 \qquad (7.53)$$

Since relation (7.53) must be fulfilled for any thermodynamic transformation, for the linear term $\varphi(u)$ equal to $\frac{1}{\theta}$, it is obtained:

$$\left(\frac{\partial\varphi(u)}{\partial z_j}\right)q=\frac{1}{\theta^2}\frac{\partial\theta}{\partial z_j}q\leq 0 \qquad (7.54)$$

Introducing the Fourier relation in (7.54) gives:

$$\dot{s}_u\left(z_j,t\right)=\frac{\chi_T}{\theta^2}\left(\frac{\partial\theta\left(z_j,t\right)}{\partial z_j}\right)^2\geq 0 \tag{7.55}$$

The relation (7.55) must be verified for any thermodynamical process, for any location along the conductor, at any micro-scale resolution and for any temperature field $\theta(z_j,t)$ yielding the thermodynamical restriction on the thermal conductivity $\chi_T\geq 0$ so that $R_\beta\geq 0$.

It may be shown that the fractional-order generalization of the Fourier transport equation, reported in eq. (7.47), involves a state function of the form:

$$\psi(x,t)=\int_{-\infty}^{t}\int_{-\infty}^{t}K\left(t-\tau_1,t-\tau_2\right)\frac{\partial\left[\nabla T\left(\tau_1,x\right)\right]}{\partial\tau_1}\frac{\partial\left[\nabla T\left(\tau_2,x\right)\right]}{\partial\tau_2}d\tau_1 d\tau_2 \tag{7.56}$$

where the kernel function $K(t-\tau_1,t-\tau_2)$ may be written in the form:

$$K(t-\tau_1,t-\tau_2)=\frac{1}{2}G(2t-\tau_1-\tau_2)=\frac{1}{2}\frac{K_\beta}{\Gamma\left(\beta\right)}\frac{1}{\left(2t-\tau_1-\tau_2\right)^\beta} \tag{7.57}$$

that, after a Frecht differentiation, it takes back the fractional-order Fourier equation reported in eq.(7.47). It may be observed that the expression for the free energy function in eq.(7.56) is obtained from the evaluation of the overall dissipation rate associated to the inhomogeneous conductor in fig. (7.1) (see e.g. [21] and [14] for details).

7.4 Numerical Experiments

In the present section the authors report some numerical experiments regarding the temperature field of anomalous conductors in presence of different boundary and initial conditions. In particular, in the next subsection the heat conduction problem in a one-dimensional (1D) slab with imposed initial temperature field and fixed temperature at the extremities, over time, is studied. The aim of the presented analysis is to show how the solution of the fractional heat conduction equation, i.e. the diffusion-wave equation, is influenced by the introduction of the

Caputo's fractional derivative in the heat flux constitutive relation by means of problems defined in simple spatial domain.
The solution of the heat equation is obtained using the method of separation of variables: an equivalent approach has already been proposed in bounded space domains by means of the finite sine transform and the Laplace transform techniques [1]. Moreover, the Green's function approach has been thoroughly studied for the Cauchy and the Signalling problem [28, 29, 30] .
In case of isotropic transport of the thermal energy across the conductor, the constitutive equation reported in eq. (7.47) becomes:

$$q(x,t) = R_\beta I \cdot \left(\mathrm{D}_{0^+}^{\beta} \nabla T \right)(x,t) \tag{7.58}$$

where I is the identity matrix and R_β is the "fractional" thermal conductivity with dimension $\left[R_\beta \right] = kg\, m K^{-1} s^{\beta-3}$. Introducing relation (7.58) in the energy balance equation, the three-dimensional (3D) fractional heat equation is obtained as:

$$\nabla^2 T(x,t) = \frac{1}{\gamma_\beta} \left({}_C\mathrm{D}_0^{1-\beta} T \right)(x,t) \tag{7.59}$$

Coefficients $\gamma_\beta = \dfrac{R_\beta}{\rho C^{(V)}}$, ρ and $C^{(V)}$ are the "fractional" thermal diffusivity, the density and the specific thermal capacity respectively, with physical dimensions reported below:

$$\left[\gamma_\beta \right] = m^2 s^{\beta-1} ; [\rho] = kg\, m^{-3} ; \quad \left[C^{(V)} \right] = m K^{-1} s^{-2} \tag{7.60}$$

The last part of this section is devoted to the solution of heat problem in cylindrical coordinates $\{O, r, \theta, z\}$; in such a case the 3D heat conduction equation (7.59) is rewritten as:

$$\frac{\partial^2 T}{\partial r^2} + \frac{1}{r}\frac{\partial T}{\partial r} + \frac{1}{r^2}\frac{\partial^2 T}{\partial \psi^2} + \frac{\partial^2 T}{\partial z^2} + = \frac{1}{\gamma_\beta} \left({}_C\mathrm{D}_0^{1-\beta} T \right)(t). \tag{7.61}$$

7.4.1 Transient Heat 1D Problem in Cartesian Coordinates

A transient boundary value problem of heat conduction for a 1D slab is considered; the initial parabolic distribution of temperature $T(x,0) = F(x)$ is shown in Fig. (7.4) : T_0 and T_M represent, the initial temperature at the ends ($x = 0$ and $x = L$) and at the center of the slab, respectively. Moreover, the faces at coordinates $x = 0$ and $x = L$ are kept, over time, at temperature T_0 and there is not heat flux at the boundary lateral surfaces.

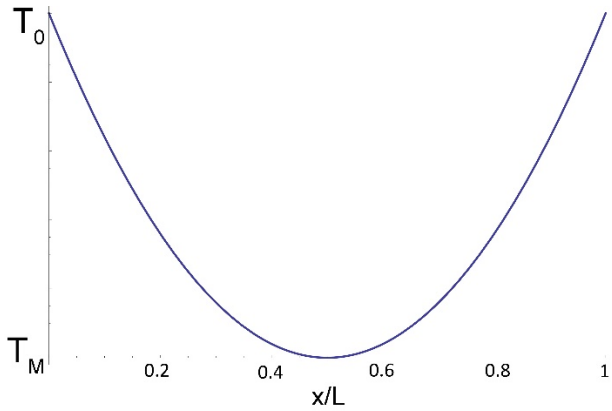

Figure 7.4 *Initial parabolic temperature distribution for problem Eq. (62a).*

The problem is to find the corresponding temperature field $T(x,t)$: its mathematical formulation is given as:

$$\frac{\partial^2 T}{\partial x^2} = \frac{1}{\gamma_\beta}\left({}_C\mathrm{D}_0^{1-\beta} T\right)(t) \quad \text{with} \quad 0 \le x < L,\, t > 0,\, 0 \le \beta < 1 \tag{7.62a}$$

$$\left|T\right|_{x=0} = T_0, \quad \forall t > 0 \tag{7.62b}$$

$$\left|T\right|_{x=L} = T_0, \quad \forall t > 0 \tag{7.62c}$$

$$\left|T\right|_{t=0} = F(x) = T_0 + 4(T_0 - T_M)\left[\left(\frac{x}{L}\right)^2 - \frac{x}{L}\right], \quad 0 < x < L \tag{7.62d}$$

The problem in Eq. (7.62a) with boundary conditions in Eqs. (7.62b) and (7.62c) and initial condition Eq. (7.62d) can be solved shifting the temperature scale, namely defining the relative temperature as below:

$$\Psi(x,t) = T(x,t) - T_0 \tag{7.63}$$

Considering Eq. (7.63), the problem in Eq. (7.49) could be reformulated as follows:

$$\frac{\partial^2 \Psi}{\partial x^2} = \frac{1}{\gamma_\beta}\left({}_C\mathrm{D}_0^{1-\beta}\Psi\right)(t) \quad \text{with} \quad 0 \le x < L,\, t > 0,\, 0 \le \beta < 1 \tag{7.64a}$$

$$\left|\Psi\right|_{x=0} = 0, \quad \forall t > 0 \tag{7.64b}$$

$$\left|\Psi\right|_{x=L} = 0, \quad \forall t > 0 \tag{7.64c}$$

$$\left|\Psi\right|_{t=0} = F(x) - T_0 = Q(x) = 4(T_0 - T_M)\left[\left(\frac{x}{L}\right)^2 - \frac{x}{L}\right], \quad 0 < x < L \tag{7.64d}$$

The solution is found using the method of separation of variables, namely separating $\Psi(x,t)$ into space-dependent and time-dependent functions as reported below:

$$\Psi(x,t) = \phi(t)\psi(x) \tag{7.65}$$

Substituting Eq. (7.65) into Eq. (7.64a) and introducing the separation constant λ, give:

$$\frac{1}{\psi}\frac{d^2\psi}{dx^2} = \frac{1}{\gamma_\beta \phi}\left({}_C\mathrm{D}_0^{1-\beta}\phi\right)(t) = -\lambda^2. \tag{7.66}$$

The relation Eq. (7.66) is equivalent to the two following differential equations:

$$\frac{d^2\psi(x)}{dx^2} + \lambda^2\psi(x) = 0 \tag{7.67a}$$

$$\left|\psi\right|_{x=0} = 0 \tag{7.67b}$$

$$\left|\psi\right|_{x=L} = 0 \tag{7.67c}$$

and

$$\left({}_C\mathrm{D}_0^{1-\beta}\phi\right)(t) + \lambda^2\gamma_\beta\phi = 0 \tag{7.68}$$

The general solution of Eq. (7.67a) is

$$\psi(x) = D_1\cos(\lambda x) + D_2\sin(\lambda x) \tag{6.69}$$

where boundary condition Eq. (7.67b) yields $D_1 = 0$, while boundary condition Eq. (7.67c) yields

$$\sin(\lambda L) = 0 \Rightarrow \lambda_n = \frac{n\pi}{L}, \text{with } n = 1, 2, 3, .. \tag{7.70}$$

The roots λ_n of relation Eq. (7.70) are the eigenvalues of the associated Sturm-Liouville problem [24]. As a consequence, the eigenfunctions of the problem are:

$$\psi_n(x) = D_2\sin(\lambda_n x) = D_2\sin\left(\frac{n\pi x}{L}\right) \tag{7.71}$$

After solving the problem corresponding to the space dimension, the solution for the time-dimensional problem, namely the fractional differential Eq. (7.68), is requested. Taking the Laplace transform of Eq. (7.68), using formula (7.31b), gives:

$$\hat{\phi}(s)s^{1-\beta} - \phi(0)s^{-\beta} + \lambda^2\gamma_\beta\hat{\phi}(s) = 0 \tag{7.72}$$

and then the solution in Laplace domain is:

$$\hat{\phi}(s) = \frac{\phi(0)s^{-\beta}}{s^{1-\beta} + \lambda^2\gamma_\beta} \tag{7.73}$$

the inverse Laplace transform of relation Eq. (7.73) is [39]:

$$\phi(t) = \phi(0)E_{1-\beta,1}\left[-\lambda^2\gamma_\beta t^{1-\beta}\right]U(t) \tag{7.74}$$

where $E_{\zeta,\eta}(z)$ is the Mittag Leffler function defined as [41]:

$$E_{\zeta,\eta}(z) = \sum_{n=0}^{\infty}\frac{(z)^n}{\Gamma(\zeta n+\eta)} \tag{7.75}$$

and $U(t)$ is the Heaviside unit-step function. The relations in Eq. (7.71) and (7.74) can be combined introducing the constant $D_n = D_2\phi(0)$ yielding, considering the relation (7.65), the general solution:

$$\Psi(x,t) = U(t)\sum_{n=1}^{\infty}D_n\sin(\lambda_n x)E_{1-\beta,1}\left[-\lambda_n^2\gamma_\beta t^{1-\beta}\right] \tag{7.76}$$

where the constant D_n is defined utilizing the initial condition (7.64d) and noting that $E_{\zeta,1}[0] = 1$ if $0 < \zeta < 1$, namely:

$$\Psi(x,0) = Q(x) = \sum_{n=1}^{\infty}D_n\sin(\lambda_n x) \tag{7.77}$$

The relation Eq. (7.77) is the Fourier series expansion of the function $Q(x)$ then, multiplying both sides of such relation by $\sin(\lambda_m x)$ and integrating over the interval $0 < x < L$ give:

$$\int_0^L Q(\xi)\sin(\lambda_m\xi)d\xi = \begin{cases} D_m\int_0^L\sin^2(\lambda_m\xi)d\xi = D_m\dfrac{L}{2} & \text{if } m = n \\ 0 \quad \text{if } m \neq n \end{cases} \tag{7.78}$$

where the property of orthogonality of the eigenfunctions $\sin(\lambda_m x)$ for arbitrary eigenvalues λ_m has been used. Summing up, Eq. (7.78) gives:

$$D_n = \frac{2}{L}\int_0^L Q(\xi)\sin(\lambda_n\xi)d\xi \tag{7.79}$$

and finally, using relations in Eq. (7.63) and (7.76), the temperature field is obtained as:

$$T(x,t) = T_0 + \sum_{n=1}^{\infty} D_n \sin(\lambda_n x) E_{1-\beta,1}\left[-\lambda_n^2 \gamma_\beta t^{1-\beta}\right] \tag{7.80}$$

The relation Eq. (7.80) can be converted into non-dimensional form by defining the non-dimensional independent variables, through the dimensional parameters of the thermal problem, as reported subsequently:

$$\underline{x} = \frac{x}{L} \tag{7.81a}$$

$$\underline{t}^{1-\beta} = \frac{\gamma_\beta t^{1-\beta}}{L^2} \tag{7.81b}$$

$$\underline{T} = \frac{T - T_0}{T_0 - T_M} \tag{7.81c}$$

$$\underline{\lambda_n} = n\pi \tag{7.81d}$$

Some examples of the non-dimensional temperature field are shown in Fig. (7.5). Compared to the time-solution $\exp\left[-\lambda_n^2 \gamma t\right]$ of the Fourier heat conduction equation $(\beta = 0)$, the solution $E_{1-\beta,1}\left[-\lambda_n^2 \gamma_\beta t^{1-\beta}\right]$ of the fractional equation $(0 < \beta < 1)$ exhibits for small times a much faster rising, and for large times, a much slower decay. In view of its slow decay, the fractional thermal conduction is usually referred to as a super-slow process. Accordingly, in Fig. (7.5) it is seen that the main feature characterizing the anomalous heat transfer is that the time-rate of change at which the resulting temperature field reaches a steady behavior gets higher as the discrepancy from the Fourier law increases. When it comes to considering how long does it take for the body to achieve thermal steadiness, the trend shown by anomalous conductors is to employ longer times than Fourier ones. Indeed, this is exactly the "long-tail memory effect", due to the power law thermal memory of such materials.

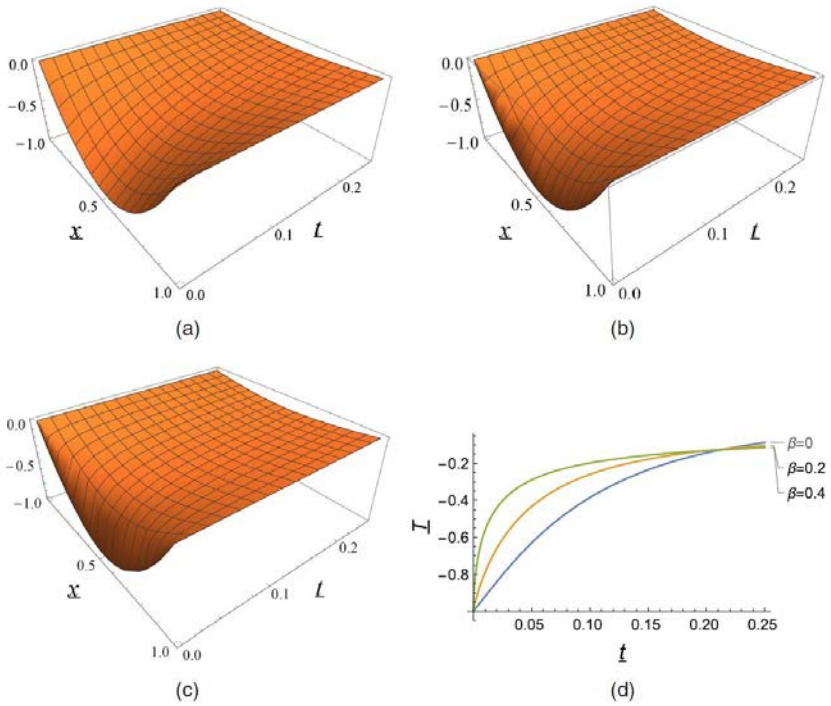

Figure 7.5 *Nondimensional temperature field* $(T - T_0)/(T_0 - T_M)$ *for different value of the exponent* β*: (a) Fourier solution* $\beta = 0$*; (b)* $\beta = 0.2$*; (c)* $\beta = 0.4$*; all the surfaces have been obtained with* $n = 10$*; (d) nondimensional temperature field at* $x = 0.5$

7.4.2 Transient Heat Problem in Cylindrical Coordinates

In this example a long solid cylinder of radius b, with initial temperature $F(r)$ is considered. For $t > 0$, the boundary surface at $r = b$ is insulated; in this case the temperature field depends only on the position along the radius r of the cylinder. The mathematical formulation of the problem is

$$\frac{\partial^2 T}{\partial r^2} + \frac{1}{r}\frac{\partial T}{\partial r} = \frac{1}{\gamma_\beta}\left({}_C\mathrm{D}_0^{1-\beta} T\right)(t) \quad \text{with} \quad 0 \le r < b, t > 0, 0 \le \beta < 1 \tag{7.82a}$$

$$\left|T\right|_{r=0} \text{ bounded}, \quad \forall t > 0 \tag{7.82b}$$

$$\left|\left({}_C\mathrm{D}_0^{\beta} \frac{\partial T}{\partial r}\right)(t)\right|_{r=b} = 0, \quad \forall t > 0 \tag{7.82c}$$

$$\left|T\right|_{t=0} = F(r), \quad 0 < r < b \tag{7.82c}$$

The solution of the problem in Eq. (7.82a) with boundary conditions Eqs. (7.82b) and (7.82c) and initial condition Eq. (7.82d) may be obtained using the method of separation of variables as in the previous example, namely by assuming a separation of $T(r,t)$ into space-dependent and time-dependent functions as

$$T(r,t) = \phi(t)\psi(r) \tag{7.83}$$

substituting Eq. (7.83) into Eq. (7.82a) and introducing the separation constant λ give:

$$\frac{1}{\psi}\left(\frac{d^2\psi}{dr^2} + \frac{1}{r}\frac{d\psi}{dr}\right) = \frac{1}{\gamma_\beta \phi}\left({}_C\mathrm{D}_0^{1-\beta}\phi\right)(t) = -\lambda^2 \tag{7.84}$$

The relation Eq. (7.84) is equivalent to the two following differential equations:

$$\frac{d^2\theta(r)}{dr^2} + \frac{1}{r}\frac{d\theta(r)}{dr} + \lambda^2\theta(r) = 0 \tag{7.85a}$$

$$\left|\theta\right|_{r=0} \quad \text{bounded} \tag{7.85b}$$

$$\left|\frac{d\theta}{dr}\right|_{r=b} = 0 \tag{7.85c}$$

and

$$\left({}_C\mathrm{D}_0^{1-\beta}\phi\right)(t) + \lambda^2\gamma_\beta\phi = 0 \tag{7.86}$$

The general solution of Eq. (7.85a) is:

$$\psi(r) = M_1 J_0(\lambda r) + M_2 I_0(\lambda r) \tag{7.87}$$

where J_m is the Bessel functions of the first kind of order m defined as:

$$J_m(z) = \left(\frac{z}{2}\right)^m \sum_{n=0}^{\infty} \frac{(-1)^n \left(\frac{z}{2}\right)^{2n}}{n!\Gamma(m+n+1)} \tag{7.88}$$

and I_0 the Bessel function of the second kind of order zero. Boundary condition (7.85b) yields $M_2 = 0$, while boundary condition (7.85c) produces eigenvalues from the corresponding transcendental equation:

$$-M_1 \lambda J_1(\lambda b) = 0 \Rightarrow \lambda_n \quad \text{with} \quad n = 0,1,2,.. \tag{6.89}$$

with $\lambda_0 = 0$. The roots λ_n of relation Eq. (7.89) are the eigenvalues of the associated Sturm-Liouville problem [24]. The eigenfunctions of the problem are, consequently

$$\psi_n(r) = M_1 J_0(\lambda_n r). \tag{7.90}$$

The solution for the time-dimensional problem, namely the fractional differential Eq. (7.86), is given by the relation Eq. (7.74). The relations (7.90) and (7.74) can be combined introducing the constant $M_n = M_1 \phi(0)$ yielding, and taking into account relation (7.83), this leads to:

$$T(r,t) = U(t) \sum_{n=0}^{\infty} M_n J_0(\lambda_n r) E_{1-\beta,1}\left[-\lambda_n^2 \gamma_\beta t^{1-\beta}\right] \tag{6.91}$$

the constant M_n is defined utilizing the initial condition Eq. (7.82d) and noting that $E_{\zeta,1}[0] = 1$ if $0 < \zeta < 1$, namely

$$T(r,0) = F(r) = \sum_{n=0}^{\infty} M_n J_0(\lambda_n r) \tag{7.92}$$

Relation Eq. (7.92) is the Fourier series expansion of the function $F(r)$ then, multiplying both sides of such relation by $J_0(\lambda_m r)$ and integrating over the interval $0 < r < b$ give:

$$\int_0^b F(\xi) J_0(\lambda_m \xi) \xi d\xi = \begin{cases} M_m \int_0^b J_0^2(\lambda_m \xi) \xi d\xi & \text{if } m = n \\ 0 & \text{if } m \neq n \end{cases} \tag{7.93}$$

where the property of orthogonality of the eigenfunctions $J_0(\lambda_m r)$ for arbitrary eigenvalues λ_m has been used. Summing up, Eq. (7.93) gives:

$$M_n = \frac{\int_0^b F(\xi) J_0(\lambda_n \xi) \xi d\xi}{\int_0^b J_0^2(\lambda_n \xi) \xi d\xi} \tag{7.94}$$

and finally, inserting relation (7.94) into Eq. (7.91) the temperature field is obtained as:

$$T(r,t) = \sum_{n=0}^{\infty} M_n J_0(\lambda_n r) E_{1-\beta,1}\left[-\lambda_n^2 \gamma_\beta t^{1-\beta}\right] \tag{7.95}$$

The non-dimensional temperature field at $t = 0$ is a linear distribution as:

$$\underline{F}(\underline{r}) = 20\underline{r} + 1 \tag{7.96}$$

As in the previous numerical example, in Fig. (7.6) it is shown the non-dimensional temperature field $\frac{T(r,t)}{F(0)}$ as a function of non-dimensional time $\underline{t}$ [Eq. (7.81b)] and non-dimensional radius $\underline{r} = \frac{r}{b}$, for different value of the exponent β. Like in the case of the uniaxial thermal rigid conductor of Fig. (7.5), the discrepancy from Fourier's law manifests itself with higher time-rates and slower time-transients.

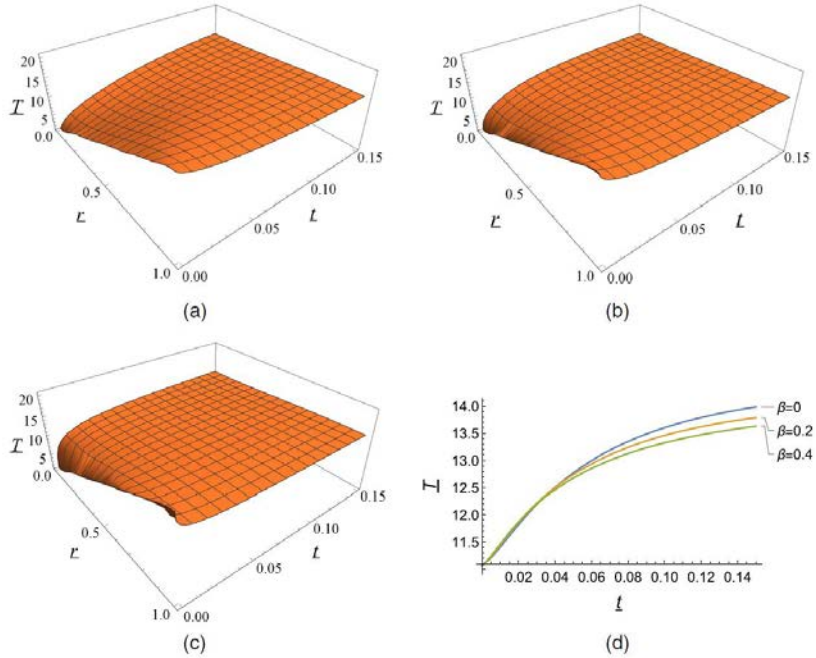

Figure 7.6 *Nondimensional temperature field T(r; t)=F(0) for different value of the exponent β: (a) Fourier solution β = 0; (b) β = 0.2; (c) β = 0.4; all the surfaces have been obtained with n = 10; (d) nondimensional temperature field at r = 0.5*

7.5 Conclusions

In this paper the authors showed that the analysis of the temperature field in an inhomogeneous rigid conductor with power-law grading of the thermodynamical parameters yields a power-law time rising of the temperature at the insulated boundary of the conductor. The order of the power-law is related to the grading exponent of the physical properties of the conductor and the use of Boltzmann superposition principle for generic histories of the incoming heat flux yields a temperature-flux relation involving fractional-order operators. The main idea that a power-law rising appears as a non-homogeneous, non-stationary flux is established in the conductor has been further expanded in the paper to yield a fractional-order generalization of the Fourier transport equation. Indeed, under the assumption of a non-homogeneous, self-similar distribution of mass micro-structure in any generic volume element of the conductor, a non-stationary flux at micro-structure level is experienced. In this setting, the assumption of a fractal mass clustering at micro-structural level with an Hausdorff dimension d yields the same kind of thermal flux, at micro-structural level, as those experienced with the non-homogeneous macroscopic

conductor. As a consequence, the resulting macroscopic relation provides the heat flux by means of the fractional-order, Caputo' type, derivative of spatial gradient of the temperature field with derivation order related to the fractal dimension of the self-similar assembly as $\beta = \frac{2-d}{2}$. The thermodynamic assessment of the introduced fractional-order generalization of the Fourier equation has been exploited with the same micro-structure arguments and more details are reported in a forthcoming paper. The numerical examples provided show the influence of anomalous conductivity and differentiation order for temperature fields in simple 1D and 2D domains. Indeed the obtained non-dimensional temperature fields have been compared to the time-solution of the Fourier heat conduction equation $(\beta = 0)$. Results show that the solution of the fractional heat equation ($0 < \beta < 1$), governed by Mittag-Leffler functions, exhibits for small times a much faster rising, and for large times, a much slower decay. Accordingly, the main property of the anomalous heat transfer is that the time-rate of change at which the resulting temperature field reaches a steady state, becomes higher as the discrepancy from the Fourier law increases: the thermal steadiness is consequently achieved, by anomalous conductors, employing longer times than Fourier ones. Such particular behavior represents the "long-tail memory effect", due to the power law thermal memory of such materials. The proposed fractional-order generalization of the Fourier heat transport equation is used in the companion paper to formulate the fractional-order linear thermoelastic problem.

References

[1] Agrawal, O. P. (2002). "Solution for a fractional diffusion-wave equation defined in a bounded domain." Nonlinear Dyn., 29(1), 145–155.

[2] Alaimo, G., and Zingales, M. (2015). "Laminar flow through fractal porous materials: The fractional-order transport equation." Commun. Nonlinear Sci. Numer. Simul., 22(1–3), 889–902.

[3] Alotta, G., Failla, G., and Pinnola, F. P. (2017). "Stochastic analysis of a non-local fractional viscoelastic bar forced by Gaussian white noise." ASCE-ASME J. Risk Uncertainty Eng. Syst. Part B, 3(3), 030904.

[4] Bongiorno, D. (2009). "On the problem of regularity in the Sobolev space $W^{1;n}{}_{loc.}$" Topol. Appl., 156(18), 2986–2995.

[5] Bongiorno, D. (2014). “Metric differentiability of Lipschitz maps.” J. Aust. Math. Soc., 96(1), 25–35.
[6] Bongiorno, D., and Corrao, G. (2015). “On the fundamental theorem of calculus for fractal sets.” Fractals, 23(2), 1550008.
[7] Caputo, M. (1999). “Diffusion of fluids in porous media with memory.” Geothermics, 28(1), 113–130.
[8] Cattaneo, C. (1948). “Sulla conduzione del calore.” Atti del Seminario di Mat. Fis. Universitá di Modena, Modena, Italy (in Italian).
[9] Challamel, N., Zorica, D., Atanackovi´c, T. M., and Spasi´c, D. T. (2013). “On the fractional generalization of Eringen’s nonlocal elasticity for wave propagation.” Comptes Rendus Mécanique, 341(3), 298–303.
[10] Compte, A., and Metzler, R. (1997). “The generalized Cattaneo equation for the description of anomalous transport process.” J. Phys. A, 30(21), 7277–7289.
[11] Cottone, G., Di Paola, M., and Santoro, R. (2010). “A novel exact representation of stationary colored Gaussian processes (fractional differential approach).” J. Phys. A, 43(8), 085002.
[12] Cottone, G., Di Paola, M., and Zingales, M. (2009). “Elastic waves propagation in 1d fractional non-local continuum.” Physica E, 42(2), 95–103.
[13] Craiem, D., and Armentano, R. (2013). “A fractional derivative model to describe arterial viscoelasticity.” Biorheology, 44(4), 251–263.
[14] Deseri, L., Di Paola, M., Zingales, M., and Pollaci, L. (2013). “Power-law hereditariness of hierarchical fractal bones.” Int. J. Numer. Methods Biomed. Eng., 29(12), 1338–1360.
[15] Deseri, L., and Zingales, M. (2015). “A mechanical picture of fractionalorder Darcy equation.” Commun. Nonlinear Sci. Numer. Simul., 20(3), 940–949.
[16] Di Lorenzo, S., Di Paola, M., Pinnola, F. P., and Pirrotta, A. (2014). “Stochastic response of fractionally damped beams.” Probab. Eng. Mech., 35, 37–43.
[17] Di Matteo, A., Kougioumtzoglou, I. A., Pirrotta, A., Spanos, P. D., and Di Paola, M. (2014). “Stochastic response determination of nonlinear oscillators with fractional derivatives elements via the wiener path integral.” Probab. Eng. Mech., 38, 127–135.
[18] Di Paola, M., Failla, G., and Pirrotta, A. (2012). “Stationary and nonstationary stochastic response of linear fractional viscoelastic systems.” Probab. Eng. Mech., 28, 85–90.
[19] Di Paola, M., Pinnola, F. P., and Zingales, M. (2013). “Fractional differential equations and related exact mechanical models.” Comput. Math. Appl., 66(5), 608–620.

[20] Di Paola, M., and Zingales, M. (2008). “Long-range cohesive interactions of non-local continuum faced by fractional calculus.” Int. J. Solids Struct., 45(21), 5642–5659.
[21] Di Paola, M., and Zingales, M. (2011). “Fractional differential calculus for 3d mechanically-based non-local elasticity.” Int. J. Multiscale Comput. Eng., 9(5), 579–597.
[22] Di Paola, M., and Zingales, M. (2012). “Exact mechanical models of fractional hereditary materials.” J. Rheol., 56(5), 983–1004.
[23] Fourier, J. B. (1882). Theorie Analitiqué de le Chaleur, Dover Publications, Paris.
[24] Hahn, D. W., and Özişik, M. N. (2012). Heat conduction, Wiley, Hoboken, NJ.
[25] Hanyga, A. (2002). “Multidimensional solutions of time-fractional diffusion wave equations.” Proc., Royal Society of London A: Mathematical, Physical and Engineering Sciences, Vol. 458, Royal Society, London, 933–957.
[26] Hilfer, R., and Anton, L. (1995). “Fractional master equations and fractal time random walks.” Phys. Rev. E, 51(2), R848.
[27] Lazopoulos, K. (2006). “Non-local continuum mechanics and fractional calculus.” Mech. Res. Commun., 33(6), 753–757.
[28] Mainardi, F. (1996a). “Fractional relaxation-oscillation and fractional diffusion-wave phenomena.” Chaos Solitons Fractals, 7(9), 1461–1477.
[29] Mainardi, F. (1996b). “The fundamental solutions for the fractional diffusion-wave equation.” Appl. Math. Lett., 9(6), 23–28.
[30] Mainardi, F. (2010). Fractional calculus and waves in linear viscoelasticity: An introduction to mathematical models, World Scientific, Singapore.
[31] Mainardi, F., Luchko, Y., and Pagnini, G. (2001). “The fundamental solution of the space-time fractional diffusion equation.” Frac. Calc. Appl. Anal., 4(2), 153–192.
[32] Meerschaert, M. M., and Tadjeran, C. (2006). “Finite difference approximations for two-sided space-fractional partial differential equations.” Appl. Numer. Math., 56(1), 80–90.
[33] Metzler, R. (2000). “Generalized Chapman-Kolmogorov equation: An unified approach to the description of anomalous transport in external fluids.” Phys. Rev. E, 62(5), 6233–6245.
[34] Metzler, R., and Klafter, J. (2000). “The random walk’s guide to anomalous diffusion: A fractional dynamics approach.” Phys. Rep., 339(1), 1–77.
[35] Metzler, R., and Nonnematcher, T. F. (1998). “Fractional diffusion, waiting time distribution and Cattaneo-type equation.” Phys. Rev. E, 57(6), 6409–6414.

[36] Mongioví, M., and Zingales, M. (2013). "A non-local model of thermal energy transport: The fractional temperature equation." Int. J. Heat Mass Transfer, 67, 593–601.
[37] Norwood, F. (1972). "Transient thermal waves in the general theory of heat conduction with finite wave ced." J. Appl. Mech., 39(3), 673–676.
[38] Piccolo, V., et al. (2017). "Fractional-order theory of thermo-elasticity. II: Quasi-static behavior of bars." J. Eng. Mech., 10.1061/(ASCE)EM .1943-7889.0001395, 04017165.
[39] Podlubny, I. (1998). Fractional differential equations, Accademic Press, New York.
[40] Povstenko, Y. Z. (2009). "Theory of thermoelasticity based on space-time fractional heat conduction equation." Phys. Scr., 2009(T136), 014017.
[41] Samko, S., Kilbas, A., and Marichev, O. (1989). Fractional integrals and derivatives, Gordon Breach, Amsterdam, Netherlands.
[42] Sayed, A. E. (1996). "Fractional-order diffusion wave equation." Int. J. Theory Phys., 35(2), 311–322.
[43] Schiessel, H., Metzler, R., Blumen, A., and Nonnenmacher, T. (1995). "Generalized viscoelastic models: Their fractional equations with solutions." J. Phys. A, 28(23), 6567–6584.
[44] Tarasov, V. E., and Aifantis, E. C. (2014). "Toward fractional gradient elasticity." J. Mech. Behav. Mater., 23(1–2), 41–46.
[45] Tarasov, V. E., and Zaslavsky, G. M. (2008). "Conservation laws and Hamiltonian's equations for systems with long-range interaction and memory." Commun. Nonlinear Sci. Numer. Simil., 13(9), 1860–1878.
[46] Zaslavsky, G. (2002). "Chaos, fractional kinetics, and anomalous transport." Phys. Rev., 371(6), 461–580.
[47] Zingales, M. (2014). "A fractional-order non-local thermal energy transport in rigid conductors." Commun. Nonlinear Sci. Numer. Simul., 19(11), 3938–3953.
[48] Zingales, M. (2016). "An exact thermodynamical model of power-law temperature time scaling." Ann. Phys., 365, 24–37.
[49] Zingales, M., and Failla, G. (2015). "The finite element method for fractional non-local thermal energy transfer in non-homogeneous rigid conductors." Commun. Nonlinear. Sci. Numer. Simul., 29(1), 116–127.

8. Fractional-Order Theory of Thermoelasticicty. II: Quasi-Static Behavior of Bars

By V. Piccolo, G. Alaimo, A. Chiappini, M. Ferrari, D. Zonta, M. Zingales and L. Deseri

Abstract

This work aims to shed light to the "thermally-anomalous" coupled behavior of slightly deformable bodies, in which the strain is additively decomposed in an elastic contribution and in a thermal part. The macroscopic heat flux turns out to depend upon the time history of the corresponding temperature gradient, and this is the result of a multi-scale rheological model developed in Part 1 of the present study, thereby resembling a long-tail memory behavior governed by a Caputo's fractional operator. The macroscopic constitutive equation between the heat flux and the time history of the temperature gradient does involve a power law kernel, resulting in the "anomaly" mentioned above. The interplay between such thermal flux and the elastic and thermal deformability are investigated for a pinned-pinned truss. This allows for focusing on the effects of the deviation from the Fourier's law on the thermoelastic coupling. Indeed, the interactions in the presented system are fully coupled as the temperature and the displacement field mutually influence one another.

8.1 Introduction

In [1] the authors raised the most natural question about the physical grounds on which the fractional-order behavior arises in various contexts (see e.g. [5, 24] etc.). In particular, it was studied the case of rigid thermal conductors characterized by anomalous heat transfer, in which the relationship between the macroscopic heat flux and the corresponding temperature gradient inherits a power law memory in time. This has been explained in [1] through a hierarchy of Fourierian rigid heat conductors across infinite observation scales, thereby resembling a fractal material. Essentially, this is equivalent to having a distribution of masses characterized by a functionally graded hierarchy of thermal conductivities and heat capacity scaling with a certain power. The latter can be related to the porosity of hierarchical media, where the thermal transport encounters obstacles (such as voids and a rigid solid matrix) that can heavily influence the overall heat diffusion. This is consistent with the findings in [23], where anomalous time scaling of the thermal energy has been explained through a statistical approach,

thereby characterizing the evolution of its non-equilibrium excess in a one dimensional conductor. There the transient behavior of the heat flux has been found to be originated by small initial excess perturbations of the thermal energy away from equilibrium, thereby leading to an anomalous diffusion scaling in time like t^{β}, being β a real number. Anomalous heat transfer is essentially an averaged, hence macroscopic, transient phenomenon affected by the scaling discussed above. Anomalous behavior has been detected in certain materials [25] although often times such materials are treated as if both their thermal conductivity and specific heat behave non-linearly with the temperature [27].

Other works have been explaining anomalous heat transfer in rigid bodies with "billiard-like" models, quantum mechanics (see e.g. [22]), etc. It is worth noting that what is found about a connection between such methods and the hierarchical structure of the media exhibiting anomalous behavior, does not bring into play the scalings of the thermal conductivities and heat capacities at the various observation scales.

The most natural generalization of the findings in [1] is to allow for a coupled linear thermo-elastic behavior of the material under external actions. This is surely an approximate way to account for the deformability of bodies whose macroscopic thermal behavior is not Fourierian. The justification for this approach resides on the modeling of what happens at each observation scale. As a first approximation, the chain of rheological systems employed in [1] can be thought to be generalized as if associated elastic stiffness present at each observation scale would generate internal forces entering the energy balance (see e.g. eqn. (3) in [1]). If, unlike the thermal conductivities and heat capacities, such stiffnesses would not change with such scales, the overall macroscopic equations would boil down to linear thermo-elasticity with thermal memory. In physical terms this may happen whenever the time scales of thermal and mechanical exchanges significantly differ at the various observation scales. In a hierarchical porous material this can be envisioned if stress re-distributions are much slower than the effects causing the impact between thermally excited particles and generating the anomalous spread of thermal energy in the solid matrix, as found in [23]. Small deformabilities of hierarchical solids undergoing heat exchanges are then based on a multi-scale ground. This is missing in all of the known approaches present in the literature.

Nonetheless, in [29, 30] recent phenomenological fractional-order theories for three dimensional thermo-elasticity with no such multi-scale origins were formulated and applied. Although in the present treatment the authors will focus on the space-time evolution of the system by neglecting inertia, a useful and comprehensive review about

propagating waves with finite speed in thermoelastic media can be found in [20]. Here, upon removing the paradox of thermal waves propagating with infinite speed in Fourier type deformable conductors, the main focus is about the dynamics of spatially anomalous thermal response of fractal materials. To the best of authors' knowledge, a multi-scale rheological explanation analog to the one given in [1] is not yet available for such a case.

While the anomalous thermal behavior in time has been extensively studied from the phenomenological and mathematical viewpoint starting from the late 1960s and continuing to today (see e.g. [10, 26, 2, 3, 16]), anomalous thermoelastic coupling in engineering applications still requires thorough investigations. To this end, for the sake of illustration, a one dimensional anomalous thermoelastic truss subject to thermal loading and pinned at both ends is examined in the sequel. The full analytical solution of the problem is provided obtaining the resulting displacement, temperature, and internal axial force. The anomalous thermal behavior of such slightly deformable system is then investigated, thereby exploring not only the transient behavior due to its deviation from the Fourier law, but also by studying a resulting overall measure of energy rate. The obtained quantity corresponds to the "thermal work" introduced in [26] and studied later in several papers (see e.g.[2, 3, 16]), for the first time for rigid conductors with memory. A more extensive study of a theory for trusses and beams would have to entail a Saint Venant-type of argument, analog to the one developed in [12] for small strain viscoelasticity. Future developments of the proposed approach accounting for material hierarchies within three dimensional geometries in the presence of coupled multi-physics phenomena (such as in [24, 21], and ref.s cited therein), are envisioned in a combination between the current approach and the methodologies developed in [13, 14, 15], [19, 18], [4] and [31].

8.2 Thermoelastic Trusses and Anomalous Bahavior

Anomalous heat conduction and its impact on evolutionary thermoelastic processes arising in one dimensional deformable solids are studied in this section. Wherever it will be not needed, the dependence on x and t in all the fields involved in the treatment will be omitted.

The constitutive equations governing the problem relate to the internal axial force (N)-strain (ε) response and to the heat flux (q) and temperature gradient ($T_{,x}$) behavior. The former entails the usual coupling between the axial internal force N arising at each cross section of the solid at the current time and the elastic strain, namely

$$N = EA(\varepsilon - \alpha(T - T_0)), \tag{8.1}$$

where E is the Young modulus of the material, A is the area of the cross section of the bar, α is the linear thermal expansion coefficient of the solid, T_0 is a reference temperature and T is the current value of the temperature field. The latter constitutive equation for the heat flux has been obtained in [1], i.e.:

$$q = -K_\beta \left({}_C D^\beta_{0^+} \right) T_{,x}. \tag{8.2}$$

In eq. (8.2) it is involved the time-fractional Caputo's derivative of order $\beta \in [0,1]$ defined as:

$$\left({}_C D^\beta_{0^+} \right) f = \frac{1}{\Gamma(1-\beta)} \int_0^t \frac{f'(\tau)}{(t-\tau)^\beta} d\tau \tag{8.3}$$

where $\Gamma(z)$ is the Euler-Gamma function that may be considered as the generalization of the factorial function because, when z assumes integer values, it yields that $\Gamma(z+1) = z!$.

A general framework for the definition of fractional-order integrals in Sobolev metric space has been provided in recent mathematical literature [6, 7]. The use of fractional-order calculus to handle functions defined on fractal subsets has been reported in terms of the fundamental theorem of integral calculus involving a corrective series beside values of the primitives at the borders of the integrals [8].

The fractional operator in eq. (8.3) is the result of the multi-scale rheological model developed in Part 1 of the present study, thereby accounting for a "long-tail" memory behavior.

In eq. (8.3) it is considered the definition of the Caputo's left fractional derivative (following [28]), for which the integral lower terminal 0 is kept fixed, and the upper terminal t is varied, with $0 < t$. However, it is also possible to consider Caputo's right fractional derivatives with moving lower terminal t and fixed upper terminal 0.

From a physical point of view, if the function $f(t)$ represents the present state of a time-evolving dynamical process started at the instant $t = 0$, then the left derivative is an operator performed on the "past" states $f(\tau)$ of the process being $\tau < t$, while the right derivative relies

on its "future" states $f(\tau)$ being $\tau > t$. Given such considerations, causality principle is satisfied by left derivative definition.

In this section the authors are interested in analyzing the impact of the anomalous heat transfer and of the deformability in the quasi-static thermo-mechanics evolution of the system. This is characterized by the main unknown fields u and T, namely the axial displacement of cross sections of the truss and the temperature, respectively.

Standard compatibility between strain and displacement reads as follows

$$\varepsilon = u_{,x}, \tag{8.4}$$

and it will be accounted for in the sequel. In the absence of accelerations, balance of linear momentum implies:

$$N_{,x} + \rho p = 0 \tag{8.5}$$

where ρ is the density of the material per unit length and p is the (distributed) axial external load. Balance of energy must further be imposed, namely:

$$q_{,x} = Q - (\rho c_v T_{,t} + T_0 \alpha E A \varepsilon_{,t}), \tag{8.6}$$

where Q is the heat flux source term, c_v is the thermal capacity of the material at constant volume. The whole term included in the brackets on the right hand side of such equation represents a specific enthalpy per unit length of the system. Relation (8.6) has been obtained in the paper by [30]. In that work, the authors start from the first law of thermodynamics (eq. 7.6) and from the balance equation of entropy density (eq. 7.7) subsequently linearized (eq. 7.27). The authors combine them and, after some manipulations, they obtain eq. 7.28 that is equivalent to eq. (8.6).

Thermo-mechanical coupling arises only through (8.1), namely the constitutive equation for N, and through (8.2), the balance of energy rate. Indeed, the employed constitutive equation for the anomalous heat conduction (8.2) does not involve any contribution coming from the mechanics. Substitution of (8.4) into (8.1) and then in (8.5) yields

$$EA(u_{,xx} - \alpha T_{,x}) + \rho p = 0, \tag{8.7}$$

while (8.2) into (8.6) delivers

$$K_\beta \left({}_C D_{0^+}^{\beta} \right) T_{,xx} - \rho c_v T_{,t} - \alpha EAT_0 u_{,tx} + Q = 0. \tag{8.8}$$

The obtained coupled system of nonstandard linear Partial Differential Equations (PDE) will be studied in the sequel for the case in which no sources terms ρp and Q are present.

In order to illustrate the outcomes of the anomalous thermo-elasticity, the same initial temperature profile assumed in [1] is considered, namely:

$$T(x,0) = T_0 + 4(T_0 - T_m)\frac{x}{L}\left(\frac{x}{L} - 1\right). \tag{8.9}$$

The corresponding displacement $u(x,0)$ is then reconstructed through the balance of linear momentum (8.7). Indeed, if $p = 0$, upon integrating (8.7) twice with respect to x, the initial displacement profile takes the following form:

$$u(x,0) = C_0 + C_1 x + 4\alpha \frac{T_0 - T_m}{L}\left(\frac{x^3}{3L} - \frac{x^2}{2}\right), \tag{8.10}$$

where C_0 and C_1 are arbitrary constants.

It is not difficult to show that one way to solve the problem is to eliminate one of the two fields, thereby obtaining a higher order on the remaining function equation. To this end, T will be eliminated and a resulting governing equation for u will be found.

On obviously integrating (8.7) with respect to x, the axial internal force N turns out to depend on t alone. Hence $N = \hat{N}(t)$ takes the following expression

$$\hat{N}(t) = EA\left(u_{,x}(x,t) - \alpha\left(T(x,t) - T_0\right)\right) \tag{8.11}$$

thereby implying that there will be cancellation on the x-dependence of $u_{,x}$ and T. For the sake of illustration, the following boundary conditions will be assumed for the temperature:

$$T(0,t) = T(L,t) = T_0 \tag{8.12}$$

which are the same as in [1], eq.s (49b,c).
Various sets of boundary conditions can be explored. Here the pinned-pinned case and the pinned-free case will be considered.

Pinned-pinned case. This case arises when both ends are fixed in time, namely when

$$u(0,t) = u(L,t) = 0. \tag{8.13}$$

Obviously this is a (quasi) statically undetermined problem, i.e. the time evolving internal normal force is not known a-priori and it must be determined through the full solution of the governing equations. The corresponding values of the constants appearing in (8.10) are the following:

$$C_0 = 0 \quad \text{and} \quad C_1 = \frac{2}{3}\frac{T_0 - T_m}{EA}L \tag{8.14}$$

Pinned-free. In this case one end of the bar is set free. This is a (quasi) static determinate problem and, if no external force is applied, then there is no normal force arising in any of the cross sections of the bar. The evolution of the "stress-free" movements and heat flux of the system can be determined by imposing $N = 0$ and either of one of the two conditions (8.13), e.g.

$$u(0,t) = 0, \quad \text{and} \quad \hat{N}(t) = 0. \tag{8.15}$$

Hence, by (8.10) and substituting (8.9) into (8.11) and imposing (8.15) give:

$$C_0 = 0 \qquad C_1 = 0 \tag{8.16}$$

By substituting the results in the balance of energy rate (8.6), it is found that the following PDE must be verified:

$$K_\beta \frac{1}{\alpha}\left({}_C D^\beta_{0^+}\right) u_{,xxx} - \left(\frac{\rho c_v}{\alpha} + \alpha E A T_0\right) u_{,tx} = \rho c_v N_{,t}(t). \tag{8.17}$$

For the pinned-free case it is obtained that the right-hand side is zero and (8.17) already represents the governing field equation for the displacement. Further differentiation of the latter relationship with respect to x allows for finding the governing PDE for the displacement in general, including the case of (quasi) static undetermined bar. This is the equation that will be studied in the sequel.
For this purpose, the auxiliary function v, defined as follows, is introduced:

$$v := u_{,xx} \tag{8.18}$$

and hence the corresponding resulting field equation becomes:

$$\left({}_C D^\beta_{0^+}\right) v_{,xx} - \delta v_{,t} = 0, \tag{8.19}$$

after setting

$$\delta^{-1} = \frac{\gamma_\beta}{1 + \dfrac{\alpha^2 E A T_0}{\rho c_v}}. \tag{8.20}$$

where $\gamma_\beta := \dfrac{K_\beta}{\rho c_v}$ has been introduced in [1] Sect.4.1.
The behavior of rigid thermal conductors can be retrieved by simultaneously letting α (the linear dilation factor) and EA (the axial rigidity) to tend to zero and to infinity respectively, and by requiring that $\lim_{EA\to\infty}^{\alpha\to 0} \alpha^2 EA = 0$.
Relation (8.19) is formally analogous to the governing equation of the anomalous heat conduction obtained in [1] eqn. (7.49a), namely

$$\left({}_C D^\beta_{0^+}\right) T_{,xx} - \delta T_{,t} = 0. \tag{8.21}$$

Nevertheless the solution for such PDE obtained there is not suitable for the case under investigation, as neither the boundary conditions nor the initial ones (7.49b,c,d) are directly applicable to the function $v = u_{,xx}$. Nonetheless, the technique used to solve the above mentioned problem is obviously applicable in this case. This is based on space-time eigenmodes series expansions for both T and u in the separated variables form for solving the original coupled system (8.7), (8.8), namely:

$$T(x,t) = T_0 + \sum_{m=1}^{+\infty} f_m(t) g_m(x) \tag{8.22}$$

$$u(x,t) = \sum_{m=1}^{+\infty} v_m(t) w_m(x). \tag{8.23}$$

Henceforth, an ansatz for v in agreement with (8.22) and (8.23) is assumed as follows

$$v(x,t) = \sum_{m=1}^{+\infty} v_m(t) z_m(x), \tag{8.24}$$

where $z_m(x) := w_m''(x)$, where $''$ indicates double differentiation with respect to x. Substituting such expression in (8.19) and imposing its validity term-by-term, does lead to the following set of two ordinary differential equations:

$$\frac{1}{\delta}\frac{z_m''(x)}{z_m(x)} = \frac{\dot{v}_m(t)}{\left({}_C D_{0^+}^{\beta}\right) v_m(t)} = -K_m^{-2}, \tag{8.25}$$

where $\dot{}$ denotes differentiation with respec to time, and K_m^2 is arbitrary, to be determined by solving the associated eigenvalue problem. To this end, eq.(8.25) leads to the following expression for z_m :

$$z_m(x) = a_m \cos(\omega_m x) + b_m \sin(\omega_m x), \tag{8.26}$$

where

$$\omega_m^2 := \delta K_m^{-2} \tag{8.27}$$

and hence, because $w_m^{''} = z_m$, the following expression for the spatial m-mode of u is obtained:

$$w_m(x) = c_m \cos(\omega_m x) + d_m \sin(\omega_m x) + h_m x + l_m. \tag{8.28}$$

It is worth noting that this function carries the dimension of length, hence v_m is dimensionless. The second equation in (8.25), namely

$$\left({}_C D_{0^+}^{\beta}\right) v_m(t) + K_m^2 \dot{v}_m(t) = 0, \tag{8.29}$$

represents the associated fractional-order homogeneous initial value problem for v_m. Of course ω_m appearing in (8.26), (8.27) and (8.28) can be determined through the boundary conditions on the displacement and, hence, K_m will follow according to relation (8.26).

Although eqn. (8.29) is nonstandard, it can be solved as in the case of anomalous heat transfer in rigid conductors, treated in [1]. There such equation has been recast in the following form:

$$\left({}_C D_{0^+}^{1-\beta}\right) v_m(t) + K_m^{-2} v_m(t) = 0. \tag{8.30}$$

Its solution has been shown to be represented as follows:

$$v_m(t) = E_{1-\beta,1}\left(-K_m^{-2} t^{1-\beta}\right), \tag{8.31}$$

where $E_{1-\beta,1}$ is the Mittag-Leffler function of order $(1-\beta,1)$. Without loss of generality the time amplitude in (8.31) is set equal to 1, as the coefficient modulating each mode will be computed through a Fourier expansion technique starting from the initial data (8.10).
A sufficient condition for (8.11) is that such relation is verified term-by-term, namely:

$$EA(w_m^{'}(x)v_m(t) - \alpha g_m(x) f_m(t)) = \hat{N}_m(t), \tag{8.32}$$

where $\hat{N}_m(t)$ represents the contribution of the m^{th}-mode of the axial force. Upon differentiating the last relation with respect to x it is found that:

$$w_m^{''}(x)v_m(t) - \alpha g_m^{'}(x) f_m(t) = 0, \tag{8.33}$$

and hence the following two equations are obtained

$$\frac{w_m^{''}(x)}{\alpha g_m^{'}(x)} = \frac{f_m(t)}{v_m(t)} = \lambda_m, \tag{8.34}$$

where λ_m are real constants. It is worth nothing that such relations do force the spatial modes for the strain gradient $u_{,xx}$ and for the temperature gradient $T_{,x}$ to be the same.

Because of (8.28) and (8.34) the spatial form of the temperature takes the form:

$$g_m(x) = \frac{1}{\alpha\lambda_m}\omega_m[-c_m sin(\omega_m x) + d_m cos(\omega_m x) + \frac{h_m + p_m}{\omega_m}]. \tag{7.35}$$

This comes from the balance of linear momentum (8.7), bearing in mind (8.23) and (8.28), and also the fact that

$$g_m'(x) = \frac{1}{\alpha\lambda_m} w''_m(x). \tag{8.36}$$

Integration of the last equation yields:

$$g_m(x) = \frac{1}{\alpha\lambda_m}\left(w_m'(x) + p_m\right), \tag{8.37}$$

where p_m has the meaning of a constant modal elastic strain. Indeed, revisiting (8.32) and knowing (8.37) and (8.28) give:

$$\hat{N}_m(t) = EA(w_m'(x) - \alpha\lambda_m g_m(x))v_m(t) = -EA\,p_m v_m(t). \tag{8.38}$$

Because of (31), at the beginning of the evolution of the system it yields that

$$\hat{N}_m(0) = -EA\,p_m, \tag{8.39}$$

which explains why p_m is a constant elastic modal strain. Obviously, no axial force could develop in the bar if either each p_m would be identically zero or if $\sum_{m=0}^{\infty} p_m v_m(t) = 0$.

As it was previously pointed out, the path for determining the eigenvalues ω_m is based on the boundary conditions. The system is mechanically over-constrained. The problem is then treated in a standard way, by first removing the extra constraint and by studying a pinned-free truss undergoing the same initial conditions of the original problem. Then two cases will be considered with the idea of eventually superimposing their effects.

Case (0) The initial distribution of temperature and its corresponding initial displacement field will be taken to act on the pinned-free bar: here it is expected the modal strains $p_0^{(m)}$ are zero as there is no axial force.

Case (1) Because of the extra constraint, an unknown axial force arises within the bar: this is the only thermo-mechanical load acting in this case.

Once the separate effects of those two cases will be worked out, the requirement for which the displacement at both ends is inhibited by the original constraint will be enforced, thereby owing the value of the axial force and the complete solution of the problem. The two cases are now examined in details.

8.2.1 Case 0: Pineed-Free System Undergoing the Initial Distributions of Temperature and Displacements

This corresponds to the boundary conditions (8.15). All the quantities relative to this case are re-labeled with the superscript (0). Upon applying (8.15) term by term to the functions $w_m^{(0)}$ and $g_m^{(0)}$ introduced above, the following set of equations to be satisfied is obtained:

$$w_m^{(0)}(0) = 0 \qquad w_m^{(0)'}(L) = \frac{1}{\alpha} g_m^{(0)}(L) \tag{8.40 1, 2}$$

$$g_m^{(0)}(0) = 0 \qquad g_m^{(0)}(L) = 0, \tag{8.40 3, 4}$$

from (8.15), (8.12), and (8.22) respectively. From (8.28) and (8.40) the following relations hold:

$$c_m^{(0)} = -l_m^{(0)} \qquad d_m^{(0)} + \frac{h_m^{(0)} + p_m^{(0)}}{\omega_m^{(0)}} = 0 \tag{8.41 1, 2}$$

and hence $(40)_2$ and $(40)_3$ become:

$$-c_m^{(0)} sin(\omega_m^{(0)} L) + d_m^{(0)} cos(\omega_m^{(0)} L) + \frac{h_m^{(0)} + p_m^{(0)}}{\omega_m^{(0)}} = 0 \tag{8.42}$$

$$= 0 - c_m^{(0)} sin(\omega_m^{(0)} L) + d_m^{(0)} cos(\omega_m^{(0)} L) + \frac{h_m^{(0)}}{\omega_m^{(0)}} = 0. \tag{8.42}$$

The last two equations imply that the modal strains $p_m^{(0)}$ must vanish, i.e.

$$p_m^{(0)} = 0, \tag{8.43}$$

and, hence, $(41)_2$ yields

$$h_m^{(0)} = -\omega_m^{(0)} d_m^{(0)}. \tag{8.44}$$

Back substitution of $(8.41)_1$, (8.43) and (8.44) on either of the (8.42) yields an homogeneous problem which is verified if either of the following three conditions hold:

$$sin(\omega_m^{(0)} L) = 0 \text{ and } cos(\omega_m^{(0)} L) = 1, \quad \text{forall } c_m^{(0)}, d_m^{(0)} \text{ hence } \omega_m^{(0)} L = 2(m-1)\pi \tag{8.45}$$

$$c_m^{(0)} = 0 \quad \text{and hence } cos(\omega_m^{(0)} L) = 1 \text{ hence } \omega_m^{(0)} L = 2(m-1)\pi \tag{8.46}$$

$$d_m^{(0)} = 0 \quad \text{and hence } sin(\omega_m^{(0)} L) = 0 \text{ hence } \quad \omega_m^{(0)} L = (m-1)\pi \tag{8.47}$$

for all integers m. In order to determine which of the three possibilities itemized above occurs, one need to appeal to the initial data of the problem. Indeed, upon applying the standard Fourier procedure, and by taking into account relations (8.43), (8.44) and $(8.41)_2$, together with the initial data (8.9) and (8.10) yields:

$$c_m^{(0)} = 0, \tag{8.48}$$

while $d_m^{(0)}$ is certainly non-zero. Henceforth, the mth-mode for the temperature takes the following form

$$g_m^{(0)}(x) = T_m^{(0)}(cos(\omega_m^{(0)} x) - 1), \tag{8.49}$$

where $\omega_m^{(0)} = \dfrac{2(m-1)\pi}{L}$ and after setting

$$T_m^{(0)} = \frac{\omega_m^{(0)} d_m^{(0)}}{\alpha \lambda_m}. \tag{8.50}$$

Summing up the pinned-free case, the displacement and temperature fields take the following forms:

$$u^{(0)}(x,t) = \sum_m^{+\infty} d_m^{(0)} \left(\sin(\omega_m^{(0)} x) - \omega_m^{(0)} x \right) E_{1-\beta,1}\left(-\frac{\omega_m^{(0)2}}{\delta} t^{1-\beta} \right) \tag{8.51}$$

$$T^{(0)}(x,t) = T_0 + \sum_m^{+\infty} \lambda_m T_m^{(0)} \left(cos(\omega_m^{(0)} x) - 1 \right) E_{1-\beta,1}\left(-\frac{\omega_m^{(0)2}}{\delta} t^{1-\beta} \right), \tag{8.52}$$

after making use of $(8.34)_2$, relating the time dependence of the mth-mode of the temperature and the one of the displacement.
The coefficients $T_m^{(0)}$ are determined, again, by standard Fourier procedure. Upon integrating both sides of $T^{(0)}(x,t) - T_0$ multiplied against $cos(\omega_m^{(0)} x)$ over the length of the bar, it is found that:

$$\lambda_m T_m^{(0)} = \frac{2(T_0 - T_M)}{\pi^2 (m-1)^2}, \ m \geq 2. \tag{8.53}$$

As expected, the higher is the order of the spatial mode the lower is its contribution to the temperature. The amplitudes of the modal displacements are evaluated, in an analogous way, through relation (8.51), to get:

$$d_m^{(0)} = \frac{\alpha (T_0 - T_m) L}{(\pi (m-1))^3}, \tag{8.54}$$

Again, it is obtained that the higher is the order of the spatial mode the lower is its contribution to the total displacement field.

8.2.2 Case 1: Pinned-free system undergoing boundary axial forces only

The pinned-free body is now analyzed as if it would be subject to the sole unknown axial forces arising at the boundary because of the extra constraint present in the original system. Each mode contributes to such a force with its component, denoted by X_m. The initial conditions for Case 1 are then the following:

$$T_m^{(1)}(x,0) = 0 \text{ and } N_m^{(1)}(x,0) = X_m, \tag{8.55}$$

where the suffix (1) emphasizes the fact that Boundary conditions $(8.40)_1$ are replaced as follows:

$$w_m^{(1)}(0) = 0 \quad \text{and} \quad w_m^{(1)'}(L) = \frac{X_m}{EA}, \tag{8.56}$$

while $(8.40)_2$ still remain valid as they are. It is straightforward to show that the boundary conditions, the initial conditions and the usual Fourier procedure yield the following results:

$$\omega_m^{(1)} L = \omega_m^{(0)} L = 2(m-1)\pi, \ \ l_m^{(1)} = c_m^{(1)} = d_m^{(1)} = 0, \ h_m^{(1)} = -p_m^{(1)} = \frac{X_m}{EA}. \tag{8.57}$$

8.2.3 The Pinned-Pinned case

Per each index m, the overall spatial mode is the result of the superposition of $w_m^{(0)}(x)$ and $w_m^{(1)}(x)$, namely

$$w_m(x)=d_m^{(0)}\sin(\omega_m^{(0)}x)+\left(\frac{X_m}{EA}-d_m^{(0)}\omega_m^{(0)}\right)x. \tag{8.58}$$

By imposing the requirement due to the pinning at $x = L$ at all times, namely $w_m(L) = 0$, and by recalling that $\sin(\omega_m^{(0)}L) = 0$, the value of the modal axial force X_m is obtained as follows:

$$X_m=EA\omega_m^{(0)}d_m^{(0)}=\frac{2\alpha EA(T_0-T_M)}{\pi^2(m-1)^2},\ m\geq 2. \tag{8.59}$$

It is worth noting that, as expected, the series of the normal force amplitudes does converge as $\sum_2^\infty(m-1)^{-2}=\pi^2/6$ and, hence, at $t = 0$ it holds that

$$\hat{N}(0)=\frac{\alpha EA(T_0-T_M)}{3}. \tag{8.60}$$

Because of the fact that time-decaying functions multiply of each term of both the temperature and of the displacement, relations (7.38) reads as follows:

$$\hat{N}(t)=2\alpha EA(T_0-T_M)\sum_{m=2}^{\infty}\frac{1}{\pi^2(m-1)^2}E_{1-\beta,1}\left(-\frac{4\pi^2(m-1)^2}{\delta}t^{1-\beta}\right), \tag{8.61}$$

after making use of (8.59), (8.57) and (8.31). This does imply that the axial force is certainly decaying in time, thereby keeping its value always bounded and eventually fully relaxing.

Relations (8.58) and (8.59) imply that the mth mode for u is purely sinusoidal, and hence the final displacement takes the following form:

$$u(x,t) =$$
$$\alpha(T_0 - T_m)L\sum_{m=2}^{\infty}\frac{1}{\pi^3(m-1)^3}\sin\left(\frac{2(m-1)\pi x}{L}\right)E_{1-\beta,1}\left(-\frac{4(m-1)^2\pi^2}{L^2\delta}t^{1-\beta}\right). \tag{8.62}$$

For the spatial modes of T, (8.49) and the results above are considered to yield the following expressions for the temperature:

$$T(x,t)= T_0 + 4(T_0 - T_M)\sum_{m=2}^{\infty}\frac{1}{\pi^2(m-1)^2}\left(cos\left(\frac{2(m-1)\pi x}{L}\right)-1\right)$$
$$E_{1-\beta,1}\left(-\frac{4(m-1)^2\pi^2}{L^2\delta}t^{1-\beta}\right). \tag{8.63}$$

Here, eq. (8.50) is used along with the fact that, actually, the λ_m arising in (8.34) do not depend on the circumstance that either of the cases 0 or 1 are examined.
It is worth noting that a non-anomalous behavior can be achieved by letting $\beta \to 0$. The result does not affect the spatial modes of neither the displacement nor of the temperature.

8.3 Thermal "Work" and Measures of Available Energy Rate and Dissipation

The localized form of the balance of energy rate (8.6) can be used for further investigating the sources of dissipation and recovery of such rate. This can be done by multiplying both sides of such equation by the rate of change of temperature at which the line density $q_{,x}$ of heat flux arises, and by integrating over time and over the length of the bar. This gives an instantaneous measure of how much thermal "work" is done on the bar thanks to heat transfer and mechanical actions. Indeed, integration by parts in space and boundary conditions yields the following expression of the overall balance equation:

$$\int_0^t\int_0^L qT_{,tx}\,dxdt = -\int_0^t\int_0^L(\rho c_v + (\alpha EA)^2 T_0)T_{,t}^2\,dxdt - \int_0^t\int_0^L \frac{N_{,t}}{EA}T_{,t}\,dxdt. \tag{8.64}$$

The interpretation of such quantity is that this is a space-time global measure of the direct expenditure of the heat flux against the gradient of the temperature rate. The dimension of such a quantity is $FLt^{-1}T$, hence it represents a power times a temperature.
The quantity on the left-hand side generalizes an idea of [9, 10] for rigid thermal conductors, specialized by [26] in the presence of thermal memory. This also corresponds to eq. (4.3) obtained in [3]. Nonetheless, in the present treatment the elastic deformability of the bar explicitly manifests itself in the second term on the right-hand side of (8.64), besides having an effect on the expressions of T and N, as it has been highlighted in the previous section.
The case under study has a very special form of memory in time, regulated by the power law $t^{-\beta}$. One can show that in the absence of a heat source within the bulk (so that the first term in (6.3) in [26] vanishes), the thermal "work" done by the heat flux given by (8.2) can be defined as follows:

$$w_T(t) := -\int_0^t \int_0^L q(T_{,x})_{,\tau}\, dx d\tau. \tag{8.65}$$

By appealing to Fubini's theorem to interchange the order of integration, and substituting (8.2) in the expression above, after some calculations the following expression for the thermal work are obtained

$$w_T(t) = \frac{K_\beta}{\Gamma(1-\beta)} \int_0^L \int_0^t \int_0^\tau \frac{T_{,x}(x,\tau)_{,\tau}\, T_{,x}(x,\rho)_{,\rho}}{(\tau-\rho)^\beta} d\rho d\tau dx. \tag{8.66}$$

It is worth remarking that (8.65) is a general notion and its definition (easily generalizable to three dimensions) does not depend on the specific solution of the Initial Boundary Value Problem under consideration. Of course neither from (8.64) nor from this latter expression of the overall balance of energy rates clearly appears which fraction of $w_T(t)$ gets dissipated and which one is actually at the disposal of the thermoelastic processes available for the system.
Indeed, the direct inspection of the right-hand side of (8.64), which only depends on the fact that it is considered a thermoelastic truss with thermal memory coming from the multi-scale procedure derived in [1], does not directly enable one to understand if part of this global energy rate gets dissipated. In order to shed light on this issue, the authors note the formal analogy of the integrand in (8.65) (or (8.66)) and with the product $\sigma\dot{\varepsilon}$ in relation (22) of [11]. Indeed, by setting

$$G(t) := -\frac{K_\beta}{\Gamma(1-\beta)} t^{-\beta}, \tag{8.67}$$

upon formally identifying q with σ and $T_{,x}$ with ε in such a relation, it holds

$$q\,(T_{,x})_{,t} = \psi_{,t}\,(x,t) + \mathcal{D}(x,t), \tag{8.68}$$

where

$$\psi(x,t) = -\frac{1}{2}\int_0^t\int_0^t G(2t-\tau_1-\tau_2)(T_{,x})_{,t}\,(x,\tau_1)(T_{,x})_{,t}\,(x,\tau_2)\,d\tau_1\,d\tau_2. \tag{8.69}$$

After some calculations, it is possible to show that the rate of change of such ψ takes the following form:

$$\psi_{,t}\,(x,t) = q\;(T_{,x})_{,t} + \frac{1}{2}\int_0^t\int_0^t \dot{G}(2t-\tau_1-\tau_2)(T_{,x})_{,t}\,(x,\tau_1)(T_{,x})_{,t}\,(x,\tau_2)\,d\tau_1\,d\tau_2. \tag{8.70}$$

Finally, by making use of (8.67), the associated specific measure of "dissipation rate" (per unit length and per unit time) turns out to read as follows

$$\mathcal{D}(x,t) = -\frac{\beta K_\beta}{2\Gamma(1-\beta)}\int_0^t\int_0^t (2t-\tau_1-\tau_2)^{-(\beta+1)}(T_{,x})_{,t}\,(x,\tau_1)(T_{,x})_{,t}\,(x,\tau_2)\,d\tau_1\,d\tau_2. \tag{8.71}$$

It is worth nothing that $\psi(x,t)$ is the analog of the free energy (21) in [11], which turns out to be in the form of Stavermal and Schwarzl. The rate of change of this last quantity represents the part of the thermal work that can be at the disposal of the body, while (8.71) gives the measure of the rate of dissipation during the thermo-mechanical loading of the bar. This is of particular interest as its overall value

$$\mathcal{D}_T(t) := \int_0^t \int_0^L \mathcal{D}(x,\tau)\, dx\, d\tau \tag{8.72}$$

will tell us how much of $w_T(t)$ gets dissipated. Indeed, upon integrating (7.68) on space and time the following equation arises:

$$w_T(t) = \psi_T(t) + \mathcal{D}_T(t), \tag{8.73}$$

where the overall measure of energy rate ψ_T takes the form:

$$\psi_T(t) = \int_0^L \psi(x,t)\, dx =$$
$$\frac{256\pi^2 K_\beta (T_0 - T_M)^2}{L^5 \delta^2 \Gamma(1-\beta)} \sum_{m=2}^{\infty} (m-1)^2 \int_0^t \int_0^t \frac{(\tau_1 \tau_2)^{-\beta}}{(2t - \tau_1 - \tau_2)^\beta}$$
$$E_{1-\beta,1-\beta}\left(-\frac{4(m-1)^2 \pi^2}{L^2 \delta} \tau_1^{1-\beta} \right) E_{1-\beta,1-\beta}\left(-\frac{4(m-1)^2 \pi^2}{L^2 \delta} \tau_2^{1-\beta} \right) d\tau_1 d\tau_2 . \tag{8.74}$$

This global measure has been evaluated in analogy with the definition (8.72). Interchanging the order of integration can be done thanks to Fubini's theorem, which requires enough smoothness to do so. The correspondent measure of the overall thermal work is evaluate in full analogy with ψ_T, to get

$$w_T(t) = \frac{512\pi^2 K_\beta (T_0 - T_M)^2}{L^5 \delta^2 \Gamma(1-\beta)} \sum_{m=2}^{\infty} (m-1)^2 \int_0^t \int_0^t \frac{(\tau_1 \tau_2)^{-\beta}}{(t - \tau_2)^\beta}$$
$$E_{1-\beta,1-\beta}\left(-\frac{4(m-1)^2 \pi^2}{L^2 \delta} \tau_1^{1-\beta} \right) E_{1-\beta,1-\beta}\left(-\frac{4(m-1)^2 \pi^2}{L^2 \delta} \tau_2^{1-\beta} \right) d\tau_1 d\tau_2 . \tag{8.75}$$

A direct inspection of the series expansion of each term of the integrand in the latter expression shows that $w_T(t)$ has a finite value only for $\beta < 1/2$ (this agrees with the fact that the original range for β is $[0,1)$ and with the convergence of the resulting singular integral). The finiteness of the global thermal work limits the degree anomaly that the heat flux can exhibit. In terms of multi-scale rheological models, there is a purely mechanical analog in [11] - Sect. 4.1, although there the

value $1/2$ can be achieved. This result has a direct consequence on the partition of the thermal work, thereby ensuring that both $\mathcal{D}_T(t)$ and $\psi_T(t)$ are finite in the same range.

8.4 Discussion

The detailed analysis performed above and the related investigation about the global measures of the thermo-mechanical work, energy and dissipation rates allow one for comparing the consequences of anomalous heat transfer in (one dimensional) deformable bodies.
All the resulting fields, namely the axial stress (8.61), the displacement (8.62), and the temperature (8.63) are influenced by the thermal and elastic deformability of the bar.
Two effects, namely (i) the deformability and (ii) the emerging deviation for the Fourier behavior, can be analyzed separately in the sequel.

1) Once $\beta = 0$ is considered, namely the latter case, and the temperature distributions (63) and (65) in [1] are compared (see Figure (8.1)) a noticeable difference in their time behavior is reported. The non-dimensional times with respect which the fields for deformable versus rigid conductors are plotted are $\underline{t}_d := \dfrac{\delta^{-1} t^{1-\beta}}{L^2}$ and $\underline{t}_r := \dfrac{\gamma_\beta t^{1-\beta}}{L^2}$, respectively. In particular, a very significant influence on the thermal and elastic deformability on the time-rise of the temperature is detected. Indeed, from (8.20), because of the thermal and of the mechanical deformability, it is seen that the time dependence of the temperature (8.63) gains a scaling factor always less than or equal than 1, thereby reducing the value of the argument of the time modulating function $E_{1-\beta,1}\left(-\dfrac{4(m-1)^2\pi^2}{L^2\delta} t^{1-\beta}\right)|_{\beta=0} = \exp-\left(\dfrac{4(m-1)^2\pi^2\gamma_0}{L^2(1+\alpha^2 EAT_0/\rho c_v)}\right)t$ for each mode. These then leads to a higher magnitudes of such modulating functions relative to the case of rigid conductors. For the only sake of illustration, numerical data such as $\rho = 7860\dfrac{Kg}{m^3}$, $C_V = 502\dfrac{J}{Kg\,^\circ C}$, $K = 30\dfrac{W}{m\,^\circ C}$, $\alpha = 12\cdot 10^{-6}\dfrac{1}{^\circ C}$, $E = 220GPa$, $T_0 = 125^\circ C$ and $T_M = 25^\circ C$ have been implemented to investigate the effects of the deformability.

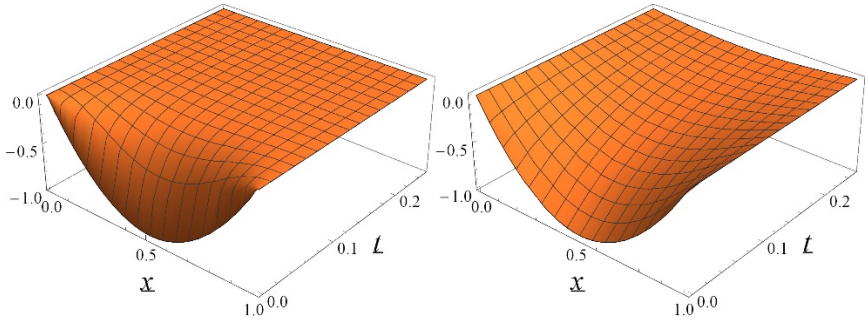

Figure 8.1 *Nondimensional temperature fields* $(T-T_0)/(T_0-T_M)$ *for* $\beta=0$*; all the surfaces have been obtained with n=20: (a) deformable conductor; (b) rigid conductor.*

An interpretation of this outcome can simply be related to the fact that in the current study the bar is fully thermoelastic, which implies that there is a continuous feedback between the temperature gradient and its rates and the strain rate itself. The redistribution of temperature and displacement is indeed due to the interplay between the balance of energy rate and the one of linear momentum. Within the former, (8.6), the heat flux (line) density has an extra forcing supply term, which is driven by the total strain rate, given by the sum of its elastic and thermal parts (e.g. (8.5)). This extra supply rate then triggers a faster temperature raise with respect to the case of rigid conductors, where neither the thermal nor the elastic dilatation can take place.

2) The influence of the deviation from the Fourier behavior of deformable conductors is summarized by comparing Figures 8.2a, 2b with the outcomes of Figure 8.1b. While the rapid rise in time to a regime value it is still seen here, the higher is the deviation from a Fourier-like behavior, the more rapid that rise gets. This is indeed an intrinsic feature of the anomalous heat transfer, now coupled with an elastic and thermally deformable bar. Another effect of the deviation from the Fourier behavior is the tendency to reach steady values in longer times. The higher the value of the anomaly exponent β in $[0,1/2)$ the faster this becomes. In particular, for higher values of β the temperature tends to reach T_0. This effect is more visible in the time evolution of the associate axial force, namely in Figure 8.2c and it is a consequence of the “long-tail memory” effect, a feature of a power law behavior given by (8.67). Indeed, as it is well known, the constitutive relation (8.2) for the heat flux can be recast as

$$q(x,t) = \int_0^t G(t-\tau)(T_{,x})_{,\tau}(x,\tau)d\tau, \tag{8.76}$$

where the "relaxation function" G is given by (8.67).

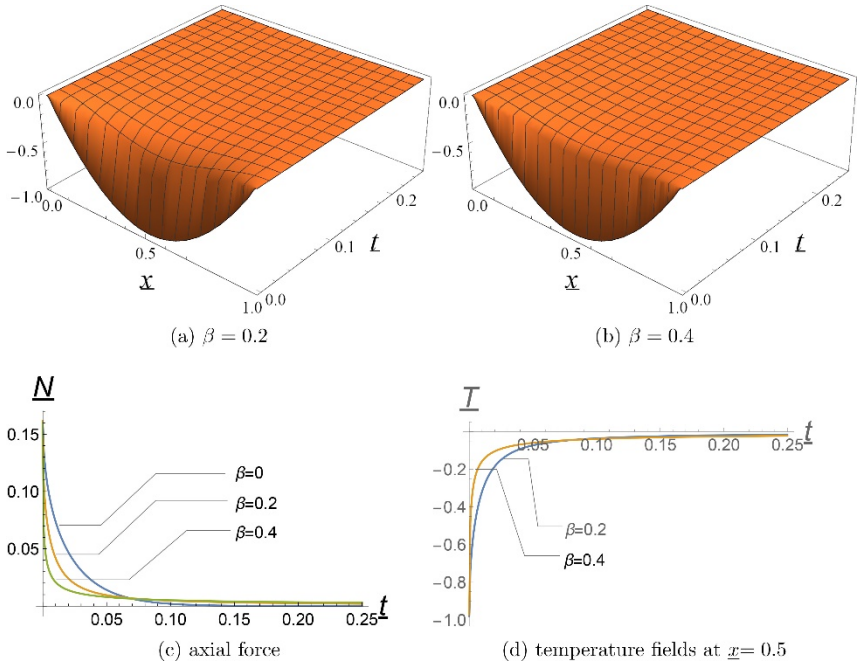

Figure 8.2 *(a and b) Nondimensional temperature fields $(T-T_0)/(T_0-T_M)$ for deformable conductors with different values of β, equal to β=0.2 and β=0.4, respectively; all the surfaces have been obtained with n=20; (c) time evolution of nondimensional axial force ˆN/(αEA(T0–TM)); (d) time evolution of nondimensional temperature fields at x=0.5.*

A comparison among the different landscapes obtained for the displacement field for the three values of β mentioned above suggests a similar trend in terms of its time evolution.

In fact, the higher is the discrepancy against the Fourier behavior the more pronounced is the long-tail effect on settling to a stationary value, which in this case is actually zero. Spatially, the resulting odd fluctuations relative to the midpoint of the span is essentially governed by the initial condition on u, a result of the balance of linear momentum.

The most interesting features of the anomalous thermoelastic coupling for bars comes from the comparison of the global measures of the

"thermal work" w_T, of the available energy rate ψ_T and the dissipation rate $\mathcal{D}_T$, (8.66), (8.74) and (8.72) respectively.

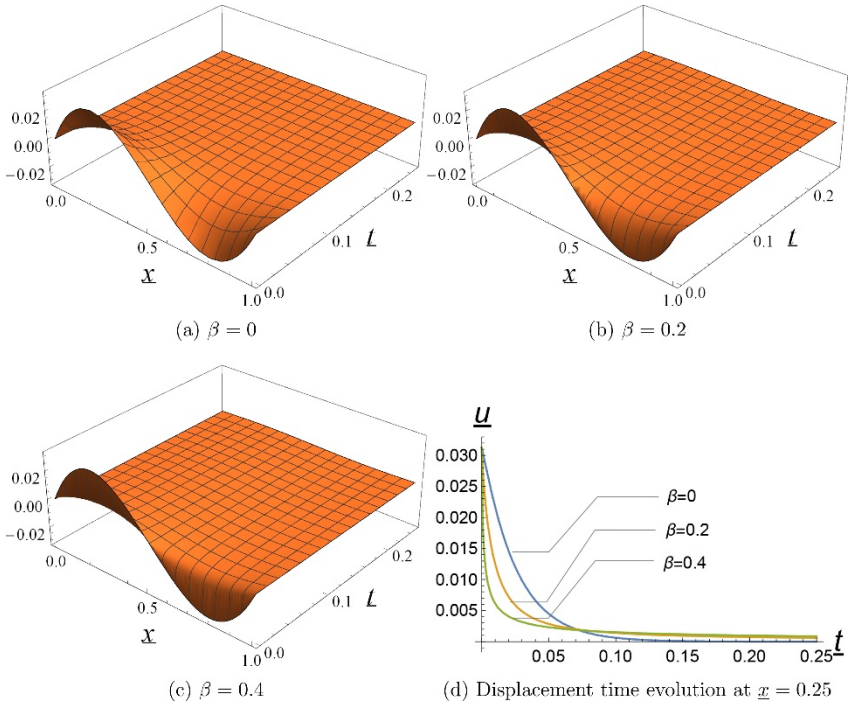

Figure 8.3 *Displacement fields for deformable conductors with different values of β; all the surfaces have been obtained with n=20: (a) β=0; (b) β=0.2; (c) β=0.4; (d) displacement time evolution at x=0.25.*

Both for the rigid and for the deformable Fourier-like cases, a smooth monotonically increase of (non-dimensional) thermal work $\underline{W}$, defined in Figures (8.4) and (8.5) respectively, is noted. For rigid conductors there is a smoother increase with respect to deformable ones with no appreciable asymptote before $\underline{t} \simeq 0.5$ and with the corresponding value of $\underline{W} \simeq 2 \cdot 10^{-3}$. On the contrary, for deformable conductors a steady value (circa 0.7) is achieved at $\underline{t} \simeq 0.10$ (see Figure (8.5)), where $\underline{t} := \underline{t}_d = \dfrac{\delta^{-1} t^{1-\beta}}{L^2}$. The higher values and the sharper time rise of $\underline{W}$, a quadratic operator involving the rate of change of temperature gradients, is primarily due to the fact that much higher rates of temperature gradient are detected in the deformable case, as Figure (8.1) shows. In both cases there is a perfect equi-partition of the quotas

of ψ_T and D_T (which in the figures are replaced by their corresponding non-dimensional counterparts $\underline{\Psi}$ and $\underline{D}$) in which the thermal work is decomposed. This fits in a striking formal analogy with linear elasticity, as $\beta = 0$ implies $q = -K_0 T_{,x}$ like $N = EA\epsilon$ for the latter case. In [17] it is seen as this results from a smart re-visitation of Clapeyron's theorem for three dimensional linear elasticity. This has been rendered free of the paradox that no dissipation would have occurred even if the total work is twice the value of the strain energy at the final values of the strain in an underlying loading process. A (rate-type) viscoelastic term allowed there to consider the effect of slow loading processes, thereby retrieving the asymptotic value of the overall dissipation and matching the other missing half of the work.

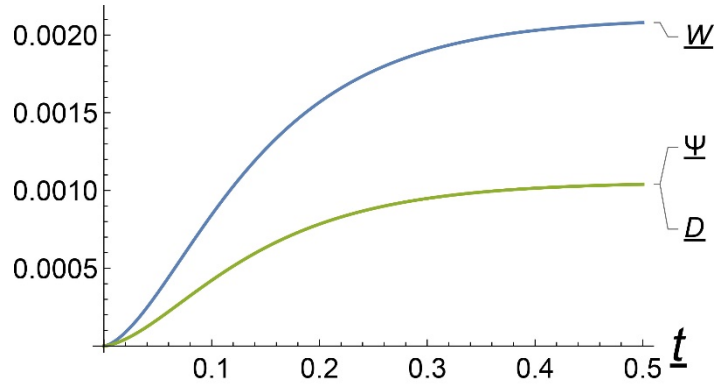

(a) $\beta = 0$

Figure 8.4 *Rigid conductors: nondimensional thermal work* $W=w_T/[512\pi 2K\beta(T_0-T_M)^2/(L\Gamma(1-\beta))*(L2/\gamma^\beta)^{2/(\beta-1)}]$, *nondimensional energy rate* $\Psi=\Psi_T/[256\pi^2K_\beta(T_0-T_M)^2/(L\Gamma(1-\beta))*(L^2/\gamma_\beta)^{(2/\beta-1)}]$, *and nondimensional dissipationrate* $D=W-\Psi$, *along with nondimensional time t, for* $\beta=0$.

Signatures of the thermal anomaly are seen in the thermal work and in the available energy and dissipation rates. First of all, it is noticeable that the higher the value of β the more the thermal work exhibit a discrepancy with respect to the Fourierian case. Furthermore, a deviation from equipartition between ψ_T and $\mathcal{D}_T$ is also detected, thereby indicating that this global measure of rate dissipation rises due to the deviation from the Fourier behavior. Anomaly then introduces a further source of dissipation, most likely due to the fact that the scaling of q like $t^{-\beta}$ resembles an hierarchy of thermal properties, as explained in [1], enhancing the possibilities of dissipating energy at the various scales. A change in signature is noticeable for $\beta = 0.2$, for which a

softening is exhibited by $\underline{W}$ after $\underline{t} \simeq 0.025$, while a plateau is then reached at $\underline{W} \simeq 0.95$. The rising of the thermal work in time is analog to what it has been discussed above to the temperature, essentially characterizing the response of the anomalous thermo-mechanics evolution of the system under study.

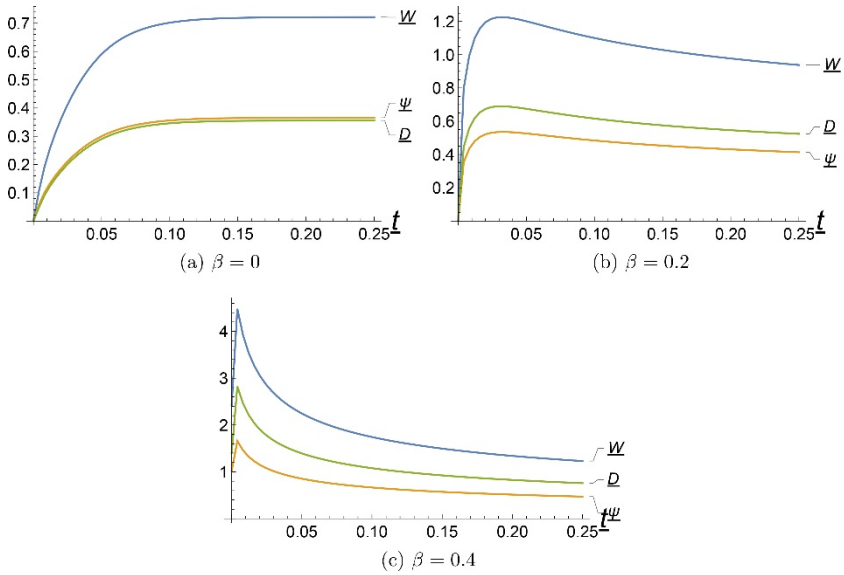

Figure 8.5 *Rigid conductors: nondimensional thermal work* $W=w_T/[512\pi 2K\beta(T_0-T_M)^2/(L\Gamma(1-\beta))*(L2/\gamma^{\beta})^{2/(\beta-1)}]$, *nondimensional energy rate* $\Psi=\Psi_T/[256\pi^2K_{\beta}(T_0-T_M)^{2}/(L\Gamma(1-\beta))*(L^2/\gamma_{\beta})^{(2/\beta-1)}]$, *and nondimensional dissipationrate* $D=W-\Psi$, *along with nondimensional time t, for different values of* β: *(a)* $\beta=0$; *(b)* $\beta=0.2$; *(c)* $\beta=0.4$

A further extreme behavior for all the quantities $\underline{W}$, $\underline{\Psi}$ and $\underline{D}$ is recorded for $\beta = 0.4$. Here the time rise becomes almost immediate, as for the corresponding temperature (see Figure (8.3c)), and the softening behavior essentially dominates their trend. The discrepancy between the global dissipation rate $\underline{D}$ and the corresponding $\underline{\Psi}$ becomes more pronounced, thereby confirming the trend noticed before. Henceforth, the more the heat flux deviates from the standard Fourier behavior the higher is the likelihood of having further dissipation during the thermoelastic evolution of the system.
A modal decomposition of the global measures of energy rates is reported in Fig. 8.6 subsequently.

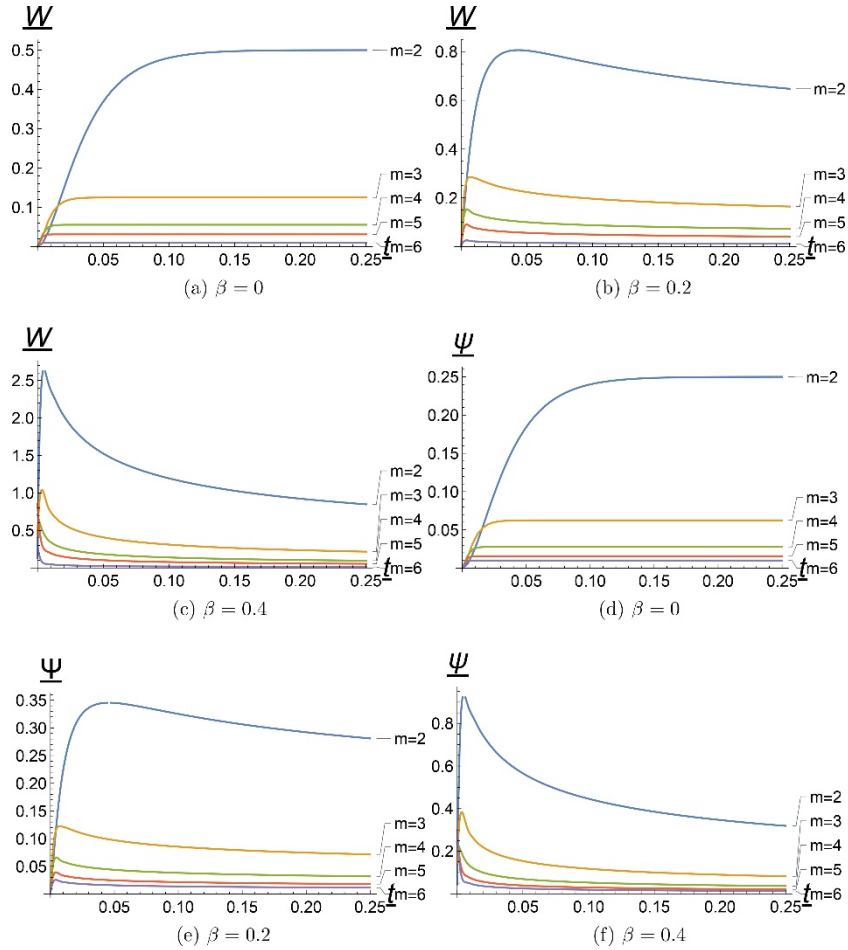

Figure 8.6 *Modal decomposition of the global measures of energy rates for different values of β: (a–c) nondimensional thermal work; (d–f) nondimensional dissipation rate: (a) β=0; (b) β=0.2; (c) β=0.4; (d) β=0; (e) β= 0.2; (f) β=0.4*

As expected, the global measures of work, energy and dissipation rates are heavily guided by the first mode, given by $m = 2$, which hence gives a qualitative idea about the global measures of energy rate response of the anomalous thermoelastic system. Given the importance of the conclusions drawn above, a comprehensive thermodynamic analysis should be performed to investigate how the deviation from the standard Fourier behavior influences the performances of such systems. This is the subject for further thorough investigations involving refined measures of the actual entropy rate, that should be calculated starting from the multi-scale rheological scheme introduced in [1].

8.5 Conclusions

In the present work the "fractional thermally-anomalous" coupled behavior of slightly deformable bodies is studied. The mentioned "anomaly" originates from the relation among the macroscopic heat flux and the time history of the temperature gradient, that involves a "long-tail" memory behavior, governed by a Caputo's fractional operator. Indeed, the macroscopic constitutive equation between the heat flux and the time history of the temperature gradient does involve a power law kernel, and it is the result of a multi-scale rheological model developed in Part 1 of the present study.
For the sake of illustration, the interplay between the thermal flux and the elastic and the thermal deformability are investigated for a pinned-pinned truss. Given the simplicity of the system geometry, together with the richness of the arising axial stress, this allows for focusing on the effects of the deviation from the Fourier's law on the thermoelastic coupling. Results show that the interactions, in such simply geometry, are fully coupled as the temperature and the displacement fields mutually influence one another.
A space-time modal analysis performed on the fractional-order system, relying on the balance of linear momentum and on the balance of energy rate, provides the explicit solutions of the problem. The time evolution of each spatial mode, for the temperature, for the displacement and for the axial force, turn out to be characterized by modulated Mittag-Leffler functions. The higher is the deviation from the Fourier-like behavior for the heat flux, the steeper is the resulting time-transient of each mode. The influence of the deformability on the one hand, and of the discrepancy from the Fourier behavior on the other hand, are thoroughly analyzed for the three fields mentioned above.
Measures of the overall "thermal work", and of the associate available and dissipation energy rates are evaluated, both mode-by-mode and globally, enabling the characterization of the coupled response of anomalous thermoelastic trusses. Besides determining the range of admissible discrepancies from the Fourier behavior, such quantities are shown to fully reveal the manifestation of the thermal anomaly together with the effects of the elastic and thermal deformabilities.

References

[1] Alaimo, G., et al. (2017). "Fractional-order theory of thermo-elasticity I: Generalization of the Fourier equation and thermodynamical consistency." J. Eng. Mech., 10.1061/(ASCE)EM.1943-7889.0001394, 04017164.

[2] Amendola, G., and Carillo, S. (2004). “Thermal work and minimum free energy in a heat conductor with memory.” Q. J. Mech. Appl. Math., 57(3), 429–446.
[3] Amendola, G., Fabrizio, M., and Golden, J. M. (2010). “Free energies for a rigid heat conductor with memory.” IMA J. Appl. Math., 75(6), 833–856.
[4] Bacigalupo, A., Morini, L., and Piccolroaz, A. (2016). “Overall thermomechanical properties of layered materials for energy devices applications.” Compos. Struct., 157, 366–385.
[5] Baleanu, D., Guvenc, Z. B., and Machado, J. T., eds. (2010). New trends in nanotechnology and fractional calculus applications, Springer, Dordrecht, Netherlands.
[6] Bongiorno, D. (2009). “On the problem of regularity in the Sobolev space W1;n loc.” Topol. Appl., 156(18), 2986–2995.
[7] Bongiorno, D. (2014). “Metric differentiability of Lipschitz maps.” J. Aust. Math. Soc., 96(1), 25–35.
[8] Bongiorno, D., and Corrao, G. (2015). “On the fundamental theorem of calculus for fractal sets.” Fractals, 23(2), 1550008.
[9] Coleman, B. D., and Mizel, V. J. (1963). “Thermodynamics and departures from Fourier’s law of heat conduction.” Arch. Ration. Mech. Anal., 13(1), 245–261.
[10] Day, W. A., and Gurtin, M. E. (1969). “On the symmetry of the conductivity tensor and other restrictions in the nonlinear theory of heat conduction.” Arch. Ration. Mech. Anal., 33(1), 26–32.
[11] Deseri, L., Di Paola, M., and Zingales, M. (2014a). “Free energy and states of fractional-order hereditariness.” Int. J. Solids Struct., 51(18), 3156–3167.
[12] Deseri, L., Gentili, G., and Golden, J. (2014b). “New insights on free energies and Saint-Venant’s principle in viscoelasticity.” Int. J. Solids Struct., 51(19–20), 3382–3398.
[13] Deseri, L., and Owen, D. R. (2003). “Toward a field theory for elastic bodies undergoing disarrangements.” J. Elast., 70(1), 197–236.
[14] Deseri, L., and Owen, D. R. (2015). “Stable disarrangement phases arising from expansion/contraction or from simple shearing of a model granular medium.” Int. J. Eng. Sci., 96, 111–130.
[15] Deseri, L., and Owen, D. R. (2016). “Submacroscopic disarrangements induce a unique, additive and universal decomposition of continuum fluxes.” J. Elast., 122(2), 223–230.
[16] Fabrizio, M., Gentili, G., and Reynolds, D. W. (1998). “On rigid heat conductors with memory.” Int. J. Eng. Sci., 36(7–8), 765–782.
[17] Fosdick, R., and Truskinovsky, L. (2003). “About Clapeyron’s theorem in linear elasticity.” J. Elast., 72(1–3), 145–172.

[18] Fraldi, M., Esposito, L., Carannante, F., Cutolo, A., and Nunziante, L. (2016). "Steady-state thermoelastic analytical solutions for insulated pipelines." Math. Prob. Eng., 2016, 1–13.
[19] Fraldi, M., and Guarracino, F. (2001). "On a general property of a class of homogenized porous media." Mech. Res. Commun., 28(2), 213–221.
[20] Ignaczak, J., and Ostoja-Starzewski, M., eds. (2009). Thermoelasticity with finite wave speeds, Oxford Science Publications, Oxford, U.K.
[21] Kimmich, R. (2002). "Strange kinetics, porous media, and nmr." Chem. Phys., 284(1–2), 253–285.
[22] Lepri, S., Livi, R., and Politi, A. (2016). "Heat transport in low dimensions: Introduction and phenomenology." Thermal transport in low dimensions: From statistical physics to nanoscale heat transfer, S. Lepri, ed., Vol. 921, Springer, London, 1–37.
[23] Liu, S., Hänggi, P., Li, N., Ren, J., and Li, B. (2014). "Anomalous heat diffusion." Phys. Rev. Lett., 112(4), 040601.
[24] Lu, T., Zhu, S., Chen, Z., Wang, W., Zhanga, W., and Zhang, D. (2016). "Hierarchical photonic structured stimuli-responsive materials as highperformance colorimetric sensors." Nanoscale, 8(19), 10316–10322.
[25] Mitkowski, W., Kacprzyk, J., and Baranowski, J., eds. (2013). Advances in the theory and applications of non-integer order systems, Vol. 257, Springer, Heidelberg, Germany.
[26] Nunziato, J. W. (1971). "On heat conduction materials with memory." Q. Appl. Math., 29(2), 187–204.
[27] Papathanasiou, T., Dal Corso, F., and Piccolroaz, A. (2016). "Thermomechanical response fem simulation of ceramic refractories undergoing severe temperature variations." J. Eur. Ceram. Soc., 36(9), 2329–2340.
[28] Podlubny, I. (1998). Fractional differential equations, Academic Press, New York.
[29] Povstenko, Y. Z. (2009). "Theory of thermoelasticity based on the spacetime-fractional heat conduction equation." Phys. Scr., 2009(T136), 014017.
[30] Sherief, H. H., El-Sayed, A., and El-Latief, A. (2010). "Fractional order theory of thermoelasticity." Int. J. Solids Struct., 47(2), 269–275.
[31] Zisis, T., Gourgiotis, P., and Dal Corso, F. (2015). "A contact problem in couple stress thermoelasticity: The indentation by a hot flat punch." Int. J. Solids Struct., 63, 226–239.

9. A Fractional Order Theory of Poroelasticity

By G. Alaimo, V. Piccolo, A. Cutolo, L. Deseri, M. Fraldi

Abstract

We introduce the memory formalism in the flux-pressure constitutive relation, ruling the water diffusion phenomenon occurring in several classes of porous media. The resulting flux-pressure law has been applied to the classical 1D Terzaghi's consolidation problem. The memory formalism, useful to capture non-Darcy behavior, is modeled by the Caputo's fractional derivative. We show that the time-evolution of both the degree of consolidation and the pressure fields is strongly influenced by the order of Caputo's fractional derivative. Also a numerical experiment aiming at simulating the Terzaghi's consolidation process of a sand sample is performed. In such a case, the classical Darcy equation may lead to inaccurate estimates of the consolidation time.

Glossary

q	fluid volume flow per unit area	$m \cdot s^{-}$
$\hat{k}$	permeability of porous medium	m^2
μ	fluid viscosity	$kg \cdot m^{-1} \cdot s^{-1}$
p	fluid pressure	$kg \cdot m^{-1} \cdot s^{-2}$
k	hydraulic conductivity	$m \cdot s^{-1}$
ρ	density	$kg \cdot m^{-3}$
g	gravity	$m \cdot s^{-2}$
γ	volumetric weight	$kg \cdot m^{-2} \cdot s^{-2}$
k_β	anomalous hydraulic conductivity	$m \cdot s^{-1+\beta}$
K	bulk modulus of porous medium	$kg \cdot m^{-1} \cdot s^{-2}$

G	shear modulus of porous medium	$kg \cdot m^{-1} \cdot s^{-2}$
B	Biot's coefficient	*dimensionless*
S	storativity	$kg^{-1} \cdot m \cdot s^{2}$
m_v	confined compressibility	$kg^{-1} \cdot m \cdot s^{2}$
ν	Poisson's coefficient of the porous medium	*dimensionless*
c	consolidation coefficient	$m^{2} \cdot s^{-1}$
c_β	anomalous consolidation coefficient	$m^{2} \cdot s^{-1+\beta}$
K_s	bulk modulus of solid phase	$kg \cdot m^{-1} \cdot s^{-2}$
η	porosity	*dimensionless*

9.1 Introduction

The mass transport of fluid particles through a porous medium is a mechanism similar to the diffusion of chemical and mass species through biological structures, i.e. cell membranes, epithelial tissues and sprayed parenchymatous organs. The first one is governed by Darcy equation whereas the latter is related to the Fick equation (meaning the relation that linearly links the flux of the chemical species in motion in a fluid medium with the concentration gradient in the direction of the transport).
Such two linear diffusive equations, both in Fick and Darcy form, have shown some discrepancies with the observed experimental data [19, 13]. The time evolution of the concentration and of the velocity predicted by such equations is described by exponential solutions, but regarding fluid flows in biological tissues os sand soils, a sort of "stretched exponential" is found, meaning a deviation from the predicted values.
During last years several methods to capture the the difference between the observed behaviour and the experimental one have been developed and adopted. Among others we recall molecular dynamics [22, 21, 20, 12] and Continuous Time Random Walk (CTRW) models that describe the random path of contaminant flux plumes in heterogeneous porous media [16, 2, 3].
A different approach to handle this problem has been framed in the contex of anomalous diffusions in terms of power-laws with real

exponents [5, 4]. The introduction of the memory formalism in Fick/Darcy transport equations is used to capture changes in the chemical/physical properties of the pores as well as of the interactions among pore channels and fluid particles of the porous media, during the transport process. For example, in water diffusion in porous media, experimental data [10] shown that the permeability of sand layers may decrease due to rearrangement of the grains and consequent compaction, or if the fluid carries solid particles which obstruct some of the pores. Accordingly, the flow would occur as if the medium had a memory, meaning that, at any instant, the diffusion process is affected by the (past) history of pressure and flow. The transport equations resulting from the application of fractional derivatives to diffusion problems are mainly phenomenological but, if accurately verified with experimental evidence, they may represent a step forward with respect to the classical equations in explaining transport phenomena or other physical processes.
However, in [7] the authors provided a mechanical justification for the presence of anomalous diffusion in porous media, as recently demonstrated in scientific literature for the hereditary behavior of the matter [9, 8] as well as in bone tissues viscoelasticity [6]. More in the details, the fractional-order force-flux relations for the flux of a viscous fluid across an elastic porous media was found for a one dimensional problem, where an unbonded porous media with a power-law variation of geometrical and physical properties was considered. Actually, having a variation of the characteristics of the media yields to a fractional-order relation among the ingoing flux and the applied pressure to the control section. Two different behaviours were found to be perhaps related to different states of the mass flow across the porous media. In fact, if it is considered a power-law decay of the physical properties from the control section then the flux is related to a Caputo fractional derivative of the pressure of order $0 \leq \omega < 1$. On the other hand, if the physical properties of the media show a power-law increase from the control section, then the flux is related to a fractional-order integral of order $0 \leq \omega \leq 1$. In this work, we show the effect resulting from the introduction of the memory effect, by means of the Caputo's fractional derivative, in the flux-pressure constitutive relation. The latter has been employed to describe the water diffusion phenomenon in porous media, and has been applied to the classic Terzaghi's consolidation problem.

9.2 Fractional Darcy Law

The force-flux relation provided by Darcy linear relation was modified to include changes in physical properties of the porous media during the

flow. The well-known Darcy law in porous media is ruled by the following equation:

$$q(x,t) = -\frac{\hat{k}}{\mu}\nabla p(x,t) \tag{9.1}$$

where $\nabla[\bullet] = \frac{\partial[\bullet]}{\partial x_1} i_1 + \frac{\partial[\bullet]}{\partial x_2} i_2 + \frac{\partial[\bullet]}{\partial x_3} i_3$ denotes the Laplacian operator, $q(x,t) = [q_1(x) \quad q_2(x) \quad q_3(x)]^T$ is the vector of specific volume flux across a generic cross-section, $\hat{k}$ is the Darcy permeability coefficient depending on the material and $p(x,t)$ is the pressure field. Introducing the hydraulic conductivity (or diffusivity) k that is defined as

$$k = \frac{\hat{k}\rho_f g}{\mu} = \frac{\hat{k}\gamma_f}{\mu} \tag{9.2}$$

where ρ_f is the fluid density, g the gravity and $\gamma_f = \rho g$ the fluid volumetric weight, relation (9.1) may be written

$$q(x,t) = -\frac{k}{\gamma_f}\nabla p(x,t) \tag{9.3}$$

The anomalous force-flux relation in advection/diffusion has been obtained in terms of a modified transport equation as:

$$f_\alpha(t) * q(x,t) = f_\beta(t) * \nabla p(x,t) \tag{9.4}$$

where the symbol $*$ indicates the well-known convolution product. We assume that $f_\alpha(t)$ and $f_\beta(t)$ are differential operators provided in the form:

$$f_\alpha(t) = m_1\delta(t) + \frac{m_2 t^{-\alpha}}{\Gamma(1-\alpha)}\frac{\partial}{\partial t}[\bullet] \tag{9.5a}$$

$$f_\beta(t) = n_1\delta(t) + \frac{n_2 t^{-\beta}}{\Gamma(1-\beta)}\frac{\partial}{\partial t}[\bullet] \tag{9.5b}$$

where $\delta(t)$ is the Dirac-delta function, α and β are real order exponents with $0 < \alpha, \beta < 1$, m_1, m_2, n_1 and n_2 are model parameters, and $\Gamma(\bullet)$ is the Euler-Gamma function which is defined through the following integral:

$$\Gamma(z) = \int_0^\infty e^{-x} x^{z-1} dx \tag{9.6}$$

Euler-Gamma may be considered as the generalization of the factorial function since when z assumes integer values, we have that $\Gamma(z+1) = z!$.

The substitution of eq. (9.4) with the transport fluid-pressure relation (9.1) has been dubbed memory formalism (see e.g. the paper by [4]). Replacing the expressions (9.5a) and (9.5b) of functions $f_\alpha(t)$ and $f_\beta(t)$ in the convolution product (9.4), the transport equation is expressed as:

$$(m_1 + m_2 D_0^\alpha) q = -(n_1 + n_2 D_0^\beta) \nabla p \tag{9.7}$$

where $D_0^\alpha(\bullet)$ and $D_0^\beta(\bullet)$ are Caputo fractional derivatives, which definitions is:

$$D_0^\omega(f) = \frac{1}{\Gamma(1-\omega)} \int_0^t \frac{f'(\tau)}{(t-\tau)^\omega} d\tau \tag{9.8}$$

valid for $0 \le \omega < 1$. Eq. (9.8) states that the value of the Caputo fractional derivative of a differentiable function f, at time t, is obtained by adding to its initial value $f(0)$ the increments $f'(\tau)d\tau$ over time ($\tau \in [0,t]$), weighted by the factor $(t-\tau)^{-\omega}$, which decreases increasing time separation from t. Accordingly, the memory formalism is obtained through the Caputo fractional derivative that, essentially, results in a weighted mean of the "past" value of the function f.

To reduce the number of parameter needed to define the transport equation (9.7), in this work we consider the case $m_2 = 0$ that is one of the most interesting in practical applications. With such assumption, equation (9.7) may be rewritten as follows:

$$\gamma_f q = -(k + k_\beta D_0^\beta)\nabla \mathbf{p} \tag{9.9}$$

where k_β is the "anomalous" hydraulic conductivity or diffusivity.

9.3 Fractional-Order Consolidation

Soft soils such as sand and clay consist of small particles, and often the pore space between the particles is filled with water. In soil mechanics this is denoted as a saturated or partially saturated porous medium. The deformation of such porous media depends upon the stiffness of the porous material, and upon the behaviour of the fluid in the pores. If the permeability of the material is small, the deformations may be considerably retarded by the viscous behaviour of the fluid in the pores. The simultaneous deformation of the porous material and the flow of the pore fluid is the subject of the theory of consolidation, often denoted as poroelasticity. The theory was originally developed by Terzaghi for the 1D case, and extended to the 3D case by Biot. In his original theory Terzaghi postulated that the deformations of a soil were mainly caused by a rearrangement of the system of the particles, and that the compression of the pore fluid and of the solid particles can practically be disregarded. In a saturated soil this means that a volume change of an element of soil can only occur by a net flow of the fluid with respect to the solid particles. This system of assumptions often is a good approximation of the real behaviour of soft soils, especially clay, and also soft sands. Such soils are highly compressible (deformations may be as large as several percents), whereas the constituents, particles and fluid, are very stiff.
In later presentations of the theory, starting with those of Biot, compression of the pore fluid and compression of the particles has been taken into account. This generalization has made it possible to also consider the deformations of stiffer materials such as sandstone and other porous rocks, which are very important in the engineering of deep reservoirs of oil or gas. In this section the authors will present the fractional-order model for consolidation. This works takes the inspiration from the previous work [7] that has been summarized in the previous section. The linear fractional theory of poroelasticity (or consolidation) relies on the following set of equations:

$$\left(K + \frac{G}{3}\right)\frac{\partial \epsilon}{\partial x} + G\nabla^2 u_x - B\frac{\partial p}{\partial x} + f_x = 0 \tag{9.10a}$$

$$\left(K+\frac{G}{3}\right)\frac{\partial \epsilon}{\partial y}+G\nabla^2 u_y - B\frac{\partial p}{\partial y}+ f_y = 0 \tag{9.10b}$$

$$\left(K+\frac{G}{3}\right)\frac{\partial \epsilon}{\partial z}+G\nabla^2 u_z - B\frac{\partial p}{\partial z}+ f_z = 0 \tag{9.10c}$$

$$B\frac{\partial \epsilon}{\partial t}+S\frac{\partial p}{\partial t} = -\nabla\cdot\mathbf{q} \tag{9.10d}$$

$$\epsilon = \nabla\cdot u \tag{9.10e}$$

$$\gamma_f\, q = -(k+k_\beta D_0^\beta)\nabla\mathbf{p} \tag{9.10f}$$

Eqs. (10a-10c) represent, in terms of displacements u, the equilibrium equations under the assumption of linear elastic isotropic solid phase and small strains regime on the porous media while eq. (10d) is the "storage" equation, namely the mass balance.
In eqs. (10) K and G are the bulk and the shear moduli of the porous medium respectively, B is the Biot's coefficient, S is the storativity, γ_f is the specific weight of the fluid, $f = [\,f_x \quad f_y \quad f_z\,]^T$ is the vector of mass forces, and ϵ is the volumetric strain defined as:

$$\epsilon = \varepsilon_{xx} + \varepsilon_{yy} + \varepsilon_{zz} \tag{9.11}$$

The system of PDEs (10) in 3D-consolidation problems usually involves the simultaneous resolution of the storage equation (10d) together with the equilibrium equations, as such equations are coupled. However, an important class of problems in which an uncoupled analysis may be performed is the case where it can be assumed that $i)$ the horizontal strains ε_{xx} and ε_{yy} are equal to zero and $ii)$ the vertical total stress σ_{zz} is constant over the time.
Assumptions $i)$ and $ii)$ were first derived by Terzaghi for the 1D case of flow and strain, as occurs during an experimental compression test. Moreover, we recall the well-known Terzaghi's principle which states that total stresses σ_{ij} can be additively decomposed into the effective stresses $\hat{\sigma}_{ij}$ and in the pore pressure p as:

$$\sigma_{ij} = \hat{\sigma}_{ij} + B\,p\hat{\delta}_{ij} \tag{9.12}$$

where $\hat{\delta}_{ij}$ is the Kronecker's symbol. If the horizontal strains are imposed to be equal to zero, it follows that the volumetric strain ϵ is equal to the vertical strain:

$$\epsilon = \varepsilon_{zz} = -m_v \hat{\sigma}_{zz} \tag{9.13}$$

where m_v is the confined compressibility defined as:

$$m_v = \frac{3}{3K + 4G} = \frac{1+\nu}{3K(1-\nu)} \tag{9.14}$$

in eq. (14) ν is the Poisson's coefficient of the porous medium. Taking into account the Terzaghi's principle, and differentiating with respect to time eq. (13) we obtain:

$$\frac{\partial \epsilon}{\partial t} = -m_v \frac{\partial \sigma_{zz}}{\partial t} + m_v B \frac{\partial p}{\partial t} \tag{9.15}$$

and inserting eq. (9.15) in the storage equation (10d) we have:

$$-Bm_v \frac{\partial \sigma_{zz}}{\partial t} + (B^2 m_v + S)\frac{\partial p}{\partial t} = -\nabla \cdot \mathbf{q} \tag{9.16}$$

Observing that for $t > 0$ we have $\frac{\partial \sigma_{zz}}{\partial t} = 0$ for the assumption ii, and taking into account the transport equation (10f), relation (16) reads:

$$\frac{\partial p}{\partial t} = \nabla \cdot \left(c \nabla \mathbf{p}\right) + \nabla \cdot \left(c_\beta D_0^\beta \left(\nabla \mathbf{p}\right)\right) \tag{9.17}$$

valid if $f = o$. In eq. (23), c and c_β are the usual and the "anomalous" (in the sense of fractional calculus) consolidation coefficients respectively, defined as:

$$c = \frac{k}{\gamma_f (B^2 m_v + S)} \tag{9.18a}$$

$$c_\beta = \frac{k_\beta}{\gamma_f (B^2 m_v + S)} \tag{9.18b}$$

In case of homogeneous porous medium, namely when the quantities $\frac{k}{\gamma_f}$ and $\frac{k_\beta}{\gamma_f}$ in eqs. (9.18a) and (9.18b) respectively are constant in space, eq. (9.17) becomes:

$$\frac{\partial p}{\partial t} = c\nabla^2 p + c_\beta D_0^\beta \left(\nabla^2 p\right) \tag{9.19}$$

In light of equation (9.19), we observe that the system (9.10) is actually uncoupled since firstly the pressure field p may be evaluated from equation (9.19) together with the associated BCs and, subsequently, the mechanical problem can be solved using the equilibrium equations (9.10a - 9.10c).
In the next section we analyze the solution of Terzaghiâ€™s consolidation problem when the porous medium is characterized by the fractional transport relation (9.10f).

9.3.1 Fractional Terzaghi's Consolidation Problem

Let us consider the transient boundary value problem of a confined homogeneous soil sample of height h, surrounded by a circular ring, and placed in a container filled with water as shown in Fig. (9.1).

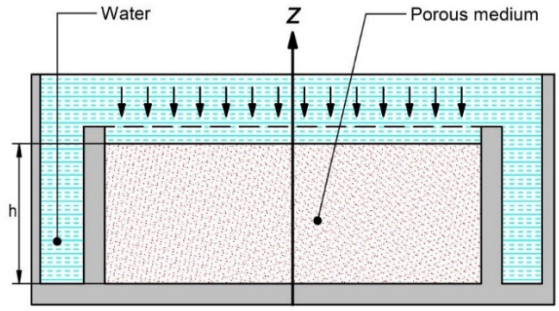

Figure 9.1 *Schematic description of Terzaghi's problem. A confined homogeneous porous medium sample of height h, is placed in a container filled with water and is loaded by a vertical stress s.*

The sample is loaded by a vertical stress $\sigma_{zz} = sU(t)$ at its upper surface, where $U(t)$ is the Heaviside unit step function; the lower boundary of the sample ($z = 0$) is considered impermeable while the upper boundary ($z = h$) is fully drained. To find the initial condition we observe that at time $t = 0$ no flux can occur through the porous medium: accordingly eq. (9.16) reads:

$$-\alpha m_v s\delta(t) + (B^2 m_v + S)\frac{\partial p}{\partial t} = 0 \tag{9.20}$$

where $\delta(t)$ is the Dirac delta function; integrating eq. (9.20) from $t = 0^-$ and $t = 0^+$ we have:

$$p_0 = \left|p\right|_{t=0^+} - \left|p\right|_{t=0^-} = \left|p\right|_{t=0^+} = s\frac{Bm_v}{B^2 m_v + S} \tag{9.21}$$

The mathematical formulation of the problem is:

$$\frac{\partial p}{\partial t} = c\nabla^2 p + c_\beta D_0^\beta\left(\nabla^2 p\right) \quad \text{with} \quad 0 \le z \le h, t > 0, 0 \le \beta < 1 \tag{9.22a}$$

$$\left|q\right|_{z=0} = 0, \quad \forall t > 0 \tag{9.22b}$$

$$\left|p\right|_{z=h} = 0, \quad \forall t > 0 \tag{9.22c}$$

$$\left|p\right|_{t=0^+} = p_0 = s\frac{Bm_v}{B^2 m_v + S}, \quad 0 \le z \le h \tag{9.22d}$$

The problem (9.22a) with boundary conditions (9.22b) and (9.22c) and initial condition (9.22d) can be solved using the method of separation of variables, namely separating $p(z,t)$ into space-dependent and time-dependent functions as reported below:

$$p(z,t) = \phi(t)\theta(z) \tag{9.23}$$

substituting (9.23) into (9.22a) and introducing the separation constant λ, we obtain

$$\frac{1}{\theta}\frac{d^2\theta}{dz^2} = \frac{1}{c\phi + c_\beta D_0^\beta(\phi)}\frac{d\phi}{dt} = -\lambda^2 \tag{9.24}$$

Relation (9.24) is equivalent to the two following differential equations:

$$\frac{d^2\theta(z)}{dz^2} + \lambda^2\theta(z) = 0 \tag{9.25a}$$

$$\left|\frac{d\theta}{dz}\right|_{z=0} = 0 \tag{9.25b}$$

$$\left|\theta\right|_{z=h} = 0 \tag{9.25c}$$

and

$$\frac{d\phi(t)}{dt} + \lambda^2 c_\beta D_0^\beta(\phi)(t) + \lambda^2 c\phi(t) = 0 \tag{9.26}$$

The general solution of the spatial evolution in eq. (9.25a) is

$$\theta(z) = D_1\cos(\lambda z) + D_2\sin(\lambda z) \tag{9.27}$$

where boundary condition (9.25b) yields $D_2 = 0$, while boundary condition (9.25c) yields

$$\cos(\lambda h) = 0 \Rightarrow \lambda_n = \frac{(2n-1)\pi}{2h}, \text{with } n = 1,2,3,.. \tag{9.28}$$

The roots λ_n of relation (9.28) are the eigenvalues of the associated Sturm-Liouville problem. As a consequence, the eigenfunctions of the problem are:

$$\theta_n(z) = D_1\cos(\lambda_n z) = D_1\cos\left[\frac{(2n-1)\pi}{2h}z\right] \tag{9.29}$$

After solving the problem corresponding to the space dimension z, we note that the solution for the time-dimensional problem, namely the

fractional differential equation (9.26), has been obtained by the Laplace transform method in [17, eq. 5.3.47]. We have:

$$\begin{aligned}\phi_n(t) &= \sum_{k=0}^{\infty}\left(-\lambda_n^2 ct\right)^k E_{1-\beta,k+1}^{k+1}\left(-\lambda_n^2 c_\beta t^{1-\beta}\right) + \\ &+\lambda_n^2 c_\beta t^{1-\beta}\sum_{k=0}^{\infty}\left(-\lambda_n^2 ct\right)^k E_{1-\beta,k+2-\beta}^{k+1}\left(-\lambda_n^2 c_\beta t^{1-\beta}\right)\end{aligned} \tag{9.30}$$

where $E_{\zeta,\eta}^{\xi}(x)$ is the Prabhakar function (see for example [15, 11, 14]) defined as:

$$E_{\zeta,\eta}^{\xi}(x) = \sum_{i=0}^{\infty}\frac{(\xi)_i (x)^i}{\Gamma(\zeta i+\eta) i!} \tag{9.31}$$

being $(\xi)_i$ the Pochhammer symbol:

$$(\xi)_i = \begin{cases} 1 \quad \text{if} \quad i=0 \\ \xi(\xi+1)\cdots(\xi+i-1) \quad \text{if} \quad i \in N \end{cases} \tag{9.32}$$

Relations (9.29) and (9.30) can be combined introducing the constant $D_n = D_1$ yielding, considering relation (9.23), the general solution:

$$p(z,t) = \sum_{n=1}^{\infty}\theta_n(z)\phi_n(t) = \sum_{n=1}^{\infty} D_n \cos\left[\frac{(2n-1)\pi}{2h} z\right]\phi_n(t) \tag{9.33}$$

where the constant D_n is defined utilizing the initial condition (9.22d) and noting that, $\forall n$, $\phi_n(0)=1$, namely:

$$p(z,0) = p_0 = \sum_{n=1}^{\infty} D_n \cos\left[\frac{(2n-1)\pi}{2h} z\right] \tag{9.34}$$

Relation (9.34) is the Fourier series expansion of the function p_0 then, multiplying both sides of such relation by $\cos(\lambda_m z)$ and integrating over the interval $[0,h]$ we obtain:

$$\int_0^h p_0 \cos(\lambda_m v) dv = \begin{cases} D_m \int_0^h \cos^2(\lambda_m v) dv = D_m \dfrac{h}{2} \quad \text{if} \quad m=n \\ 0 \quad \text{if} \quad m \neq n \end{cases} \tag{9.35}$$

where the property of orthogonality of the eigenfunctions $\cos(\lambda_m z)$, for arbitrary eigenvalues λ_m, has been used. Summing up, from eq. (9.35) we have:

$$D_n = \frac{2}{h}\int_0^h p_0 \cos(\lambda_n v)dv = \frac{4p_0}{\pi}\frac{(-1)^n}{1-2n} \tag{9.36}$$

and finally, using relation (9.33) with eqs. (9.36) and (9.30), we obtain the expression for the pressure field as

$$p(z,t) = \frac{4p_0}{\pi}\sum_{n=1}^{\infty}\frac{(-1)^n}{1-2n}\cos\left[\frac{(2n-1)\pi}{2h}z\right]\phi_n(t) \tag{9.37}$$

In the next section we report a numerical experiment regarding the fractional Terzaghi's consolidation problem. In particular, the consolidation problem in a 1D sample with imposed load and fixed, over time, pressure and flux at the extremities, is studied. The aim of the presented analysis is to show, by means of a problem defined in a simple spatial domain, how the solution of the consolidation problem is influenced by the introduction of the Caputo's fractional derivative in the pressure - flux constitutive relation.

9.4 Numerical Experiment

In order to further reduce the number of parameters in eq. (9.10f), in this section we set a zero value of the consolidation coefficient ($c = 0$) which implies that the flux tends to zero as $t \to \infty$. This assumption may be considered sufficiently valid also in light of the following considerations. Firstly, we note that only few experimental works regarding fractional Darcy transport equation are available in literature and most of them have been focused on the transient phase of the diffusion phenomenon (see for example the paper by [10]. The authors of the above mentioned work observed that the flux seems to reach a stationary state after a relatively small time interval (about 10 hours), but they cannot rule out that it is asymptotically nil; in other words, no certain indications about the flux stationary value can be obtained from their experiments. Moreover, the pressure field time-evolution evaluation is not a simple task because of the convergence issues related to the series involved in expression (9.30), since a very large number of terms are required to obtain a sufficiently accurate evaluation. Integral relations representing relation (9.30) can be more useful but, to the authors' knowledge, they are not available in literature.

Given that no other more reliable indications of the flux asymptotic value was available, we consider the transient boundary value problem of the fractional Terzaghi's consolidation when $c = 0$. The mathematical formulation of the problem is:

$$\frac{\partial p}{\partial t} = c_\beta D_0^\beta \left(\nabla^2 p\right) \quad \text{with} \quad 0 \le z \le h, t > 0, 0 \le \beta < 1 \tag{9.38a}$$

$$\left|q\right|_{z=0} = 0, \quad \forall t > 0 \tag{9.38b}$$

$$\left|p\right|_{z=h} = 0, \quad \forall t > 0 \tag{9.38c}$$

$$\left|p\right|_{t=0^+} = p_0 = s\frac{Bm_v}{B^2 m_v + S}, \quad 0 \le z \le h \tag{9.38d}$$

As detailed in the previous, also in this case we used the method of separation of variables. The spatial evolution of the pressure field $p(z,t)$ reported in eq. (9.29) is still valid also in the case $c = 0$ under consideration. As concerns the fractional differential equation ruling the time evolution, it is straightforward to observe that it becomes:

$$\frac{d\phi(t)}{dt} + \lambda^2 c_\beta D_0^\beta(\phi)(t) = 0 \tag{9.39}$$

eq. (9.39) may be solved using the Laplace transform method [17, eq. 5.3.39] yielding:

$$\phi_n(t) = \phi_0 E_{1-\beta,1}\left(-\lambda_n^2 c_\beta t^{1-\beta}\right) \tag{9.40}$$

By means of eq. (9.40), the solution of problem (9.38a) is obtained as:

$$p(z,t) = \\ = \frac{4p_0}{\pi}\sum_{n=1}^{\infty}\frac{(-1)^n}{1-2n}\cos\left[\frac{(2n-1)\pi}{2}\frac{z}{h}\right]E_{1-\beta,1}\left[-\frac{(2n-1)^2\pi^2}{4}\frac{c_\beta t^{1-\beta}}{h^2}\right] \tag{9.41}$$

Relation (9.41) can be converted into a non-dimensional form by defining the non-dimensional independent variables, through the

dimensional parameters of the consolidation problem, as reported below:

$$\underline{p} = \frac{p}{p_0} \tag{9.38a}$$

$$\underline{z} = \frac{z}{h} \tag{9.38b}$$

$$\underline{t} = \frac{c_\beta t^{1-\beta}}{h^2} \tag{9.38c}$$

$$\underline{\lambda}_n = \frac{(2n-1)\pi}{2} \tag{9.38d}$$

Adopting the non-dimensional variables of eqs. (9.42) we obtain the non dimensional pressure field as:

$$\underline{p}(\underline{z},\underline{t}) = \frac{4}{\pi}\sum_{n=1}^{\infty}\frac{(-1)^n}{1-2n}\cos\left(\underline{\lambda}_n \underline{z}\right) E_{1-\beta,1}\left(-\underline{\lambda}_n^2 \underline{t}\right). \tag{9.43}$$

We also consider the time evolution of the displacement $u(t)$ at the free end of the sample. It can be obtained by integration of the strain ε_{zz} through the height (see eq. (9.13)):

$$u(t) = -\int_0^h \varepsilon_{zz} dz = \int_0^h m_v \hat{\sigma}_{zz} dz \tag{9.44}$$

considering the Terzaghi's principle (9.12), relation (9.44) reads:

$$\begin{aligned} u(t) &= \int_0^h m_v \left(\sigma_{zz} - p\right) dz = m_v s h - m_v \int_0^h p dz = \\ &= h m_v \left\{ s - \frac{8 p_0}{\pi^2}\sum_{n=1}^{\infty}\frac{1}{(1-2n)^2} E_{1-\beta,1}\left[-\frac{(2n-1)^2\pi^2}{4}\frac{c_\beta t^{1-\beta}}{h^2} \right] \right\} \end{aligned} \tag{9.45}$$

The final displacement u_∞ is obtained as $t \to \infty$, namely when all the pore have dissipated the pressure. Considering that

$$\lim_{t\to\infty} E_{1-\beta,1}\left[-\frac{(2n-1)^2\pi^2}{4}\frac{c_\beta t^{1-\beta}}{h^2}\right]=0, \tag{9.46}$$

we have:

$$u_\infty = \lim_{t\to\infty} u(t) = hm_v s. \tag{9.47}$$

Moreover, the initial displacement is evaluated as follows:

$$u_0 = \lim_{t\to 0^+} u(t) = hm_v\left[s-\frac{8p_0}{\pi^2}\sum_{n=1}^{\infty}\frac{1}{(1-2n)^2}\right] = hm_v\left(s-p_0\right) \tag{9.48}$$

taking into account that the following relation helds:

$$\lim_{t\to 0} E_{1-\beta,1}\left[-\frac{(2n-1)^2\pi^2}{4}\frac{c_\beta t^{1-\beta}}{h^2}\right]=1 \tag{9.49}$$

As done for the pressure field, we introduce a dimensionless measure of the displacement, namely the degree of consolidation $w(t)$ that, considering relations (9.47) and (9.48) yields:

$$\begin{aligned} w(t) &= \frac{u(t)-u_0}{u_\infty-u_0} = \\ &= 1-\frac{8}{\pi^2}\sum_{n=1}^{\infty}\frac{1}{(1-2n)^2}E_{1-\beta,1}\left[-\frac{(2n-1)^2\pi^2}{4}\frac{c_\beta t^{1-\beta}}{h^2}\right] \end{aligned} \tag{9.50}$$

9.4.1 Consolidation of a Sand Sample and Comparison Between Fractional and Classical Darcy's Law

In this section we show how the introduction of the memory effect, by means of the Caputo fractional derivative in the transport equation, affects both the pressure and the consolidation coefficient time evolutions in the Terzaghi's problem. The analysis is carried out relying on the experimental data obtained first in [4] and after confirmed in [10]. As noted before, the authors did several experiments to measure the mass flow-rate of water through a sample of sand embedded in a cylinder, with applied a constant pressure gradient between its surfaces. The experiments have been performed applying a pressure on one side,

through a water column, and measuring the flow on the other side. It has been observed that at the beginning of the experiments the flux was almost $40g \cdot s^{-1}$ while, after 10 hours, it decreased to about $27g \cdot s^{-1}$, showing that the mass flow-rate induced by the applied constant gradient pressure was not constant as ruled by the Darcy's law.
Assuming a constitutive flux-pressure relation as in eq. (9.10f) with $k = 0$, which implies $c = 0$, it follows that the diffusion phenomenon under observation is ruled by two parameters, namely the order of the Caputo derivative β, and the anomalous diffusivity k_β. The authors found that the data obtained during their experiments are well fitted with the following values: $\beta = 0,51$ and $k_\beta = 0,11m \cdot s^{-1+\beta}$. Moreover, the classical hydraulic conductivity can also be estimated from their experiments, resulting in the value $k = 1,6 \cdot 10^{-3} m \cdot s^{-1}$ that is compatible with the range of hydraulic conductivity for sand, namely 10^{-6} to $10^{-3} m \cdot s^{-1}$ (see for example [1]). It is also not surprising that the value of anomalous hydraulic conductivity is out of the range of the classic for sand, since the two quantities represent different physics and dimensions.
Assuming for the porous medium a bulk modulus of $K = 8GPa$, a Poisson's coefficient $\nu = 0,2$, a porosity $\eta = 0,19$ and for sand a bulk modulus of $K_s = 36GPa$ respectively [18], we can estimate the Biot's coefficient as:

$$B = 1 - \frac{K}{K_s} = 0,78 \tag{9.51}$$

the confined compressibility (see eq. (9.14)) as:

$$m_v = 6,3 \cdot 10^{-11} kg^{-1} \cdot m \cdot s^2 \tag{9.52}$$

and the storativity S as:

$$S = \frac{\eta}{K_f} + \frac{(B - \eta)}{K_s} = 9,9 \cdot 10^{-11} kg^{-1} \cdot m \cdot s^2 \tag{9.53}$$

where, in eq. (9.53) $K_f = 2,3GPa$ is the bulk modulus of water. Through eq. (9.18) it is then possible to evaluate the consolidation coefficients:

$$c = 1,2 \cdot 10^{3}\, m^{2} \cdot s^{-1} \tag{9.54a}$$

$$c_{\beta} = 8,0 \cdot 10^{4}\, m^{2} \cdot s^{-1+\beta} \tag{9.54b}$$

the time evolution of both non-dimensional pressure field and degree of consolidation are shown in Fig. (9.3).

9.5 Discussion

Some examples of the non-dimensional pressure field obtained by eq. (9.43) are shown in Fig. (9.2).

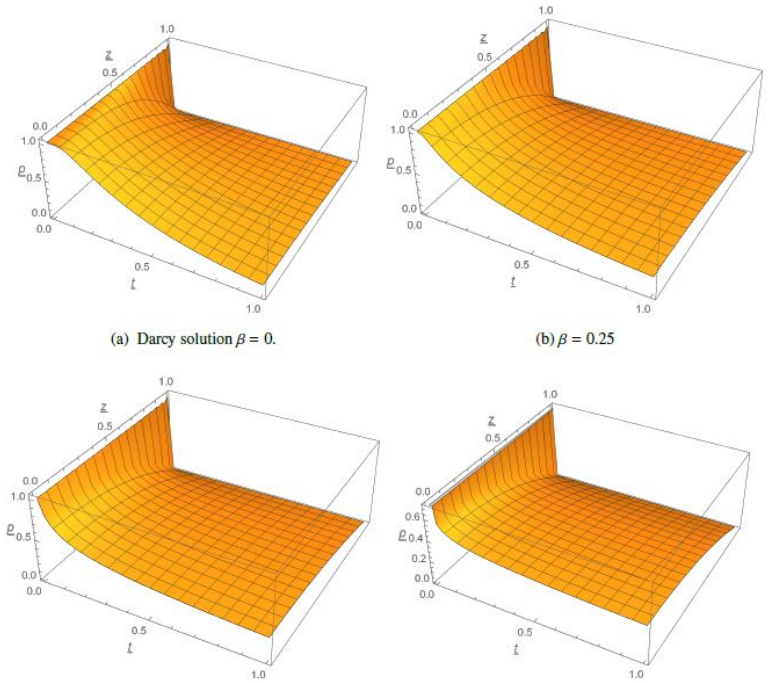

Figure 9.2 *Non-dimensional pressure field* $\underline{p}$ *for different value of the exponent* β. *All the surfaces have been obtained with n=100.*

When it comes to considering how long does it take for the porous medium to achieve consolidation steadiness, the trend shown in presence of anomalous porous media is, compared to classical ones, to employ longer non-dimensional times. From a physical point of view, such phenomenon is observed when rearrangement of the grains and

consequent compaction occurs, or if the fluid carries solid particles which obstruct some of the pores grain. Basically, in the case of fluid transport in porous medium, this results into a change in time of the permeability. Accordingly, from a mathematical point of view, this effect may be taken into account considering force-flux relations with a “memory effect”.

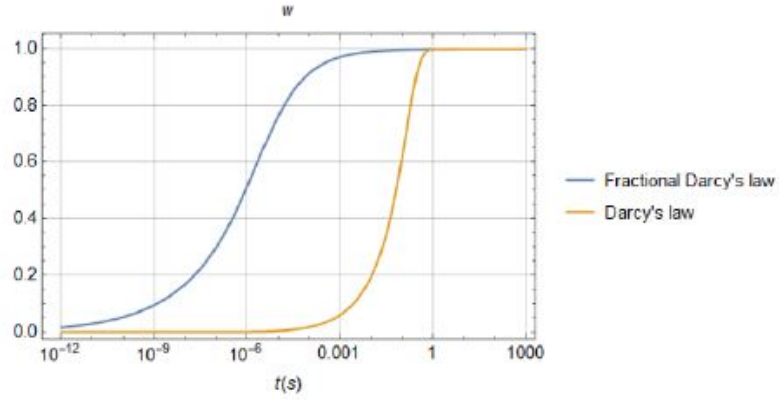

(a) Comparison of the degree of consolidation time-evolution $w(t)$ (eq. (50)).

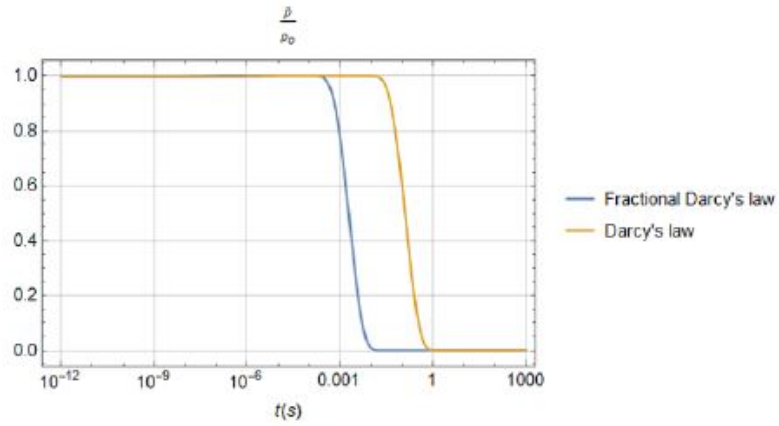

(b) Comparison of the adimensional pressure time-evolution p/p_0 (eq. (41)) at $z = 0$.

Figure 9.3 *Solution of the Terzaghi’s problem in terms of degree of consolidation and pressure time evolution. The solution related to the classical Darcy’s law has been obtained imposing* $\beta = 0$.

From the analysis of Fig.(9.3) it is seen that the main feature characterizing the anomalous consolidation is that the time-evolution of both displacement and pressure field is strongly influenced by the order

of the Caputo fractional derivative. The influence of the deviation from the Darcy behavior of porous media reveals itself in the initial rapid rise in time, followed by the tendency to reach steady values in longer times: the higher the deviation from a Darcy-like behavior, the more pronounced this effect becomes. In addition, for the time-evolution of the pressure field, a significant time-shift compared to what obtained with Darcy law has been observed; beside such time-shift, the degree of consolidation also exhibits a sensibly different behavior.

9.6 Conclusion

In this work the authors study the effects, for consolidation problems, of introducing a memory effect in the flux-pressure constitutive relation employed to describe the water diffusion phenomenon in porous media. In particular, the classic 1D Terzaghi's consolidation problem has been studied. The introduction of the memory effect has proven to be useful to capture non-Darcy behavior, as highlighted by some works reporting experimental data. The fractional Darcy's law assumed in this work is characterized by the Caputo's fractional derivative.

The main result of this work is to show that the time-evolution of both the displacement and pressure fields is strongly influenced by the order of Caputo fractional derivative. Higher is the order of the Caputo's derivative, higher will be the initial rise in time, with the tendency to reach steady values in longer times.

The authors also performed a numerical experiment aiming at simulating and predicting the Terzaghi's consolidation process of a sand sample, assuming a fractional Darcy's law. The authors show that the classical Darcy equation may mainly lead to inaccurate estimates of the consolidation time, as well as of the pressure field time-evolution. When in presence of rearrangement of grains and consequent compaction, or if the fluid carries solid particles which obstruct some of the pores, more accurate results can obtained by simple, 2-parameters fractional models.

From a mathematical point of view, in the majority of cases, the time-evolution of the pressure field and of the degree of consolidation, is obtained by simply substituting the classical exponential law with a Mittag-Leffler type function. Moreover, from an experimental point of view, the fitting of the proposed fractional model does not require a significantly more burdensome effort, since only two parameters have to be evaluated. Also, the experimental setup required is, in all respects, the same as the one used in the classical permeability evaluation.

Fractional models would reveal their efficiency also when dealing with consolidation problems of clay soils that, as observed for sand, basically consist of small particles surrounded by water. Accordingly, the

phenomena observed in sand soils such as compaction or transport of solid particles obstructing pores can occur in clay soils. For the latter, characteristic consolidation times are order of magnitude higher than sand considered in this work thus the approximation introduced by the use of the classical Darcy's law could be not negligible for practical use. Unfortunately, to the best of authors' knowledge, experimental data reporting the time evolution of the flux for clay soils are not available in literature.
Experimental test aiming at evaluate the 2-parameters of the fractional Darcy's law for clay soils could be conducted, to further study the applicability of the proposed model for this type of porous medium.

References

[1] Jacob Bear. Dynamics of fluids in porous media. Courier Corporation, 2013.
[2] D. A. Benson, R. Schumer, M. M. Meerschaert, and S. W. Wheatcraft. Fractional dispersion, lévy motion and the made tracer tests. Geophys. Res. Lett., 42:211–240, 2001.
[3] B. Berkowitz, A. Cortis, M. Dentz, and H. Scher. Modeling non-fickian transport in geological formations as a continuous time random walk. Rev. Geophys., 44, 2006.
[4] M. Caputo and W. Plastino. Diffusion in porous layers with memory. Geophys. Int. J., 158:385–396, 2004.
[5] M. Caputo. Models of flux in porous media with memory. Water Resources Research, 36(3):693–705, 2000.
[6] L. Deseri, M. Di Paola, M. Zingales, and P. Pollaci. Power-law hereditariness of hierarchical fractal bones. Int. J. Numer. Methods Biomed. Eng., BHO:BHO, 2013.
[7] L. Deseri and M. Zingales. A mechanical picture of fractional-order darcy equation. Commun Nonlinear Sci Numer Simulat, (20):940–949, 2015.
[8] M. Di Paola, F. P. Pinnola, and M. Zingales. A discrete mechanical model of fractional hereditary materials. Int. J. Theor. Appl. Mech., 48:1573–1586, 2013.
[9] M. Di Paola and M. Zingales. Exact mechanical models of fractional hereditary materials. J. Rheol, 56:983–1004, 2012.
[10] G Iaffaldano, M Caputo, and S Martino. Experimental and theoretical memory diffusion of water in sand. Hydrology and Earth System Sciences Discussions, 2(4):1329–1357, 2005.
[11] Anatoly A Kilbas, Megumi Saigo, and Ram K Saxena. Generalized mittag-leffler function and generalized fractional

calculus operators. Integral Transforms and Special Functions, 15(1):31–49, 2004.

[12] M. Kojić, M. Milosević, N. Kojić, M. Ferrari, and A. Ziemys. Numeric modeling of diffusion in complex media with surface effects. Contemp. Mater., III(2):153–166, 2012.

[13] R. L. Magin, O. Abdullah, D. Baleanu, and X. J. Zhou. Anomalous diffusion expressed through fractional order differential operators in the bloch-torrey equation. J. Mag. Reson., 190:255–270, 2008.

[14] Francesco Mainardi and Roberto Garrappa. On complete monotonicity of the prabhakar function and non-debye relaxation in dielectrics. Journal of Computational Physics, 293:70–80, 2015.

[15] Tilak Raj Prabhakar. A singular integral equation with a generalized mittag leffler function in the kernel. The Yokohama mathematical journal, 19(1):7–15, 1971.

[16] H. Schrer, G. Margolin, R. Metzler, and J. Klafter. The dynamical foundation of fractal stream chemistry: the origin of extremely long retention times. Geophys. Res. Lett., 29:1061, 2009.

[17] Hari Mohan Srivastava, Juan J Trujillo, et al. Theory and applications of fractional differential equations. North-Holland Math. Stud, 204, 2006.

[18] G Van der Kamp and JE Gale. Theory of earth tide and barometric effects in porous formations with compressible grains. Water Resources Research, 19(2):538–544, 1983.

[19] M. Weiss, H. Hashimoto, and T. Nilson. Anomalous protein diffusion in living cells as seen by fluorescence correlation spectroscopy. Biophysical J., 84(6):4043–4052, 2003.

[20] A. Ziemys, M. Ferrari, and C. N. Cavasotto. Molecular modeling of glucose diffusivity in silica nanochannels. J. Nanosci. Nanotechnol., 9:6349–6359, 2009.

[21] A. Ziemys, A. Grattoni, D. Fine, F. Hussian, and M. Ferrari. Confinement effects on monosaccharide transport in nanochannels. J. Phys. Chem. B, 114(34):1117–1126, 2010.

[22] A. Ziemys, M. Kojić, M. Milosević, N. Kojić, F. Hussian, M. Ferrari, and A. Grattoni. Hierarchical modeling of diffusive transport through nano-channels by coupling molecular dynamics with finite element method. J. Comput. Phys., 230:5722–5731, 2011.

10. Summary and Conclusions

10.1 Summary

Novel analytical models for challenging multiscale problems arising in complex ordered submicroscopic systems have been presented. Such activities have been supported by analytical, numerical and experimental studies. For instance, this is the case when studying the response of polymeric nano-composites to electromagnetic and mechanical stimuli. Such actions are notorious to be important for sensors, polymeric films, artificial muscles, cell membranes, metamaterials, hierarchical composite interfaces and other novel class of materials.

Complex nanostructured systems have been investigated, both from an experimental point of view and from an analytical one, with different configurations, from 3D colloidal crystals to 2D gratings made via colloidal route as strain sensors. 3D colloidal crystals have also been investigated to see their response to organic solvents in order to study the swelling and diffusion process.

These kind of analysis regarding diffusive and transport problems have been carried out also from a purely analytical point of view in the last three chapters of this thesis in order to provide novel models able to scaling up from an ordered microstructure to a macroscopic structure, providing a relation for the diffusive and transport phenomena.

It has been demonstrated that ordered submicrometric materials may exhibit some physical properties, such as the thermal and the mechanical creep/relaxation ones, with time-rate dependent response. In fact, the analysis of the temperature field in an inhomogeneous rigid conductor with power-law grading of the thermodynamic parameters has shown a power-law time increase of the temperature at the insulated boundary of the conductor. The order of the power law is strictly linked to the grading exponent of the physical properties of the conductor, and the use of the Boltzmann superposition principle for generic histories of the incoming heat flux has yielded a temperature-flux relation involving fractional-order operators. The main idea that a power-law increase appears as a nonhomogeneous, nonstationary flux is established in the conductor has been further expanded to yield a fractional-order generalization of the Fourier transport equation. As a consequence, the resulting macroscopic relation has provided the heat flux by means of the fractional-order, Caputo type, derivative of the spatial gradient of the temperature field with derivation order related to the fractal dimension of the self-similar assembly.

Then the attention has been focused on the coupling of this phenomenon with the mechanics, meaning the "fractional thermally anomalous" coupled behavior of slightly deformable bodies. Results have shown that the interactions in a simple geometry (like a truss) are fully coupled because the temperature and the displacement fields mutually influence one another. A space-time modal analysis performed on the fractional-order system has provided the explicit solutions of the problem. The time evolution of each spatial mode for the temperature, displacement, and axial force turned out to be characterized by modulated Mittag-Leffler functions. The higher the deviation from the Fourier-like behaviour for the heat flux, the steeper the resulting time-transient of each mode. The influence of the deformability on the one hand and the discrepancy from the Fourier behavior on the other hand have been thoroughly analysed. Measures of the overall thermal work and of the associated available and dissipation energy rates have been evaluated both mode by mode and globally, enabling the characterization of the coupled response of anomalous thermoelastic trusses. In addition to determining the range of admissible discrepancies from the Fourier behavior, such quantities have been shown to fully reveal the manifestation of the thermal anomaly together with the effects of the elastic and thermal deformabilities.
In the last chapter the effects, for consolidation problems, of introducing a memory effect in the flux-pressure constitutive relation employed to describe the water diffusion phenomenon in porous media have been studied. In particular, the classic 1D Terzaghi's consolidation problem has been taken into account. The introduction of the memory effect has proven to be useful to capture non-Darcy behaviour. The main results shown that the time-evolution of both the displacement and pressure fields is strongly influenced by the order of Caputo fractional derivative. Higher is the order of the Caputo's derivative, higher will be the initial rise in time, with the tendency to reach steady values in longer times. Assuming the classical Darcy equation may mainly lead to inaccurate estimates of the consolidation time, as well as of the pressure field time evolution. When in presence of grain rearrangement and consequent compaction, or if the fluid carries solid particles which obstruct some of the pores, more accurate results can be obtained by simple, 2-parameters fractional models, both in case of sands and clay soils.

10.2 Conclusions

The research activity that has been developed is characterized by a significant multidisciplinary value and coordinates competences in

photonics, structure of matter, materials science, applied mathematics, analytical mechanical model for coupled phenomena and a hint of numerical simulations.
The realization of this thesis has increased the knowledge in important scientific and technological areas, ranging from fundamental physics to novel applications, through materials science and photonics and will give a specific contribution to the needs expressed in different institutional documents (Photonics21, Horizon 2020) about the perspectives in the field of optics, photonics and technology of matter, or those technologies and sciences that have a key role in the development of new goods and services in different sectors.
The obtained results pave the way to develop a technology for the creation of a new class of systems chromatically sensitive to external stimuli. This kind of structure may be considered as a low cost sensor that can be applied in different strategic areas ranging from food security to civil infrastructures; areas that have an impact on our quality of life and safety.
In fact, the final objective lies in using these systems to perform health monitoring of buildings, measuring, for example, the state of deformation and cracks or the determination of volatile organic compounds.
The originality of this class of systems is the working scheme of the structures, in fact, the application of an external stimulus will result in a variation of the optical and structural properties of the polymeric system, changing the optical responce as a function of the external stimuli (applied strain, organic solvents).
Now, thanks to the optimized design, it has been possibible also to detect by naked eye the changes in the system, without the necessity of external probes. It is worth mentioning that the created devices do not need external power for their operation.

While the first part of this thesis is focused on the strict connection between experiments, design and analytical models using real sample of colloidal photonic crystals or special kind of gratings made via colloidal route, the second part is maily focused on the development of novel model for coupled phenomena in order to capture the real physical behaviour of structured systems from an analytical point of view.
With the development of these novel analytical models using fractional derivatives it has been shown that ordered submicroscopic systems do not behave like bulky materials. This “special” behaviour is enhanced in the case of coupled phenomena as demonstrated in the case of thermomechanics and consolidation.

These novel models could lead to a new way of both interpretations of data and prediction of the expected behaviour more close to the real phenomenon with respect to the theoretical one.
For example, in has been demonstrated that a fractional model works for sandy soils and an experimental test aiming at evaluating the 2-parameters of the fractional Darcy law for clay soils could be conducted to further study the applicability of the proposed model for this type of porous medium.
These models for physical phenomena could lead to new trends in the interpretation and prediction of physical events that an engineer or researcher might experience in his everyday life which deals with complex systems.